UNIVERSIDAD DE GRANADA

FACULTAD DE CIENCIAS

DEPARTAMENTO DE QUÍMICA ORGÁNICA

PROGRAMA DE DOCTORADO EN QUÍMICA

HIDROGELES SUPRAMOLECULARES PEPTÍDICOS PARA LA OBTENCIÓN DE MATERIALES MULTICOMPONENTE CON APLICACIONES TECNOLÓGICAS

MEMORIA DE TESIS DOCTORAL

presentada por

SARA ILLESCAS LÓPEZ

para optar al título de DOCTOR por la UNIVERSIDAD DE GRANADA

dentro del Programa de Doctorado en Química

con mención de DOCTOR INTERNACIONAL

Directores:

Luis Álvarez de Cienfuegos Rodríguez y José Antonio Gavira Gallardo

Granada, 2024

Editor: Universidad de Granada. Tesis Doctorales
Autor: Sara Illescas López
ISBN: 978-84-1195-644-4
URI: https://hdl.handle.net/10481/98135

El trabajo recogido en esta memoria ha sido realizado en el grupo de investigación "Materiales Orgánicos Funcionales" (FQM-367) del Departamento de Química Orgánica de la Facultad de Ciencias de la Universidad de Granada y en el Laboratorio de Estudios Cristalográficos (LEC) del Instituto Andaluz de Ciencias de la Tierra (IACT) adscrito al Centro Superior de Investigaciones científicas (CSIC). Este trabajo está financiado por fondos FEDER/Junta de Andalucía-Consejería de Transformación Económica, Industria, Conocimiento y Universidades y por fondos del Ministerio de Ciencia, Innovación y Universidades. El trabajo se ha realizado gracias a un contrato de investigación predoctoral con Cargo al Proyecto a los proyectos P18-FR-3533, PID2020-118498GBI00 and PID2020-116261GB-I00.

Agradecimientos

"- Podrías decirme, por favor, ¿qué camino debo seguir para salir de aquí? - dijo Alicia.

- Esto depende en gran parte del sitio al que quieras llegar - dijo el Gato.

- No me importa mucho el sitio… - dijo Alicia.

- Entonces tampoco importa mucho el camino que tomes - dijo el Gato."

"Alicia en el País de las Maravillas" de Lewis Carroll.

Resumen

Los ***hidrogeles supramoleculares*** formados por ***péptidos cortos*** han ido ganado un creciente interés en la comunidad científica desde hace unos 20 años. Este hecho se debe, principalmente a que, al estar formados por moléculas presentes en los organismos vivos, presentan unas grandes características de ***biocompatibilidad y biodegradabilidad***, siendo adecuados para uso con fines ***terapéuticos y biomédicos***.

Sin embargo, si hay una característica que los hace aún más interesantes es su ***versatilidad desde el punto de vista químico***, dado que pueden adaptarse sus propiedades seleccionando diferentes aminoácidos que incorporen al esqueleto peptídico todas las propiedades deseadas para el material final, desde interacciones hidrofóbicas (aminoácidos aromáticos) a totalmente hidrofílicas (aminoácidos polares), así como la introducción de grupos de anclaje para distintos componentes, como las nanopartículas metálicas (metionina o cisteína). Esta ***gran variedad y adaptabilidad*** ha hecho que sus campos de aplicación se amplíen también hacía otros menos intuitivos como la ***electrónica molecular***. Así, este trabajo emplea la versatilidad de estos hidrogeles para desarrollar nuevos materiales multicomponente, abriendo nuevas fronteras de aplicación.

El ***capítulo 3*** desarrolla la aplicación de hidrogeles peptídicos en el recubrimiento de nanotubos de carbono y nanoláminas de grafeno para estudiar las propiedades del efecto de ***filtrado de espín inducido por quiralidad*** (***CISS***, por sus siglas en inglés) en estos sistemas. Así, se logran resultados muy prometedores para la aplicación de estos materiales híbridos en el campo de la ***espintrónica***.

El ***capítulo 4*** estudia la posibilidad de utilizar estos hidrogeles como plantilla de crecimiento de cristales inorgánicos, en este caso ***metal-organic frameworks*** (***MOFs***), con el objetivo de desarrollar nuevas familias de MOFs integrados con biomateriales o ***bio-MOFs***. Así, se han conseguido desarrollar dos nuevas familias de bio-MOFs, una basada en ZIF-8 y la otra en MOF-808. Además, como prueba de concepto se ha utilizado esta última en la ***eliminación de fosfatos*** de ambientes acuosos, donde pueden provocar graves problemas medioambientales como la eutrofización. Así como en la ***degradación de un pesticida*** de fósforo, el metilparaoxón, que es altamente tóxico, consiguiendo transformarlo en dos componentes menos dañinos, el 4-nitrofenol y el dimetilfosfato, con un mayor rendimiento que la contraparte sin biopolímero.

El ***capítulo 5*** emplea la capacidad de estos hidrogeles para ***coordinarse con distintos cationes metálicos*** y poder utilizarlos ***como plantilla para la formación de nanopartículas plasmónicas de plata y oro***. Se sigue un protocolo de ***química verde*** en el que no se usan reductores externos, sino que el hidrogel actúa como agente protector y reductor de las nanopartículas. También se ha desarrollado un ***material compuesto de varios geladores*** que consigue una mayor ***biocompatibilidad***. Estos hidrogeles han demostrado tener además una ***gran capacidad antimicrobiana***, siendo activos ante bacterias Gram-positivas, Gram-negativas y hongos. Además, han demostrado tener bastante ***eficacia frente a biofilms polimicrobianos***. Habiéndose probado también en sistemas *in vivo* y habiendo conseguido buenos resultados de cicatrización y tratamiento de heridas infectadas con *Staphylococcus aureus.*

Por último, el ***capítulo 6*** emplea algunos de los ***hidrogeles híbridos*** desarrollados en los tres capítulos anteriores como ***medio de crecimiento de cristales de***

proteína compuestos. Así, se ha conseguido un ***material sólido de estudio de efecto CISS*** por la obtención de cristales de lisozima en hidrogeles dopados con nanotubos de carbono. También se han desarrollado ***cristales de lisozima dopados con nanopartículas de plata y oro*** en un hidrogel diseñado para proteger las nanopartículas durante el crecimiento de los cristales proteicos, abriendo la puerta al empleo de estos sistemas en aplicaciones de antibacterianas de amplio espectro. Por último, se han obtenido ***cristales de proteína de tamaño controlado*** para su ***dopaje con paladio*** y su empleo como ***catalizadores en química bioortogonal***, con resultados prometedores para su uso como implantes en sistemas *in vivo*.

Summary

Supramolecular hydrogels formed by ***short peptides*** have garnered increasing interest in the scientific community over the past 20 years. This is primarily due to their composition of molecules found in living organisms, which grants them significant ***biocompatibility and biodegradability***, making them suitable for ***therapeutic and biomedical applications***.

However, one of their most compelling characteristics is their ***chemical versatility***. By selecting different amino acids, the properties of these hydrogels can be adapted, incorporating desired features into the peptide backbone. These properties can range from hydrophobic interactions (aromatic amino acids) to entirely hydrophilic ones (polar amino acids), as well as the introduction of anchoring groups for various components, such as metal nanoparticles (methionine or cysteine). This ***wide range of adaptability*** has expanded their potential applications to less intuitive fields, such as ***molecular electronics***. Accordingly, this work harnesses the versatility of these hydrogels to develop new multi-component materials, further broadening their application scope.

Chapter 3 explores the use of peptide hydrogels in coating carbon nanotubes and graphene nanosheets to study the properties of ***chirality-induced spin selectivity*** (***CISS***) effect in these systems. Promising results were obtained for the application of these hybrid materials in the field of ***spintronics***.

Chapter 4 investigates the potential of using these hydrogels as templates for the growth of inorganic crystals, specifically ***metal-organic frameworks (MOFs)***, with the aim of developing new families of MOFs integrated with biomaterials, or ***bio-MOFs***. As a result, two new families of bio-MOFs were developed, one

based on ZIF-8 and the other on MOF-808. Furthermore, as a proof of concept, the latter was used for the ***removal of phosphates*** from aqueous environments, where they can cause severe environmental issues such as eutrophication. The material was also applied in the ***degradation of a highly toxic phosphorus-based pesticide***, methyl paraoxon, transforming it into two less harmful compounds, 4-nitrophenol and dimethyl phosphate, with higher efficiency than its counterpart without biopolymer.

Chapter 5 utilizes the capacity of these hydrogels to ***coordinate with various metal cations,*** employing them as ***templates for the formation of plasmonic silver and gold nanoparticles***. A ***green chemistry*** protocol was followed, where no external reducing agents were used; instead, the hydrogel acted as both a protective and reducing agent for the nanoparticles. A composite ***material of multiple gelators*** was also developed, achieving greater ***biocompatibility***. These hydrogels have demonstrated ***strong antimicrobial activity***, showing efficacy against Gram-positive and Gram-negative bacteria, as well as fungi. Additionally, they were found to be ***effective against polymicrobial biofilms***. In vivo systems also showed promising results in wound healing and the treatment of infections caused by *Staphylococcus aureus*.

Finally, ***Chapter 6*** employs some of the ***hybrid hydrogels*** developed in the previous chapters ***as growth media for composite protein crystals***. A ***solid-state material*** was achieved for studying the ***CISS effect*** by obtaining lysozyme crystals in hydrogels doped with carbon nanotubes. ***Lysozyme crystals doped with silver and gold plasmonic nanoparticles*** were also developed within a hydrogel designed to protect the nanoparticles during protein crystal growth, paving the way for the use of these systems in broad-spectrum antibacterial

applications. Additionally, ***size-controlled protein crystals*** were obtained for ***doping with palladium*** and their use as ***catalysts in bioorthogonal chemistry***, showing promising results for potential *in vivo* implant applications.

Acronyms and abbreviations

1D	One-dimensional
3D	Three-dimensional
A	L-Alanine
a	Carbon-carbon distance to the nearest carbon for SOC
AFM	Atomic Force Microscopy
AgNP	Silver nanoparticle
AuNP	Gold nanoparticle
B	Magnetic field
C	L-Cysteine
CD	Circular Dichroism
CISS	Chiral Induced Spin Selectivity
CLSM	Confocal Laser Scanning Microscopy
CNTs	Carbon nanotubes
Cryo-EM	Cryogenic Electron Microscopy
Cryo-SEM	Cryogenic Scanning Electron Microscopy

Cryo-TEM	Cryogenic Transmission Electron Microscopy
D	L-Aspartic acid
DLS	Dynamic Light Scaterring
DMSO	Dimethylsulfoxide
DSC	Differential Scanning Calorimetry
DWCNT	Double-walled carbon nanotubes
E	L-Glutaminc acid
e.g.	*exempli gratia* (for example)
EM	Electron Microscopy
EMChA	Electromagnetochiral anisotropy
ESEM	Environmental Scanning Electron Microscopy
F	L-Phenylalanine
FF	Diphenylalanine
Fmoc	Fluorenylmethoxycarbonyl protecting group
Fmoc-AA	Fmoc-dialanine
Fmoc-FF	Fmoc-diphenylalanine
Fmoc-GG	Fmoc-diglycine

Fmoc-MF	Fmoc-methionine-pehylalanine
Fmoc-RGD	Fmoc-arginine-glycine-aspartic acid (Fmoc-Arg-Gly-Asp) tripeptide
FT-IR	Fourier-transform Infrared Spectroscopy
G	Glycine
G'	Elastic or storage modulus
G''	Viscosity or loss modulus
G*	Complex modulus
GdL	glucono-δ-lactone
GLs	Graphene layers
GO	Graphene oxide
H	L-Histidine
HmIm	2-methylimidazole
I	L-Isoleucine
I	Current
i.e.	*id est* (that is to say)
IR	Infrared radiation
K	L-Lysine

L	L-Leucine
LMWG	Low Molecular Weight Gelator
M	L-Methionine
m	Magnetization
MC	Magnetoconductance
mIm	2-methylimidazolate
MLG	Multi-Layer Graphene
MNP	Metal nanoparticle
MOF	Metal-organic frameworks
MR	Magnetoresistance
MWCNT	Multi-walled carbon nanotubes
N	L-Asparagine
NMR	Nuclear Magnetic Resonance
P	L-Proline
Q	L-Glutamine
R	L-Arginine
R	Resistance
r	Nanotube radius

RBM	Radial breathing mode
rGO	Reduced graphen oxide
S	L-Serine
SEM	Scanning electron microscopy
SLG	Single Layer Graphene
SOC	Spin-orbit coupling
SPPS	Solid-Phase Peptide Synthesis
STM	Scanning Tunneling Microscopy
SWCNT	Single Wall Carbon Nanotubes
T	L-Threonine
T	Temperature
TEM	Transmission Electron Microscopy
TM	Tangencial mode
UV-vis	Ultraviolet-Visible Spectroscopy
V	L-Valine
VRH	Variable range hopping
W	L-Tryptophan
XRD	X-ray diffraction

Y	L-Tyrosine
γ	Parameter for SOC in CNTs with values between 0,01 and 1
Δ	Normalized parameter for the quantification of magnetoresistance
θ	Magnetic field angle

Table of Contents

Appendices

Chapter 1

Introduction

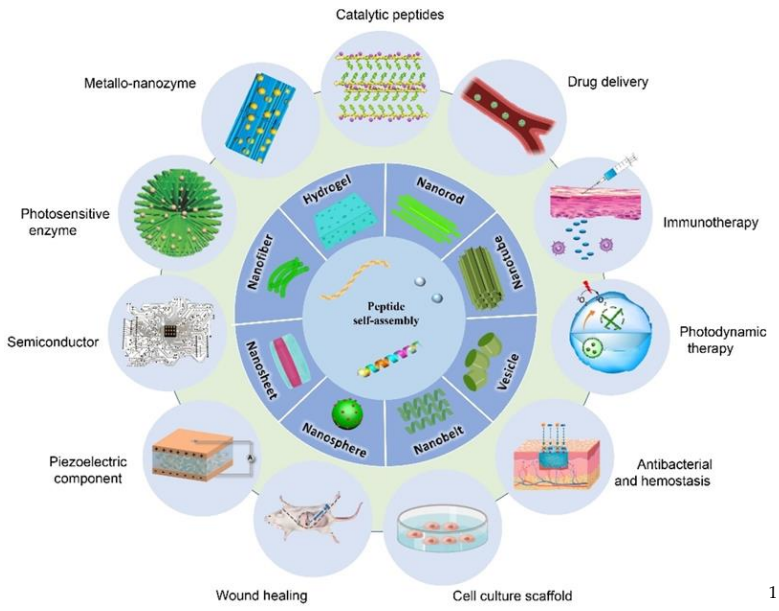

[1]

[1] Huo, Y.; Hu, J.; Yin, Y.; Liu, P.; Cai, K.; Ji, W. *ChemBioChem* **2023**, *24* (2), e202200582.

1. Concept and classification of gels

The word *gel* is common in daily life due to its presence in a wide variety of fields as diverse as cosmetics, medicine, personal care, or nutrition.[2] However, it is necessary to establish a clear concept of what a gel is from the point of view of its composition, structure, and properties. Therefore, an appropriate framework will be established to understand the fundamental concept around which this thesis revolves, and which will be developed later, that is, ***peptide supramolecular hydrogels.***

As Dorothy Jordan-Lloyd wrote in 1926, and many authors have cited during the last century, "the colloidal condition, the gel, is one which is easier to recognize than to define".[3] In fact, the first approach to the concept of gel dates to 1861 when Thomas Graham included a series of slowly diffusing substances in the category of *colloidal substances*.[4]

However, it was not until 1949, when P.H. Hermans formulated a more precise definition according to which a gel met three premises "a) they are coherent colloid systems of at least two components, b) they exhibit mechanical properties characteristic of a solid, and c) both the dispersed component and the dispersion medium extend themselves continuously throughout the whole system".[5]

---

[2] Djabourov, M. Chapter 1: Gels. In *New Developments in NMR*; De Deene, Y., Ed.; The Royal Society of Chemistry, 2020; pp 1–44.
[3] Jordan-Lloyd, D.; In. Colloid Chemistry. *red. Alexander J., Chem. Cat. Co., New York* **1926**, *1*.
[4] Graham, T. *Philos. Trans. R. Soc.* **1861**, *151*, 183–224.
[5] Hermans, P. H. Colloid Science. In *Colloid Science.*; Kruyt, H. R., Ed.; Elsevier Publishing Company Inc., Amsterdam., 1949; pp 483–651.

The above definition seemed to limit gels to two-components mixtures, excluding many of the substances known to form gels. Due to this problem, one of the most widespread and accepted definition of gel comes from Paul J. Flory, who in 1974 stated that "the one feature identified almost universally as an essential characteristic of a gel is its solid-like behaviour. When deformed its response is that of an elastic body. […], the modulus of elasticity is low. […] they must possess a continuous structure of some sort, the range of continuity of the structure being of macroscopic dimensions. […] the continuity of structure must possess a degree of permanency-at least for a period of time commensurate with the duration of the experiment".[6]

The term gel has been changing and adjusting for just over a century and a half. Therefore, to clarify this concept and establish a current definition, this thesis will include the definition established by the IUPAC and which says that a gel is a "non-fluid colloidal network or polymer network that is expanded throughout its whole volume by a fluid. Notes: 1) A gel has a finite, usually rather small, yield stress. 2) A gel can contain: (i) a covalent polymer network, […]; (ii) a polymer network formed through the physical aggregation of polymer chains […]; (iii) a polymer network formed through glassy junction points, […]; (iv) lamellar structures including mesophases, […]; (v) particulate disordered structures, […]".[7]

---

[6] Flory, P. J. *Faraday Discuss. Chem. Soc.* **1974**, *57*, 7–18.

[7] Alemán, J.; Chadwick, A. V.; He, J.; Hess, M.; Horie, K.; Jones, R. G.; Kratochvíl, P.; Meisel, I.; Mita, I.; Moad, G.; Penczek, S.; Stepto, R. F. T. Definitions of Terms Relating to the Structure and Processing of Sols, Gels, Networks, and Inorganic-Organic Hybrid Materials (IUPAC Recommendations 2007). In *Pure and Applied Chemistry*; 2007; Vol. 79, pp 1801–1829.

Once the gel concept has been fixed, a brief summary will be made of how the different types can be classified based on their origin, the medium in which they are formed, their constitution and the type of interaction between the *gelators*, i.e., the molecules that form the fibers of the final three-dimensional (3D) network in the gels, called *organogelators* when the liquid phase in which self-assembly occurs is an organic solvent and ***hydrogelators*** if the liquid phase is water.[8]

Depending on the medium or solvent that fibers contain, they can be ***hydrogels*** if the liquid phase is water, *organogel* if it is an organic solvent or *aero/xerogel* when the solvent trapped between the fibers is eliminated. Considering the origin of the gelators, it is possible to divide gels into *natural*, e.g., collagen, gelatine or agar, and *artificial*, i.e., formed by synthetic compounds such as polyester, poly(vinyl alcohol) or peptide derivatives. The latter can be subdivided according to their constitution into *macromolecular* gels formed by covalently or non-covalently interacting polymers, and ***supramolecular*** gels formed by the self-assembly of low molecular weight gelators through a combination of non-covalent interactions such as solvophobic forces, π-π stacking, van der Waals interactions or H-bonding. The following figure illustrates the concepts developed above and their interconnections.[9]

---

[8] a) Du, X.; Zhou, J.; Shi, J.; Xu, B. *Chem. Rev.* **2015**, *115* (24), 13165–13307. b) Gerbelli, B. B.; Vassiliades, S. V; Rojas, J. E. U.; Pelin, J. N. B. D.; Mancini, R. S. N.; Pereira, W. S. G.; Aguilar, A. M.; Venanzi, M.; Cavalieri, F.; Giuntini, F.; Alves, W. A. *Macromol. Chem. Phys.* **2019**, *220* (14), 1900085.

[9] a) Sangeetha, N. M.; Maitra, U. *Chem. Soc. Rev.* **2005**, *34* (10), 821–836. b) Du, X.; Zhou, J.; Shi, J.; Xu, B. *Chem. Rev.* **2015**, *115* (24), 13165–13307. c) Gerbelli, B. B.; Vassiliades, S. V; Rojas, J. E. U.; Pelin, J. N. B. D.; Mancini, R. S. N.; Pereira, W. S. G.; Aguilar, A. M.; Venanzi, M.; Cavalieri, F.; Giuntini, F.; Alves, W. A. *Macromol. Chem. Phys.* **2019**, *220* (14), 1900085.

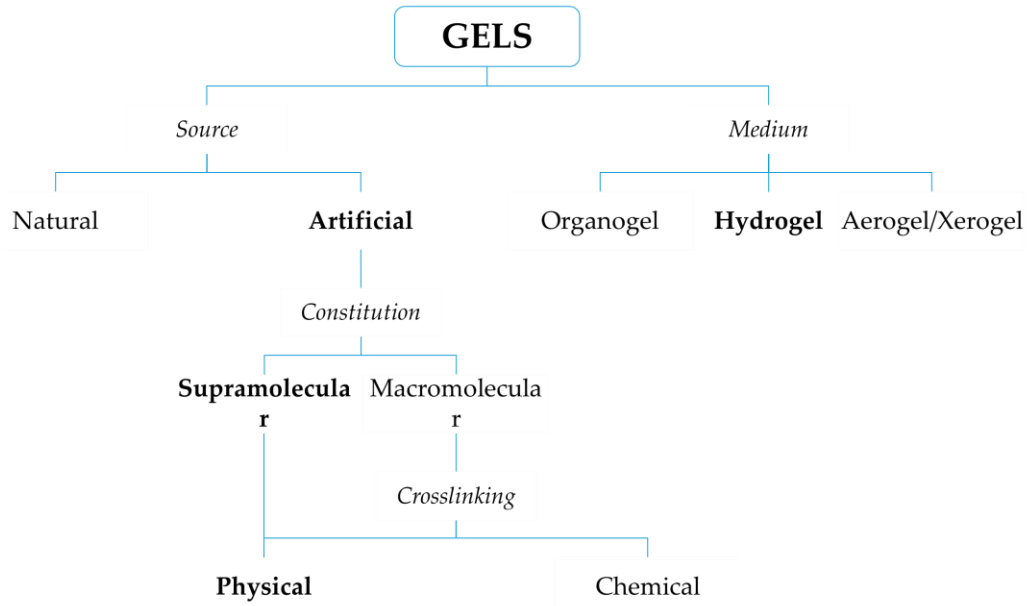

Figure 1. Classification of gels.

The concepts provided thus far have been aimed at laying the foundations for a correct understanding of the key concept in this work, which, as anticipated at the beginning, is peptide supramolecular hydrogels. This concept will be further developed in the following section.

2. Peptides as building blocks

For more than 30 years, peptides have been of great research interest for use in supramolecular chemistry and materials science. The main reason for this interest in these biomolecules is that they are formed by the bonding of amino acids and are present in all living organisms and are involved in many of the biological functions carried out in these organisms.[10]

Short peptides can be synthesised in solution phase, but larger molecules or peptides with particular sequences can be difficult to obtain in high purity and yield. Hence the development of solid-phase peptide synthesis (SPPS) in 1963 by R. B. Merrifield, awarded the 1984 Nobel Prize in Chemistry precisely for this milestone, enabled the rapid advancement of this field of research.

[10] a) Wang, Y.; Geng, Q.; Zhang, Y.; Adler-Abramovich, L.; Fan, X.; Mei, D.; Gazit, E.; Tao, K. *J. Colloid Interface Sci.* **2023**, *636*, 113–133. b) Reyes, C.; Patarroyo, M. A. *Int. J. Biol. Macromol.* **2024**, *259*, 128944. c) Huo, Y.; Hu, J.; Yin, Y.; Liu, P.; Cai, K.; Ji, W. *ChemBioChem* **2023**, *24* (2), e202200582.

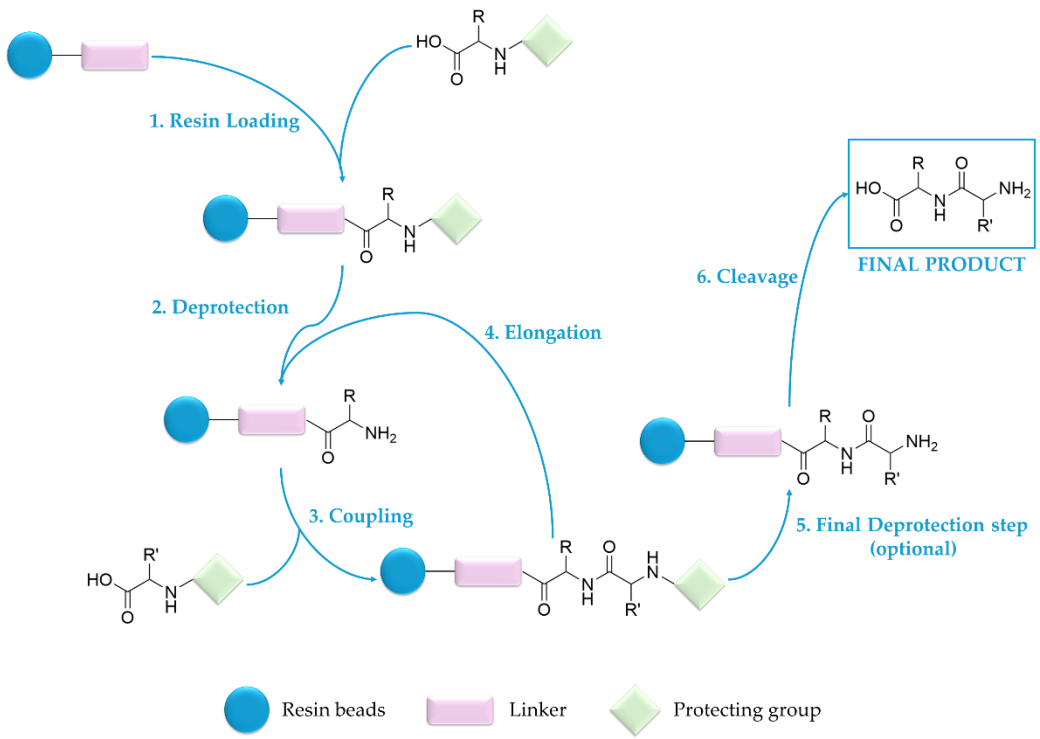

Figure 2. Schematic Representation of Solid-Phase Peptide Synthesis (SPPS).

This synthetic methodology proved to be very effective in obtaining peptide chains and short proteins with the desired amino acid sequence. In fact, the existence of 20 natural amino acids that could be combined at will opened up an almost infinite range of possibilities for sequences with defined and adjustable properties, both in terms of the biological functions they could perform and the way they could interact with other molecules, peptide or otherwise. The ability of certain molecules to interact and form supramolecular structures under specific experimental conditions, known as ***molecular self-assembly,*** will be a cornerstone of the research carried out in this thesis.[11]

[11] Reyes, C.; Patarroyo, M. A. *Int. J. Biol. Macromol.* **2024**, *259*, 128944.

Self-assembly of biomolecules, such as proteins and peptides, is ubiquitous in nature and supports many vital activities and biological functions. Peptides can self-assemble into nanomaterials with unique structures whose properties can be tuned by choosing an appropriate amino acid sequence. Inspired by nature, the self-assembly of short peptides is being widely explored due to its ease of preparation, biocompatibility and low cost. This phenomenon is dynamic and is governed by kinetic and thermodynamic control that balances intramolecular forces such as hydrophobicity, pH, ionic strength, temperature and solvent properties. Thermodynamic control depends on energy differences between states, while kinetic control is influenced by experimental conditions, allowing the formation of metastable states such as gels.[12]

Most early hydrogels consisted of small organic molecules, such as urea derivatives and amphiphilic amino acids, but further research has led to the development of a wide range of low molecular weight molecules that self-assemble into nanofibers to form a 3D network. These molecules are known as ***low molecular weight gelators*** (LMWG).[13] In this context, peptide molecules or derivatives tend to self-assemble, forming hydrogels with a three-dimensional fibrillar structure that traps a large amount of water.[14]

---

[12] a) Huo, Y.; Hu, J.; Yin, Y.; Liu, P.; Cai, K.; Ji, W. *ChemBioChem* **2023**, *24* (2), e202200582. b) Reyes, C.; Patarroyo, M. A. *Int. J. Biol. Macromol.* **2024**, *259*, 128944.

[13] a) Gagni, P.; Lodigiani, G.; Frigerio, R.; Cretich, M.; Gori, A.; Bergamaschi, G. *Chem. – A Eur. J.* **2024**, e202400974. b) Bianco, S.; Hasan, M.; Ahmad, A.; Richards, S.-J.; Dietrich, B.; Wallace, M.; Tang, Q.; Smith, A. J.; Gibson, M. I.; Adams, D. J. *Nature* **2024**, *631* (8021), 544–548.

[14] Hamley, I. W. *ACS Appl. Bio Mater.* **2023**, *6* (2), 384–409.

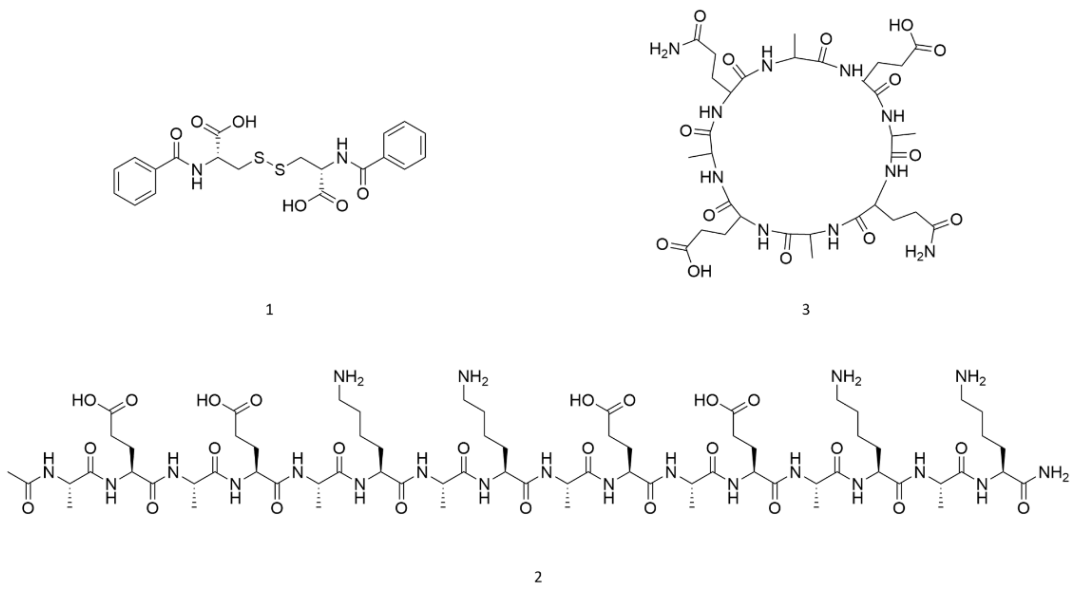

Figure 3. Chemical structure of the first peptide-based gelators.

The first known low molecular weight hydrogelator is dibenzoyl-L-cystine (1), as reported by Hoffman in 1921. This molecule was described almost two decades earlier by Karl Brenzinger. However, it was not until more than a hundred years later, in 2000, that Fredric Menger and Kevin Caran used methods such as X-ray crystallography, electron microscopy or rheology to study the gels formed with this molecule and its derivatives. These studies provided fundamental details to establish many of the principles that can be followed when designing new effective low molecular weight hydrogelators. One of the most relevant results of this study was that aromatic moieties are very effective in enhancing assembly in water. For good reason, this type of interaction can be found in nature during the evolution of proteins.[15] As will be seen throughout this report, this has contributed to the development of many hydrogelators with

[15] a) Gortner, R. A.; Hoffman, W. F. *J. Am. Chem. Soc.* **1921**, *43* (10), 2199–2202. b) Menger, F. M.; Caran, K. L. *J. Am. Chem. Soc.* **2000**, *122* (47), 11679–11691. c) Du, X.; Zhou, J.; Shi, J.; Xu, B. *Chem. Rev.* **2015**, *115* (24), 13165–13307.

aromatic rings that enable these interactions. These motifs, in peptide-based hydrogelators, are often included as side chains of the amino acid backbone, modifications at the N-terminal or C-terminal ends, or both.

Although the first hydrogelator was reported in 1921, it was not until the 1990s that studies of peptide molecules capable of forming different structures by self-assembly began to be published. Zhang et al. discovered in the early 1990s, serendipitously, that a yeast-derived peptide sequence, called EAK16, was able to form a membrane upon assembly. This fact led them to decide to study on the self-assembly of EAK16 (acetylated and aminated at the N-terminus and C-terminus, respectively) (2) and a series of EAK16 sequence-related peptides. This study established a comparison between the molecules derived from the sequence (2) and other peptides known to form β-sheets. Thus, the results obtained allowed them to propose that the formation of the membrane was due to the electrostatic interaction between the negatively charged glutamic acid (E) and positively charged lysine (K) side chains. Also, in 1993, Ghadiri et al. published a study on the self-assembly of a cyclic peptide (3) that in acidic media formed a nanotube by establishing intermolecular hydrogen bonds between the side chains of glutamic acid (E) and glutamine (Q).[16]

[16] a) Zhang, S.; Holmes, T.; Lockshin, C.; Rich, A. *Proc. Natl. Acad. Sci. U. S. A.* **1993**, *90* (8), 3334–3338. b) Reyes, C.; Patarroyo, M. A. *Int. J. Biol. Macromol.* **2024**, *259*, 128944. c) Ghadiri, M. R.; Granja, J. R.; Milligan, R. A.; McRee, D. E.; Khazanovlch, N. *Nature* **1993**, *366* (6453), 324–327. d) Raymond, D. M.; Nilsson, B. L. *Chem. Soc. Rev.* **2018**, *47* (10), 3659–3720.

Based on the examples above, one might think that the self-assembly of molecules might be related to the length of the molecules, but this is not the case. In 2001, Gazit et al. found the key role of phenylalanine (F) amino acid in the formation of β-amyloid fibers responsible for the Alzheimer's disease. This discovery opened the door to an broad field of research based on molecules that contain phenylalanine as an assembly motif in their structure.[17] The field that studies the self-assembly of short peptides (less than 5 amino acids) based on derivatives of this amino acid modified with aliphatic or aromatic groups at its C-terminal end is what has made possible the entire study carried out during this work, as will be seen below.

In 2019, Yuan et al.[18] investigated the mechanism underlying the self-assembly of short peptides or amino acids from a homogeneous solution to a supramolecular three-dimensional structure. Their findings revealed that this process occurs through the formation of dense liquid droplets. The formation of these droplets is a consequence of a liquid-liquid phase separation (LLPS) process. The formation of nanofibrils is thermodynamically favoured once the droplets have formed. It can therefore be surmised that the nucleation precursors are the solute-rich liquid droplets. The solvated nanoclusters present within these droplets act as heterogeneous nucleation centres, thereby reducing the nucleation barrier to the solid phase significantly through the presence of LLPS, which facilitates a metastable liquid phase. This is a notable difference from the

[17] Azriel, R.; Gazit, E. *J. Biol. Chem.* **2001**, *276* (36), 34156–34161.
[18] Yuan, C.; Levin, A.; Chen, W.; Xing, R.; Zou, Q.; Herling, T. W.; Challa, P. K.; Knowles, T. P. J.; Yan, X. *Angew. Chemie - Int. Ed.* **2019**, *58* (50), 18116–18123.

classical one-step nucleation observed in homogeneous solutions. This mechanism is summarized in Figure 4.

The preferred secondary structure that LMWG adopt during self-assembly is determined by the rigidity of the amide bonds, the polarity of the side chains, and their size. Thus, various types of secondary structures can be found in peptide systems, such as β-sheet, β-hairpin, α-helix, collagen triple helix, and coiled-coil. Despite the variety of possible organizations, it is worth noting that for LMWG with sequences shorter than 10 amino acids, the most common organization is the β-sheet. The helical structures need longer peptide sequences because the stabilization of the structure requires numerous intrastrand hydrogen bonds. The folding of the secondary structure is stabilized by hydrogen bonds between the carbonyl oxygen of one molecule and the amide hydrogen of the adjacent one.[19]

[19] a) Singh, N.; Kumar, M.; Miravet, J. F.; Ulijn, R. V.; Escuder, B. *Chem. - A Eur. J.* **2017**, *23* (5), 981–993. b) Amit, M.; Yuran, S.; Gazit, E.; Reches, M.; Ashkenasy, N. *Adv. Mater.* **2018**, *30* (41), 1707083.

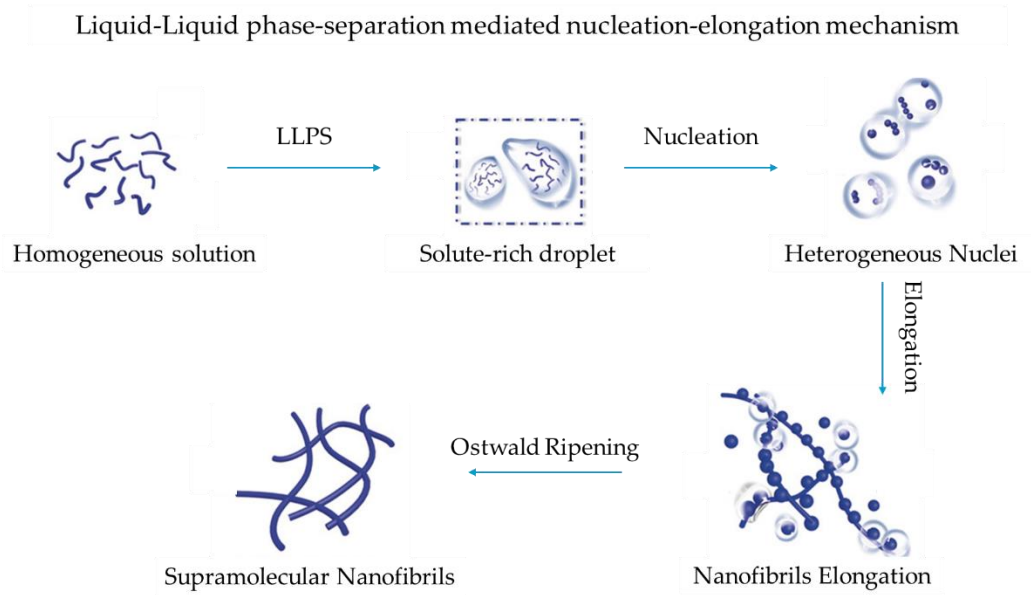

Figure 4. Peptide self-assembly process from solution to hydrogels.[20]

The side chains of the peptide sequence can form non-covalent interactions that help establish and define the 3D supramolecular structure. Thus, charged amino acids establish electrostatic interactions, polar amino acids contribute to the network of hydrogen bonds established between molecules, and aromatic amino acids are involved in π-π stacking interactions. On the other hand, from the point of view of their interaction with the water, peptides and their derivatives can be classified as hydrophobic, hydrophilic or amphiphilic. It is precisely the latter that attract most attention when designing hydrogelators with effective self-assembly.[21]

[20] Yuan, C.; Levin, A.; Chen, W.; Xing, R.; Zou, Q.; Herling, T. W.; Challa, P. K.; Knowles, T. P. J.; Yan, X. *Angew. Chemie - Int. Ed.* **2019**, *58* (50), 18116–18123.

[21] a) Amit, M.; Yuran, S.; Gazit, E.; Reches, M.; Ashkenasy, N. *Adv. Mater.* **2018**, *30* (41), 1707083. b) Singh, N.; Kumar, M.; Miravet, J. F.; Ulijn, R. V.; Escuder, B. *Chem. - A Eur. J.* **2017**, *23* (5), 981–993.

Amphiphilic peptides possess both hydrophobic and hydrophilic segments. Although the literature contains examples of amphiphilic peptides of increasing interest to researchers, such as bolaamphiphilic, i.e., sequences with a hydrophobic core and two hydrophilic ends, the most common design involves attaching an aliphatic or aromatic chain to one terminal end of a peptide sequence, which generally tends to form β-sheets.[22]

The morphology of the supramolecular structures formed is influenced not only by the chemical structure of the peptides themselves, but also by the medium in which the process takes place, since self-assembly is a kinetically controlled process. Thus, factors such as polarity, pH, ionic strength or the presence of other molecules will determine the type of structures formed. It is worth noting that, thanks to the combination of medium and chemical structure, peptide molecules have the ability to interact with other molecules, ions or surfaces, making it possible to obtain hybrid materials.[23]

The presence of aromatic groups and the amphiphilicity of the molecules are two complementary properties that help to establish effective interactions, leading to the formation of supramolecular structures. One of the modifications that has proven to be most effective and has been investigated for almost 20 years is the attachment of the fluorenylmethyloxycarbonyl (Fmoc) group to the N-terminal end of a short peptide sequence. Amazingly, in 2006, two independent studies by Ulijn and Gazit converged on the effectiveness of the peptide **Fmoc-**

[22] a) Amit, M.; Yuran, S.; Gazit, E.; Reches, M.; Ashkenasy, N. *Adv. Mater.* **2018**, *30* (41), 1707083. b) Hamley, I. W. *ACS Appl. Bio Mater.* **2023**, *6* (2), 384–409.

[23] a) Amit, M.; Yuran, S.; Gazit, E.; Reches, M.; Ashkenasy, N. *Adv. Mater.* **2018**, *30* (41), 1707083. b) Singh, N.; Kumar, M.; Miravet, J. F.; Ulijn, R. V.; Escuder, B. *Chem. - A Eur. J.* **2017**, *23* (5), 981–993.

diphenylalanine (Fmoc-FF) (8) to form rigid hydrogels. This molecule continues to be one of the most studied in the formation of supramolecular structures due to its unquestionable properties to form hydrogels with great mechanical properties and biocompatibility.[24]

Fmoc-FF settled the foundations for research on hydrogels based on short Fmoc-derived peptides. The versatility of this molecule in forming peptide hydrogels with a wide variety of applications and properties will be demonstrated below, particularly when combined with other components to form hybrid materials. However, not only has Fmoc-FF been used, but other Fmoc-derivative dipeptides have also been employed, either for comparison with Fmoc-FF or as achiral analogues. This includes **Fmoc-diglycine** (Fmoc-GG) (4), as the achiral analogue, **Fmoc-dialanine** (Fmoc-AA) (5), which it cannot establish π-π interactions through its side chains, and **Fmoc-methionine-phenylalanine** (Fmoc-MF) (7) or **Fmoc-cysteine-phenylalanine** (Fmoc-CF) (6), modified to include the thioether group as a strong interaction point for metallic nanoparticles formation. Furthermore, additional peptide analogues, such as **Fmoc-arginine-glycine-aspartic acid** (Fmoc-RGD) (9), have the potential to enhance the biocompatibility of hydrogels.

[24] a) Singh, N.; Kumar, M.; Miravet, J. F.; Ulijn, R. V.; Escuder, B. *Chem. - A Eur. J.* **2017**, *23* (5), 981–993. b) Amit, M.; Yuran, S.; Gazit, E.; Reches, M.; Ashkenasy, N. *Adv. Mater.* **2018**, *30* (41), 1707083. c) Reches, M.; Gazit, E. *Science.* **2003**, *300* (5619), 625–627. d) Jayawarna, V.; Ali, M.; Jowitt, T. A.; Miller, A. F.; Saiani, A.; Gough, J. E.; Ulijn, R. V. *Adv. Mater.* **2006**, *18* (5), 611–614. e) Mahler, A.; Reches, M.; Rechter, M.; Cohen, S.; Gazit, E. *Adv. Mater.* **2006**, *18* (11), 1365–1370.

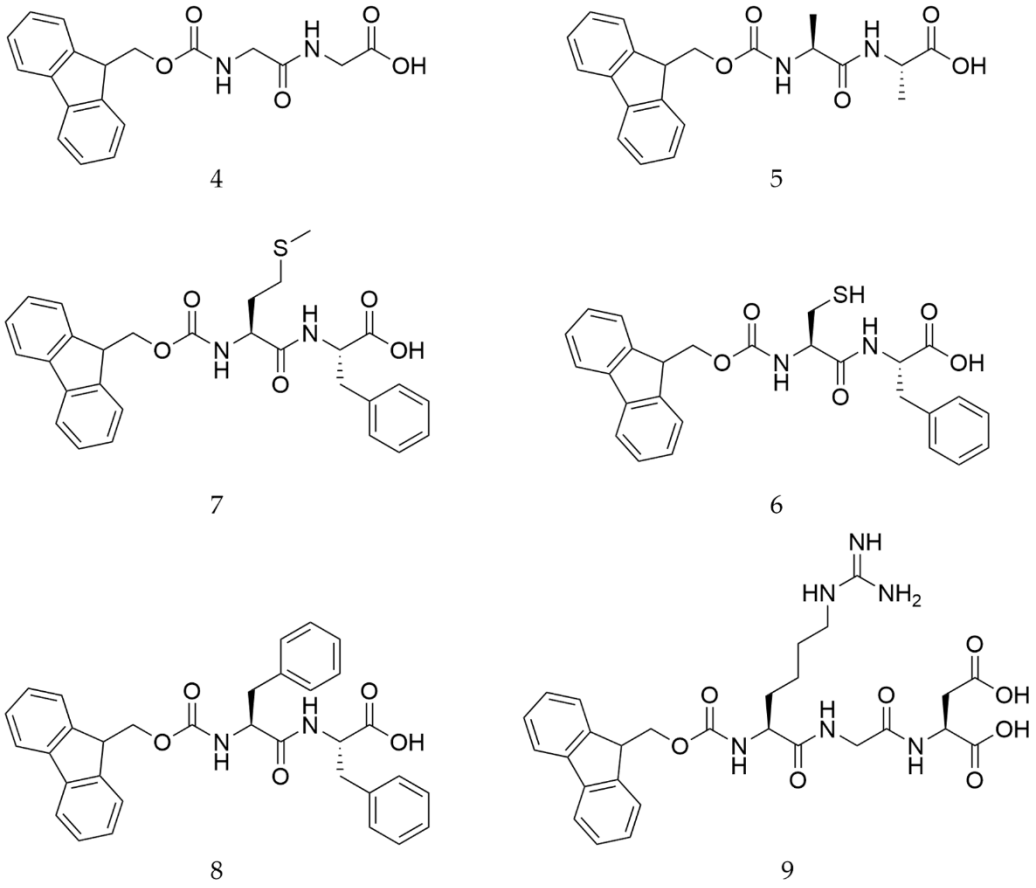

Figure 5. Peptide self-assembly process from solution to hydrogels.

3. Peptide-based Supramolecular Hydrogels

3.1. Introduction

Supramolecular chemistry was defined and popularized by Jean-Marie Lehn, who won the Nobel Prize of Chemistry in 1987 alongside Donald J. Cram and Charles J. Pederson "or their development and use of molecules with structure-specific interactions of high selectivity".

Lehn first used this concrete concept in 1978 in his work on macrocycles and inclusion complexes titled "Cryptates: Inclusion complexes of macropolycyclic receptor molecules".[25] However, it was not until 1988 when a broader and more precise definition was collected, integrating various characteristics established in previous works. Lehn defined supramolecular chemistry as the study of how non-covalent interactions between molecules form complex structures organized directionally through defined recognition motifs.[26]

The emergence of supramolecular chemistry has enabled the development of new nanostructures with complex and biomimetic functions. These structures are made up of molecular building blocks, e.g., peptide molecules, which are assembled to a high degree of arrangement. Moreover, these building blocks are often highly versatile and easily modifiable to suit the intended function of the final material, as discussed in section 2. Peptide-based supramolecular

[25] Lehn, J. M. *Pure Appl. Chem.* **1978**, *50* (9–10), 871–892.
[26] a) Lehn, J. *Angew. Chemie Int. Ed.* **1988**, *27* (1), 89–112. b) Gagni, P.; Lodigiani, G.; Frigerio, R.; Cretich, M.; Gori, A.; Bergamaschi, G. *Chem. – A Eur. J.* **2024**, e202400974.

nanomaterials often exhibit greater stability and performance than their individual building blocks.[27]

As mentioned above, a supramolecular hydrogel is obtained by the spontaneous self-assembly in water of the hydrogelators that compose it, obtaining a three-dimensional network that is maintained by non-covalent interactions. This structure traps a large amount of water between the fibers. These materials can also be defined as semi-solid gelatinous materials that are mostly composed of water, in some cases reaching over the 99% of their composition, which makes them excellent candidates for use in biomedical applications such as drug delivery, tissue engineering or as scaffolds for the growth of organic and inorganic structures.[28]

The following subsections will focus on a brief discussion of the driving forces behind these materials, the different protocols employed to prepare them and the characterisation techniques available for these materials.

3.2. Driving forces

Nature uses non-covalent interactions in numerous cases to stabilise complete structures such as the DNA double helix, the secondary, tertiary and quaternary structures of proteins or the lipid bilayer of cell membranes. The most common non-covalent interactions that occur in supramolecular systems are hydrogen

[27] Qi, G. Bin; Gao, Y. J.; Wang, L.; Wang, H. *Adv. Mater.* **2018**, *30* (22), 1703444.
[28] a) Du, X.; Zhou, J.; Shi, J.; Xu, B. *Chem. Rev.* **2015**, *115* (24), 13165–13307. b) Gagni, P.; Lodigiani, G.; Frigerio, R.; Cretich, M.; Gori, A.; Bergamaschi, G. *Chem. – A Eur. J.* **2024**, e202400974. c) Hamley, I. W. *ACS Appl. Bio Mater.* **2023**, *6* (2), 384–409. d) Amit, M.; Yuran, S.; Gazit, E.; Reches, M.; Ashkenasy, N. *Adv. Mater.* **2018**, *30* (41), 1707083.

bonds, hydrophobic and van der Waals interactions, π-π interactions and electrostatic interactions.

The chemical nature of the amino acids that make up the peptide sequence determines the type of interactions they can form with each other. Thus, non-polar amino acids, both aliphatic and aromatic, give rise to assembly by hydrophobic effects, forming hydrophobic or π-π stacking interactions respectively. Polar amino acids are divided into charged and uncharged, which makes the type of interaction they form different. Uncharged amino acids form hydrogen bonds, while charged amino acids participate in electrostatic interactions.[29]

[29] a) Ekiz, M. S.; Cinar, G.; Khalily, M. A.; Guler, M. O. *Nanotechnology* **2016**, *27* (40), 402002. b) Li, T.; Lu, X. M.; Zhang, M. R.; Hu, K.; Li, Z. *Bioact. Mater.* **2022**, *11*, 268–282.

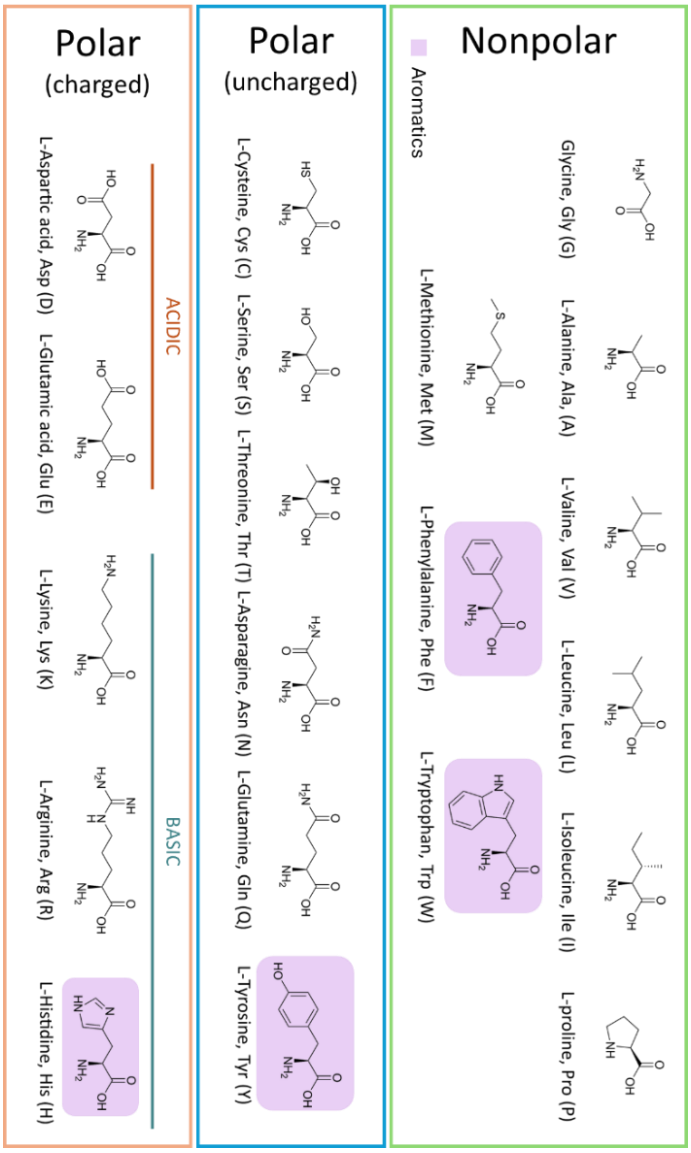

Figure 6. Classification of amino acids.[30]

[30] Dalangin, R.; Kim, A.; Campbell, R. E. *Int. J. Mol. Sci.* **2020**, *21* (17), 1–36.

However, it is not only the amino acids side chains that are responsible for stabilising the supramolecular structure, the peptide backbone itself also contributes to the supramolecular structure through hydrogen bonds between the oxygen of the carbonyl groups and the hydrogen of the amide group of the peptide bond. Previously it has been discussed that peptides can adopt an α-helix or β-sheet conformation, which in turn can be parallel or antiparallel. The difference between adopting one structure or the other is whether the hydrogen bonds are intermolecular, as in the case of β-sheets, or intramolecular, as in the case of α-helices. The α-helices can also wind around each other to form coiled coils. Although individually these interactions are weak, together they lead to the formation and stabilisation of the final superstructure and ensure a high degree of specificity in the system.[31]

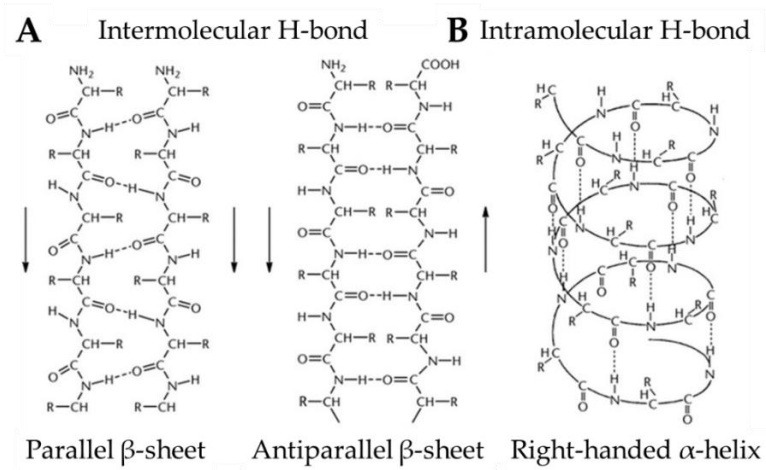

Figure 7. Hydrogen bonds stabilization in a) β-sheets and b) α-helixes.[32]

[31] a) Ekiz, M. S.; Cinar, G.; Khalily, M. A.; Guler, M. O. *Nanotechnology* **2016**, *27* (40), 402002. b) Li, T.; Lu, X. M.; Zhang, M. R.; Hu, K.; Li, Z. *Bioact. Mater.* **2022**, *11*, 268–282. c) Qi, G. Bin; Gao, Y. J.; Wang, L.; Wang, H. *Adv. Mater.* **2018**, *30* (22), 1703444.

[32] Qi, G. Bin; Gao, Y. J.; Wang, L.; Wang, H. *Adv. Mater.* **2018**, *30* (22), 1703444.

3.2.1. Hydrogen-bonding interactions

As already seen, hydrogen bonds are one of the most common forces involved in the self-assembly process and largely determine the final supramolecular structure. This bond has a strength intermediate between covalent bonding and van der Waals interactions, with a strength of 10-40 kJ/mol (at 298 K). The selectivity and directionality that hydrogen bonds have can lead to different nanostructures being formed. However, a hydrogel that can only establish hydrogen bonds during self-assembly is susceptible to solvation before it can form a hydrogel. Therefore, the design of hydrogelators is often amphiphilic, since it allows the establishment of complementary forces that favour the formation of hydrogels. Peptides have a large number of sites that can form hydrogen bonds, but adapting the number or position of these points can adjust the final properties of the hydrogel obtained. Moreover, these hydrogels are highly influenced by pH values.[33]

3.2.2. Hydrophobic interactions

Hydrophobic interactions are associated with the tendency of molecules with hydrophobic residues to reduce their contact with water. From a thermodynamic point of view, these interactions present an increment in entropy because the water molecules become more disordered by reducing their interaction with the hydrophobic residues, although the peptide molecules do decrease their degrees of freedom by 'ordering' themselves through these interactions. From an enthalpic point of view, it tends to have quite small values which, although

[33] a) Li, T.; Lu, X. M.; Zhang, M. R.; Hu, K.; Li, Z. *Bioact. Mater.* **2022**, *11*, 268–282. b) Omar, J.; Ponsford, D.; Dreiss, C. A.; Lee, T. C.; Loh, X. J. *Chem. - An Asian J.* **2022**, *17* (9), e202200081.

sometimes unfavourable to the global value of free energy, do not counteract the entropic part.[34]

As in the case of hydrogen bonding interactions, molecules that form hydrogels via hydrophobic interactions tend to show an amphiphilic character. Again, the strength of these hydrogels can be modulated by changing the number of residues that tend to form such interactions. Just as hydrogen-bonded hydrogels are strongly influenced by the pH value, here the most affecting factors are temperature and presence of salts.[35]

3.2.3. π-π interactions.

π-π stacking interactions are also common in peptide self-assembly. They are established between the side chains of aromatic amino acids and between aromatic groups such as Fmoc. These interactions can lead to directional growth and, contrary to hydrophobic interactions, present an ordered pattern. Molecules assembled through these interactions form very stable structures in water, as the presence of aromatic groups usually leads to a decrease in water solubility.[36]

---

[34] a) Singh, N.; Kumar, M.; Miravet, J. F.; Ulijn, R. V.; Escuder, B. *Chem. - A Eur. J.* **2017**, *23* (5), 981–993. b) Li, T.; Lu, X. M.; Zhang, M. R.; Hu, K.; Li, Z. *Bioact. Mater.* **2022**, *11*, 268–282.

[35] a) Omar, J.; Ponsford, D.; Dreiss, C. A.; Lee, T. C.; Loh, X. J. *Chem. - An Asian J.* **2022**, *17* (9), e202200081. b) Singh, N.; Kumar, M.; Miravet, J. F.; Ulijn, R. V.; Escuder, B. *Chem. - A Eur. J.* **2017**, *23* (5), 981–993.

[36] Li, T.; Lu, X. M.; Zhang, M. R.; Hu, K.; Li, Z. *Bioact. Mater.* **2022**, *11*, 268–282.

3.2.4. Electrostatic interactions

Electrostatic interactions are commonly used to induce structural specificity using charged peptides, are usually non-directional and have a rather weak binding energy. These interactions include attractive and repulsive electrostatic forces, as well as inter- and intramolecular interactions between different sites. The pH and ionic strength of the medium are two factors that strongly influence these interactions as they affect the charge of the amino acids.[37]

3.2.5. Dynamic covalent bonding

This section covers a type of interactions that, although they do not generally occur in the formation of peptide hydrogels, can be decisive for the properties of the final material when they appear. These interactions have a dynamic covalent nature and are reversible under certain mild conditions. These are the disulphide bridges that can be formed between cysteine residues and the imine bonds that are created by the reaction of aldehydes and amines.[38]

3.3. Formation protocols

There are different methods reported in literature for inducing the gelation of peptide molecules, including pH change, solvent change, heating/cooling cycles, enzymatic methods, light-induced reactions or the addition of salts.[39] In this section, only those methods that were used during the development of this thesis will be discussed.

---

[37] Li, T.; Lu, X. M.; Zhang, M. R.; Hu, K.; Li, Z. *Bioact. Mater.* **2022**, *11*, 268–282.
[38] Li, T.; Lu, X. M.; Zhang, M. R.; Hu, K.; Li, Z. *Bioact. Mater.* **2022**, *11*, 268–282.
[39] a) Zhang, S.; Holmes, T.; Lockshin, C.; Rich, A. *Proc. Natl. Acad. Sci. U. S. A.* **1993**, *90* (8), 3334–3338. b) Hamley, I. W. *ACS Appl. Bio Mater.* **2023**, *6* (2), 384–409.

3.3.1. Solvent switch

Molecules with a large number of hydrophobic groups, such as Fmoc-FF, are soluble in organic solvents, e.g., dimethyl sulfoxide (DMSO), acetone or ethanol, among others. In this way, a concentrated solution of hydrogelator can be prepared in one of these solvents. The ***solvent switch*** method consists of adding water to this stock solution, which triggers the formation of supramolecular aggregates that initially scatter light, and, after a few minutes, the mixture becomes transparent again. This change seems to indicate a reorganisation of the aggregates, which in their final phase form small, intertwined fibres smaller than the wavelength corresponding to visible light. This method was employed to form supramolecular peptide hydrogels by Gazit et al. in 2006 in their study about the self-assembly of Fmoc-FF.[40]

The organic solvent in which the original stock solution is made can have a great effect on the final morphology of the fibres and can even induce a chiral inversion of the fibre nanostructure.[41]

[40] a) Wang, Y.; Geng, Q.; Zhang, Y.; Adler-Abramovich, L.; Fan, X.; Mei, D.; Gazit, E.; Tao, K. *J. Colloid Interface Sci.* **2023**, *636*, 113–133. b) Diaferia, C.; Morelli, G.; Accardo, A. *J. Mater. Chem. B* **2019**, *7* (34), 5142–5155. c) Reches, M.; Gazit, E. *Science.* **2003**, *300* (5619), 625–627.

[41] a) Wang, Y.; Geng, Q.; Zhang, Y.; Adler-Abramovich, L.; Fan, X.; Mei, D.; Gazit, E.; Tao, K. *J. Colloid Interface Sci.* **2023**, *636*, 113–133. b) Li, T.; Lu, X. M.; Zhang, M. R.; Hu, K.; Li, Z. *Bioact. Mater.* **2022**, *11*, 268–282.

3.3.2. pH-switch

The change of pH is an effective and simple method to promote the self-assembly of peptide molecules with sensitive groups that can be protonated or deprotonated by the addition of small amounts of acid or base. Moreover, it can be easily followed with the use of a pH-meter or indicator paper. The ***pH-switch*** method usually requires first adjusting the pH of an aqueous gelator solution until its complete dissolution and then adjusting it back in the opposite direction to promote the self-assembly. Changes in pH lead to changes in the charge of the polar side chains influencing electrostatic interactions but can also alter the formation of hydrogen bonds by varying the bond strength between gelator and water molecules.[42]

The change in pH for the assembled systems leads to a change in apparent pKa for the fibres with respect to the building blocks, which for peptide systems based on molecules protected with the Fmoc group means that hydrogel formation is achieved at near neutral values when the theoretical pKa of the free peptides is around 3. This method was tested by Ulijn et al. in 2006, when they were investigating the gelation of Fmoc-derived systems. The first methodology was to adjust the pH of the gelator stock solution to 10.5 to avoid deprotection of the Fmoc group and then to acidify the medium by controlled addition of small amounts of hydrochloric acid (HCl). This led to the formation of heterogeneous gels due to a fast change in the pH of the medium.[43]

---

[42] a) Singh, N.; Kumar, M.; Miravet, J. F.; Ulijn, R. V.; Escuder, B. *Chem. - A Eur. J.* **2017**, *23* (5), 981–993. b) Du, X.; Zhou, J.; Shi, J.; Xu, B. *Chem. Rev.* **2015**, *115* (24), 13165–13307.

[43] a) Singh, N.; Kumar, M.; Miravet, J. F.; Ulijn, R. V.; Escuder, B. *Chem. - A Eur. J.* **2017**, *23* (5), 981–993. b) Diaferia, C.; Morelli, G.; Accardo, A. *J. Mater. Chem. B* **2019**, *7* (34), 5142–5155.

The introduction of mechanical mixing methods was the first solution to try to achieve more homogeneous gels. However, Adams et al. implemented a pH-switch using the hydrolysis of glucono-δ-lactone (GdL) to gluconic acid, which allowed a gradual pH change, resulting in more homogeneous and reproducible gels.[44]

3.3.3. Salts addition

This methodology was developed by Adams et al. in 2011 when they theorised that certain peptide solutions at high pH could be assembled by addition of divalent cations in a similar way to other biopolymers such as pectin or alginate. This occurred when they noticed that some of the peptide solutions in basic media had a viscous appearance, which could indicate aggregation of the molecules into worm-like micelles. So, they tried adding different solid salts to basic peptide solutions, obtaining gels with both divalent and monovalent cations. Although the gels obtained were heterogeneous when the salts were added in the solid state, they proposed the alternative of adding small amounts of very concentrated solutions of the salts in water, which resulted in more homogeneous gels.

[44] a) Diaferia, C.; Morelli, G.; Accardo, A. *J. Mater. Chem. B* **2019**, *7* (34), 5142–5155. b) Du, X.; Zhou, J.; Shi, J.; Xu, B. *Chem. Rev.* **2015**, *115* (24), 13165–13307. c) Chen, L.; Morris, K.; Laybourn, A.; Elias, D.; Hicks, M. R.; Rodger, A.; Serpell, L.; Adams, D. J. *Langmuir* **2010**, *26* (7), 5232–5242. d) Chen, L.; Pont, G.; Morris, K.; Lotze, G.; Squires, A.; Serpell, L. C.; Adams, D. J. *Chem. Commun.* **2011**, *47* (44), 12071–12073. e) Chen, L.; Revel, S.; Morris, K.; Adams, D. J. *Chem. Commun.* **2010**, *46* (24), 4267. f) Aufderhorst-Roberts, A.; Frith, W. J.; Kirkland, M.; Donald, A. M. *Langmuir* **2014**, *30* (15), 4483–4492. g) Li, T.; Lu, X. M.; Zhang, M. R.; Hu, K.; Li, Z. *Bioact. Mater.* **2022**, *11*, 268–282. h) Wang, Y.; Geng, Q.; Zhang, Y.; Adler-Abramovich, L.; Fan, X.; Mei, D.; Gazit, E.; Tao, K. *J. Colloid Interface Sci.* **2023**, *636*, 113–133.

Regarding the self-assembly process, they suggested that gel formation was caused by the formation of salt bridges between the carboxylates of the building blocks of the different aggregates. Other studies propose that this methodology can also be very effective in controlling the supramolecular chirality of fibres.[45]

3.2.6. Temperature

Self-assembly can show reversibility with temperature due to the temperature dependence of non-covalent interactions. The most common approach is to cool from a high temperature where a perfect solution of molecules occurs, but by lowering the temperature the aggregates begin to form leading to hydrogels. The opposite behaviour is also reported where the molecules form a precipitate at higher temperatures. This procedure was used to prepare the agarose hydrogel, so the chosen approach was a heating-cooling cycle.[46]

3.4. Characterization techniques

Supramolecular hydrogels require extensive characterization to achieve a comprehensive understanding of how small molecules assemble into fibers. This knowledge can facilitate the rational design of hydrogelators, and the development of new materials based on supramolecular arrangements. Several techniques can be used to study these materials, including ***rheology***, ***electron***

[45] a) Chen, L.; Pont, G.; Morris, K.; Lotze, G.; Squires, A.; Serpell, L. C.; Adams, D. J. *Chem. Commun.* **2011**, *47* (44), 12071–12073. b) Dou, X.; Mehwish, N.; Zhao, C.; Liu, J.; Xing, C.; Feng, C. *Acc. Chem. Res.* **2020**, *53* (4), 852–862.

[46] a) Dou, X.; Mehwish, N.; Zhao, C.; Liu, J.; Xing, C.; Feng, C. *Acc. Chem. Res.* **2020**, *53* (4), 852–862. b) Du, X.; Zhou, J.; Shi, J.; Xu, B. *Chem. Rev.* **2015**, *115* (24), 13165–13307. c) Zhang, Y.; Gu, H.; Yang, Z.; Xu, B. *J. Am. Chem. Soc.* **2003**, *125* (45), 13680–13681.

microscopy (EM), ***Fourier-transform infrared spectroscopy*** (FT-IR), ***circular dichroism*** (CD), and ***ultraviolet-visible spectroscopy*** (UV-Vis), among other.[47]

This section will provide an overview of the techniques commonly employed during the development of this thesis. It is worth highlighting that there are many examples in literature that use techniques like *nuclear magnetic resonance* (NMR), *fluorescence spectroscopy*, *differential scanning calorimetry* (DSC), *X-ray diffraction* (XRD) or *dynamic light scattering* (DLS) and that can be consulted.

3.4.1. Visual inspection

The simplest and quickest way to make an initial assessment of a gel is to use the 'vial inversion' method. This method gives a first impression of the shape and strength of the gel and allows the contents of the vial to be quickly classified as a solution, viscous liquid, semi-gel or self-supporting gel, which can help in an initial screening of gelation conditions or candidate gelator molecules.[48]

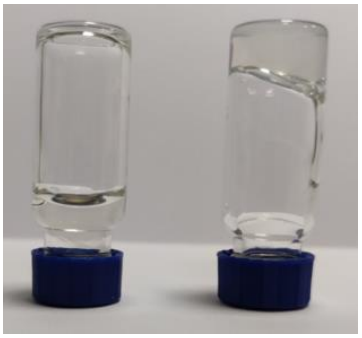

Figure 8. Vial inversion test of solution (left) and a self-supported hydrogel (right).

[47] a) Du, X.; Zhou, J.; Shi, J.; Xu, B. *Chem. Rev.* **2015**, *115* (24), 13165–13307. b) Amit, M.; Yuran, S.; Gazit, E.; Reches, M.; Ashkenasy, N. *Adv. Mater.* **2018**, *30* (41), 1707083. c) Ekiz, M. S.; Cinar, G.; Khalily, M. A.; Guler, M. O. *Nanotechnology* **2016**, *27* (40), 402002. d) Yu, G.; Yan, X.; Han, C.; Huang, F. *Chem. Soc. Rev.* **2013**, *42* (16), 6697–6722. e) Tao, K.; Levin, A.; Adler-Abramovich, L.; Gazit, E. *Chem. Soc. Rev.* **2016**, *45* (14), 3935–3953.
[48] Du, X.; Zhou, J.; Shi, J.; Xu, B. *Chem. Rev.* **2015**, *115* (24), 13165–13307.

3.4.2. Rheology

Rheology offers information about the type, quantity, and strength of the networks present in a hydrogel. Various geometries can be employed to perform tests, such as parallel plates, concentric cylinders, or plate-and-cone systems, all of which promote the formation of a thin layer of hydrogel between a stationary and a movable component. The fundamental principle of oscillatory rheometry is to measure the response of supramolecular hydrogels to an applied oscillatory stress, quantified by the elastic properties, such as the complex modulus (G*), the elastic or storage modulus (G′), and the loss modulus or viscosity (G′′). In the field of supramolecular hydrogels, two prevalent rheological experiments are performed: the linear response of the modulus (G′ and G′′) to a small, fixed amplitude while varying the frequency, and the nonlinear behaviour of the modulus at a fixed frequency while varying the shear stress. For typical supramolecular gels, the elastic modulus (G′) should remain frequency-invariant up to a yield point, which means the transition from a gel state to a sol state and should exceed the loss modulus (G′′) by at least one order of magnitude. A rapid decrease in G′ beyond the elastic limit indicates the disruption of the network structures.[49]

[49] a) Yu, G.; Yan, X.; Han, C.; Huang, F. *Chem. Soc. Rev.* **2013**, *42* (16), 6697–6722. b) Du, X.; Zhou, J.; Shi, J.; Xu, B. *Chem. Rev.* **2015**, *115* (24), 13165–13307.

3.4.3. Electron microscopy

Electron microscopy has the ability to study structures at nanometre resolution, as it uses an accelerated electron beam as a light source and the wavelength of an electron is very short. The techniques included in this area are ***transmission electron microscopy*** (TEM), ***scanning electron microscopy*** (SEM), *atomic force microscopy* (AFM) and ***confocal laser scanning microscopy*** (CLSM). The study of supramolecular hydrogels using these techniques provides information on the morphology of the self-assembled aggregates. However, the dehydration process to which they must be subjected and the use of staining elements to increase the resolution mean that the information obtained with these techniques may contain artifacts that can make it difficult to interpret. One way of trying to overcome this problem is the use of cryogenic techniques such as *cryogenic electron microscopy* (Cryo-EM) or the use of ***environmental scanning electron microscopy*** (ESEM). Generally, each technique provides complementary information to the others, so they tend to be used together.[50]

Transmission Electron Microscopy (TEM)

The electron beam employed in this technique interacts with the sample as it passes through, producing a two-dimensional image. Transmission electron microscopy (TEM) can yield extremely high-resolution images, enabling the study of supramolecular structures at the sub-nanometer scale. However, as previously noted, the drying and staining processes can alter the samples, resulting in observed morphologies that may not accurately reflect their true structure. The application of Cryo-TEM, which involves freezing samples in

[50] a) Du, X.; Zhou, J.; Shi, J.; Xu, B. *Chem. Rev.* **2015**, *115* (24), 13165–13307. b) Yu, G.; Yan, X.; Han, C.; Huang, F. *Chem. Soc. Rev.* **2013**, *42* (16), 6697–6722.

liquid nitrogen, can help minimize inconsistencies that arise when using xerogels.[51]

Scanning Electron Microscopy (SEM)

The images produced by this technique are obtained through a focused electron beam that scans the sample. The interaction between the electrons and the sample generates various signals, which are collected by different detectors to provide information about the topography and composition of the sample. Conventional SEM requires a high vacuum, requiring the use of dry hydrogels, which can lead to the appearance of artifacts. While Cryo-SEM is available, like Cryo-TEM, a more advantageous approach for scanning techniques is the use of ESEM. This technique allows for the analysis of hydrated samples under extremely low vacuum conditions, preserving the integrity of the material and providing more accurate and realistic information.[52]

Atomic-Force Microscopy (AFM)

Atomic force microscopy (AFM) enables the analysis of hydrated samples *in situ*, facilitating the examination of surface roughness and allowing classification based on mechanical properties. AFM collects information using a "spring-broad"-like cantilever that contacts the sample surface. This technique achieves resolution at the level of fractions of a nanometer. The cantilever bends in response to the attractive or repulsive forces of the surface that interacts with the tip, generating mechanical signals that are subsequently translated into data. An

[51] a) Yu, G.; Yan, X.; Han, C.; Huang, F. *Chem. Soc. Rev.* **2013**, *42* (16), 6697–6722. b) Ekiz, M. S.; Cinar, G.; Khalily, M. A.; Guler, M. O. *Nanotechnology* **2016**, *27* (40), 402002.
[52] a) Amit, M.; Yuran, S.; Gazit, E.; Reches, M.; Ashkenasy, N. *Adv. Mater.* **2018**, *30* (41), 1707083. b) Yu, G.; Yan, X.; Han, C.; Huang, F. *Chem. Soc. Rev.* **2013**, *42* (16), 6697–6722.

important limitation of AFM is that the probe tip can make hydrogels appear softer than their actual consistency.[53]

Confocal Laser Scanning Microscopy (CLSM)

This technique integrates fluorescence microscopy with laser scanning to deliver high-resolution optical images at various depths. This capability is particularly valuable and notable, as it facilitates the acquisition of point-by-point images, which are subsequently reconstructed to yield three-dimensional representations of samples with highly complex topologies.[54]

3.4.4. Spectroscopy

Spectroscopic techniques detect interactions between molecules or between molecules with the solvent that occur in primary and secondary structures. This detection provides information on the formation of supramolecular hydrogels.[55] This section will collect only Fourier-transform infrared spectroscopy (FT-IR), ultraviolet-visible spectroscopy (UV-Vis) and circular dichroism (CD) that are the technique used in this work, but the use of fluorescence spectroscopy and nuclear magnetic resonance (NMR) to study the interactions in supramolecular systems has also been reported.

---

[53] a) Yu, G.; Yan, X.; Han, C.; Huang, F. *Chem. Soc. Rev.* **2013**, *42* (16), 6697–6722. b) Du, X.; Zhou, J.; Shi, J.; Xu, B. *Chem. Rev.* **2015**, *115* (24), 13165–13307. c) Ekiz, M. S.; Cinar, G.; Khalily, M. A.; Guler, M. O. *Nanotechnology* **2016**, *27* (40), 402002.

[54] Yu, G.; Yan, X.; Han, C.; Huang, F. *Chem. Soc. Rev.* **2013**, *42* (16), 6697–6722.

[55] Du, X.; Zhou, J.; Shi, J.; Xu, B. *Chem. Rev.* **2015**, *115* (24), 13165–13307.

Infrared Spectroscopy (IR)

The assembly of supramolecular hydrogels can also be studied by infrared (IR) spectroscopy. This technique works in the infrared region of the electromagnetic spectrum and can provide valuable information confirming the presence of various interactions responsible for the self-assembly of building blocks. IR measure signals related to the molecular vibrations and throws information about conformational changes in molecules and aggregates. This technique is especially interesting to study these changes within regions of amide A (≈ 3200-3300 cm^{-1}), amide I (≈ 1600-1700 cm^{-1}), amide II (≈ 3200-3300 cm^{-1}) and amide III (≈ 3200-3300 cm^{-1}).[56]

Ultraviolet-visible Spectroscopy (UV-Vis)

This technique works in the ultraviolet-visible (UV-Vis) region of the electromagnetic spectrum in which molecules undergo electronic transitions. Molecules containing π electrons or non-bonding electron pairs can absorb visible or ultraviolet light and cause those electrons to be excited to a higher antibonding molecular orbital. The absorption spectrum shows the transition from the ground state to the excited state of the electrons.

[56] a) Yu, G.; Yan, X.; Han, C.; Huang, F. *Chem. Soc. Rev.* **2013**, *42* (16), 6697–6722. b) Du, X.; Zhou, J.; Shi, J.; Xu, B. *Chem. Rev.* **2015**, *115* (24), 13165–13307. c) Tao, K.; Levin, A.; Adler-Abramovich, L.; Gazit, E. *Chem. Soc. Rev.* **2016**, *45* (14), 3935–3953. d) Ekiz, M. S.; Cinar, G.; Khalily, M. A.; Guler, M. O. *Nanotechnology* **2016**, *27* (40), 402002.

This technique can provide information on π−π stacking or metal coordination and it is useful in combination with CD to provide information about the supramolecular chirality of the hydrogels, correlating the peaks that appear in a spectrum recorded in the region of 190-350 nm with those that will be obtained for CD spectra.[57]

Circular Dichroism (CD)

Circular dichroism (CD) is based on the different ability of chiral molecules and structures to absorb circularly polarized light and has significant advantages, including high sensitivity, the use of very small sample quantities and being a non-destructive technique. CD can operate in the same region as UV-vis instruments, but for studies involving Fmoc-derivative peptides, signals are recorded between 190 nm and 350 nm to capture the bisignate band corresponding to the Cotton effect, where the signal at 270-310 nm comes the π-π* electron transitions from the Fmoc group, while the other signals, related to the chromophore groups in peptides, are observed at 190-230 nm. This technique provides information about the conformational changes due to external stimuli; secondary structure, allowing the detection of β-sheets, α-helix or random coil; supramolecular chirality or interactions of peptides with other molecules or ions.[58]

---

[57] a) Yu, G.; Yan, X.; Han, C.; Huang, F. *Chem. Soc. Rev.* **2013**, *42* (16), 6697–6722. b) Du, X.; Zhou, J.; Shi, J.; Xu, B. *Chem. Rev.* **2015**, *115* (24), 13165–13307. c) Tao, K.; Levin, A.; Adler-Abramovich, L.; Gazit, E. *Chem. Soc. Rev.* **2016**, *45* (14), 3935–3953.

[58] a) Yu, G.; Yan, X.; Han, C.; Huang, F. *Chem. Soc. Rev.* **2013**, *42* (16), 6697–6722. b) Du, X.; Zhou, J.; Shi, J.; Xu, B. *Chem. Rev.* **2015**, *115* (24), 13165–13307. c) Ekiz, M. S.; Cinar, G.; Khalily, M. A.; Guler, M. O. *Nanotechnology* **2016**, *27* (40), 402002. d) Tao, K.; Levin, A.; Adler-Abramovich, L.; Gazit, E. *Chem. Soc. Rev.* **2016**, *45* (14), 3935–3953.

If an achiral sample is studied by CD, the resulting spectrum will be null, as it absorbs both polarizations in the same manner. However, chiral molecules generate a non-zero signal spectrum, due to the different behaviour they exhibited for absorbing polarized light. If the chiral molecules being compared are enantiomers, the spectra will be non-superimposable mirror images of each other.

Circular dichroism allows the study of the transfer of chirality from hydrogelators to supramolecular structures and also enables the investigation of changes in supramolecular chirality of fibers when combined with other molecules or when interactions are altered.[59]

3.5. Applications of Peptide Supramolecular Hydrogels

Supramolecular peptide hydrogels have been widely used in the field of biomedicine due to their high compatibility and low production costs. They have been applied as drug delivery systems, cell culture scaffolds, or tissue engineering, although these are not the only areas where they have been used.[60] The following figure pick up a variety of applications where these materials have been employed.

[59] a) Yu, G.; Yan, X.; Han, C.; Huang, F. *Chem. Soc. Rev.* **2013**, *42* (16), 6697–6722. b) Du, X.; Zhou, J.; Shi, J.; Xu, B. *Chem. Rev.* **2015**, *115* (24), 13165–13307. c) Ekiz, M. S.; Cinar, G.; Khalily, M. A.; Guler, M. O. *Nanotechnology* **2016**, *27* (40), 402002.

[60] Gagni, P.; Lodigiani, G.; Frigerio, R.; Cretich, M.; Gori, A.; Bergamaschi, G. *Chem. – A Eur. J.* **2024**, e202400974.

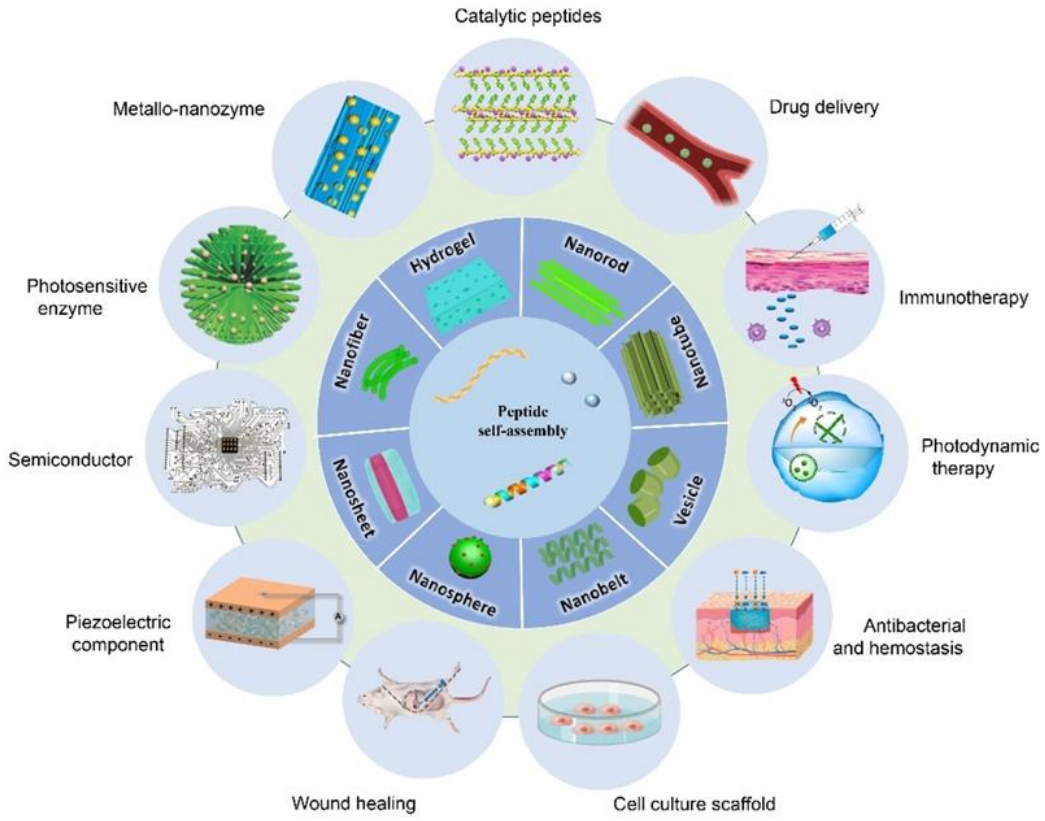

Figure 9. Some applications of peptide supramolecular materials.[61]

In addition to the numerous applications developed in the field of biomedicine, these hydrogels have been used as biosensors, photoactive materials, and their properties as semiconductors have been extensively studied.[62]

[61] Huo, Y.; Hu, J.; Yin, Y.; Liu, P.; Cai, K.; Ji, W. *ChemBioChem* **2023**, *24* (2), e202200582.

[62] a) Gerbelli, B. B.; Vassiliades, S. V; Rojas, J. E. U.; Pelin, J. N. B. D.; Mancini, R. S. N.; Pereira, W. S. G.; Aguilar, A. M.; Venanzi, M.; Cavalieri, F.; Giuntini, F.; Alves, W. A. *Macromol. Chem. Phys.* **2019**, *220* (14), 1900085. b) Huo, Y.; Hu, J.; Yin, Y.; Liu, P.; Cai, K.; Ji, W. *ChemBioChem* **2023**, *24* (2), e202200582. c) Singh, N.; Kumar, M.; Miravet, J. F.; Ulijn, R. V.; Escuder, B. *Chem. - A Eur. J.* **2017**, *23* (5), 981–993. d) Diaferia, C.; Morelli, G.; Accardo, A. *J. Mater. Chem. B* **2019**, *7* (34), 5142–5155. e) Tao, K.; Levin, A.; Adler-Abramovich, L.; Gazit, E. *Chem. Soc. Rev.* **2016**, *45* (14), 3935–3953. f) Abbas, M.; Ovais, M.; Atiq, A.; Ansari, T. M.; Xing, R.; Spruijt, E.; Yan, X. *Coord. Chem. Rev.* **2022**, *460*, 214481.

The number of research publications in the field of peptide supramolecular hydrogels is considerable, and as previously stated, includes a diverse range of applications. These applications have been extensively developed, and the literature contains numerous reviews categorized by themes. Therefore, this section will provide a summary of very recent selected articles, with the aim of offering a general context to prove the importance and versatility of these materials.

The control and tuneability of chiroptical properties in different systems have been extensively investigated. Two recent articles with peptide-based systems have been published relating to this field.

First, peptide derivatives with naphthalimide have been described that demonstrate ultrasonically activated supramolecular chirality, which is governed by the odd-even law of alkyl spacers. These dipeptides, which are conjugated to naphthalimide luminophores, undergo a transition from chiral nanoparticles to helical structures with distinct chiral optical properties, such as the Cotton effect and circularly polarized luminescence (CPL), upon ultrasound treatment.[63]

g) Cai, Y.; Zheng, C.; Xiong, F.; Ran, W.; Zhai, Y.; Zhu, H. H.; Wang, H.; Li, Y.; Zhang, P. *Adv. Healthc. Mater.* **2021**, *10* (1), 2001239. h) Sun, B.; Tao, K.; Jia, Y.; Yan, X.; Zou, Q.; Gazit, E.; Li, J. *Chem. Soc. Rev.* **2019**, *48* (16), 4387–4400. i) Tao, K.; Makam, P.; Aizen, R.; Gazit, E. *Science.* **2017**, *358* (6365). j) Sato, K.; Hendricks, M. P.; Palmer, L. C.; Stupp, S. I. *Chem. Soc. Rev.* **2018**, *47* (20), 7539–7551. k) Gagni, P.; Lodigiani, G.; Frigerio, R.; Cretich, M.; Gori, A.; Bergamaschi, G. *Chem. – A Eur. J.* **2024**, e202400974.

[63] Wang, Z.; Lu, J.; Hao, A.; Xing, P. *Small* **2024**, 2405698.

Also, a study on CPL in a low molecular weight dipeptide (Ala-Phe) bound to a tetraphenyl-ethylene (TPE) luminophore, which is known for its aggregation-induced emission (AIE) properties, has also been published. The study compares homochiral and heterochiral systems and finds that, in aqueous media, heterochiral systems form sheet-like structures with stronger CPL signals and higher dissymmetry values.[64]

The proliferation of multi-resistant microorganism renders imperative the development of new broad-spectrum antimicrobial materials. Thus, co-assembled hydrogels made from Fmoc-phenylalanine and Fmoc-lysine have been developed by Das Gupta et al. These hydrogels show enhanced antimicrobial properties not seen in the individual components. The Fmoc-lysine is covering a core of Fmoc-phenylalanine, forming fibers with the surface positively charged. This arrangement improves interaction with bacterial membranes, leading to effective membrane disruption and cell death.[65]

Additionally, Wiita et al. have investigated the small peptide KLVFF, that self-assembles into a fibrillar network, forming a self-healing hydrogel that can reversibly transition between gel and liquid states under shear stress. This hydrogel exhibits strong antibacterial and antifungal properties while being biocompatible and non-toxic to mammalian cells.[66]

---

[64] Bera, S.; Umesh, N.; Bhattacharya, S. *Chem. Sci.* **2024**, *15* (34), 13987–13997.
[65] Das Gupta, B.; Halder, A.; Vijayakanth, T.; Ghosh, N.; Konar, R.; Mukherjee, O.; Gazit, E.; Mondal, S. *J. Mater. Chem. B* **2024**, *25* (13), 23.
[66] Wiita, E. G.; Toprakcioglu, Z.; Jayaram, A. K.; Knowles, T. P. J. *ACS Appl. Mater. Interfaces* **2024**.

Cancer is a disease of global concern, considering that an increasing number of people are afflicted by it and that there are no effective treatments targeting only cancer cells. Therefore, the development of novel treatments that improve outcomes is the primary objective of many research efforts.

In their study, Ji et al. propose the use of a dual-target peptide as a potential therapeutic strategy for cancer treatment. This peptide is capable of selectively and rapidly self-assembling into cancer cell membranes, thereby facilitating the enrichment of luminogenic type I aggregation-induced emission-induced photosensitizers (AIEgen) through bioorthogonal reactions. Following irradiation with light, pyroptosis of the cancer cells is promoted by the PS.[67]

Furthermore, an additional study by Liu et al. develops an *in vivo* self-sorted peptide system for cancer therapy through the evolution of *in situ* assembly. The E3C16-SS-EIY peptide is composed of two distinct segments, E3C16SH and SHEIY, which can independently assemble into nanorods. Initially, the peptide forms nanorods; however, upon exposure to glutathione (GSH), it undergoes a conversion into self-ordered nanorods, which target the anti-apoptotic protein XIAP and the endoplasmic reticulum (ER), ultimately leading to cancer cell death by apoptosis.[68]

[67] Ji, S.; Pan, T.; Wang, K.; Zai, W.; Jia, R.; Wang, N.; *et al*. *Angew. Chemie Int. Ed.* **2024**, e202415735.
[68] Liu, X.; Tian, F.; Zhang, Z.; Liu, J.; Wang, S.; Guo, R. C.; *et al*. *J. Am. Chem. Soc.* **2024**, *146* (34), 24177–24187.

On the other hand, the study of Han et al. shows the importance of supramolecular systems in the detection of cancer. Thus, they present a stable bio detection interface utilising a trifunctional branched cyclopeptide that self-assembles into platinum nanoparticle (PtNP)-modified electrodes via strong Pt-S interactions, offering greater stability than Au-S bonds. This method enhances resilience to displacement in biological fluids and facilitates the sensitive detection of the breast cancer marker ErbB2 in human serum, enabling the differentiation of cancer patients from healthy individuals. The strategy markedly enhances the durability and performance of biosensors in complex environments.[69]

The combination of peptide hydrogels with other compounds to obtain hybrid materials open the door to extend their applicability fields. Mañas-Torres et al. incorporated magnetic nanoparticles into Fmoc-based biocompatible hydrogels with the objective of improving their mechanical properties, stability and injectability. Their findings demonstrated that these magnetic hydrogels promote cell growth, exhibit faster self-healing in mice and are suitable for minimally invasive biomedical applications due to their non-toxicity and remote-control capability using magnetic fields.[70]

[69] Han, R.; Li, Y.; Zhang, Y.; Wang, P.; Ding, C.; Luo, X.; Lv, S. *Sensors Actuators B Chem.* **2024**, *418*, 136321.

[70] Mañas-Torres, M. C.; Gila-Vilchez, C.; Vazquez-Perez, F. J.; Kuzhir, P.; Momier, D.; Scimeca, J.-C.; *et al. ACS Appl. Mater. Interfaces* **2021**, *13* (42), 49692–49704.

In other study, Mondal et al. present a method for creating high persistence length 1D arrays of metal nanoparticles using self-assembled peptide fibrils with asymmetrical charge distribution. This enables specific nanoparticle deposition, allowing the formation of 1D arrays with larger diameters and higher persistence lengths.

Also, uniform porous $CaCO_3$ microparticles with varying surface properties were employed to study dipeptide self-assembly by Ma et al. They found that negatively charged dipeptides assembled preferentially on hydrophobic and positively charged surfaces due to electrostatic and hydrophobic interactions.[71]

Finally, Rajchakit et al. have been employed different Fmoc-derivatives and their analogues as stabilizers and growth controllers for gold nanoparticles (AuNPs), obtaining a hydrogel with antimicrobial activity against *Staphylococcus aureus* and *Pseudomonas aeruginosa*.[72]

On the other hand, peptide systems are also ideal for the combination with proteins. Contreras-Montoya et al. developed a method for enhancing the stability and release profile of protein therapeutics was developed, with human insulin serving as a model. Two novel thermally stable insulin composite crystal formulations were reported, developed by crystallising insulin within agarose and Fmoc-AA hydrogels. The choice of hydrogel influences the crystals' stability and dissolution rates, with Fmoc-AA providing superior stability.[73]

---

[71] Ma, Y.; Wang, A.; Li, J.; Li, Q.; Han, Q.; Jing, Y.; Zheng, X.; Cao, H.; Yan, X.; Bai, S. *ACS Appl. Mater. Interfaces* **2023**, *15* (1), 2486–2497.
[72] Rajchakit, U.; Glossop, H. D.; Wang, K.; Lu, J.; Sarojini, V. *J. Pept. Sci.* **2024**, 1–12.
[73] Contreras-Montoya, R.; Arredondo-Amador, M.; Escolano-Casado, G.; Mañas-Torres, M. C.; González, M.; Conejero-Muriel, M.; *et al. ACS Appl. Mater. Interfaces* **2021**, *13* (10), 11672–11682.

Recently, Adams et al. has published a work that studies the employability of a peptide supramolecular hydrogel to stabilize proteins in buffer solution without the need for additional adjuvants, components, or keeping the cold chains, until their release through a mechanical device that retains the constituents of the supramolecular hydrogel, thus preventing their unwanted insertion into living systems.[74]

Furthermore, there is an increasing range of applications for supramolecular hydrogels, even well-known and established hydrogelators can be reinvented as in the study carried out by Tikhonova et al. where they developed a defrost sensor made from self-assembled Fmoc-FF-based hydrogels for monitoring pharmaceutical cold chains. This sensor uses changes in hydrogel turbidity to detect temperature variations.[75]

Also, Pirovano et al. have developed a supramolecular catalyst obtained through the self-assembly of diphenylalanine peptides conjugated to a triphenylphosphine Au(I) complex in acetonitrile.[76]

[74] Bianco, S.; Hasan, M.; Ahmad, A.; Richards, S.-J.; Dietrich, B.; Wallace, M.; Tang, Q.; Smith, A. J.; Gibson, M. I.; Adams, D. J. *Nature* **2024**, *631* (8021), 544–548.
[75] Tikhonova, T. N.; Cohen-Gerassi, D.; Arnon, Z. A.; Efremov, Y.; Timashev, P.; Adler-Abramovich, L.; Shirshin, E. A. *ACS Appl. Mater. Interfaces* **2022**, *14* (50), 55392–55401.
[76] Pirovano, V.; Brini, P.; Brambilla, E.; Gelmi, M. L.; Romanelli, A. *J. Pept. Sci.* **2024**, e3630.

Additionally, Gazit et al. have developed a novel glass composition comprising the aromatic tripeptide YYY, which forms spontaneously by non-covalent cross-linking with water. This supramolecular glass is characterised by its rigidity and self-healing properties at room temperature. Furthermore, it exhibits adhesive properties and is transparent in the visible and mid-infrared light spectrum.[77]

Finally, an increasingly studied and attention-grabbing field is the study and development of out-of-equilibrium systems, with a growing number of research efforts. In this context, transient systems fueled by EDC, developed by Professor Boekhoven's group, are garnering significant interest and are proposed to investigate the origins of life.[78]

[77] Finkelstein-Zuta, G.; Arnon, Z. A.; Vijayakanth, T.; Messer, O.; Lusky, O. S.; Wagner, A.; *et al*. *Nature* **2024**, *630* (8016), 368–374.

[78] a) Kriebisch, B. A. K.; Jussupow, A.; Bergmann, A. M.; Kohler, F.; Dietz, H.; Kaila, V. R. I.; Boekhoven, J. *J. Am. Chem. Soc.* **2020**, *142* (49), 20837–20844. b) Würbser, M. A.; Schwarz, P. S.; Heckel, J.; Bergmann, A. M.; Walther, A.; Boekhoven, J. *ChemSystemsChem* **2021**, *3* (5), e2100015. c) Späth, F.; Maier, A. S.; Stasi, M.; Bergmann, A. M.; Halama, K.; Wenisch, M.; Rieger, B.; Boekhoven, J. *Angew. Chemie Int. Ed.* **2023**, *62* (41), e202309318. d) Chen, X.; Soria-carrera, H.; Zozulia, O.; Boekhoven, J. **2023**, 17–23. e) Chen, X.; Stasi, M.; Rodon-Fores, J.; Großmann, P. F.; Bergmann, A. M.; Dai, K.; Tena-Solsona, M.; Rieger, B.; Boekhoven, J. *J. Am. Chem. Soc.* **2023**, *145* (12), 6880–6887. f) Späth, F.; Donau, C.; Bergmann, A. M.; Kränzlein, M.; Synatschke, C. V.; Rieger, B.; Boekhoven, J. *J. Am. Chem. Soc.* **2021**, *143* (12), 4782–4789.

Chapter 2

General Objectives

General objectives

The main objective of this thesis is to develop new hybrid materials that are of significant scientific interest and have potential applications in biotechnology and medicine. To this end, hybrid materials will be created through a directed design process, focusing on the study of their physicochemical properties and their applicability in various research areas. This research aims to improve our fundamental understanding of these areas and to broaden the potential applications of these materials.

The new gel-state hybrid materials will be obtained by combining Fmoc-derived dipeptides, which will be LMWGs, with other materials such as carbon allotropes (carbon nanotubes (CNTs) or graphene layers (GLs)) or inorganic salts that induce self-assembly while acting as growth promoters for inorganic nanoparticles or crystals.

The election of amino acids that make up the peptide sequence will play a key role in the final properties of the material due to the interactions they establish with each other and with the rest of the compounds. Therefore, different peptides will be synthesised to include specific motifs that allow the insertion of different desirable properties in each case.

The self-assembly of peptides in the presence of the compounds referred above will lead to the formation of hybrid systems that will exhibit a modification of the properties of these gels compared to their undoped counterparts. This will allow their use in fields such as spintronics and antibacterial materials, as well as acting as templates for the design of metal-organic frameworks (MOFs) or protein crystals doped with these compounds to confer new properties.

The general objectives for the development of this research are therefore as follows:

1. Synthesis and formation of supramolecular hydrogels, both control and in the presence of the different dopants.
2. Analysis of the physicochemical properties of hybrid hydrogels and examination of their applicability in diverse areas.
   2.1. Utilization of CNTs and GLs-doped materials to study the Chirality-Induced Spin Selectivity (CISS) effect.
   2.2. Investigation of the applicability of hybrid hydrogels with silver and gold metal nanoparticles as antibacterial materials.
3. Application of hybrid hydrogels as templates for the growth of inorganic crystals (MOFs) and protein crystals.
   3.1. Examination of the physicochemical properties of gel-MOF hybrid materials and assessment of their application in bioremediation.
   3.2. Characterization of doped protein crystals and evaluation of their application in various fields, such as the study of the CISS effect, broad-spectrum antibacterial drug delivery vehicles, or biocompatible catalytic supports.

Chapter 3

Chirality-Induced Spin Selectivity in Chiral Networks of Supramolecular Functionalized Carbon Allotropes

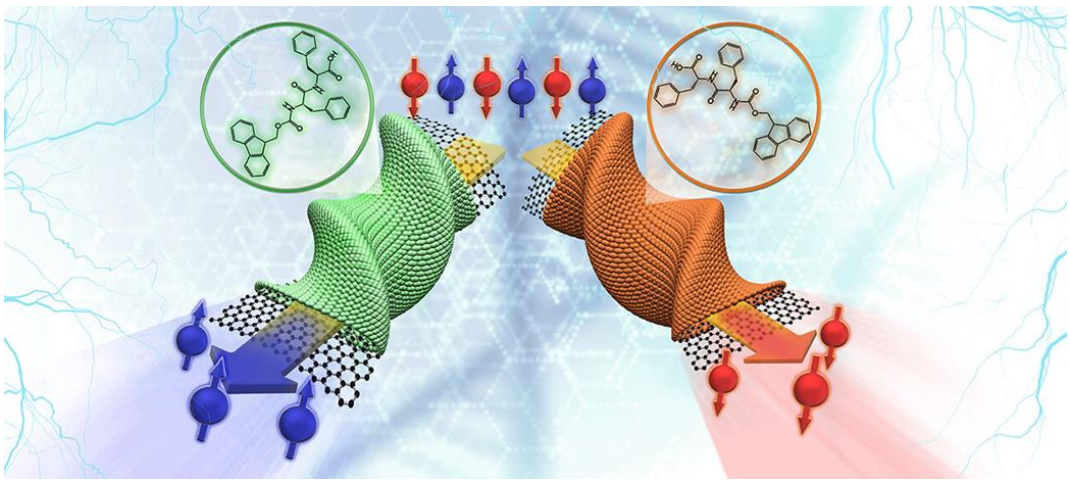

[79]

[79] Firouzeh, S.; Illescas-Lopez, S.; Hossain, M. A.; Cuerva, J. M.; Álvarez de Cienfuegos, L.; Pramanik, S. Chirality-Induced Spin Selectivity in Supramolecular Chirally Functionalized Graphene. *ACS Nano* **2023**, *17* (20), 20424–20433.

1. Background

The ***chirality-induced spin selectivity*** (CISS) effect was first described by Ron Naaman in 1999. This effect can manifest itself for both electron transmission and displacement current and refers to the phenomenon that occurs when the unpolarised electron carriers acquire a chirality-dependent spin polarization after being transmitted through a chiral medium. The attention that the CISS effect is receiving from the research community is due to its potential applications in various fields such as spintronics, optoelectronics, enantioseparation, and spin-selective electrochemical and biological processes.[80]

The fundamental point of the CISS effect is that chiral structures show a preference for transmitting a particular spin orientation, which can be used to create efficient, non-magnetic spin filters at the molecular scale. The point set out above is important for the miniaturization of spintronic devices and the design of quantum technologies. This effect leads to the generation of spin polarization when electrons pass through a chiral medium or to spin detection by chiral materials (Figure 10.a). Thus, the chiral medium can act as a spin polarizer or spin analyser, which is essential for spintronic devices. Although the origin of

[80] a) Ray, K.; Ananthavel, S. P.; Waldeck, D. H.; Naaman, R. *Science.* **1999**, *283* (5403), 814–816. b) Bloom, B. P.; Paltiel, Y.; Naaman, R.; Waldeck, D. H. *Chem. Rev.* **2024**, *124* (4), 1950–1991. c) Firouzeh, S.; Hossain, M. A.; Cuerva, J. M.; Álvarez de Cienfuegos, L.; Pramanik, S. *Acc. Chem. Res.* **2024**, *57* (10), 1478–1487. d) Evers, F.; Aharony, A.; Bar-Gill, N.; Entin-Wohlman, O.; Hedegård, P.; Hod, O.; *et al. Adv. Mater.* **2022**, *34* (13), 2106629. e) Aiello, C. D.; Abendroth, J. M.; Abbas, M.; Afanasev, A.; Agarwal, S.; Banerjee, A. S.; *et al. ACS Nano* **2022**, *16*, 4989–5035.

the CISS effect is still under debate, it is believed that the spin-orbit interaction of the medium play an important role.[81]

Spin filtering occurs due to the inherent asymmetry of enantiomers. When a charged particle, such as an electron, moves through a chiral molecule or medium, it experiences an electronic potential defined by the medium's intrinsic chirality. This potential generates a magnetic field that interacts with the electron's spin. Upon magnetization, electrons with a spin orientation opposite to the direction of this magnetic field encounter greater resistance to transport. Consequently, when a beam of unpolarized electrons passes through a chiral medium, the interaction between each electron's spin and the induced magnetic field results in one spin orientation being favoured over the other, leading to spin selectivity.[82]

Chirality is a property that has played a fundamental role in chemistry and biology because it is an intrinsic property of many organic molecules of interest in both fields, and it governs the interactions that determine their activity. This property refers to entities whose mirror images cannot be superimposed and there are different types of molecular chirality (Figure 10.b). The study of the interaction between chirality and the magnetic field, and its manifestation in

[81] a) Aiello, C. D.; Abendroth, J. M.; Abbas, M.; Afanasev, A.; Agarwal, S.; Banerjee, A. S.; *et al. ACS Nano* **2022**, *16*, 4989–5035. b) Evers, F.; Aharony, A.; Bar-Gill, N.; Entin-Wohlman, O.; Hedegård, P.; Hod, O.; *et al. Adv. Mater.* **2022**, *34* (13), 2106629. c) Michaeli, K.; Varade, V.; Naaman, R.; Waldeck, D. H. *J. Phys. Condens. Matter* **2017**, *29* (10), 103002. d) Firouzeh, S.; Illescas-Lopez, S.; Hossain, M. A.; Cuerva, J. M.; Álvarez de Cienfuegos, L.; Pramanik, S. *J. Chem. Phys.* **2023**, *159* (3). e) Firouzeh, S.; Illescas-Lopez, S.; Hossain, M. A.; Cuerva, J. M.; Álvarez de Cienfuegos, L.; Pramanik, S. *ACS Nano* **2023**, *17* (20), 20424–20433.

[82] Naaman, R.; Paltiel, Y.; Waldeck, D. H. *Nat. Rev. Chem.* **2019**, *3* (4), 250–260.

various optical and transport processes, has also been of growing interest in past decades.[83]

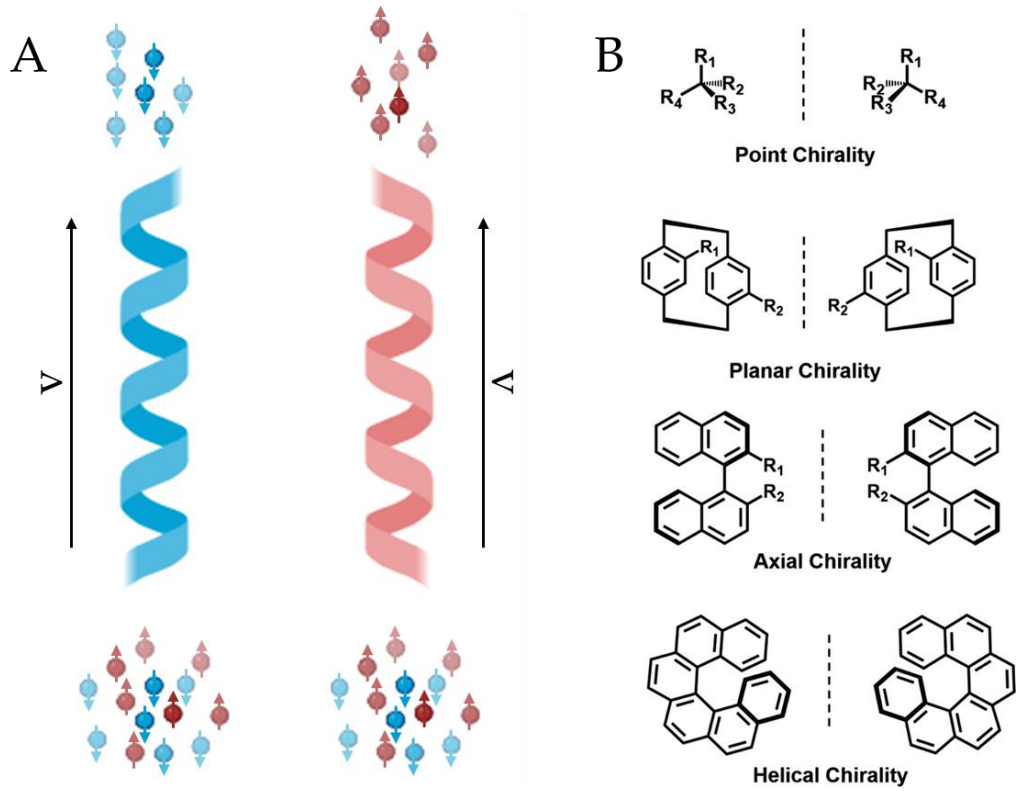

Figure 10. a) Schematic description of the CISS effect. b) Different types of molecular chirality.[84]

[83] a) Hembury, G. A.; Borovkov, V. V.; Inoue, Y. *Chem. Rev.* **2008**, *108* (1), 1–73. b) Atzori, M.; Train, C.; Hillard, E. A.; Avarvari, N.; Rikken, G. L. J. A. *Chirality* **2021**, *33* (12), 844–857. c) Zhao, T.; Duan, P.; Liu, M. Circularly Polarized Luminescence from Gelator Molecules: From Isolated Molecules to Assemblies. In *Circularly Polarized Luminescence of Isolated Small Organic Molecules*; Springer Singapore: Singapore, 2020; pp 249–272.

[84] Zhao, T.; Duan, P.; Liu, M. Circularly Polarized Luminescence from Gelator Molecules: From Isolated Molecules to Assemblies. In *Circularly Polarized Luminescence of Isolated Small Organic Molecules*; Springer Singapore: Singapore, 2020; pp 249–272.

Molecules such as DNA, amino acids, polypeptides, helices and many others are chiral, which has made them the molecules of choice for CISS studies. However, these molecules have an insulating character, which poses a problem when integrating them into electronic devices and circuits. On the other hand, inorganic conducting materials, which are promising for applications in spintronics and electronics, lack chirality, which means that they do not exhibit the CISS effect in their natural form. In order to solve this problem, materials have been developed that integrate both systems, such as the strategy followed in the development of this thesis, in which it has been shown that it is possible to induce the CISS effect in non-chiral carbon materials when they are functionalized with chiral molecules.[85]

[85] a) Göhler, B.; Hamelbeck, V.; Markus, T. Z.; Kettner, M.; Hanne, G. F.; Vager, Z.; Naaman, R.; Zacharias, H. *Science.* **2011**, *331* (6019), 894–897. b) Xie, Z.; Markus, T. Z.; Cohen, S. R.; Vager, Z.; Gutierrez, R.; Naaman, R. *Nano Lett.* **2011**, *11* (11), 4652–4655. c) Dor, O. Ben; Yochelis, S.; Mathew, S. P.; Naaman, R.; Paltiel, Y. *Nat. Commun. 2013 41* **2013**, *4* (1), 1–6. d) Kiran, V.; Mathew, S. P.; Cohen, S. R.; Hernández Delgado, I.; Lacour, J.; Naaman, R. *Adv. Mater.* **2016**, *28* (10), 1957–1962. e) Kulkarni, C.; Mondal, A. K.; Das, T. K.; Grinbom, G.; Tassinari, F.; Mabesoone, M. F. J.; Meijer, E. W.; Naaman, R. *Adv. Mater.* **2020**, *32* (7), 1–7. f) Rahman, M. W.; Firouzeh, S.; Mujica, V.; Pramanik, S. *ACS Nano* **2020**, *14* (3), 3389–3396. g) Rahman, M. W.; Mañas-Torres, M. C.; Firouzeh, S.; Illescas-Lopez, S.; Cuerva, J. M.; Lopez-Lopez, M. T.; de Cienfuegos, L. Á.; Pramanik, S. *ACS Nano* **2022**, *16* (10), 16941–16953. h) Firouzeh, S.; Illescas-Lopez, S.; Hossain, M. A.; Cuerva, J. M.; Álvarez de Cienfuegos, L.; Pramanik, S. *J. Chem. Phys.* **2023**, *159* (3). i) Hossain, M. A.; Illescas-Lopez, S.; Nair, R.; Cuerva, J. M.; Álvarez de Cienfuegos, L.; Pramanik, S. *Nanoscale Horizons* **2023**, *8* (3), 320–330. j) Firouzeh, S.; Illescas-Lopez, S.; Hossain, M. A.; Cuerva, J. M.; Álvarez de Cienfuegos, L.; Pramanik, S. *ACS Nano* **2023**, *17* (20), 20424–20433.

In the work presented here, Fmoc-peptides have been used to functionalize the carbon materials. These molecules are ideal for dispersing and solvate these materials due to their hydrophobic character of the aromatic groups that form part of their chemical structure. In this way, homogeneous hydrogels can be obtained in which the carbon material is well distributed throughout the 3D structure. The group's first work in this area showed that the incorporation of CNTs into a peptide hydrogel significantly improved its mechanical properties while at the same time providing electrical conductivity. This work opened the door to the use of these hybrid materials in the study of the CISS effect.[86]

As discussed during the general introduction chapter, the self-assembly of Fmoc-dipeptides, especially Fmoc-FF, in water is mainly mediated by hydrophobic interactions between the peptide molecules. This process can be triggered by different stimuli, and once self-assembly is promoted, fiber formation is strongly favoured.

This formation of fibers causes that, if there are solid particles in the medium, these remain included within the fibers, forming part of the final supramolecular structure, obtaining hybrid materials. This process favours the establishment of a strong interaction between the peptide fibers and the particles, whose surface ends up fully functionalized. In addition, if the solid material is flexible, it can undergo morphological alterations in its structure, with the peptide fibers as a template. At the same time, the supramolecular conformation of the peptides can also be altered by the interaction with the particles, resulting in some cases in a

[86] Contreras-Montoya, R.; Escolano, G.; Roy, S.; Lopez-Lopez, M. T.; Delgado-López, J. M.; Cuerva, J. M.; Díaz-Mochón, J. J.; Ashkenasy, N.; Gavira, J. A.; Álvarez de Cienfuegos, L. *Adv. Funct. Mater.* **2019**, *29* (5), 1807351.

reversal of the supramolecular chirality, which can be verified by changes in the sign of the Cotton bands in the CD spectra.[87]

There are two common configurations for performing CISS effect measurements. On the one hand, when the object of study is one or a few molecules, ***magnetoconductance*** (MC) measurements are usually performed using the tip of an atomic force microscope (AFM) (Figure 11.a) , while when a large number of molecules or networks of a material are studied, a solid-state device with a two-terminal geometry is usually used (Figure 11.b). The former configuration requires many scans under identical conditions and statistical post-processing of all these measurements, since the uncertainty in establishing good contact between the tip and the molecule leads to significant fluctuations in the measurements. With respect to the solid-state configuration, the signals obtained are usually weaker than in the previous one, probably due to the heterogeneity of the medium, which generates spin polarizations in different current paths that are not equivalent.[88]

Since the CISS effect is to be studied here in a network of supramolecular functionalized carbon material, the configuration used is a solid-state device with a two-terminal geometry in which the chiral material is placed between two electrodes, a non-magnetic gold (Au) and a ferromagnetic nickel (Ni) electrode.

---

[87] Fichman, G.; Adler-Abramovich, L.; Manohar, S.; Mironi-Harpaz, I.; Guterman, T.; Seliktar, D.; Messersmith, P. B.; Gazit, E. *ACS Nano* **2014**, *8* (7), 7220–7228.

[88] a) Xie, Z.; Markus, T. Z.; Cohen, S. R.; Vager, Z.; Gutierrez, R.; Naaman, R. *Nano Lett.* **2011**, *11* (11), 4652–4655. b) Kiran, V.; Mathew, S. P.; Cohen, S. R.; Hernández Delgado, I.; Lacour, J.; Naaman, R. *Adv. Mater.* **2016**, *28* (10), 1957–1962. c) Kulkarni, C.; Mondal, A. K.; Das, T. K.; Grinbom, G.; Tassinari, F.; Mabesoone, M. F. J.; Meijer, E. W.; Naaman, R. *Adv. Mater.* **2020**, *32* (7), 1–7. d) Mathew, S. P.; Mondal, P. C.; Moshe, H.; Mastai, Y.; Naaman, R. *Appl. Phys. Lett.* **2014**, *105* (24).

The chiral medium can be considered a spin filter in which the spin polarization will have a component parallel or antiparallel to the current depending on the chirality of the material. Thus, as the ***magnetization*** (*m*) of the Ni electrode changes from parallel to antiparallel (+*m* or -*m*) to the current (*I*) through a magnetic field (*B*), there are different spin transmission probabilities, which generate different currents (I^+ and I^-), and this difference is often referred to as the CISS effect. This magnitude can be quantified by various parameters such as the differential conductance (ΔG), the relative change in resistance with respect to a reference resistance ($\Delta R/R$) or the relative change in current with respect to a reference current ($\Delta I/I$). The key point is that the sign of any of these parameters is reversed for each enantiomer.[89]

The spin unpolarized charge carriers are injected from the Au electrode and travel through the material by phonon-assisted and electric field-assisted hopping, moving from one localized state to another in the transport direction (Figure 11.c). These localized states correspond to the conducting regions of the nanotubes, separated by electrical barriers created by molecular functionalization or by inter-tube junctions and defects. Polarization occurs

[89] a) Aiello, C. D.; Abendroth, J. M.; Abbas, M.; Afanasev, A.; Agarwal, S.; Banerjee, A. S.; *et al. ACS Nano* **2022**, *16*, 4989–5035. b) Göhler, B.; Hamelbeck, V.; Markus, T. Z.; Kettner, M.; Hanne, G. F.; Vager, Z.; Naaman, R.; Zacharias, H. *Science.* **2011**, *331* (6019), 894–897. c) Xie, Z.; Markus, T. Z.; Cohen, S. R.; Vager, Z.; Gutierrez, R.; Naaman, R. *Nano Lett.* **2011**, *11* (11), 4652–4655. d) Kiran, V.; Mathew, S. P.; Cohen, S. R.; Hernández Delgado, I.; Lacour, J.; Naaman, R. *Adv. Mater.* **2016**, *28* (10), 1957–1962. e) Kulkarni, C.; Mondal, A. K.; Das, T. K.; Grinbom, G.; Tassinari, F.; Mabesoone, M. F. J.; Meijer, E. W.; Naaman, R. *Adv. Mater.* **2020**, *32* (7), 1–7. f) Lu, H.; Wang, J.; Xiao, C.; Pan, X.; Chen, X.; Brunecky, R.; Berry, J. J.; Zhu, K.; Beard, M. C.; Vardeny, Z. V. *Sci. Adv.* **2019**, *5* (12). g) Liu, T.; Wang, X.; Wang, H.; Shi, G.; Gao, F.; Feng, H.; Deng, H.; Hu, L.; Lochner, E.; Schlottmann, P.; Von Molnár, S.; Li, Y.; Zhao, J.; Xiong, P. *ACS Nano* **2020**, *14* (11), 15983–15991. h) Al-Bustami, H.; Khaldi, S.; Shoseyov, O.; Yochelis, S.; Killi, K.; Berg, I.; Gross, E.; Paltiel, Y.; Yerushalmi, R. *Nano Lett.* **2022**, *22* (12), 5022–5028.

when the functionalization of the carbon materials is chiral, as mentioned above. This polarization is maintained over ≈ 1 μm and generally at temperatures below 50 K, where electron transmission occurs by tunneling through the chiral barriers, whereas at higher temperatures electrons pass through the barriers by thermionic emission, a process that is not spin selective, resulting in the loss of the CISS signal.[90]

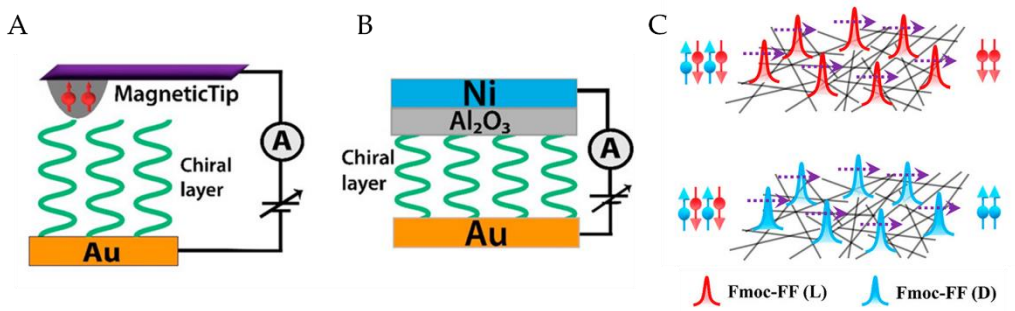

Figure 11. Common geometries for CISS measurements. a) Measurements of a few molecules using an AFM tip. b) Measurements of an ensemble of molecules using a two-terminal planar geometry. c) Schematic representation of charge transport through chiral functionalized carbon networks. Adapted with permission. Copyright 2022 American Chemical Society.[91]

The theoretical understanding of the CISS effect remains an open problem, although three factors seem to be necessary for its observation: a) the spin-orbit coupling, b) the structural inversion asymmetry given by the chirality of the medium, and c) the temporal inversion asymmetry given by the magnetic field. Some studies suggest that the response produced by the spin-orbit coupling in the electrodes, which causes the orbital polarization to be transformed into a spin

[90] a) Kaiser, A.; Düsberg, G.; Roth, S. *Phys. Rev. B - Condens. Matter Mater. Phys.* **1998**, *57* (3), 1418–1421. b) Rahman, M. W.; Mañas-Torres, M. C.; Firouzeh, S.; Cuerva, J. M.; Álvarez de Cienfuegos, L.; Pramanik, S. *ACS Nano* **2021**, *15* (12), 20056–20066.

[91] Rahman, M. W.; Mañas-Torres, M. C.; Firouzeh, S.; Illescas-Lopez, S.; Cuerva, J. M.; Lopez-Lopez, M. T.; de Cienfuegos, L. Á.; Pramanik, S. *ACS Nano* **2022**, *16* (10), 16941–16953.

polarization, could be the origin of the CISS effect. This response is dependent on the magnetic field and is known as the *electromagnetochiral effect* (EMCh).[92]

The EMCh phenomenon introduces a resistance term in the form $\chi^{L/D}B{\cdot}I$, L and D indicate the chirality of the material, where $\chi^{D} = -\chi^{L}$. Since the chiral medium offers different resistance between different magnetic fields (positive or negative) due to the EMCh, this can affect the charge accumulated in the insulating layer. Thus, a change in the effective potential barrier between the electrodes could occur, leading to an MC effect, observed in the CISS effect experiments. The EMCh representation implies that when *B* and *I* are perpendicular, the EMCh contribution should be zero, which means that there should be no EMCh-induced MC asymmetry between +*B* and -*B* for a fixed bias and chirality. Thus, if there is a CISS effect that does not depend on this phenomenon, it should be observable in experiments carried out in a transverse configuration, i.e., where *B* is perpendicular to *I*.[93]

In terms of evaluating the influence of ***spin-orbit coupling*** (SOC), the use of carbon nanotubes fulfils a very interesting function from the point of view that they behave as one-dimensional molecular conductors with delocalized molecular orbitals along their entire length, which determines their electronic

[92] a) Atzori, M.; Train, C.; Hillard, E. A.; Avarvari, N.; Rikken, G. L. J. A. *Chirality* **2021**, *33* (12), 844–857. b) Liu, Y.; Xiao, J.; Koo, J.; Yan, B. *Nat. Mater.* **2021**, *20* (5), 638–644. c) Xiao, J.; Zhao, Y.; Yan, B. arXiv:2201.03623v3 (2023). d) Firouzeh, S.; Illescas-Lopez, S.; Hossain, M. A.; Cuerva, J. M.; Álvarez de Cienfuegos, L.; Pramanik, S. *J. Chem. Phys.* **2023**, *159* (3).

[93] a) Xiao, J.; Zhao, Y.; Yan, B. arXiv:2201.03623v3 (2023). b) Atzori, M.; Train, C.; Hillard, E. A.; Avarvari, N.; Rikken, G. L. J. A. *Chirality* **2021**, *33* (12), 844–857. c) Rikken, G. L. J. A.; Fölling, J.; Wyder, P. *Phys. Rev. Lett.* **2001**, *87* (23), 236602-1-236602–236604. d) Krstic, V.; Roth, S.; Burghard, M.; Kern, K.; Rikken, G. L. J. A. *J. Chem. Phys.* **2002**, *117* (24), 11315–11319. e) Hossain, M. A.; Illescas-Lopez, S.; Nair, R.; Cuerva, J. M.; Álvarez de Cienfuegos, L.; Pramanik, S. *Nanoscale Horizons* **2023**, *8* (3), 320–330.

properties. CNTs exhibit a strong spin-orbit coupling, usually of the form $\Gamma \sim \gamma a \Delta_A^{SOC}/r$, where the parameter γ can have a value between 0.01 and 1, a is the carbon-carbon distance to the nearest carbon, ΔSOC is the atomic spin-orbit interaction of carbon and r is the radius of the nanotube. Considering that the magnitude of SOC depends on the radius of the CNTs, the evaluation of its influence on the CISS effect can be done by using nanotubes with different radii. Thus, single-walled (SW), double-walled (DW) and multi-walled (MW) nanotubes were used, whose radii have an increasing value according to the order SW<DW<MW.[94]

Moreover, as already explained in this section, CNTs can be functionalized with many chiral molecules in a non-covalent way, which leads to a minimal deterioration of the crystalline structure they present. It should be noted that in the case of functionalization with peptide molecules, it is the overall supramolecular chirality of the system that determines the CISS signal and not the intrinsic chirality of each molecule or of the nanotubes, which is an interesting point when it comes to tuning the chirality of the system by using different stimuli.[95]

---

[94] a) Firouzeh, S.; Illescas-Lopez, S.; Hossain, M. A.; Cuerva, J. M.; Álvarez de Cienfuegos, L.; Pramanik, S. *J. Chem. Phys.* **2023**, *159* (3). b) Gagni, P.; Lodigiani, G.; Frigerio, R.; Cretich, M.; Gori, A.; Bergamaschi, G. *Chem. – A Eur. J.* **2024**, e202400974. c) Wang, Y.; Rencus-Lazar, S.; Zhou, H.; Yin, Y.; Jiang, X.; Cai, K.; Gazit, E.; Ji, W. *ACS Nano* **2024**, *18* (2), 1257–1288. d) Gao, F.; Yang, X.; Song, W. *Small Methods* **2024**, *8* (4), 2300753. e) Hu, X.; Liao, M.; Gong, H.; Zhang, L.; Cox, H.; Waigh, T. A.; Lu, J. R. *Curr. Opin. Colloid Interface Sci.* **2020**, *45*, 1–13. f) Tao, K.; Wu, H.; Adler-Abramovich, L.; Zhang, J.; Fan, X.; Wang, Y.; Zhang, Y.; Tofail, S. A. M.; Mei, D.; Li, J.; Gazit, E. *Prog. Mater. Sci.* **2024**, *142*, 101240. g) Singh, R.; Sharma, S.; Kautu, A.; Joshi, K. B. *Chem. Commun.* **2024**, *60* (60), 7687–7696.

[95] Firouzeh, S.; Illescas-Lopez, S.; Hossain, M. A.; Cuerva, J. M.; Álvarez de Cienfuegos, L.; Pramanik, S. *J. Chem. Phys.* **2023**, *159* (3).

The group has previously demonstrated that 2D networks of CNTs functionalized with Fmoc-dipeptides exhibit enhanced binding capacity, which increases with the aromaticity of the peptide. For instance, using Fmoc-FF(L/D) results in stronger interactions between the aromatic phenylalanine side chains and the CNT walls, compared to Fmoc-AA(L/D), whose side chains lack an aromatic ring. These experiments were carried out by obtaining homochiral hydrogels by inducing self-assembly with a salt, sodium bicarbonate (Na_2CO_3) in this case, to avoid the influence of other chiral molecules, which could add a point of variability that is difficult to assess.[96]

Having established that homochiral networks alone can induce the CISS effect, the role of a chiral 'dopant' in generating heterochiral networks in these systems can be investigated. These heterochiral networks are obtained by promoting self-assembly using glucono-δ-lactone (GdL), a chiral molecule widely used for hydrogel formation. As will be seen in section 3, the amount of GdL present in the samples is very low and does not seem to affect the effective interaction of the CNTs with the peptides. However, it is present in the medium, which, as mentioned above, can induce a change in the supramolecular chirality of the system and thus affect the signal of the CISS effect.[97]

[96] Rahman, M. W.; Mañas-Torres, M. C.; Firouzeh, S.; Cuerva, J. M.; Álvarez de Cienfuegos, L.; Pramanik, S. *ACS Nano* **2021**, *15* (12), 20056–20066.

[97] a) Rahman, M. W.; Mañas-Torres, M. C.; Firouzeh, S.; Illescas-Lopez, S.; Cuerva, J. M.; Lopez-Lopez, M. T.; de Cienfuegos, L. Á.; Pramanik, S. *ACS Nano* **2022**, *16* (10), 16941–16953. b) Perlitz, Y.; Michaeli, K. *Phys. Rev. B* **2018**, *98* (19), 1–12.

Finally, it should be noted that although carbon nanotubes are materials with very interesting properties and their use in the study of the CISS effect is very promising, they are not the only one. Graphene and its derivatives such as graphene oxide (GO) or reduced graphene oxide (rGO) are also promising materials for applications in electronics and spintronics. In order to use some of these materials to study the CISS effect, rGO layers have been functionalized with Fmoc-FF(L/D). This functionalization induces a distortion in the nanosheets, causing them to adopt a 'conformational chirality', which leads to the detection of the CISS signal. This signal is also influenced by other parameters, such as the thickness of the nanolayers.[98]

[98] a) Tombros, N.; Jozsa, C.; Popinciuc, M.; Jonkman, H. T.; Van Wees, B. J. *Nat. 2007 4487153* **2007**, *448* (7153), 571–574. b) Firouzeh, S.; Hossain, M. A.; Cuerva, J. M.; Álvarez de Cienfuegos, L.; Pramanik, S. *Acc. Chem. Res.* **2024**, *57* (10), 1478–1487. c) Firouzeh, S.; Illescas-Lopez, S.; Hossain, M. A.; Cuerva, J. M.; Álvarez de Cienfuegos, L.; Pramanik, S. *ACS Nano* **2023**, *17* (20), 20424–20433.

2. Objectives

Based on all that has been presented in the background section, the field of study of the CISS effect is very broad and that, although relatively new, it has been growing steadily over the last 25 years. Moreover, the trend in recent years suggests that it will continue to do so because of the opportunities it offers for the development of new technologies or for a deeper understanding of how many biological processes work. This chapter summarises the work carried out in this field during this thesis, with the following specific objectives.

1. Heterochiral 2D networks of SWCNTs functionalized with Fmoc-dipeptides (Fmoc-FF(L/D) and Fmoc-GG) were prepared by promoting self-assembly with GdL, a chiral molecule, to study the influence of the presence of a chiral 'dopant' on the CISS signal.
2. To study the dependence of the CISS effect on the bias using planar carbon nanotube networks functionalised with chiral molecules. This will shed light on the following points:
    2.1. The existence of transverse magnetoconductance (MC) and whether it may be indicative of the CISS effect.
    2.2. The validity of Onsager's principles of reciprocity in two-terminal systems.
    2.3. Study whether the electromagnet chiral effect (EMCh) is the origin of the CISS signal or whether there is an alternative origin.
3. Assess the effect, if any, of the strength of the spin-orbit coupling on the CISS effect signal.

4. To investigate if it is possible to induce the CISS effect in rGO layers supramolecular functionalized with Fmoc dipeptides, in order to further expand the materials with which spintronic devices can be fabricated.

3. Results and discussion

The studies detailed in this section were conducted using samples of carbon nanotubes (CNTs) or graphene layers (GLs) functionalized with Fmoc-dipeptides and subsequently gelified. The dipeptides employed are Fmoc-GG, which act as an achiral control, and both enantiomers (L and D) of Fmoc-FF. The chemical structures of all dipeptides are listed in the Figure 12.

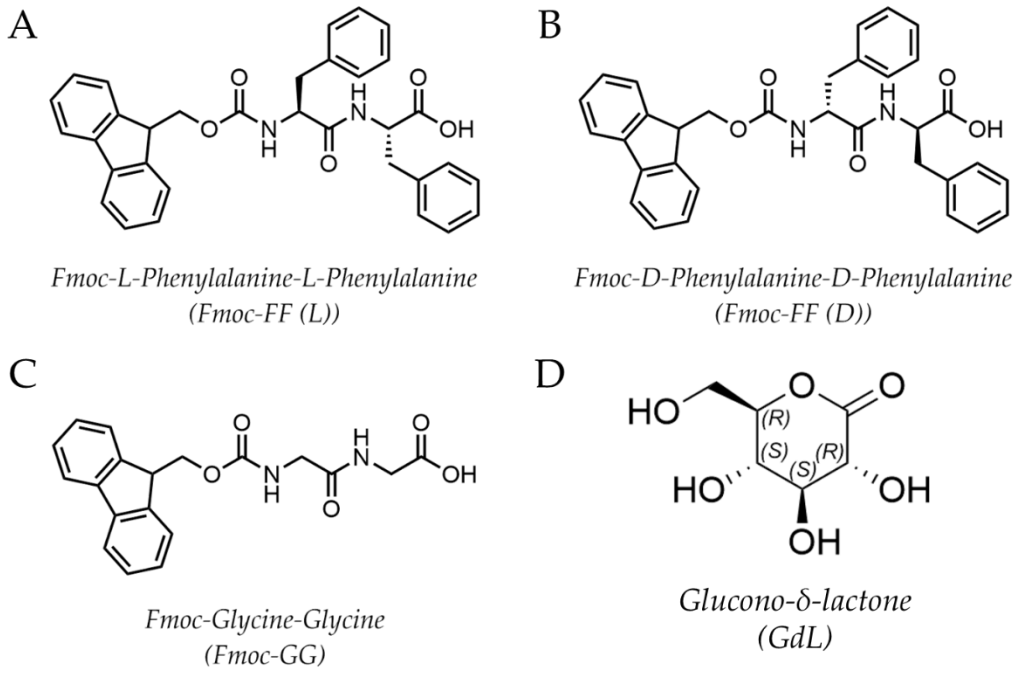

Figure 12. Chemical structure of a) Fmoc-GG, b) Fmoc-FF (L), c) Fmoc-FF(D) and d) Glucono-δ-lactone (GdL). This molecule has four chiral centers 3R, 4S, 5S, and 6R, where the number defines the position of the chiral carbon.

The functionalized carbon allotropes networks are prepared following a protocol described previously by the group. A summary of this procedure will be presented here; however, the detailed protocol for each composite material, as well as the gelation protocol used, can be found in the experimental section (Chapter 8), which contains the experimental part of this work. Briefly, the first step is to prepare a suspension of carbon material (CNTs or GLs) in an aqueous basic solution of the Fmoc-dipeptides. The mixture is sonicated to facilitate the appropriate interactions between the peptides and the carbon material. The obtention of a black suspension without appreciable precipitation confirms the existence of interaction between the two components, establish through π−π stacking interactions between aromatic groups in the peptides and the walls of the carbon allotropes. Once this suspension is obtained, self-assembly is promoted by lowering the pH with GdL or by adding sodium carbonate (Na_2CO_3), leading to the final formation of the hydrogels, the final appearance of which can be seen in Figure 13 . The formation of fibers occurs through hydrogen bonding established between peptide backbone and π−π interactions between aromatic groups. Except for the Fmoc-GG, the Fmoc-dipeptides employed are chiral, and enantiopure networks have been obtained, where the interactions with carbon materials are expected to induce chirality-dependent effects in charge transport.

Figure 13. Composite hydrogels

The results obtained by Raman spectroscopy for both hybrid and raw carbon materials provide detailed information on the effect of peptide functionalisation on the original material. Figure 14.a, b and c show the different Raman spectra obtained for each of the functionalizations.

According to the spectra obtained for the CNT materials, several interesting points can be observed both for the different molecules with which they are functionalized, i.e. Fmoc-FF(L/D) and Fmoc-GG, and for the type of functionalized nanotubes, i.e. SW-, DW- or MW-. It will also be possible to assess whether there is any effect on the interaction between peptides and CNTs depending on whether chiral dopants, such as GdL, are present in the medium or not, when the final material is obtained by the addition of Na_2CO_3.

The Raman characterization of the CNTs (functionalized and raw) is shown in Figure 14.a, and b. The G^+ peak typically appears around ≈ 1580-1600 cm^{-1} and is due to the longitudinal vibration of the atoms in the graphitic network of the nanotubes. The fact that this peak appears with a strong intensity indicates that the graphitic nature of the nanotubes remains largely unchanged after functionalisation. However, it should be noted that it appears to narrow and shift

upon functionalisation, which may be due to fractionation of the charge transfer between the nanotubes and the peptides.

The G^- (≈ 1540-1550 cm^{-1}) is due to tangential vibrations of the carbon atoms and is unique to CNTs due to their cylindrical geometry. This peak is significantly suppressed by functionalization (Figure 14.a), especially when carried out with Fmoc-FF, most likely because it establishes strong π-π interactions with the nanotube walls through their side chains. Fmoc-GG causes a less dramatic effect on G^- suppression, due to its lesser interaction with CNTs that is only established through the Fmoc- group. In addition to the suppression, G^- undergoes a shift when the functionalization is stronger.

The relative intensity of G^-/G^+ (Figure 87.a, in Chapter 8) is also indicative of the strength of the interaction, as it decreases with increasing interaction. Furthermore, a comparison of the relative intensity of these peaks in the material obtained with GdL compared to the hydrogels formed with Na_2CO_3 (Figure 87.b, in Chapter 8) shows that there are no significant differences in the values at equal functionalization, indicating that the peptide-CNT interaction is not affected in the presence of a chiral dopant.

Figure 14.a and b also show other important peaks. First is the D peak or defect peak at ≈ 1350 cm^{-1}. This peak occurs mainly after the sonication stage (see experimental part in chapter 7) and is due to the broken ends of the nanotubes. Finally, radial breathing modes (RBM) are also observed at ≈ 260-280 cm^{-1}. These peaks are due to molecular vibrations caused by the radial expansion and contraction of the CNTs. RBM do not appear for functionalized DWCNTs and MWCNTs because their frequency is inversely dependent on the radius of the

nanotubes, so the larger diameter of this type of nanotubes makes their detection difficult.

If looking now at the Raman spectrum for the graphene materials (Figure 14.c), being single layer graphene (SLG), multi-layer graphene (MLG) and raw material, typical peaks appear corresponding to D (≈ 1350 cm^{-1}), G (≈ 1580 cm^{-1}) and D' (≈ 1610 cm^{-1}). The raw graphene sheets, both SLG and MLG, have large G peaks, while the D' peak is dominant in the functionalized samples. This peak is an indicator of the presence of defects and structural disorder. The high intensity of D', coupled with the G and D peaks after functionalization, indicates lattice distortion. This may be due to the self-assembly of the peptide molecules, which stresses the bound SLG and MLG layers. Moreover, especially in the functionalized samples, additional peaks appear at ≈ 1479 cm^{-1}, which are related to the structural changes induced after the association with the peptide molecules and to the vibrational modes of the functional groups. A peak at ≈ 1294 cm^{-1} also appears, indicating the presence of oxygen and carboxyl groups. Finally, weaker bands such as 2D (≈ 2710 cm^{-1}) and D+G (≈ 2950 cm^{-1}) are observed. The fact that 2D is weaker and broader is related to the presence of disorder and defects characteristic of rGO.

Continuing with the material characterization, circular dichroism (CD) is a technique that allows studying the conservation of the enantiomeric ratio in the different supramolecular aggregates and how it is affected in the presence of the different carbon materials and chiral dopants.

An in-depth analysis of the spectra obtained with each material will be made in the corresponding subsection, while here it will be presented the general aspects of a typical spectra of the basic solutions of Fmoc-FF(L/D) at 5 mM (Figure 14.d), as well as the typical null spectrum of Fmoc-GG (Figure 14.e) at the same concentration.

Figure 14.a shows that the spectra of the Fmoc-FF enantiomers are mirror images. The peptide supramolecular aggregates show two characteristic Cotton bands. One band appears at 220 nm and corresponds to the n-π^* transition of the amino acids, while the other band appears at 270 nm and belongs to the π-π^* transition of the Fmoc group. The sign of the CD spectra can be related to the CISS effect in that they mark a change in the supramolecular chirality of the aggregates when this is altered. As will be seen below, these experiments support the results of the CISS effect experiments, correlating the reversal of the sign of the Cottons in the CD spectrum for each type of material with the change of sign obtained in the CISS measurements for the same hybrid material.

Finally, the two-terminal planar device is fabricated by transferring a hydrogel slice between pairs of gold-nickel (Au-Ni) electrodes fabricated on SiO_2/Si. The device is then vacuum annealed to improve connectivity and electrical contacts. The Ni contact is protected by a photoresist layer to prevent environmental oxidation, which is only removed when the hydrogel is to be placed. Note that the contacts have significantly larger dimensions to minimize contact resistance contributions in two-terminal CISS measurements. The unpolarized electron current is injected through the Au electrode and travels through the chiral flakes that composed the xerogel to the Ni electrode (Figure 14.f).

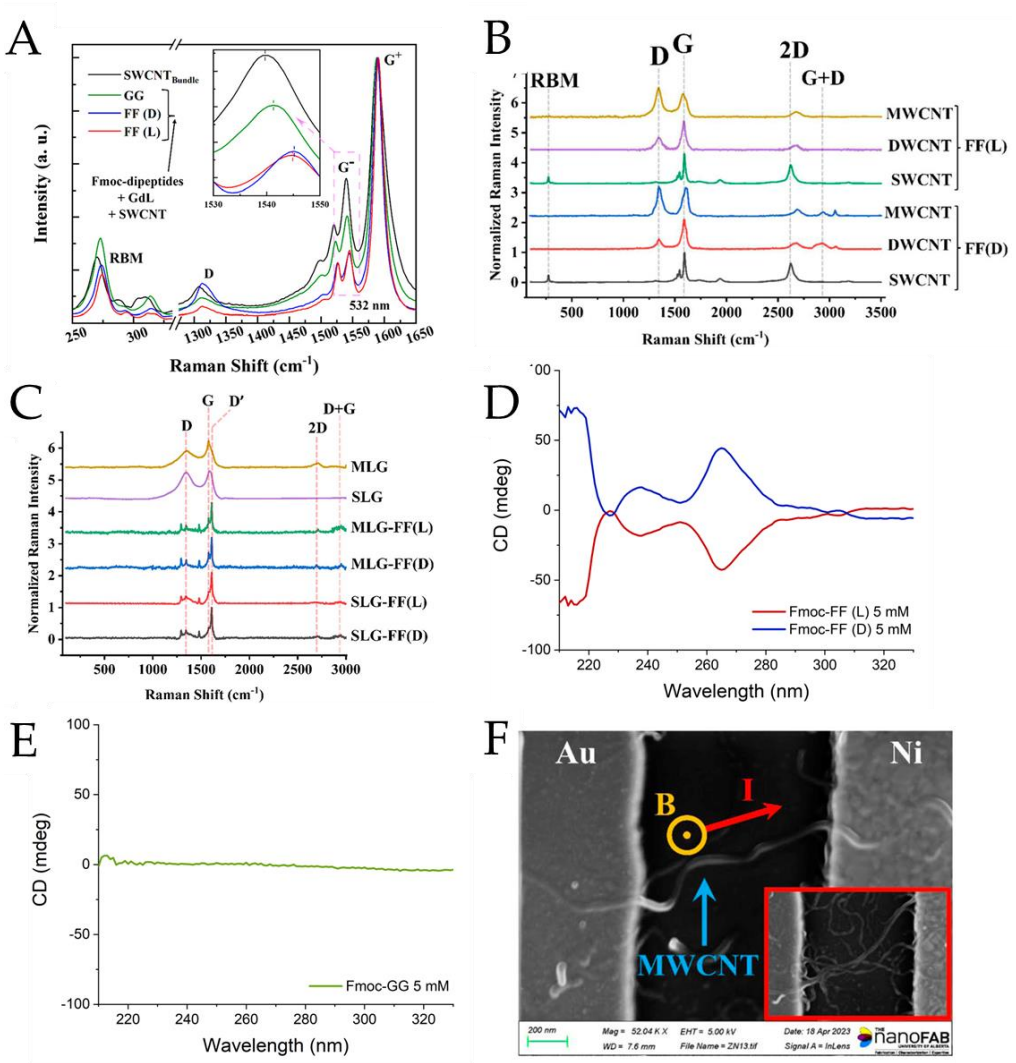

Figure 14. Raman spectra of a) SWCNT functionalized with Fmoc-dipeptides and GdL, b) and c). Characteristic CD spectrum of d) Fmoc-FF (L/D) basic solutions at 5 mM and e) Fmoc-GG basic solutions at 5 mM. f) SEM image of the device.

This device has a number of advantages compared to vertically stacked molecular layers:

a) It has not pinhole shorts and it avoids any spurious effects that may affect the transport data.
b) Due to its high conductivity compared to molecules, it is possible to directly measure conductance in the linear low polarization range.
c) Finally, the high conductivity of CNTs also reduces any charge accumulation and the associated electromagnetochiral anisotropy effect (EMChA).

In addition, as mentioned in the background, the data suffer less fluctuations, which eliminates the need for many measurements and statistical treatment.

All experiments conducted with this typology of device and carried out in the group of the Professor Pramanik, a transverse magnetic field is employed, oriented perpendicular to the plane. As previously mentioned, this configuration eliminates the influence of the electromagnetochiral effect (EMCh), since the plane is composed of the device with the sample. Consequently, the magnetic field B is perpendicular to the conduction channels and, consequently, to the current, resulting in the component $B \cdot I = 0$.

3.1. Influence of the presence of a chiral 'dopant' on the CISS signal.

The supramolecular chirality of a system can be modulated by using different stimuli to promote the self-assembly, as discussed previously. These stimuli can be, e.g., the use of different solvents, pH values, or the addition of salts.

The aim of this work is to study how the presence of an 'extra' chiral molecule in the hydrogel matrix affects the properties of the hybrid materials related to CISS effect. This will be done using hybrid hydrogels of SWCNTs (700 μg/mL) functionalized with Fmoc-FF (L), Fmoc-FF (D) or Fmoc-GG at 10 mM of peptide concentrations. The difference lies in the use of GdL or Na_2CO_3 as promoters of self-assembly. The hydrogels obtained with Na_2CO_3 will act as control material, while those with GdL will be the object of study. Furthermore, the use of Fmoc-GG, achiral molecule, allows a direct study of the influence of GdL as the sole source of chirality, whereas in the case of Fmoc-FF (L/D) its effect on the supramolecular chirality of the enantiomers can be studied.

The interactions between nanotubes and Fmoc-GG are established exclusively through the Fmoc group, whereas Fmoc-FF (L/D) also interacts via its aromatic lateral chains. It is important to note that GdL does not directly interact with CNTs or alter peptide-nanotube interactions, as discussed above. However, it is present within the network and adds additional chiral centres. Its chemical structure is shown in the Figure 12.

First point that can be compared between the two types of gels (Na_2CO_3 or GdL) is the effectiveness of both molecules in forming gel fibres. Those gels formed by the addition of GdL show a higher strength, according to the rheological measurements in Figure 15. This may be indicative of better interactions between the peptides and the CNTs, resulting in a better integrated material.

Rheological measurements of the viscoelasticity under oscillatory shear for Fmoc-FF (L/D) hydrogels (Figure 15.a) show that the material obtained with the addition of GdL is significantly stronger than the one obtained with Na_2CO_3. The first one has elastic modulus (G') values of about 5000 Pa, while the latter is a much weaker gel with G' values around 25 Pa. It is noteworthy that both enantiomers, Fmoc-FF (L) and Fmoc-FF (D), behave similarly in each case, as expected.

Figure 15.b illustrates the viscoelasticity values of the Fmoc-GG hydrogels, both in the presence of GdL and Na_2CO_3. Similarly to Fmoc-FF, the material obtained with GdL has a higher strength, with a G' value of approximately 279 Pa, than that formed by the addition of Na_2CO_3 (G' ≈ 6 Pa). However, it is evident than the materials formed with Fmoc-GG are comparatively weaker than the Fmoc-FF hydrogels and can be classified as weak hydrogels for GdL and extremely weak for the Na_2CO_3. This latter observation has implications for charge transport, which will be discussed below.

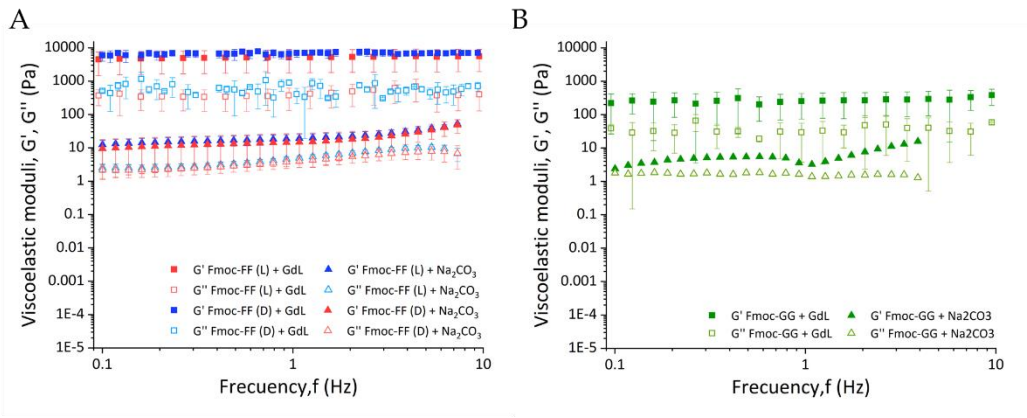

Figure 15. Mechanical characterization of the hydrogels and comparison of the effect of GdL and Na_2CO_3 as gelation promoters on the rheological properties of A) Fmoc-FF(L/D) and B) Fmoc-GG.

In order to ascertain the impact of GdL on the CISS signal, the data obtained from the Fmoc-GG hydrogels will be presented initially. The lack of chirality in Fmoc-GG results in the formation of two-handed fibres in equal proportions upon self-assembly. Consequently, if GdL exerts an influence on the supramolecular chirality of the system and, consequently, on the CISS effect, this will be more readily discernible in hydrogels comprising Fmoc-GG.

The current-voltage (*I-V*) plots obtained for the Fmoc-GG with GdL (Figure 16.a) show a strong semiconductor behaviour as a function of temperature (*T*). It can be seen in the inset of the graph how the resistance (*R*) decreases by more than an order of magnitude as T increases from 9 to 300 K. This behaviour has been described before for CNT networks. However, results obtained for Fmoc-GG hydrogels with Na_2CO_3 show weaker semiconducting behaviour with *R* decreasing by only 60% as the temperature varies from 9 to 300 K.

The behaviour of CNT networks is usually modelled using a variable range hopping (VRH) model where the transition from one localized state to another occurs because the charge carriers undergo phonon-assisted tunnelling. Here, temperature-dependent resistance *R(T)* is fitted (Figure 16.b for GdL and d for Na_2CO_3) with a two-dimensional VRH model following the equation shown in Equation 1, where T_0 is a parameter called 'characteristic temperature'.

$$R(T) \propto exp\left(\frac{T_0}{T}\right)^{\frac{1}{3}}$$

Equation 1. Two-dimensional VRH adjustment.

Figure 16.b shows a linear fit over a wide temperature range for Fmoc-GG with GdL. These findings support the physical carrier transport describe above. The fit for Na_2CO_3 hydrogels shown in Figure 16.d is poorer.

The fact that Fmoc-GG establishes a weaker interaction with CNTs when Na_2CO_3 is employed for gelation, as reflected by the rheological results, may provide an explanation for the observed weak semiconducting behaviour of these hydrogels. These weak interactions also result in more delocalized carriers and, consequently, in poorer barrier formation. Therefore, quasi-metallic behaviour of the nanotube networks plays a strong role. This tends to offset any semiconducting behaviour that originates from functionalization and carrier localization, thereby explaining the weaker temperature dependence of the transport characteristics when hydrogels without GdL are compared with those that contain GdL.

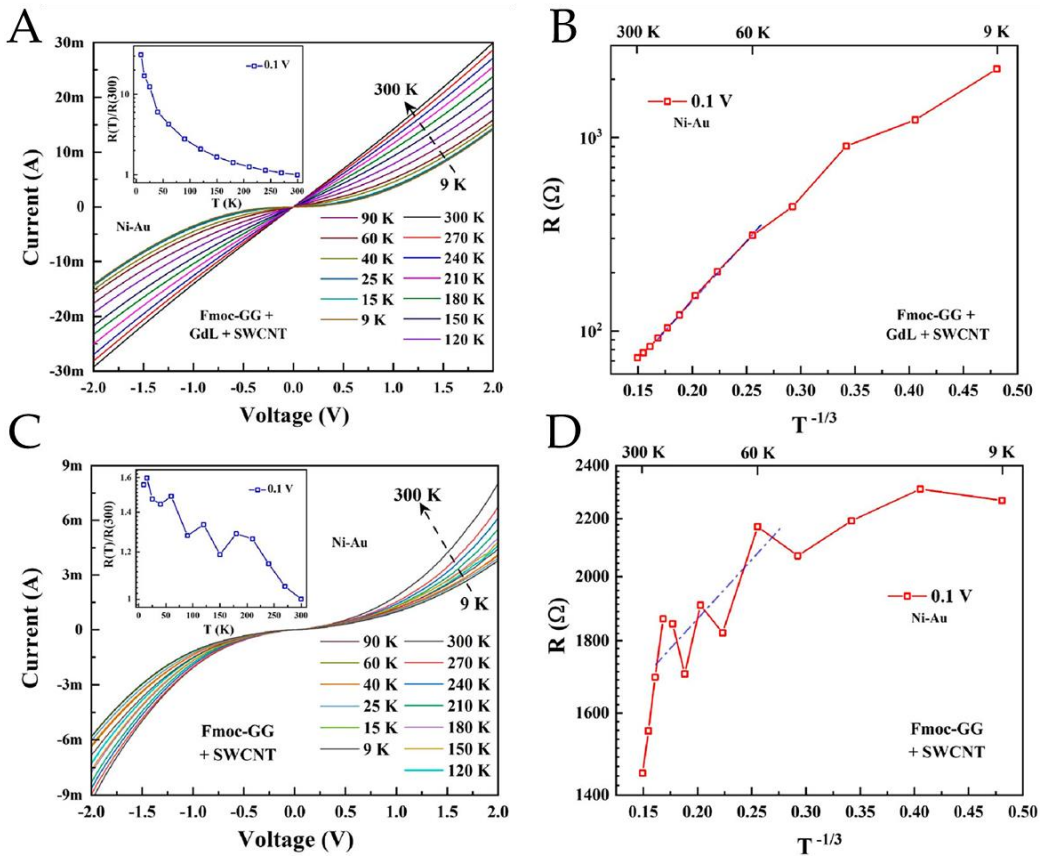

Figure 16. Characteristics graphs *I-V* (a and b) and fitting with two-dimensional variable range hopping (VRH) model (c and d) for Fmoc-GG+CNT samples. a and b show results for hydrogels with GdL and c and d without GdL.

CISS effect signal can be quantified using different parameters, as discussed in the background. Here, the ***magnetoresistance*** (MR) response of the device will be measured. A CISS signal is present when a MR asymmetry (R(-12 kG)≠R(+12 kG)) is observed and the sign of that asymmetry changes with the chirality of the sample. This response will be quantified using a normalized parameter, represented as Δ (Equation 2).

$$\Delta = \frac{[R(-12\ \mathrm{kG}) - R(+12\ \mathrm{kG}]}{\min\left(R(\pm 12\ \mathrm{kG})\right.}$$

Equation 2. Mathematical formula for Δ.

It should be noted that, in the configuration selected for this study, the magnetic field is perpendicular to the current paths. This allows for the elimination of any contribution from the EMChA to the signal. However, a background negative MR signal is observed, which arises from the interference effect between the forward and backward hopping paths. This phenomenon has been previously discussed by Rahman *et al*.[99]

Figure 17.A, B and C shows MR data CNT networks functionalized with Fmoc-GG. Figure 17.A and B correspond to the hybrid materials with GdL and Figure 17.C is from those without GdL (with Na_2CO_3). Figure 17.D shows the evolution of Δ as a function of temperature for both cases, highlighting the difference due to GdL. Although the data shown in Figure 17.C have much more noise, in view of these plots the conclusion can be drawn that the presence of GdL contributes to the appearance of an asymmetry in MR ($\Delta \neq 0$).

[99] Rahman, M. W.; Firouzeh, S.; Pramanik, S. *Nanotechnology* **2021**, *32* (45), 455001.

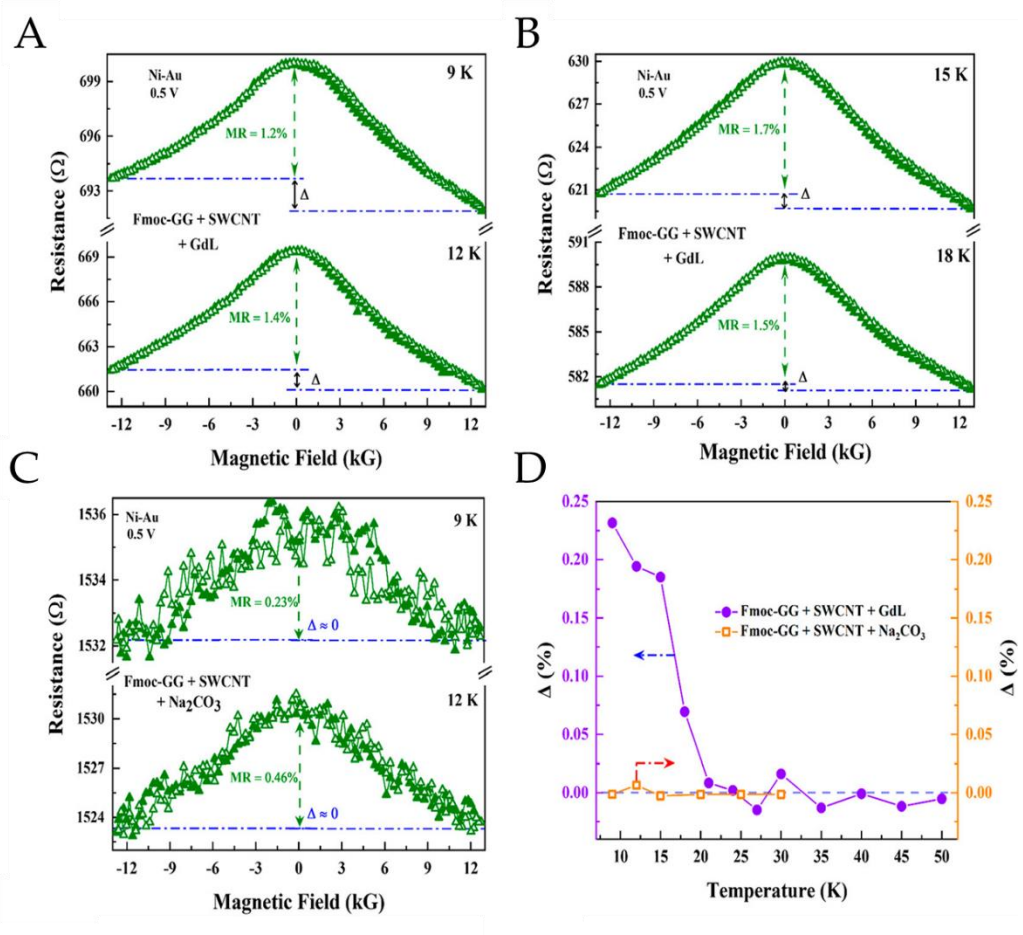

Figure 17. Two-terminal (Ni and Au) MR responses of Fmoc-GG-functionalized CNT networks in the presence (a, b) and in the absence (c) of GdL. Forward and backward magnetic field scan results are shown (open and filled markers). In the case of (a) and (b), the scans are highly reproducible, with the error bar on the order of the marker size. A clear MR asymmetry Δ is present in this case. In the case of (c) the error bar is larger and no Δ is detected above the noise level. (d) MR asymmetry Δ as a function of temperature in both cases

The presence of this non-zero Δ may be attributed to the potential influence of GdL on the supramolecular chirality as the Fmoc-GG aggregates form. To ascertain whether this is the case, the CD spectra obtained for the samples with GdL and with Na_2CO_3 are examined. It should be noted here that the hydrogels with nanotubes could not be measured due to the opacity of the medium, which causes light scattering and the inability to obtain an unsaturated spectrum.

Consequently, hydrogels without CNTs have been measured. Further details can be found in Chapter 8.

The CD spectra presented in Figure 18 illustrate a comparative analysis of the hydrogel formed without and with GdL (Figure 18.a and b, respectively). The spectrum shown in Figure 18.a is completely null. In contrast, the spectrum obtained in the presence of GdL shows weak signals, which could indicate that GdL may slightly favour the formation of supramolecular aggregates. In light of these considerations and the enhanced interaction between Fmoc-GG and CNTs in the presence of GdL, a non-zero Δ could be obtained, since the signal depends on the supramolecular organization of the medium and not on the chirality of the individual molecules.

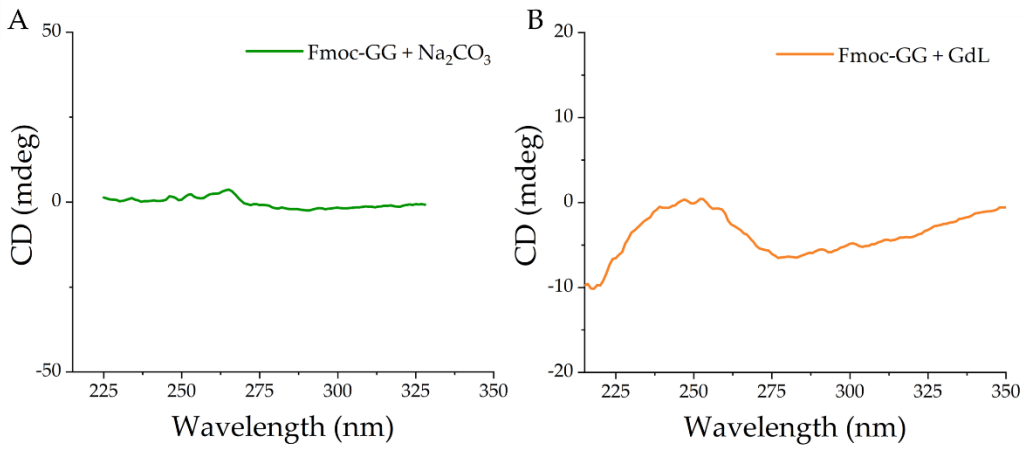

Figure 18. CD spectra of the hybrid samples a) without and b) with GdL.

The presence of GdL has a clear effect on the materials formed with Fmoc-GG, now it is worth asking whether it will also influence the results obtained for the Fmoc-FF(L/D) materials.

In this case, gel formation persists despite the utilization of Na_2CO_3, yet the gel quality is superior when GdL is employed, as evidenced in Figure 15. This is clear in the *I-V* responses of these samples, as illustrated in Figure 19.a, c, e, g. Semiconducting behaviour is observed, with a decrease in device resistance of more than 1 order of magnitude as the sample temperature is increased from 9 to 300 K. As shown in Figure 19.b, d, f, h, the data exhibit a reasonable agreement with the two-dimensional VRH model, with a linear fit over a wide temperature range. However, minor deviations are discernible in the low temperature range, a phenomenon that has been previously described.[100]

[100] Rahman, M. W.; Firouzeh, S.; Mujica, V.; Pramanik, S. *ACS Nano* **2020**, *14* (3), 3389–3396.

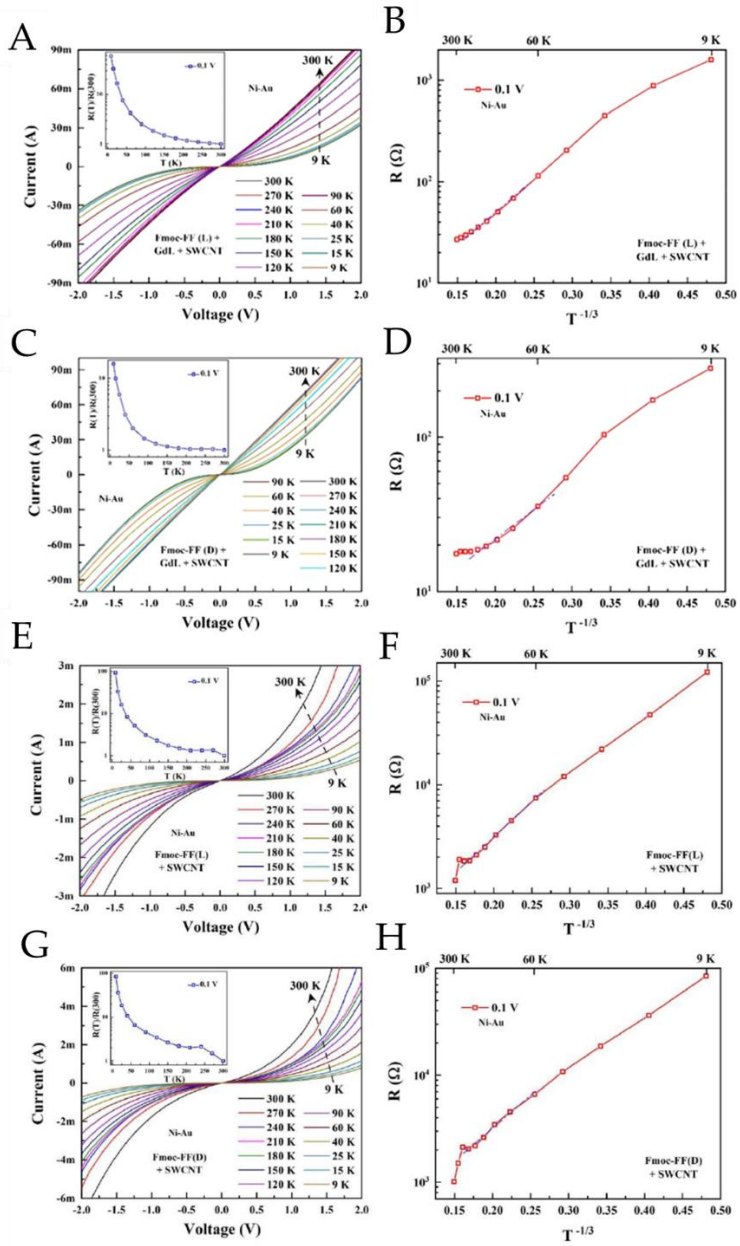

Figure 19. Current–voltage (*I-V*) characteristics of a) Fmoc-FF(L)+GdL- and c) Fmoc-FF(D)+GdL-functionalized SWCNTs and e) Fmoc-FF(L)+ Na_2CO_3- and g) Fmoc-FF(D)+ Na_2CO_3-functionalized SWCNTs with Ni–Au contacts. (b, d, f, h) Fitting of device resistance *R* with the two-dimensional variable range hopping (VRH) model of Fmoc-FF(L)+GdL-, Fmoc-FF(D)+GdL-, Fmoc-FF(L)+ Na_2CO_3- and Fmoc-FF(D)+ Na_2CO_3-functionalized SWCNTs, respectively.

Figure 20 shows the MR response of the Fmoc-FF functionalized nanotubes. A clear MR asymmetry (non-zero Δ) is evident, which depends on the chirality of the medium. Figure 20.a-c presents the curves obtained for xerogels with GdL, wherein Δ is positive, indicating that *R*(-12 kG) is greater than *R*(+12 kG) for Fmoc-FF(L), while Δ is negative for Fmoc-FF(D). Figure 20.d-f shows the MR responses of the material in the presence of Na_2CO_3. In this case, the MR asymmetry is opposite to that observed previously, with Δ being positive for Fmoc-FF(D) samples and negative for Fmoc-FF(L). It is evident that the presence of GdL molecules in the medium results in an inversion of the CISS signal.

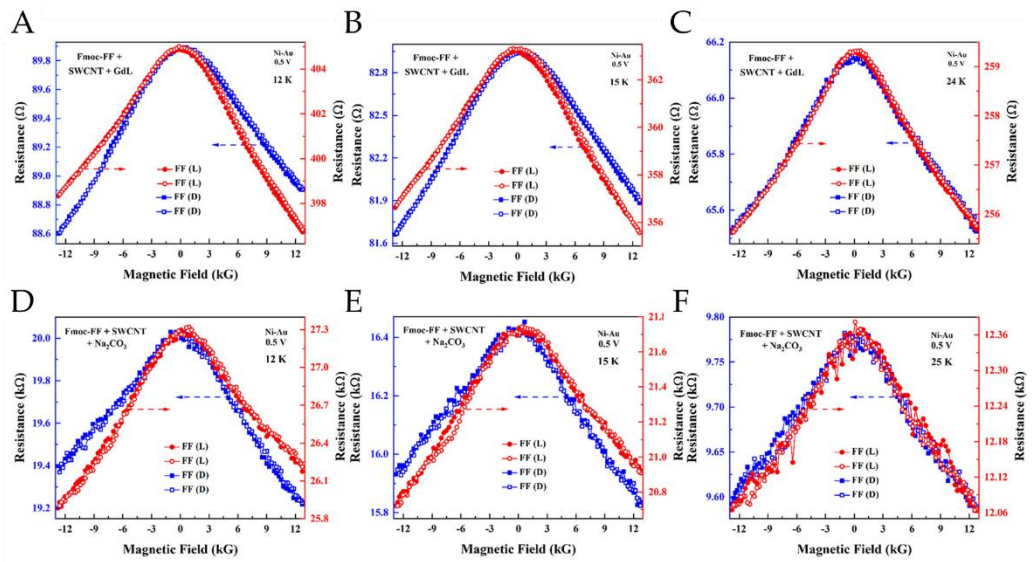

Figure 20. (a–c) Asymmetric MR (θ = 90°) of SWCNTs functionalized with Fmoc-FF(L/D)+GdL at various temperatures. (d–f) Asymmetric MR (θ = 90°) of SWCNTs functionalized with Fmoc-FF(L/D)+Na2CO3 at various temperatures. The applied bias is 0.5 V in all cases. Solid (open) symbols indicate a magnetic field scan from negative (positive) to positive (negative) fields. MR asymmetry has been found to be chirality dependent and has opposite signs with and without GdL.

This inversion of the sign of Δ may be attributed to a stereoinversion of the supramolecular chirality of the peptide aggregates. As with the previous experiments, the CD spectra provide further insight into the effects of GdL

(Figure 21). The addition of GdL reverses the sign of the peak observed at 280 nm, which corresponds to the π-π* transition of the Fmoc group. This results in a change of the sign of Δ compared to the results obtained using Na_2CO_3, supporting the results obtained when measuring MR.

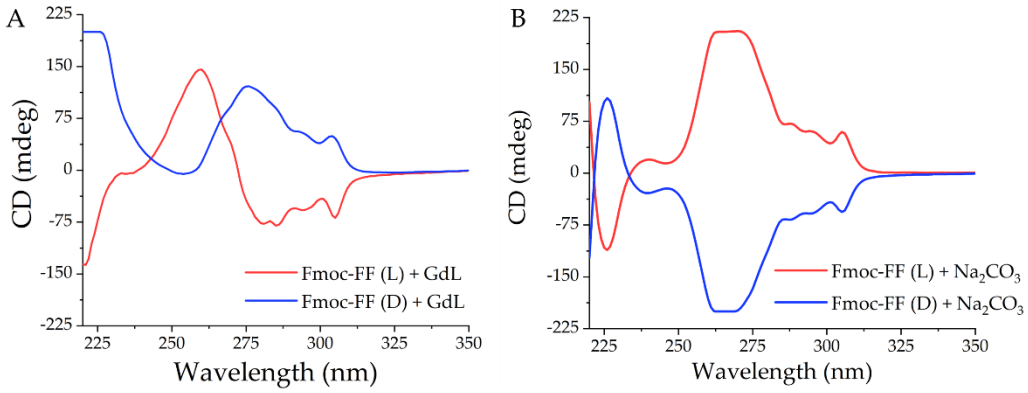

Figure 21. CD spectra of the hydrogels a) with and b) without GdL.

The role of GdL molecules in the MR asymmetry is also evident when one considers the plots of differential resistance (dV/dI) versus polarization (V) (Figure 22). The non-zero Δ has been observed in the nonlinear polarization regime, which does not contradict the reciprocity principles.

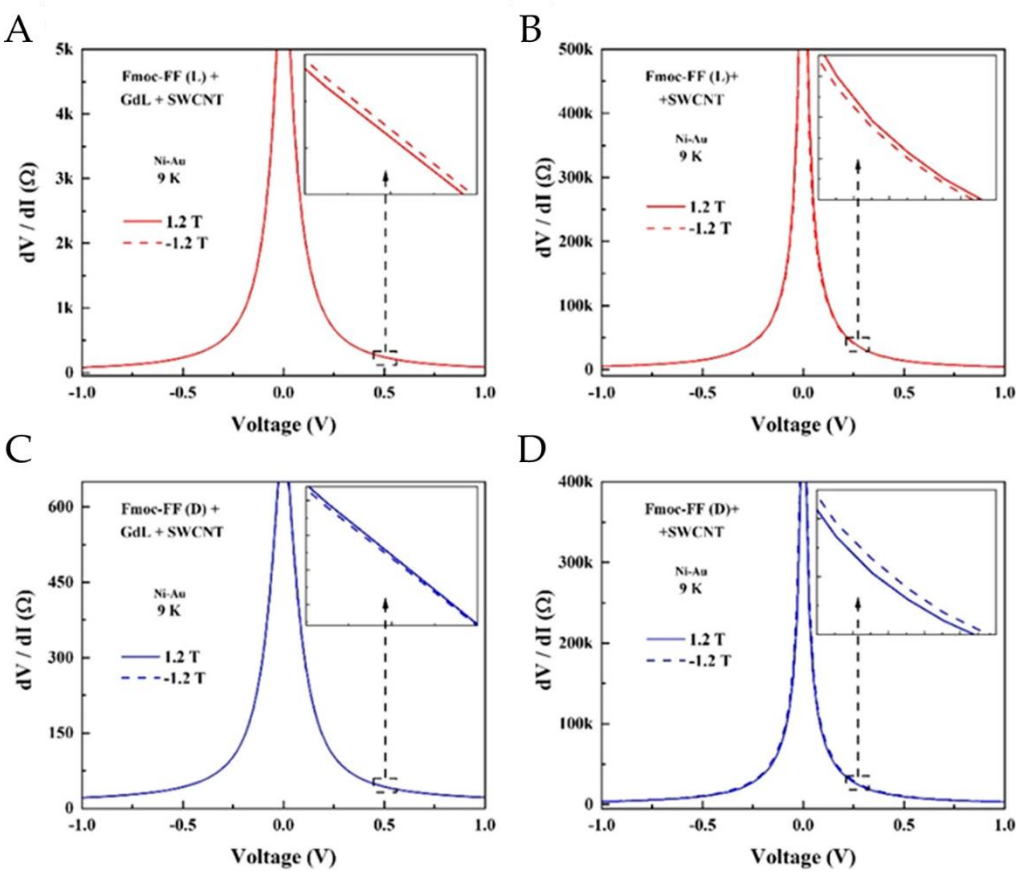

Figure 22. (a, c) Differential resistance (dV/dI) vs bias (V) of SWCNTs functionalized with Fmoc-FF(L/D)+GdL (θ = 90°). (b, d) Differential resistance (dV/dI) vs bias (V) of SWCNTs functionalized with Fmoc-FF(L/D)+Na_2CO_3 (θ = 90°). As seen from the insets, the resistance value is sensitive to the chirality of the medium as well as to the presence or absence of GdL.

The temperature dependence of the MR response is a topic of considerable controversy. For large area solid-state CISS devices, some papers report values at room temperature, while others report only low-temperature responses.[101]

[101] a) Kiran, V.; Mathew, S. P.; Cohen, S. R.; Hernández Delgado, I.; Lacour, J.; Naaman, R. *Adv. Mater.* **2016**, *28* (10), 1957–1962. b) Liu, T.; Wang, X.; Wang, H.; Shi, G.; Gao, F.; Feng, H.; Deng, H.; Hu, L.; Lochner, E.; Schlottmann, P.; Von Molnár, S.; Li, Y.; Zhao, J.; Xiong, P. *ACS Nano* **2020**, *14* (11), 15983–15991. c) Lu, H.; Wang, J.; Xiao, C.; Pan, X.; Chen, X.; Brunecky, R.; Berry, J. J.; Zhu, K.; Beard, M. C.; Vardeny, Z. V. *Sci. Adv.* **2019**, *5* (12).

Figure 23.a,b shows that, regardless of the details of the molecular functionalization, the magnitude of Δ decreases with increasing temperature. This phenomenon may be attributed to enhanced random spin scattering as temperature increases. Moreover, as previously discussed, at elevated temperatures, electrons will conduct through the barriers via thermionic emission, a process that is not inherently spin selective, thereby eliminating any CISS signal.

Figure 23.c,d depict the evolution of normalized Δ as a function of magnetic field direction for different functionalizations. Normalization for each molecule was performed relative to the corresponding maximum Δ value (Δ_{max}), allowing for direct comparison between the molecules.

The magnetic field plays two key roles: first, it sets the direction of Ni magnetization, which acts as a spin detector, and second, it influences the local magnetization of the Au electrode under equilibrium conditions (zero bias and zero current). This local magnetization is also dependent on the chirality of the molecules. As a result, the evolution of Δ is a complex function of the magnetic field angle (θ), showing a periodicity of approximately 360°, consistent with the behaviour expected in chiral systems where the magnetization of Ni and the chirality of the medium together select one direction along which current flow is favoured.

It is noteworthy that the sign of Δ is chirality-dependent only at specific field angles, such as around 90° and 270°. Figure 23.c,d clearly demonstrates that at these angles, the sign of Δ reverses depending on whether GdL is present in the medium.

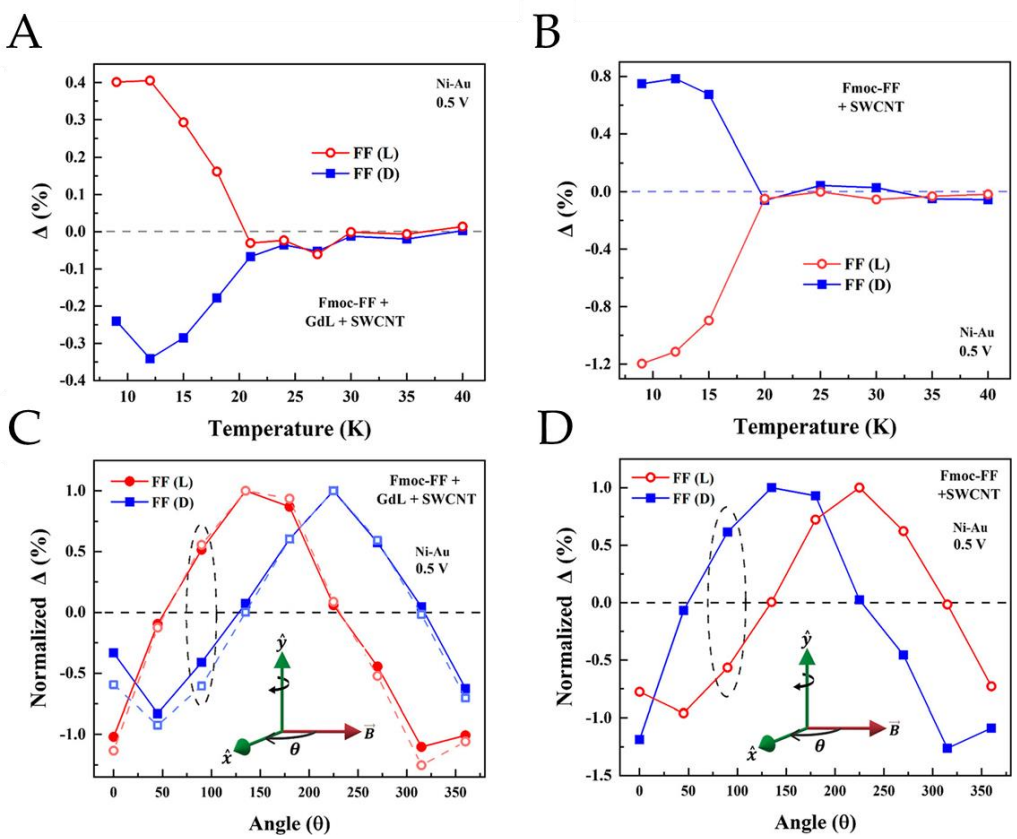

Figure 23. a, b) MR asymmetry Δ (%) as a function of temperature (measured at θ = 90°) for Fmoc-FF(L/D) + GdL- and Fmoc-FF(L/D) + Na_2CO_3-functionalized SWCNTs, respectively. c, d) Normalized Δ (%) at different orientations of Ni magnetization. For each sample, normalization is done relative to the corresponding maximum value of Δ. The sample is in the x–y plane, with the bias direction along ±x. For θ = 0°, the magnetic field coincides with the positive x axis. For angle-dependent measurements, the sample plane is rotated relative to the y axis as shown in the insets, while the direction of the magnetic field is kept fixed. Responses from two different samples are shown in c, for each functionalization, demonstrating the reproducibility of the data. The applied bias is 0.5 V in all cases.

3.2. Transverse magnetoconductance in two-terminal chiral spin-selective devices.

To evaluate the existence of a transverse in-plane magnetoconductance (MC) and its possible relationship with the CISS effect, samples of single-walled carbon nanotubes functionalized with Fmoc-FF(L/D) and gelled with GdL have been studied. The measurements were performed using the two-terminal planar device described above and the behaviour of the CNT networks has been simulated using the VRH model again.

The low temperature *I-V* characteristics (Figure 24) of both functionalizations (Fmoc-FF (L/D)) measured at a *B* value of ±12 kG exhibit chirality dependence. Samples functionalized with the L enantiomer (Figure 24.a) show that the magnitude of the current at -12 kG is lower than at +12 kG for any value of polarization, while the D enantiomer (Figure 24.b) shows the opposite behaviour. This change in behaviour from one enantiomer to the other is considered a signal of the CISS effect and, by manifesting itself in this geometry where the EMChA effect is non-existent, highlights that the origin of this signal has a different mechanism than this one. Moreover, the dependence of the chirality and the asymmetry of the current on the field values rule out any contribution from the Hall effect.

The geometry of the device would expect the chirality-induced spins to be in the x-y plane, since the unpolarized charge carriers are injected from the Au electrode into the planar xerogel lattice and it is the supramolecular chiral structure of the fibers that induces the chirality-dependent spins. The Ni electrode is magnetized in the out-of-plane direction. Therefore, it is expected

that the planar spin components are transmitted equally for both magnetizations (+z and -z), which would result in the same current and a zero CISS signal. In contrast, the +z and -z spins are injected from Ni into the lattice of CNTs, which are oriented in different plane directions. This makes both spins equally likely to be transmitted through the chiral medium, resulting in a null CISS signal. However, as noted above, the currents are different and chirality dependent, indicating the presence of an out-of-plane spin component, even though there is no net current in the z-direction. The supramolecular chirality of the medium favours one spin component while suppressing the other, resulting in a spin dipole in the transverse direction. Thus, transverse MC measurements can have a chirality-dependent response.

Figure 24 also shows that the *I-V* curves exhibit nonlinear behaviour, especially in the ±1 V range. Furthermore, they have an antisymmetric dependence on polarization. Onsager's reciprocity principle, for a given chirality, should prevent a difference in these curves in the linear response range, i.e., when $V \rightarrow 0$. The validity of this principle in this case is discussed below.

Looking at the *I-V* curves at a smaller voltage range (±10 mV) still shows the nonlinearity discussed above (Figure 24.c,d). The insets show that the curves are significantly closer together compared to Figure 24.a,b. However, the error bars are not overlapping, implying the existence of a difference between the measurements at ±12 kG.

Now, looking at the Figure 24.e,f the voltage range for which curves *I-V* are displayed is further decreased, around ±5 mV. In this case, the curves are observed to be practically linear, with a notable overlap between the measurements taken for opposite field values. This leads to the conclusion that the current values are essentially identical.

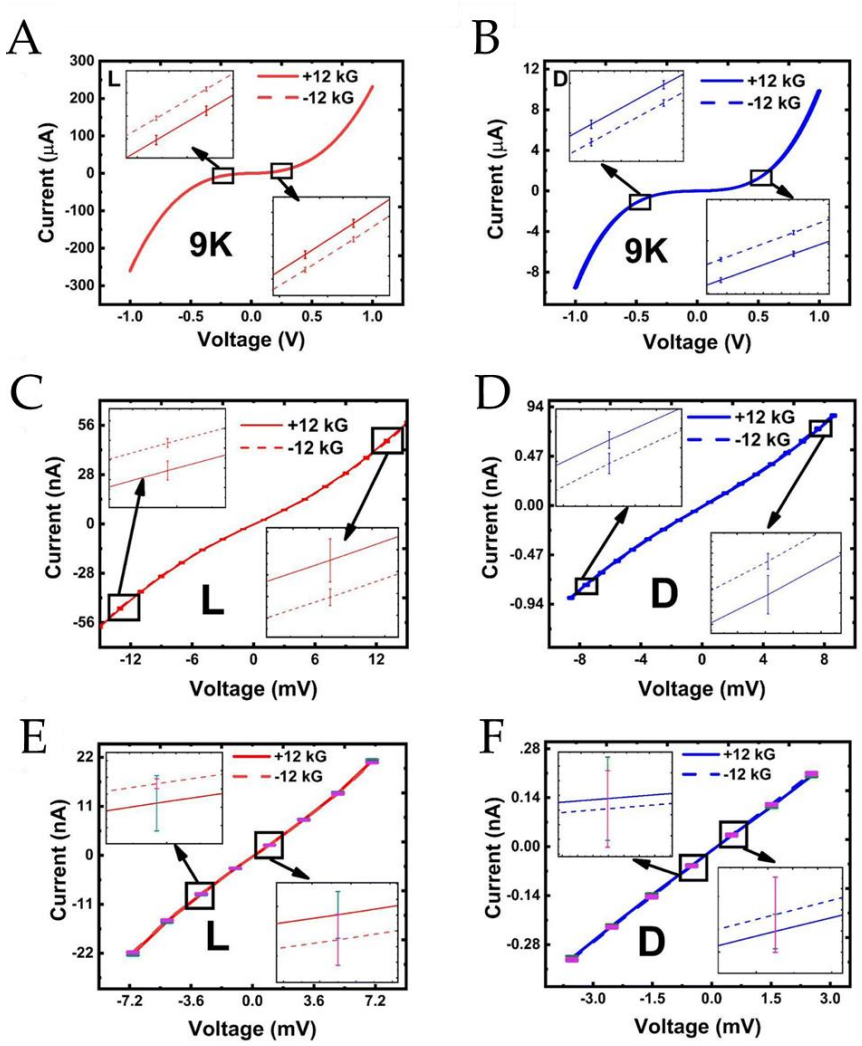

Figure 24. a and b) Non-linear *I–V* characteristics of the L and D functionalized CNT networks in the ± 1 V range. c and d) *I–V* curves in a narrower voltage range of ±10 mV. e and f) *I–V* curves in an even narrower voltage range of ± 5 mV. All measurements have been performed at 9 K.

The analysis done up to this point clearly shows the current difference (ΔI = I (+12 kG, +V) - I (-12 kG, + V)) tends to 0 in the linear range. Figure 25 show the magnitude of the difference in current (ΔI) as a function of polarization for both enantiomers. The noise floor for these measurements has been established by calculating the average error (the mean of the standard deviations for ±12 kG measurements). It can be observed that the value of $|\Delta I|$ gradually decreases as it reaches the zero value of polarization, becoming practically undetectable when $|\Delta I|$ is below the level of error in the linear range. This demonstrates that Onsager's reciprocity principle is satisfied, as evidenced by the observation that when $V \rightarrow 0$, $\Delta I \rightarrow 0$.

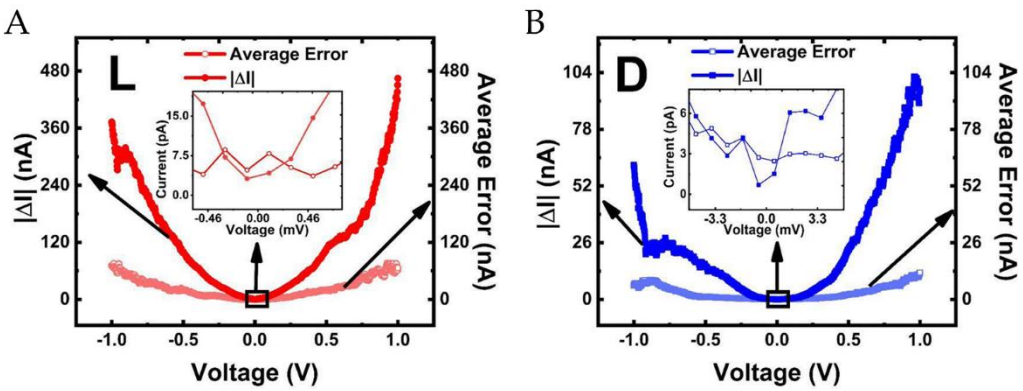

Figure 25. CISS signal magnitude $|\Delta I|$ as a function of bias (V) for a) L and b) D functionalized samples. Average error for the current measurements has also been plotted in each case.

Considering that the I-V characteristics are non-linear, the conductance values in the linear region must be estimated as it is described in the **Supporting information** of this part in Chapter 8.

Figure 26 collects the *I-V* curves at low bias at ±12 kG for both enantiomers, D (Figure 26.a,b) and L (Figure 26.c,d). Experimental data can be fitted by a straight line in all cases whose slopes are G_1^D(+12 kG) = 85.9 nS, G_1^D(-12 kG) = 87.5 nS, G_1^L(+12 kG) = 2.99 μS and G_1^L(-12 kG) = 2.946 μS, respectively. The differences between both enantiomers for the same magnetization value (+m o -m) are not statistically significant due to the overlapping of the curves, as mentioned above. Based on the above, it can be concluded that $\Delta G_1 \rightarrow 0$ cuando $V \rightarrow 0$, donde $\Delta G_1 = G_1^{D/L}(+m) - G_1^{D/L}(-m)$. Thus, once again, Onsager's reciprocity principle is validated in a CISS system.

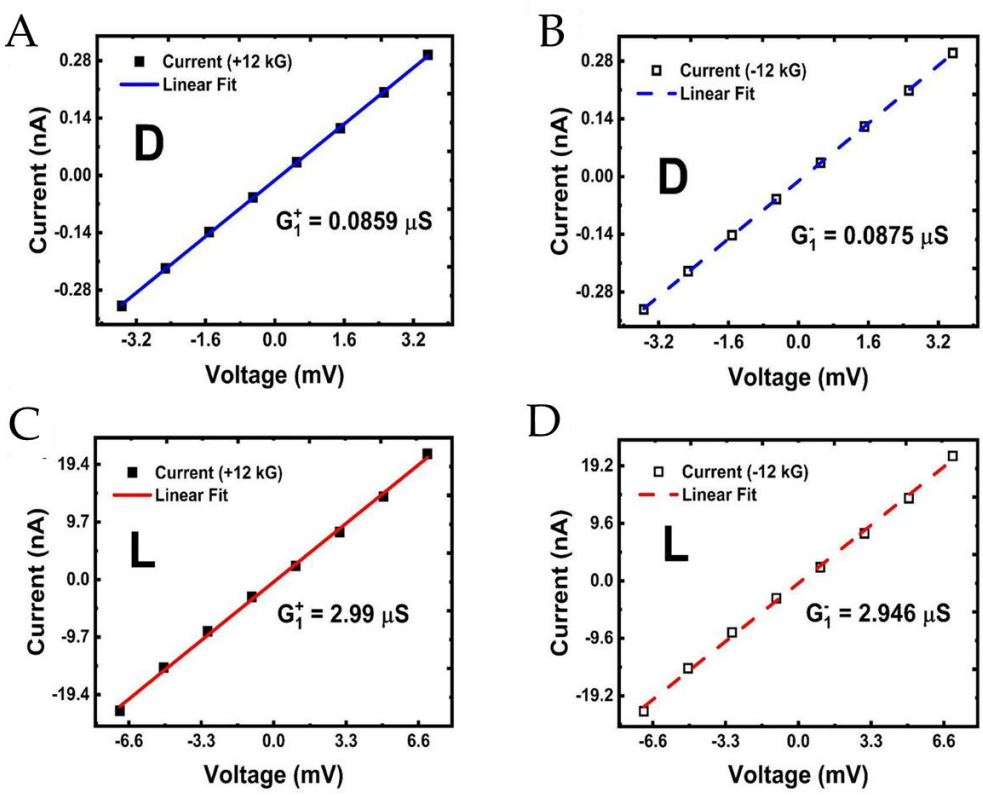

Figure 26. a and b) Linear range conductance measurements for D functionalized samples for ±12 kG. The values are nominally identical, considering the noise margin in this bias range. d and d) Linear range conductance measurements for L functionalized samples for ±12 kG. The values are nominally identical, considering the noise margin in this bias range.

The preceding evidence demonstrates a clear correlation between transport nonlinearity and CISS magnetoconductance (MC CISS) in a system such as the one under investigation in this study. The CISS effect manifests gradually as the polarization increases and the transport becomes more nonlinear, while it is inexistent in the linear range.

Linear response generally refers to a small "perturbation" of the equilibrium by a small voltage *V*, so that the current response is linear with respect to the applied voltage. The response can be considered linear regardless of temperature if the *I-V* relationship is linear or if the slope of *dV*/*dI* is not affected by bias.

Direct measurements of MC also allow to evaluate the dependence of the transversal CISS effect on bias. Typical MC curves in the nonlinear range of transport (0.5 V) are shown in Figure 27.a and b, where again a positive MC background is observed, symmetric with respect to B. It has been commented above that this background is due to magnetic field-dependent hopping phenomena. These plots clearly show an asymmetry in the conductance values at ±12 kG, which is consistent with the *I-V* characteristics described above. Moreover, this asymmetry is chirality dependent, being opposite depending on whether one enantiomer or the other is evaluated.

Figure 27.c and d show the conductance change, $\Delta G(B)$, defined as $\Delta G(B) = \frac{1}{2}[G(B) - G(-B)]$. This allows for the elimination of the positive symmetric background of MC. As can be observed, the plot reaches a saturation point at approximately -8 kG, which coincides with the saturation of the Ni contact magnetization. It is evident that samples L and D exhibit opposite behaviours in terms of resistance change. Given that the Ni electrode is magnetized out-of-plane, in accordance with the conventional CISS description, the detected

conductance change must align with the spin components in the out-of-plane direction. Consequently, this behaviour is also chirality dependent.

ΔG shows a decreasing trend as the bias is reduced, as can be seen in Figure 27.e and f, which plots the measured MC results at different bias values. This is consistent with the previous discussion where the CISS effect gradually disappears as the bias is reduced.

Although the transverse geometry cancels out the EMChA effect, it can be evaluated whether there is any residual manifestation of it by the dependence of the CISS signal on the bias. In this case, the intensity difference (ΔI) in an intermediate range of 0.2 V was evaluated, since this is where this effect should manifest itself, which may introduce a second-order contribution to the current. The mathematical expression for this calculation can be found in **Supporting information** of this part in Chapter 8.

Figure 27.g and h show the even and odd components for ΔI. Even component is calculated as $(\Delta I(+V) + \Delta I(-V))/2$, while the odd component is calculated as $(\Delta I(+V) + \Delta I(-V))/2$. The even component is almost 0 indicating the absence of any residual contribution of EMChA, which makes it clear that this cannot be the underlying mechanism by which the CISS effect manifests itself.

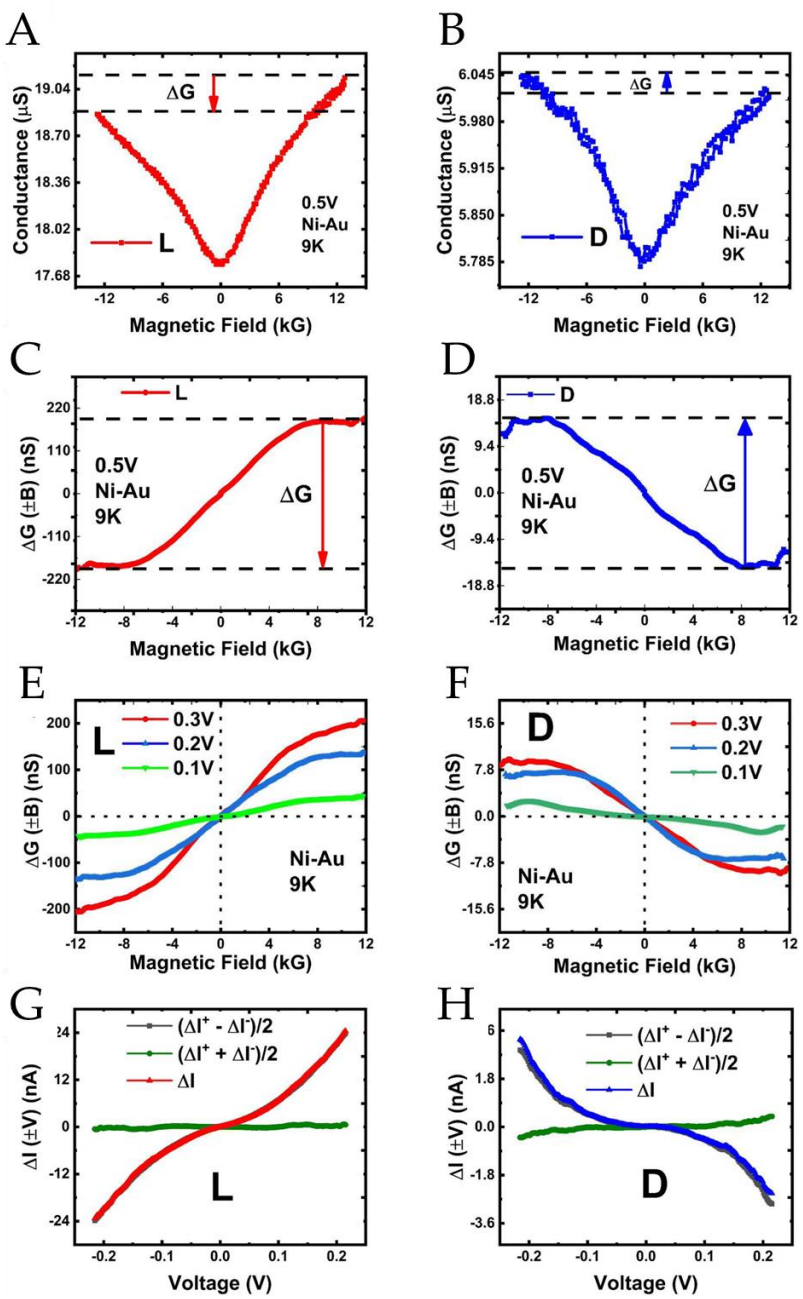

Figure 27. a and b) MC measurements on L and D chiral samples, respectively, in the non-linear range (0.5 V bias). Both forward and backward field scans are recorded. c and d) Elimination of the background MC signal and ΔG vs. B plots. e and f) ΔG vs. B as a function of bias, showing that ΔG gradually decreases with lowering bias. h and g) Even and odd parts of the CISS signal ΔI in the 0.2 V bias window (non-linear range). The even part is almost negligible, implying that the CISS signal must have an odd functional dependence on the bias.

Finally, the role of both the gold electrode and the chiral medium must be established. The Au contact used for the fabrication of the devices has a thickness of approximately 100 nm, and the dipeptide molecules are attached to the carbon nanotubes, as previously established at the beginning of this discussion. Therefore, it should not exhibit ferromagnetic hysteresis as has been reported in thin layers of gold, about 15 nm, coated with chiral molecules. This means that the Au electrode cannot be considered to have ferromagnetic behaviour. In addition, the thermal annealing step to which the device is subjected ensures good ohmic contact and the charge carriers are injected directly into the nanotubes rather than at the interface.

All this, together with the fact that the transport behaviour fits the VRH model, and that the global supramolecular chirality of the medium governs the response of the device, indicates that the observed effect originates from the spin polarization accumulated during transport through the bulk of the sample, not in the interface Au/chiral medium.

3.3. Role of spin-orbit coupling on the CISS effect signal.

The spin-orbit coupling (SOC) is considered to play a fundamental role in the manifestation and intensity of the CISS effect. In order to evaluate how it influences the CISS effect signal, results obtained on samples with different SOC will be evaluated in this section.

The SOC depends inversely on the nanotube radius, as discussed in the background, so that the larger the radius, the lower the SOC. Thus, the sample spectrum prepared for this section comprises single-walled (SW-), double-walled (DW-) and multi-walled (MW-) Fmoc-FF(L/D) functionalized carbon nanotubes

(CNTs), the latter being understood as all CNTs having more than two layers. The gelation of the samples is carried out using GdL.

The diameters of the CNTs provided by the manufacturer were 0.82, 0.9 and 9.5 nm (SW, DW- and MW-, respectively), although they have been independently confirmed by radial breathing mode (RBM) Raman spectra obtained for the raw SW- and DWCNTs and scanning electron microscopy (SEM) for the functionalized MWCNTs (for more details see experimental section in chapter 8). Figure 28.a shows a cross section of the MWCNTs, as well as the direction of transport of the charge carriers in the device.

MWCNTs consist of multiple coaxial graphene cylinders with different diameters. This assumes that in most situations, including the one at hand, electrical contact is only made with the external layer. Therefore, current is injected and extracted through this outermost layer. Furthermore, considering the weak interlayer coupling that prevents electron hopping at low temperatures, the current flows mainly through the external layer. This layer is the one functionalized with Fmoc-FF (L/D) molecules, so the charge carriers are subject to the chiral potential during their transport through it.

The SW and DW samples show a more temperature sensitive resistance than MWCNTs, as can be seen from the Figure 28.b. This is due to heterogeneous carrier transport. It has been previously commented that the transport of CNTs is done through phonon-assisted tunnels or by hopping from one localized segment to another. Furthermore, in the network of CNTs there are potential barriers that arise from defects in the nanotubes and from crossover points between one another. Narrower nanotubes (SW and DW) have higher energy bands, resulting in higher semiconducting behaviour. Thus, they exhibit higher

resistance sensitivity to temperature. Moreover, the band gap depends inversely on the diameter of the CNTs, and those with larger diameters (MWCNTs) tend to exhibit more metallic behaviour. Thus, the resistance of SW and DWCNTs is significantly higher than that of MWCNTs.

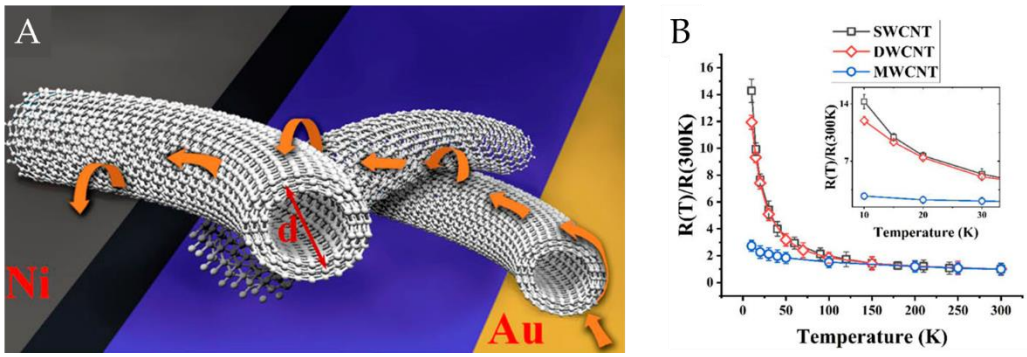

Figure 28. a) Transversal section and direction of transport in MWCNTs. b) Dependence of resistance on temperature in the range 10-300 K.

Magnetoresistance (MR) measurements were performed on the same type of two-terminal planar geometry as in the previous cases. Figure 29.a, c and e show the MR curves for SW, DW and MWCNTs, respectively. Once again, SW, DW and MWCNTs B ($R(+B) \neq R(-B)$ has been detected and this asymmetry exhibits a dependence with chirality.

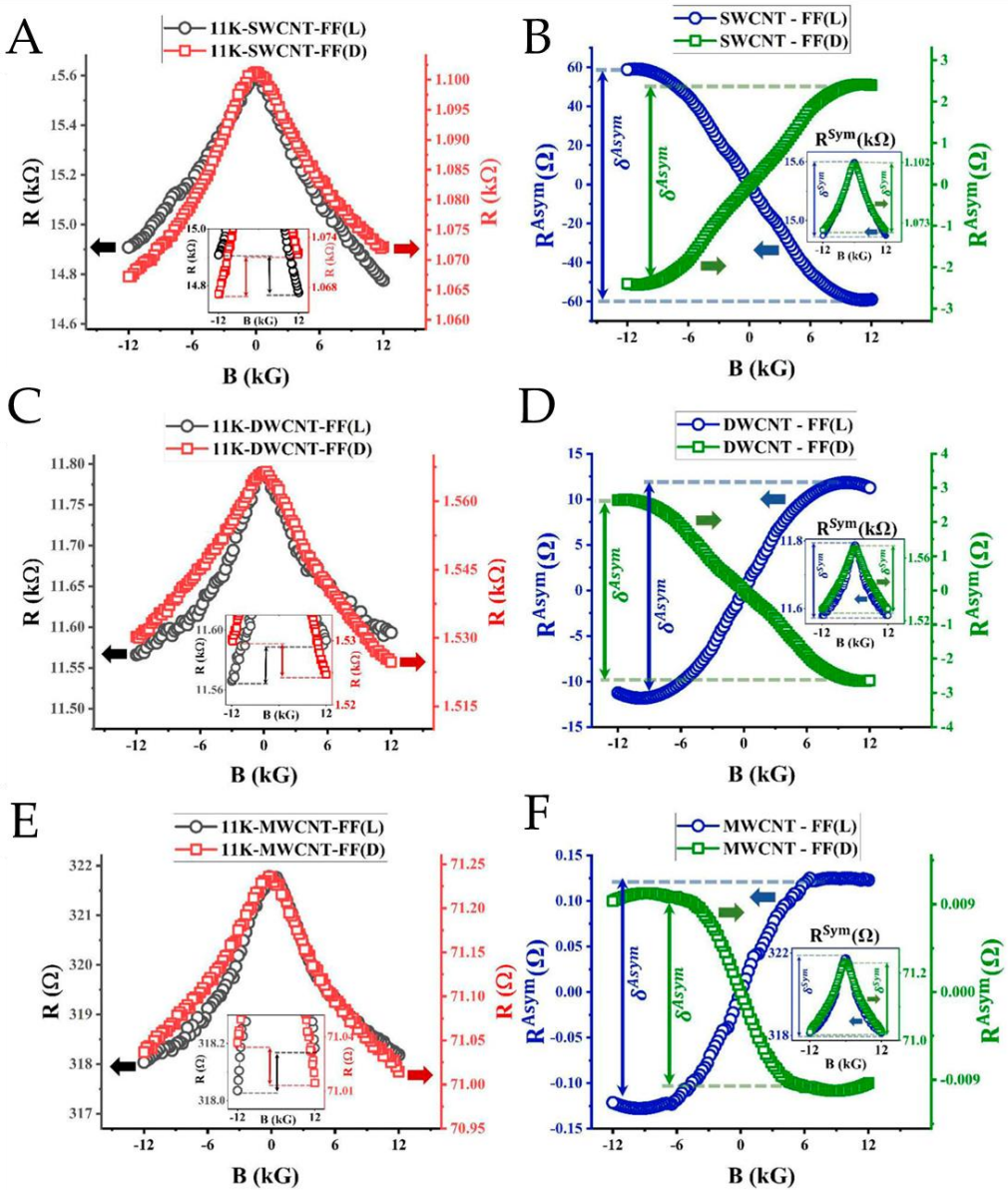

Figure 29. a), c) and e) Chirality-dependent MR effects in SWCNT, DWCNT, and MWCNT networks, respectively. b), d), and f) Asymmetric (main image) and symmetric (inset) components of the MR responses.

Figure 29.b, d and f show asymmetric and symmetric components of the MR response, calculated as described in Chapter 8. These components were computed as a normalizes signal where $\delta^{Asym}/\delta^{Sym} \times 100\%$ and are shown in Figure 30 for all samples.

The CISS-induced asymmetry in the MR response decreased as the average diameter of the CNTs increased, i.e., the magnitude of the signals for SWCNTs were always stronger than for MWCNTs, while DWCNTs showed intermediate intensities. CISS signal was calculated as shown in Equation 9 in Chapter 8 and the absolute value ($|\delta^{CISS}|$) was plotted in Figure 30.b.

$|\delta^{CISS}|$ showed the same trend as the ratio $\delta^{Asym}/\delta^{Sym}$, with MWCNTs having the weakest CISS signal by an order of magnitude compared to the signals obtained for SW and DWCNTs. This makes sense considering that the average diameters of DW and MWCNTs differ by exactly one order of magnitude. This reduction in diameter, and thus radius, causes the spin-orbit coupling strength for DWCNTs and SWCNTs to increase by the same amount as for MWCNTs. The CISS signal increased in the same way and for the same reason, as shown in the Figure 30.b. If the signal intensities for SWCNTs and DWCNTs are compared, the same conclusions can be drawn as above. In this case, the intensities differ by a factor of 2.2 when their diameters differ by a factor of 1.1. Thus, it can be concluded that the reduction observed for the CISS effect signal intensity with nanotube diameter is due to the reduction of spin-orbit coupling as the diameter increases.

Regarding the behaviour of the signal ratio $\delta^{Asym}/\delta^{Sym}$ with the change of temperature ((Figure 30.c), it was observed that the intensity decreased as the temperature increased, as already mentioned in previous sections. Here, what was noteworthy was that the CISS effect signal manifested itself in the 10-30 K range, corresponding to an energy scale of 0.86-2.58 meV. Coincident values with the spin-orbit energy scale for CNTs which is around 1 meV.

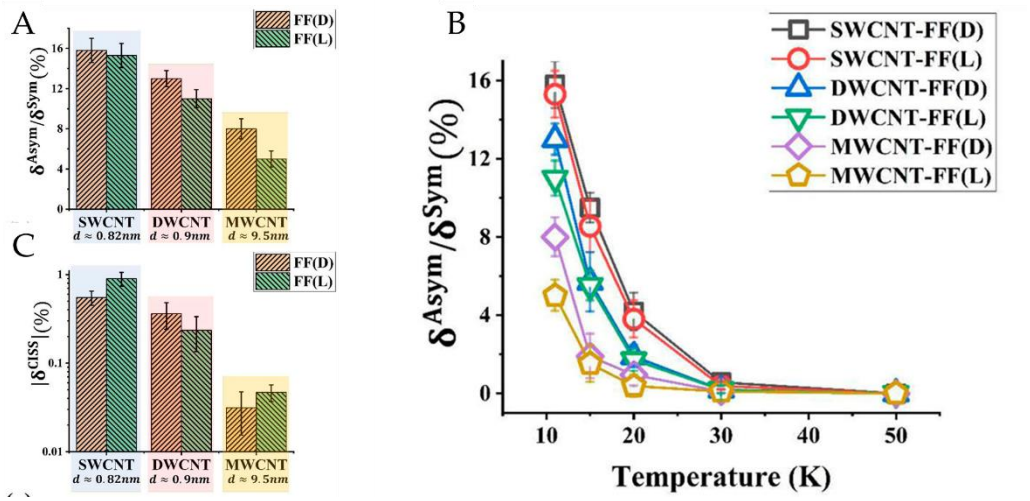

Figure 30. a) CISS-induced asymmetry of the MR curves as a function of tube diameter. b) CISS signal as a function of tube diameter. c) MR asymmetry as a function of temperature for SW-, DW-, and MWCNTs.

SWCNTs exhibited opposite behaviour to DW and MWCNTs, in agreement with the MR measurements (Figure 29). The CD spectra of the dilute solutions of each type of CNT with the different functionalizations threw the same results, where it appeared that a chiral inversion occurred.

This chiral inversion has already been seen in the presence of gold nanoparticles (AuNPs), where the molecular interaction with the different curvatures of these nanoparticles induces an inversion in the supramolecular chirality. The differences in the diameter of the nanotubes here, leads to a different curvature.[102]

The results showed in Figure 31 of the CD spectra support the observation of the reversal of the sign of the CISS signal, since the same occurs with the Cotton effect signals in the samples containing SWCNTs with respect to the CNT-free solutions of Fmoc-FF (L/D), while this inversion is not observed for the other types of nanotubes.

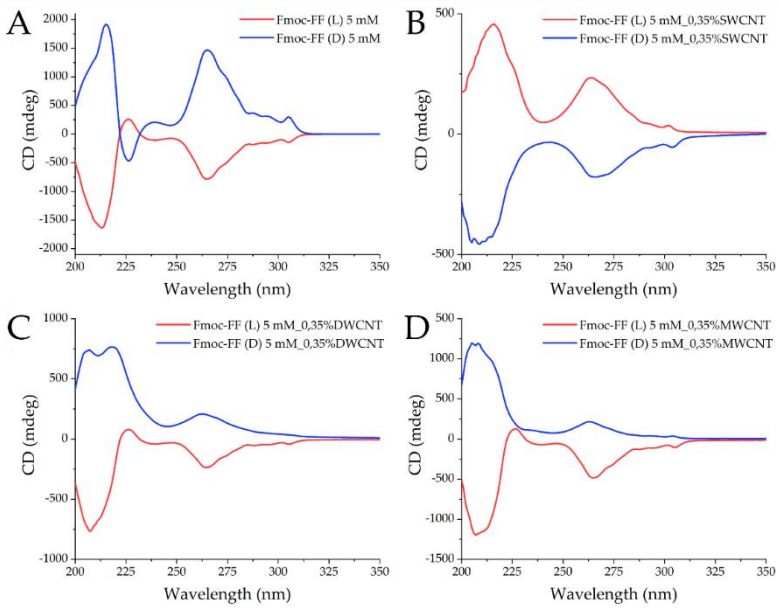

Figure 31. CD spectra of the a) Fmoc-FF peptide solutions, b) Fmoc-FF–SWCNT suspensions, c) Fmoc-FF–DWCNT suspensions and d) Fmoc-FF–MWCNT suspensions. In all measurements, the peptide concentration was 5 mM, and the CNT concentration was 0.35%. The red colour corresponds to the Fmoc-FF (L) derivative, and the blue colour corresponds to the Fmoc-FF (D) derivative. CD spectra had been normalized for comparative purposes.

[102] Gong, Y.; Cao, Z.; Zhang, Z.; Liu, R.; Zhang, F.; Wei, J.; Yang, Z. *Angew. Chemie - Int. Ed.* **2022**, *61* (10), e202117406.

3.4. CISS effect in functionalized graphene layers.

The ability to induce CISS signal in reduced graphene oxide (rGO) sheets would significantly expand the use of new materials in devices that can be employed in spintronics, as noted in the background. It has also been previously discussed that peptide fibers can act as a template and induce curvature in flexible solid particles upon assembly. Moreover, the presence of solid particles could inverse the supramolecular chirality of the supramolecular aggregates, as discussed in the previous section.

The study of samples of rGO layers of different thickness (single layer (SLG) or multilayer (MLG)) functionalized with Fmoc-FF (L/D) as chiral components and with Fmoc-GG as achiral control will shed light on these questions.

CD spectra of the diluted Fmoc-FF (L/D) basic solutions, of these with SLG and with MLG as well as of the SLG and MLG solutions with Fmoc-GG are shown in the Figure 32. Samples with SLG show a reversal of the signs of the Cotton effect when compared to basic solutions without graphene, indicating a reversal of the supramolecular chirality in the aggregates. This inversion is not observed in the samples containing GLM. Regarding the samples functionalized with Fmoc-GG, a null CD is obtained, as expected. The previous sections have shown that CD spectra can correlate with the appearance of a CISS effect signal, so these results may indicate the same observation.

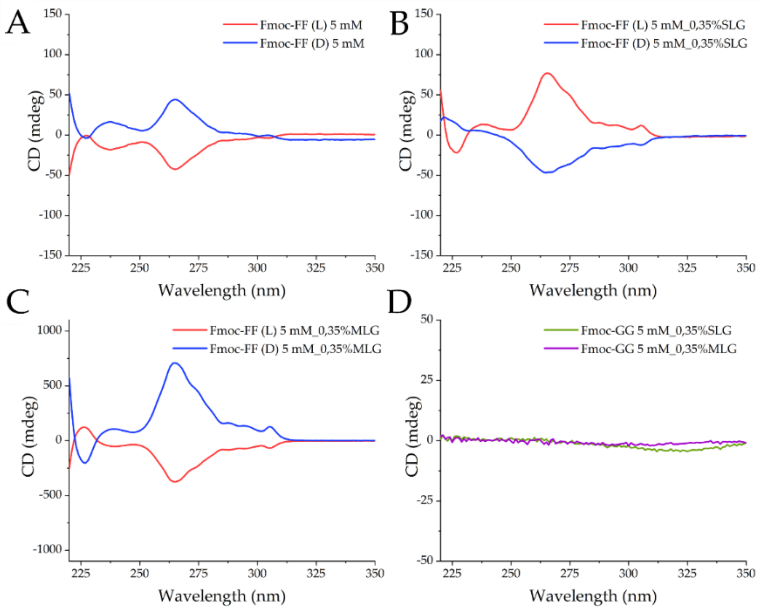

Figure 32. CD spectra of the a) Fmoc-FF (L/D) solutions, b) Fmoc-FF (L/D)-SLG suspensions, c) Fmoc-FF (L/D)-MLG suspensions and d) Fmoc-GG-SLG and Fmoc-GG-MLG suspensions.

Figure 33.a illustrates the appearance of SLG flakes in the absence of any functionalization. It is evident that the flakes are completely flat and exhibit well-defined, straight edges. In contrast, Figure 33.b and c show functionalized SLGs that appear to be partially rolled due to the self-assembly process.

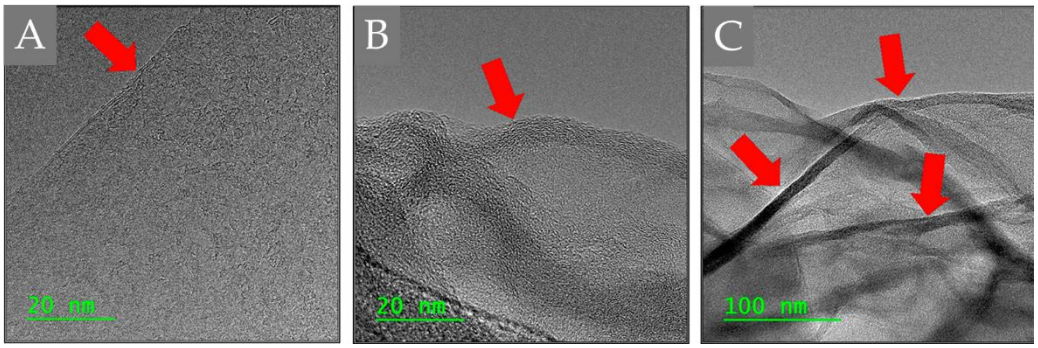

Figure 33. a) TEM image of a pristine (unfunctionalized) graphene flake. Arrow shows the straight edge of the flake. b) and c) TEM images of functionalized flakes. The arrows show the curved flakes.

As in devices fabricated from peptide xerogels with nanotubes, electron transport occurs from flake to flake through field-assisted tunneling, which are heterogeneously distributed in the chiral film between the Ni and Au electrodes, as shown in Figure 34.a. Additionally, Figure 34.b shows a FESEM image of the real device.

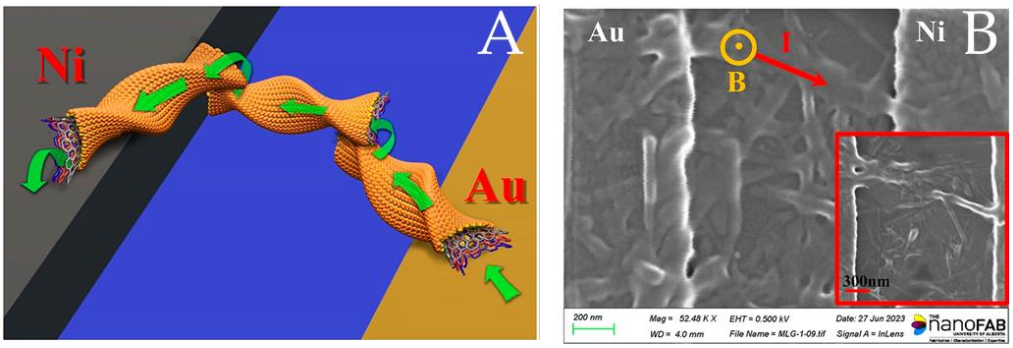

Figure 34. c) Schematic of a typical current path through the chiral graphene flakes, which have both in- plane (primary) and out-of-plane (secondary) components. b) FESEM image of a two-terminal device in which a chiral-functionalized graphene layer is contacted by Au and Ni electrodes. Applied magnetic field is out-of-plane.

Characteristics *I-V* as a function of temperature measured at *B*=0 for the Fmoc-FF (L/D) samples with SLGs are shown in Figure 35.a and b. The results indicate that these characteristics are not linear with respect to bias and exhibit semiconducting behaviour. Again, this response can be explained with the VRH model, as shown in the insets. The dependence obtained is linear, which is consistent with this type of structures.

Figure 35.c and d show the dependence of the resistance with temperature for Fmoc-GG functionalized SLG and MLG. It can be seen that the dependence of the SLG is more pronounced than for the GLM samples, which may be due to the fact that in the latter, only the outermost layer is functionalized.

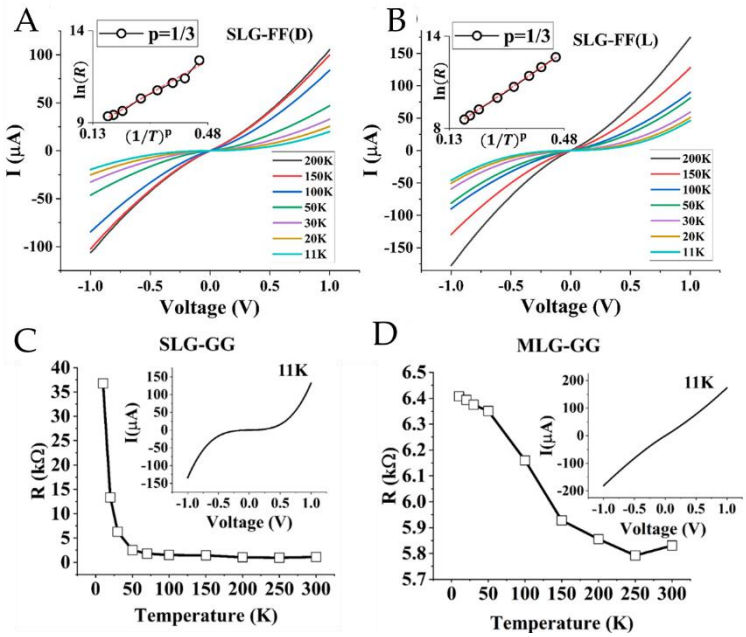

Figure 35. a) and b) Main image: Current–voltage (*I–V*) characterization of Fmoc-FF (L/D) functionalized SLG samples. Insets: Fitting with the VRH model. c) and d) Temperature dependence and *I-V* characteristics for SLG and MLG functionalized with Fmoc-GG.

Magnetoresistance (MR) measurements, performed with the same two-planar configuration as in all previous sections, of the Fmoc-GG functionalized SLG and MLG samples are reported in the Figure 36.a and b. It can be seen that showed symmetry, i.e., *R*(+12 kG) = *R*(-12 kG). In addition, the MLG samples have lower MR values than those containing SLG, which can be explained by the multiple conduction paths that can be established through the MLG inner layers. These inner layers are not functionalized, so there are fewer barriers, and this reduces the overall resistance of these samples. In contrast, evaluating the MR responses for the Fmoc-FF (L/D)-functionalized SLG and MLG samples (Figure 36.c and d, it is observed that there is an asymmetry, *R* (+12 kG) ≠ *R* (-12 kG), dependent on chirality, which translates into the detection of a CISS signal. In addition, this

asymmetry presents an opposite behaviour if samples are compared with SLG and with MLG.

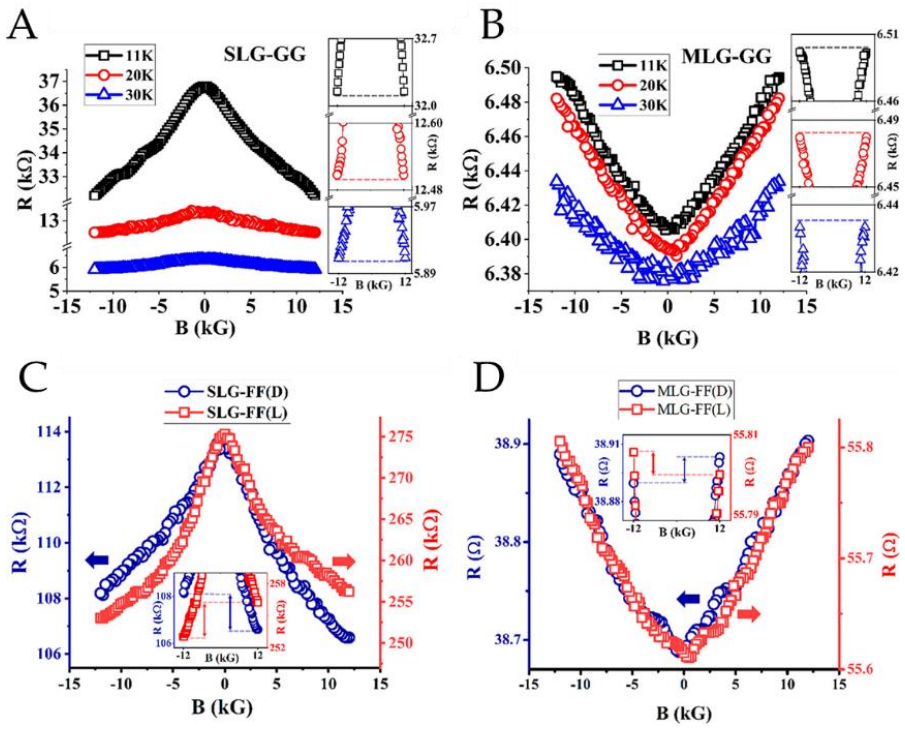

Figure 36. a) and b) Main image: MR characterization of SLG and MLG samples, respectively, functionalized with achiral Fmoc-GG molecules. The insets show the symmetry of the MR response. Resistance values are measured at 0.5 V. c) and d) Main images: MR responses of Fmoc-FF L/D functionalized SLG and MLG samples, respectively. The insets show the asymmetry of the MR responses. Resistance values are measured at 0.5 V

The behaviour describe above can be seen more clearly in the Figure 37, that represents the asymmetric contribution of the MR response. This opposite behaviour correlates well with the results obtained for the CD spectra. Thus, it seems to indicate that the supramolecular chirality of the fibers is efficiently transferred to the graphene layers and may be a predictor of the appearance of a CISS signal, as discussed previously.

The contribution of the chiral molecules to the MR response is represented in the R^{Asym} value, while the CISS-independent contribution is represented by R^{Sym}, both calculated following the Equation 6 . CISS signal is represented by $\delta^{Asym}/\delta^{Sym}$ x 100%, as indicated in the previous section, calculating both components with Equation 7 and Equation 8 with the values obtained to a field of ± 12 kG. Figure 37.a and b show R^{Asym} and R^{Sym} and Figure 37.c and d represent the CISS signal ($\delta^{Asym}/\delta^{Sym}$ x 100) dependence with temperature for SLG and MLG samples. It seems to follow the same trend as for the samples with CNTs with the CISS signal disappearing as the temperature increases.

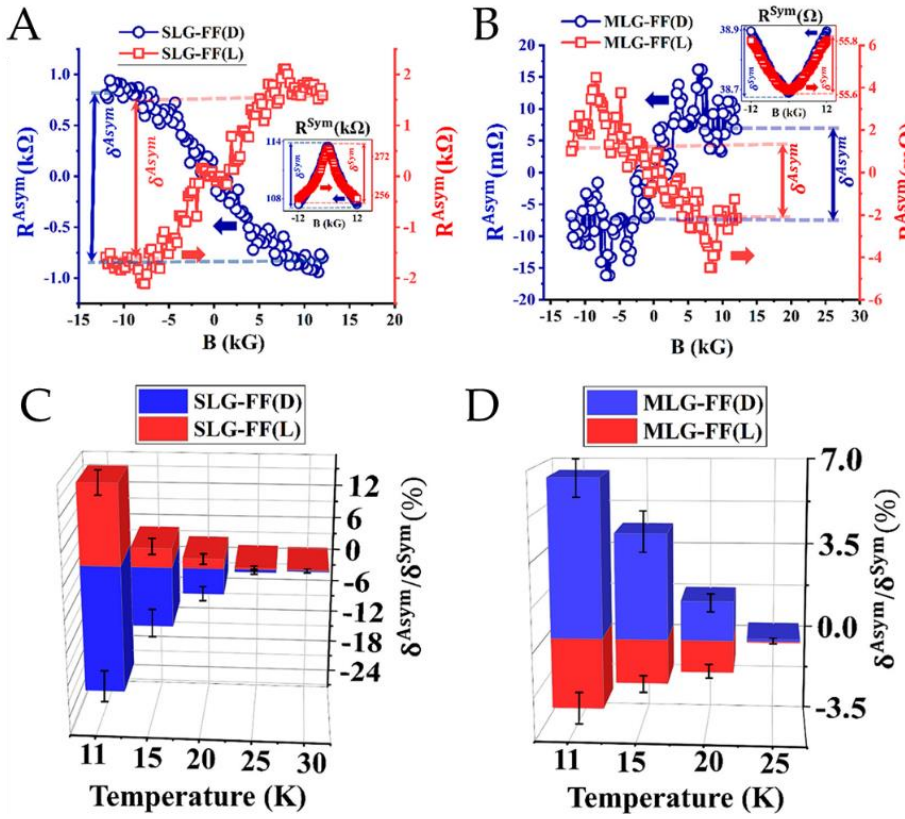

Figure 37. a) and b) Odd (main image) and even (insets) components of the MR response. c) and f) CISS signal as a function of temperature for both types of samples.

Finally, the validity of Onsager's reciprocity principle can also be studied in these systems by studying the differential current signal, ΔI, as a function of voltage (Figure 38). It must be satisfied that ΔI=0 at least in the linear region, which can be clearly seen in the plot as the voltage approaches 0 V. Thus, it can be concluded that these systems also comply with Onsager's reciprocity principle. Moreover, the signal saturates at around 0.5 V, therefore, the MR curves discussed have been obtained at this optimum bias value.

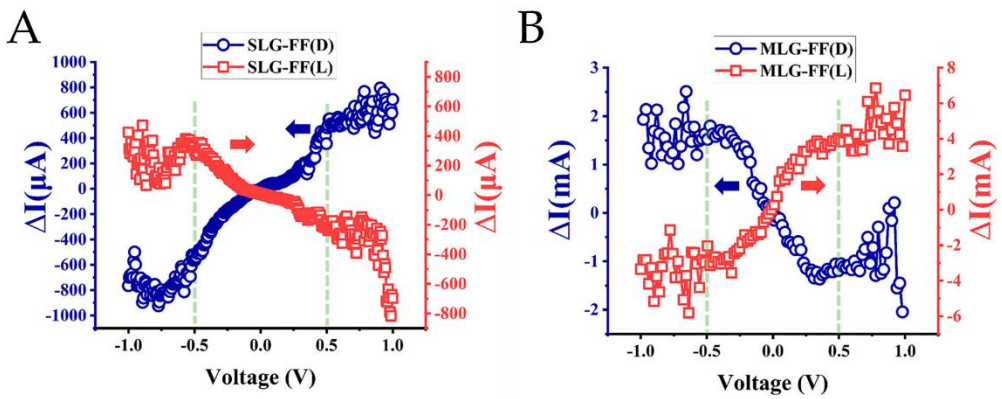

Figure 38. Bias dependence of ΔI, computed as I (+12 kG) – I (−12 kG), for Fmoc-FF (L/D) functionalized samples with a) SLG and b) MLG.

The fact of being able to observe the CISS effect in graphene sheets is not intuitive, *a priori*, due to the weak spin-orbit interaction of pure graphene. However, there are several factors to be considered to explain the detection of this effect.

First, curved graphene layers exhibit an additional spin-orbit term due to the mixing of σ and π bands that is produced by the local curvature. This have been demonstrated by theoretical calculations and this interaction is estimated to be about one order of magnitude higher than the intrinsic spin-orbit coupling of

graphene.[103] This curvature is present in the systems studied here as seen in Figure 33, thanks to the self-assembly of the Fmoc-FF (L/D) molecules that coat the graphene flakes. In addition, the curvature is higher in the samples with SLG than with MLG, due to the higher structural stiffness of the latter, which implies a higher difficulty when bending them. This is also consistent with the fact that the intensity of the CISS signal is much higher in the SLG samples.

Second, the graphene layers used in these samples are rGO. The synthesis of this material results in the incorporation of atoms other than carbon, such as hydrogen, into its structural composition. These impurities can cause a local distortion in the graphene lattice due to sp^3 hybridization, increasing the spin-orbit interaction at the local level.

In addition to these factors, there are sources of magnetic defects that also contribute to an increase in spin-orbit coupling. Thus, hydrogen atoms that are present as impurities can give rise to local magnetic moments. They can also come from carbon vacancies that arise during synthesis and reduction by thermal exfoliation of GO to rGO.

All these factors together make possible the detection of the CISS signal in the systems studied here.

[103] Huertas-Hernando, D.; Guinea, F.; Brataas, A. *Phys. Rev. B - Condens. Matter Mater. Phys.* **2006**, *74* (15).

4. Conclusions

1. The CISS effect depends on the supramolecular chirality of the hybrid materials. The sign of the CISS effect can be controlled or generated depending on the stimulus used for the formation of the supramolecular gels, e.g. GdL or Na_2CO_3.
2. The experimentally measured signal of the CISS effect, represented by the normalised parameter Δ, is an average generated by multiple spin-dependent chiral scatterings in the CNT network. However, the magnetoresistance (MR) signal obtained is in a similar range to that of chiral molecules ordered under comparable conditions, surprisingly.
3. The planar geometry of the devices used in these studies provides a more reliable signal than measurements in vertical arrangements, because the latter produce undesired couplings between the electrodes that negatively affect the signal. In addition, devices that integrate complementary spin layers on a single platform could be fabricated thanks to the possibility of modulating the CISS effect.
4. The transverse CISS MC and its chirality dependence have been investigated using a transverse measurement configuration, in which magnetic field and transport direction are perpendicular. This geometry also allows to avoid any contribution from the EMChA effect, measuring a 'pure' CISS effect. Therefore, it has been concluded that transverse MC exists even in absence of EMChA and exhibits tell-tale signatures of the CISS effect.
5. The transverse CISS effect disappears in the linear response regime, which proves the validity of Onsager's reciprocity principle. Moreover, at higher bias gradually appears as the linearity of the transport characteristics is lost.

On the other hand, the non-linear CISS signal exhibits an odd functional relationship with the applied bias, which could assist in uncovering the potential underlying mechanism of CISS.

6. The strength of this pure CISS signal increases proportionally with the spin-orbit intensity of the medium. Thus, CISS cannot be explained by the EMChA alone and it becomes clear that the spin-orbit coupling of the medium plays a key role.
7. A priori, the weak spin-orbit interaction of graphene makes it unlikely that the CISS effect can be manifested in this material. However, it has been possible to induce the CISS effect in rGO films functionalised with Fmoc-dipeptides thanks to the supramolecular organisation of these molecules, which has given them a 'conformational chirality'. This conformational chirality has induced a curvature in the graphene which, together with the impurities in the rGO, has improved the spin-orbit coupling, leading to the CISS signal.

Chapter 4

Development of a Novel Family of Metal-Organic Frameworks Biocomposites within Peptide Supramolecular Hydrogels

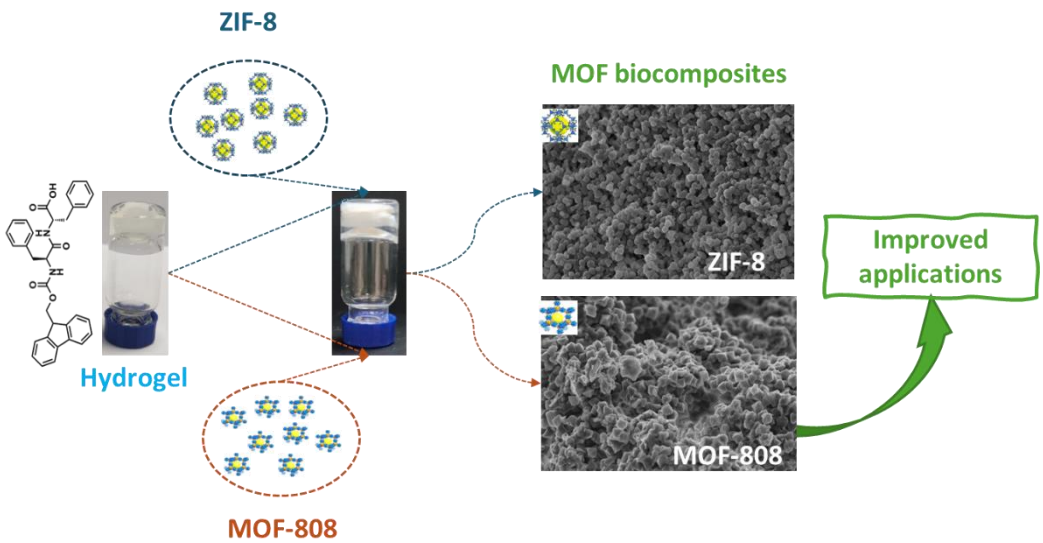

1. Background

Metal-organic frameworks (MOFs) are porous, crystalline materials that are distinguished by their high surface area, tuneable structures, and numerous regularly arranged adsorption sites. These properties make MOFs exceptional candidates for use as adsorbents or catalysts for detoxification in environmental and medical applications. However, MOFs are often produced as crystalline powders, which complicates their processing and fabrication as adsorbents, limiting their practical application in everyday technologies.[104]

One strategy frequently employed to address this challenge is the combination of MOFs and biopolymers, which results in a novel class of composite materials known as MOF biocomposites or bio-MOFs. These biomaterials offer distinct advantages, including simplified processing and enhanced biocompatibility. The synthetic method and the type of biopolymer used have a great impact on the physicochemical properties of the resulting material. This opens the possibility of exploring a wide range of options for obtaining different derivatives with new or improved properties.[105]

---

[104] a) Zhou, H. C.; Long, J. R.; Yaghi, O. M. *Chem. Rev.* **2012**, *112* (2), 673–674. b) Matsuda, R.; Kitaura, R.; Kitagawa, S.; Kubota, Y.; Belosludov, R. V.; Kobayashi, T. C.; Sakamoto, H.; Chiba, T.; Takata, M.; Kawazoe, Y.; Mita, Y. *Nature* **2005**, *436* (7048), 238–241. c) Mon, M.; Bruno, R.; Ferrando-Soria, J.; Armentano, D.; Pardo, E. *J. Mater. Chem. A* **2018**, *6* (12), 4912–4947. d) Rojas, S.; Baati, T.; Njim, L.; Manchego, L.; Neffati, F.; Abdeljelil, N.; Saguem, S.; Serre, C.; Najjar, M. F.; Zakhama, A.; Horcajada, P. *J. Am. Chem. Soc.* **2018**, *140* (30), 9581–9586.e) Furukawa, S.; Reboul, J.; Diring, S.; Sumida, K.; Kitagawa, S. *Chem. Soc. Rev.* **2014**, *43* (16), 5700–5734.

[105] a) Imaz, I.; Rubio-Martínez, M.; An, J.; Solé-Font, I.; Rosi, N. L.; Maspoch, D. *Chem. Commun.* **2011**, *47* (26), 7287–7302. b) Doonan, C.; Riccò, R.; Liang, K.; Bradshaw, D.; Falcaro, P. *Acc. Chem. Res.* **2017**, *50* (6), 1423–1432. c) Rojas, S.; Devic, T.; Horcajada, P. *J. Mater. Chem. B* **2017**, *5* (14), 2560–2573. d) Zhang, M.; Gu, Z. Y.; Bosch, M.; Perry, Z.; Zhou,

In situ growth, that is, the assembly of the MOFs components inside the biopolymer matrix, favours better dispersion of the MOFs, thereby enhancing the homogeneity of the biocomposite and improving its adhesion to the organic matrix. A multitude of biopolymers have been used for this type of growth such as cellulose, cotton, chitosan, alginate, agarose or gelatin. These compounds have been employed for the growth of different MOFs such as HKUST-1, ZIF-8, ZIF-90, ZIF-67 and MIL-100. The bio-MOFs obtained have demonstrated enhanced activity due to augmented stability and accessibility.[106] Despite the wide variety of biopolymers mentioned, it is clear that studies on this strategy have been limited to the use of natural polymers, leaving other types of biocompatible hydrogels unexplored.

Peptide supramolecular hydrogels thus emerge as a possible successful option to apply this bio-MOFs growth strategy thanks to the variety of advantages, already discussed, such as precise composition, affordability, or mechanical, chemical and biological properties that can be adjusted almost on demand. This is coupled with the fact that self-assembly can be promoted by the addition of different metal salts, which can be a structural part of the MOFs. Thus,

---

H. C. *Coord. Chem. Rev.* **2015**, *293–294*, 327–356. e) El Hankari, S.; Bousmina, M.; El Kadib, A. *Prog. Mater. Sci.* **2019**, *106*, 100579.

[106] a) Küsgens, P.; Siegle, S.; Kaskel, S. *Adv. Eng. Mater.* **2009**, *11* (1–2), 93–95. b) da Silva Pinto, M.; Sierra-Avila, C. A.; Hinestroza, J. P. *Cellulose* **2012**, *19* (5), 1771–1779. c) Rodríguez, H. S.; Hinestroza, J. P.; Ochoa-Puentes, C.; Sierra, C. A.; Soto, C. Y. *J. Appl. Polym. Sci.* **2014**, *131* (19), 40815. d) Ozer, R. R.; Hinestroza, J. P. *RSC Adv.* **2015**, *5* (20), 15198–15204. e) Matsumoto, M.; Kitaoka, T. *Adv. Mater.* **2016**, *28* (9), 1765–1769. f) Laurila, E.; Thunberg, J.; Argent, S. P.; Champness, N. R.; Zacharias, S.; Westman, G.; Öhrström, L. *Adv. Eng. Mater.* **2015**, *17* (9), 1282–1286. g) Zhu, H.; Zhang, Q.; Zhu, S. *ACS Appl. Mater. Interfaces* **2016**, *8* (27), 17395–17401. h) Gil-Hernández, B.; MacLaren, J. K.; Höppe, H. A.; Pasán, J.; Sanchiz, J.; Janiak, C. *CrystEngComm* **2012**, *14* (8), 2635–2644. i) Garai, A.; Shepherd, W.; Huo, J.; Bradshaw, D. *J. Mater. Chem. B* **2013**, *1* (30), 3678–3684.

biocomposites could be obtained in which the growth of peptide fibers and MOFs is triggered by the same stimulus.[107]

The objective of this study was to ascertain the conditions necessary for the *in situ* growth of two MOFs, ZIF-8 ($Zn(mIm)_2$, mIm = 2-methylimidazolate) and MOF-808 ($Zr_6O_4(OH)_4(trimesate)_2(formate)_6$), on Fmoc-FF and Fmoc-AA supramolecular gels. The selection of these MOFs was based on the fact that their synthesis in water is described at room temperature, which allows for the use of peptide supramolecular hydrogels without compromising their structure.

MOF-808 is particularly interesting because of its high stability and promising activity in detoxifying water contaminated with phosphorus compounds, such as phosphate ions or organophosphate pesticides (OP).[108]

[107] a) Tao, K.; Levin, A.; Adler-Abramovich, L.; Gazit, E. *Chem. Soc. Rev.* **2016**, *45* (14), 3935–3953. b) Draper, E. R.; Adams, D. J. *Chem* **2017**, *3* (3), 390–410. c) Mañas-Torres, M. C.; Illescas-Lopez, S.; Gavira, J. A.; de Cienfuegos, L. Á.; Marchesan, S. *Isr. J. Chem.* **2022**, e202200018. d) Contreras-Montoya, R.; Arredondo-Amador, M.; Escolano-Casado, G.; *et al*. *ACS Appl. Mater. Interfaces* **2021**, *13* (10), 11672–11682. e) Chen, L.; Pont, G.; Morris, K.; *et al*. *Chem. Commun.* **2011**, *47* (44), 12071–12073. f) Chen, L.; McDonald, T. O.; Adams, D. J. *RSC Adv.* **2013**, *3* (23), 8714–8720. g) Cardoso, A. Z.; Mears, L. L. E.; Cattoz, B. N.; Griffiths, P. C.; Schweins, R.; Adams, D. J. *Soft Matter* **2016**, *12* (15), 3612–3621. h) Mañas-Torres, M. C.; Ramírez-Rodríguez, G. B.; Garcia-Peiro, J. I.; *et al*. *Inorg. Chem. Front.* **2022**. i) Criado-Gonzalez, M.; Peñas, M. I.; Barbault, F.; Müller, A. J.; Boulmedais, F.; Hernández, R. *Nanoscale* **2024**, *16* (20), 9887–9898.

[108] Ma, K.; Wasson, M. C.; Wang, X.; Zhang, X.; Idrees, K. B.; Chen, Z.; Wu, Y.; Lee, S. J.; Cao, R.; Chen, Y.; Yang, L.; Son, F. A.; Islamoglu, T.; Peterson, G. W.; Mahle, J. J.; Farha, O. K. *Chem Catal.* **2021**, *1* (3), 721–733.

The toxicity of OPs is based on their ability to bind to the enzyme acetylcholinesterase (AChE), which is responsible for regulating neurotransmitter function. OPs inhibit the enzymatic activity of AChE by binding to it causing paralysis, respiratory failure, seizures and even death. MOF-808 has been shown to act as a potential antidote for OP poisoning by removing OP compounds from simulated physiological media.[109]

[109] González, L.; Martín-Romera, J. D.; Sánchez-Sánchez, P.; Navarro, J. A. R.; Barea, E.; Maldonado, C. R.; Carmona, F. J. *Inorg. Chem.* **2023**, *62* (13), 5049–5053.

2. Objectives

The versatility of peptide supramolecular hydrogels and their endless applications, as well as their ability to self-assemble under different stimuli such as changes in pH, temperature, solvent, enzymatic activity or addition of salts, have been extensively discussed in previous chapters.

On the other hand, the development of new materials combining MOFs with biopolymers, known as bio-MOFs or MOF biocomposites, allows increasing the applications of these porous materials of great interest and providing them with new or improved properties that make their use in biomedical or biotechnological applications feasible.

This work explores the potential of ***using peptide supramolecular hydrogels as a template for the growth of MOF particles***, promoting the self-assembly of peptides with required components for MOF formation (Figure 39). Additionally, it will examine the capacity of a newly developed biocomposite (Fmoc-FF@MOF-808) to remove or degrade phosphorus pollutants (P-pollutants).[110]

The new bio-MOFs, particularly the biocomposite with ZIF-8, provide the opportunity to test two different protocols for obtaining more homogeneous and well-integrated composite materials. The first protocol, which we refer to as the ***diffusion protocol***, allows for the in situ formation of ZIF-8 by diffusion of 2-methylimidazole (HmIm) in Fmoc-FF gels that have been preformed with

[110] a) Tovar Jimenez, G. I.; Valverde, A.; Mendes-Felipe, C.; *et al*. *ChemSusChem* **2021**, *14* (14), 2892–2901. b) González, L.; Gil-San-Millán, R.; Navarro, J. A. R.; Maldonado, C. R.; Barea, E.; Carmona, F. J. *J. Mater. Chem. A* **2022**, *10* (37), 19606–19611.

$Zn(OAc)_2$. The second protocol, or ***simultaneous protocol***, involves mixing all the components at the same time to promote the formation of peptide fibers and ZIF-8 crystals simultaneously. Due to the difficulty of solubilizing trimesic acid at the required concentrations for the diffusion protocol, the MOF-808 composite is obtained following the simultaneous protocol.

Thus, the specific objectives of this chapter are:

1. Evaluate the ability of Fmoc-FF and Fmoc-AA dipeptides to self-assemble by the addition of $Zn(OAc)_2$ and promote the formation of ZIF-8 by the two protocols described above.
2. Determine the optimal conditions for the formation of ZIF-8 by testing different parameters such as the amount and ratio of $Zn(OAc)_2$ to 2-methylimidazole (HmIm).
3. Investigate the impact of peptide fibers on the size, crystallinity, polymorphism, and morphology of ZIF-8 crystals.
4. Assess the capacity of MOF-808 formation in Fmoc-FF hydrogel obtained by lowering pH due to the addition of formic acid, a required component for MOF-808.
5. Assess the catalytic/adsorption capacity of MOF-808 biocomposites in comparison with pristine MOF-808 for the detoxification of an aqueous solution containing phosphorus pollutants.

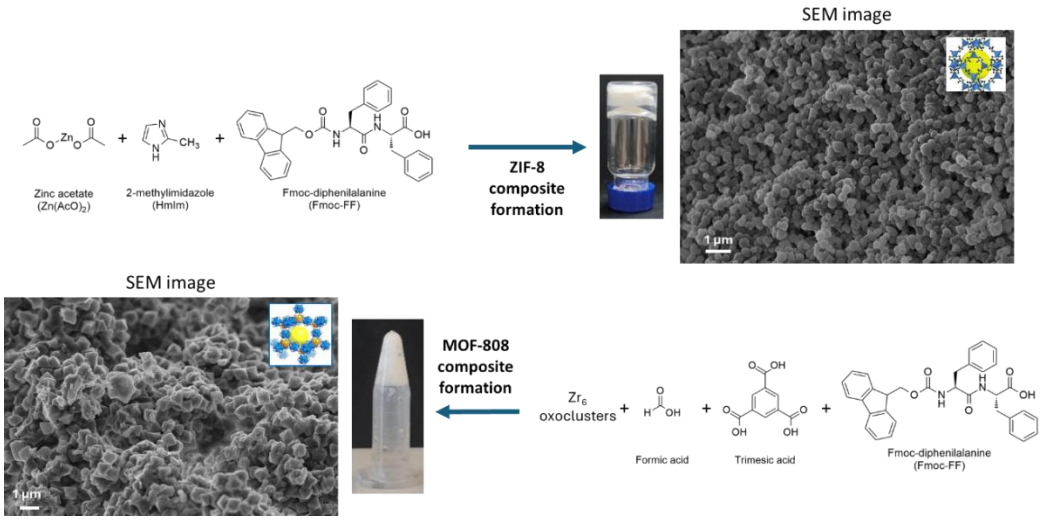

Figure 39. Families of target biocomposite MOFs.

3. Results and discussion

3.1. Peptide Self-Assembly Induced by Zinc Acetate

It is important to note that the ability of the peptides to form ZIF-8 on these gels is dependent on the addition of $Zn(OAc)_2$. Therefore, initially, the capacity of Fmoc-FF to form a complex with the addition of $Zn(OAc)_2$ (50 mM in water) to a basic peptide solution at 10 and 20 mM was investigated (see the complete procedure in Chapter 8). This resulted in the rapid formation of a transparent hydrogel, as illustrated in Figure 40.a.

Figure 40.b illustrates a TEM image of the xerogel of Fmoc-FF (10 mM) with Zn^{2+}. Long fibers with width between 10 and 20 nm could be observed and represent a very common feature of these peptides.

Metal ions can influence the growth mechanism, the secondary structure acquired by peptide fibers, as well as the kinetics of self-assembly.[111] Therefore, it is not surprising that the circular dichroism (CD) spectrum of the basic Fmoc-FF solutions changes dramatically upon addition of Zn^{2+} cations (Figure 40.c and d, respectively).

[111] a) Yuan, C.; Levin, A.; Chen, W.; *et al. Angew. Chemie - Int. Ed.* **2019**, *58* (50), 18116–18123. b) Ji, W.; Yuan, C.; Zilberzwige-Tal, S.; *et al. ACS Nano* **2019**, *13*, 7300–7309. c) Mañas-Torres, M. C.; Gila-Vilchez, C.; González-Vera, J. A.; *et al. Mater. Chem. Front.* **2021**, *5* (14), 5452–5462.

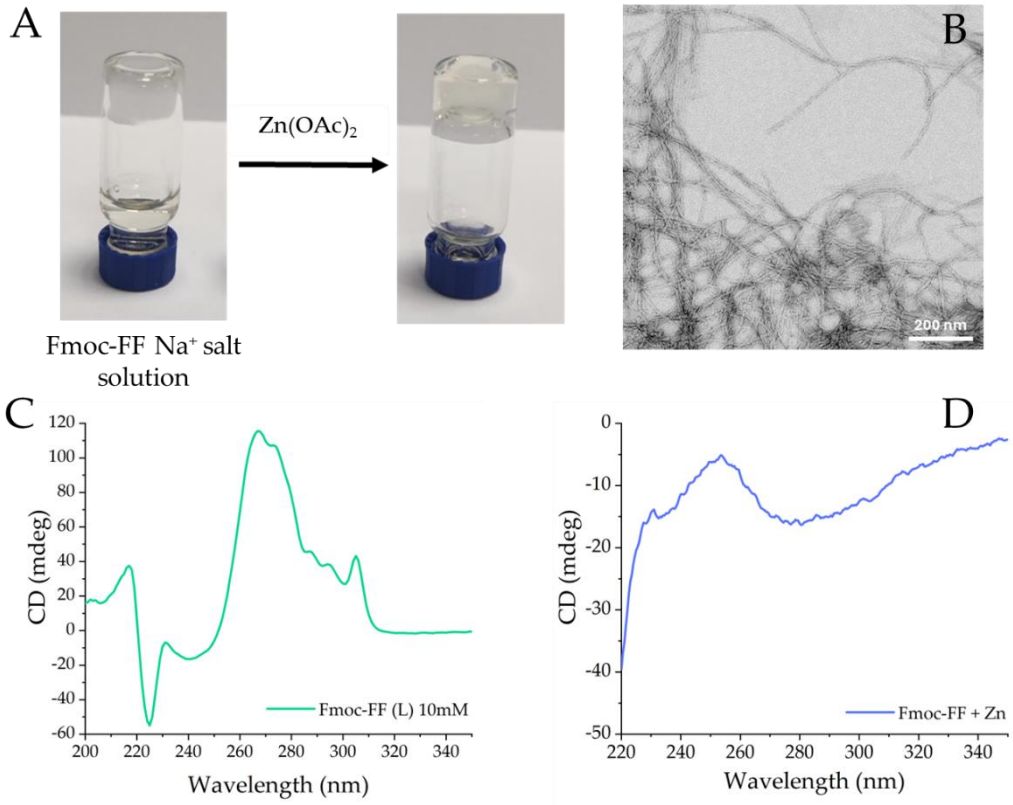

Figure 40. a) Fmoc-FF hydrogel formation with the addition of zinc acetate. b) TEM image of Fmoc-FF with Zn^{2+}. CD spectra of Fmoc-FF c) basic solution and d) after addition of Zn^{2+}.

The impact of the metal cation on the mechanical characteristics of the hydrogels was assessed through rheological analysis. The results obtained Figure 41) corresponded to the behaviour of a typical gel, as evidenced by the values of the storage (G') and loss (G'') moduli, which remain practically constant as the oscillation frequency varies. Additionally, G' maintained values that were significantly higher than G'', as can be seen in Figure 41.a.

It can also be observed that the gels formed at higher Fmoc-FF concentrations demonstrate greater strength, which is consistent with the higher peptide concentration. Figure 41.b shows that gel formation was almost instantaneous, occurring within 5 minutes of zinc salt addition, and that gels at higher concentrations also appeared to assemble slightly faster.

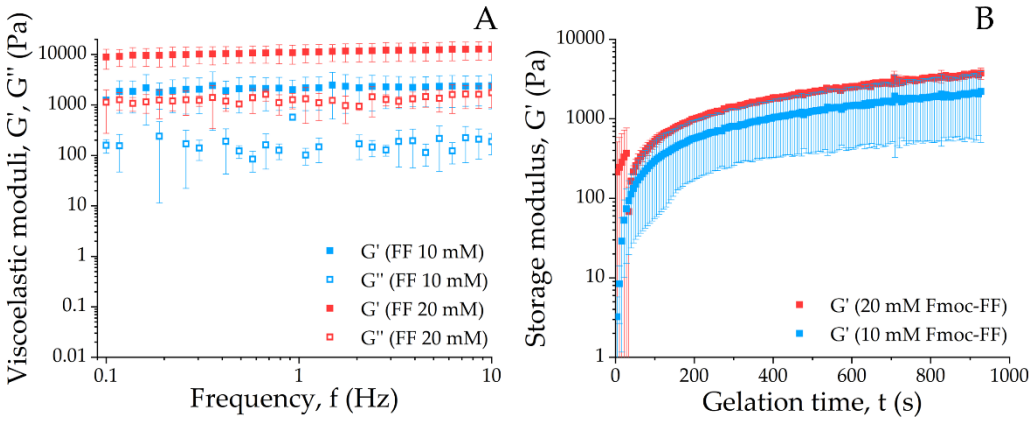

Figure 41. Mechanical properties of Fmoc-FF (10mM) with Zn^{2+}. a) Mechanical spectra under shear and b) evolution of the storage modulus (G′) during gelation.

Once the ability of the peptides to assemble via coordination with the Zn^{2+} cation was established, the efficacy of the different protocols could test, starting with the diffusion protocol and continuing with the simultaneous protocol. A schematic representation of both is shown in Figure 42.a and b.

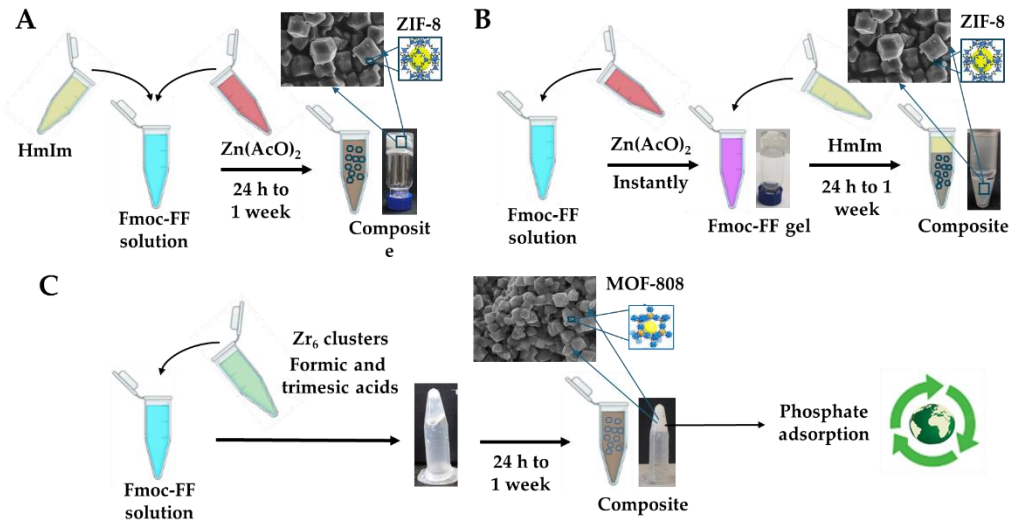

Figure 42. Schematic representation of the different protocols used for MOF synthesis: a) *in situ* ZIF-8 growth by simultaneous gel formation (simultaneous protocol); b) *in situ* ZIF-8 growth by HmIm diffusion (diffusion protocol); c) *in situ* MOF-808 growth by simultaneous gel formation using Zr6 clusters as seeds.

3.2. *In situ* growth of ZIF-8: Diffusion protocol

This protocol, as previously mentioned, consisted of adding an aqueous solution of HmIm on the Fmoc-FF hydrogels formed with Zn^{2+} allowing its diffusion into the matrix and forming ZIF-8 crystals according to interaction with the Zn^{2+} nuclei. Three different concentrations of HmIm were tested, which were 100, 250 and 500 mM, resulting in HmIm/Zn ratios of 2, 5 and 10, respectively. The appearance of a white precipitate confirmed the formation of crystals within the hydrogel and, after 24 hours, the entire volume of the gel turned white as shown in the Figure 43.

The mechanical properties of the composite obtained were evaluated after one week of incubation. Considering the results obtained for the material with a HmIm/Zn ratio of 5:1, it can be observed that the composite gels were significantly weaker than the gels before the formation of ZIF-8, decreasing by an order of magnitude the value of G' for the Fmoc-FF samples at 20 mM (Figure 43.b). Furthermore, the trend of G' and G'' was erratic and the ratio between the two moduli was less than 10, which is typical for gels that are not well formed. Thus, it can be concluded that there is a degradation of the gel structure once the MOF particles are formed. This degradation could be explained by the competition that exists between both components for Zn^{2+}, since ZIF-8 requires it to grow and the fibers to assemble and maintain themselves.

X-ray powder diffraction (XRPD) analysis of the freeze-dried samples revealed that, for all the HmIm/Zn ratios evaluated (2, 5 and 10), ZIF-8 was formed exclusively as a crystalline polymorph, although with the 2:1 ratio some impurities appeared (Figure 43.c). This finding is significant, since using the same protocol in aqueous solution, maintaining the same values and pH variations (Chapter 8), only ZIF-8 is obtained with a HmIm/Zn ratio of 10:1. With a ratio of 5:1, another non-porous polymorph, dia(Zn), is formed exclusively, and with a ratio of 2:1, an amorphous material is obtained (Figure 95. Chapter 8).

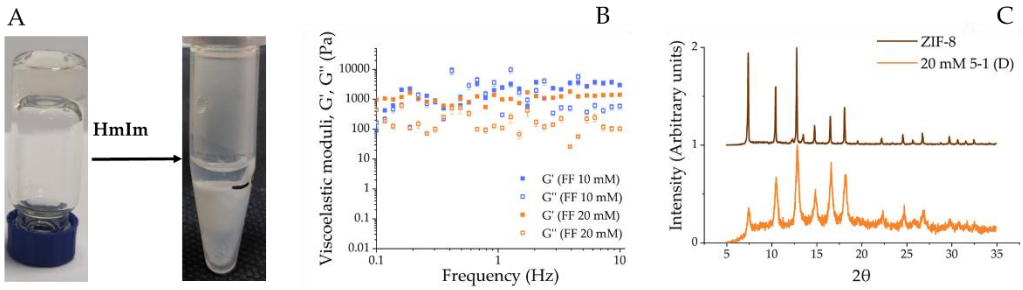

Figure 43. a) Picture of a composite hydrogel after HmIm diffusion; b) rheology of composite hydrogels (Fmoc-FF 10 and 20 mM; HmIm/Zn ratio of 5:1) after 1 week of incubation; c) XRPD pattern of ZIF-8 obtained in water (in brown) and that obtained in the Fmoc-FF Zn2+ hydrogel (in orange) at a HmIm/Zn ratio of 5:1 after 1 week of incubation.

The particles obtained in water had a mean size of 1.2 ± 0.2 μm and adopted a rhombic dodecahedron shape (Figure 44.a). Other reported protocols, both in water and gel phase, indicate that the HmIm/Zn ratio needed to form ZIF-8 must be higher than 10:1.[112] The reason behind this decrease in the necessary ratio is not entirely clear. However, preliminary results suggested that Zn^{2+} cations disperse well in the peptide fibers, which facilitates their interaction with imidazole molecules and acts as nucleation centers for the formation of ZIF-8 crystals.

The SEM images in Figure 44.b and c supported this theory by showing the presence of a large number of significantly small (0.14 ± 0.02 to 0.25 ± 0.06 μm), well-distributed ZIF-8 crystals. This suggests a crystallization process in which nucleation is greatly enhanced even at an HmIm/Zn ratio of 2:1. The particles exhibited a cubic to spherical morphology with poorly defined edges, indicative

[112] a) Jian, M.; Liu, B.; Liu, R.; Qu, J.; Wang, H.; Zhang, X. *RSC Adv.* **2015**, *5* (60), 48433–48441. b) Kida, K.; Okita, M.; Fujita, K.; Tanaka, S.; Miyake, Y. *CrystEngComm* **2013**, *15* (9), 1794–1801. c) Pan, Y.; Liu, Y.; Zeng, G.; Zhao, L.; Lai, Z. *Chem. Commun.* **2011**, *47* (7), 2071–2073. d) Garai, A.; Shepherd, W.; Huo, J.; Bradshaw, D. *J. Mater. Chem. B* **2013**, *1* (30), 3678–3684.

of a rapid nucleation process. However, the morphological analysis of these samples yielded limited results due to the necessity of accounting for the presence of peptide fibers. As previously described by other authors, the formation of particles of such a small size is only possible when the HmIm/Zn ratio increases to 35, 70, and 100. The higher amount of HmIm in these cases promotes nucleation, increasing the number of particles formed at the cost of reducing the average size.[113]

SEM images of the samples after 24 hours of incubation demonstrated that the particles had undergone a transformation in shape, acquiring a more spherical form (Figure 44.e). Furthermore, samples incubated at 37 °C for one month exhibited more defined faces and larger sizes, indicating that, as with growth in water, these crystals can evolve with time (Figure 44.f).

Energy dispersive X-ray spectroscopy (EDX) analysis of the ZIF-8 composites (Fmoc-FF 10 mM; HmIm/Zn ratio of 5:1) revealed a uniform distribution of Zn within the composites (Figure 44.d).

To obtain a more detailed image of the composite material, an environmental scanning electron microscopy (ESEM) analysis of the hydrogel samples was also conducted. This technique preserves the three-dimensional structure of the hydrogel, preventing its collapse, which is crucial for studying the hydrogel morphology and the integration of its various components. ESEM images of the composite hydrogels, obtained with HmIm/Zn ratios of 2:1 and 5:1, are presented

[113] a) Jian, M.; Liu, B.; Liu, R.; Qu, J.; Wang, H.; Zhang, X. *RSC Adv.* **2015**, *5* (60), 48433–48441. b) Kida, K.; Okita, M.; Fujita, K.; Tanaka, S.; Miyake, Y. *CrystEngComm* **2013**, *15* (9), 1794–1801. c) Pan, Y.; Liu, Y.; Zeng, G.; Zhao, L.; Lai, Z. *Chem. Commun.* **2011**, *47* (7), 2071–2073.

in Figure 44.g and h. The hydrogel structure is shown to be completely covered by MOF particles, indicating effective integration between the peptide fibers and the MOF. The homogeneous distribution of the MOF particles, together with their small and uniform size, suggests that the peptide fibers act as nucleation centers by chelating Zn^{2+}.

The composite hydrogels (Fmoc-FF 20 mM; HmIm/Zn ratio of 5:1) were also observed by confocal laser scanning microscopy (CLSM), exploiting the intrinsic fluorescence of both Fmoc-peptides and ZIF-8. As shown in Figure 44.i, the peptide fibers, which are decorated with small spherical particles corresponding to ZIF-8, exhibited uniform green fluorescence emission. This analysis corroborates the hypothesis that ZIF-8 particles are distributed homogeneously along the peptide network. Images corresponding to water-grown ZIF-8, and Fmoc-FF hydrogels are collected in Chapter 8.

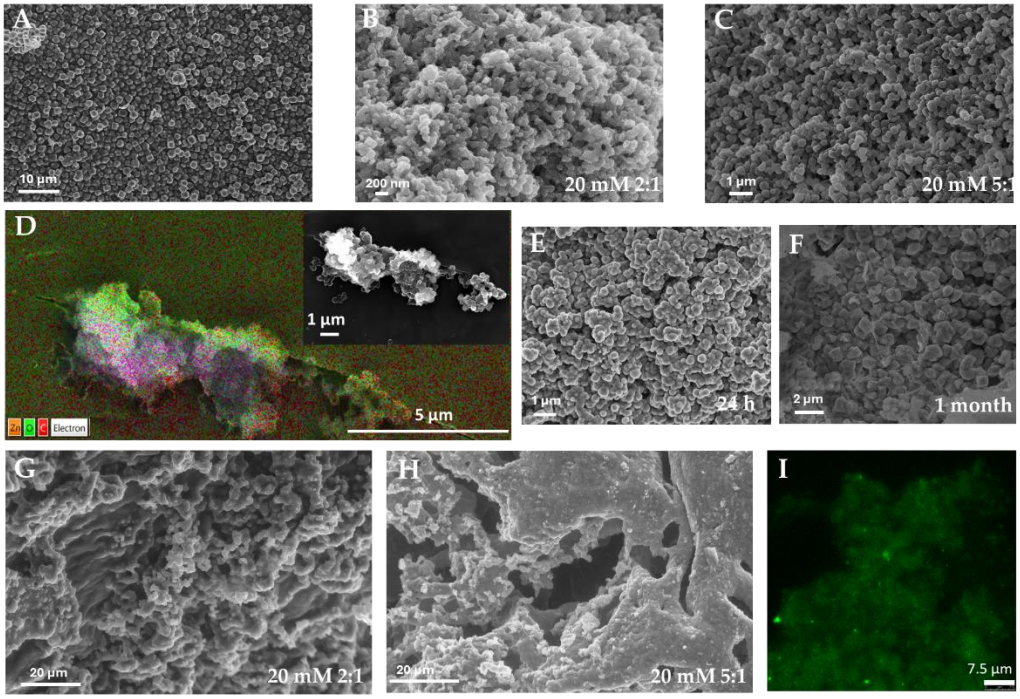

Figure 44. a) SEM picture of ZIF-8 obtained in water; b), c) SEM pictures of ZIF-8 obtained in the Fmoc-FF Zn2+ hydrogel after 1 week of incubation at a HmIm/Zn ratio of 2:1 and 5:1, respectively; d) EDX analysis of the ZIF-8 composite (Fmoc-FF 10 mM; HmIm/Zn ratio of 5:1) after 1 week of incubation; e), f) SEM picture of ZIF-8 obtained in the Fmoc-FF Zn2+ hydrogel after 24 h and 1 month of incubation, respectively; g), h) ESEM pictures of ZIF-8◉Fmoc-FF Zn2+ composite hydrogels after 1 week of incubation at a HmIm/Zn ratio of 2:1 and 5:1, respectively; i) CLSM of the ZIF-8 composite hydrogel (Fmoc-FF 20 mM, HmIm/Zn ratio of 5:1) after 1 week of incubation.

Once the characterization of ZIF-8 grown in Fmoc-FF hydrogels was complete, we proceeded to evaluate the influence of the chemical nature of the peptide, as well as the concentration and temperature, on the MOF crystallization process (Figure 45). Hydrogels of Fmoc-FF at 10 mM and Fmoc-AA at 10 and 20 mM with a HmIm ratio of 2:1 have been the subject of study. Samples were incubated at 4 and 37 °C to evaluate the influence of temperature. The results obtained were similar to those previously collected, although it is worth noting that the MOF particles appear more crystalline at 37 °C, as seen in the Figure 45.c and f.

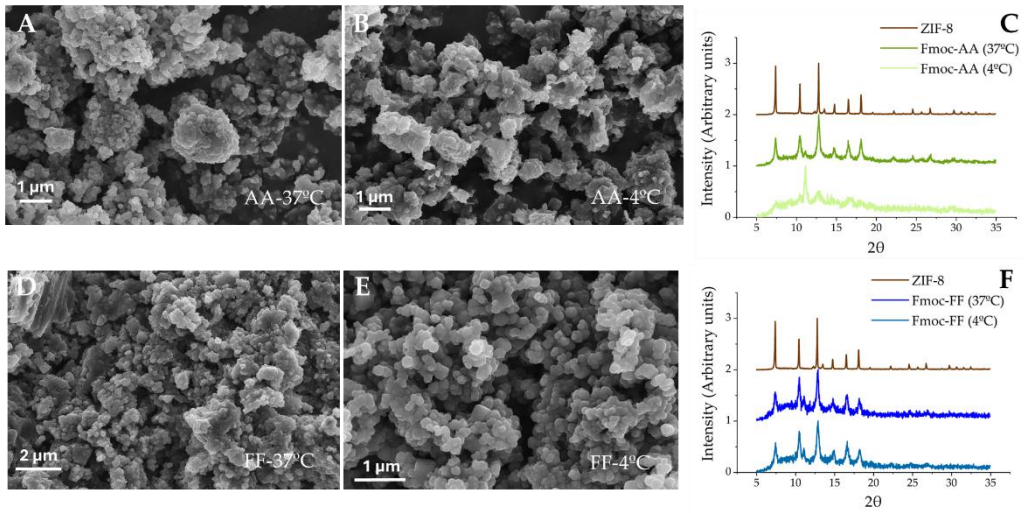

Figure 45. a) SEM image of ZIF-8 composite formed by diffusion protocol at 37 ºC (Fmoc-AA 10 mM hydrogel, HmIm:Zn 2:1 ratio); b) SEM image of ZIF-8 composite formed by diffusion protocol at 4 ºC (Fmoc-AA 20 mM hydrogel, HmIm:Zn 2:1 ratio); c) XRPD of ZIF-8 composite formed in water (brown), by diffusion protocol in Fmoc-AA hydrogel (10 mM) and HmIm:Zn ratio 2:1 at 37 ºC (dark green), by diffusion protocol in Fmoc-AA hydrogel (10 mM) and HmIm:Zn ratio of 2:1 at 4 ºC (light green); d) SEM image of ZIF-8 composite formed by diffusion protocol at 37 ºC (Fmoc-FF 20 mM hydrogel, HmIm:Zn 2:1 ratio); e) SEM image of ZIF-8 composite formed by diffusion protocol at 4 ºC (Fmoc-FF 20 mM hydrogel, HmIm:Zn 2:1 ratio); f) XRPD of ZIF-8 composite formed in water (brown), by diffusion protocol in Fmoc-FF hydrogel (20 mM) and HmIm:Zn ratio 2:1 at 37 ºC (dark blue), by diffusion protocol in Fmoc-FF hydrogel (20 mM) and HmIm:Zn ratio of 2:1 at 4 ºC (light blue).

Moreover, the impact of scale-up (Figure 46) was evaluated using a tenfold increase in volume. The tested conditions involved Fmoc-FF and Fmoc-AA at 20 mM, with a ratio of HmIm/Zn of 2:1, maintained at a constant temperature of 37 °C. The findings demonstrated that ZIF-8 was formed in both peptides, exhibiting comparable crystallinity characteristics to those observed in previous assays.

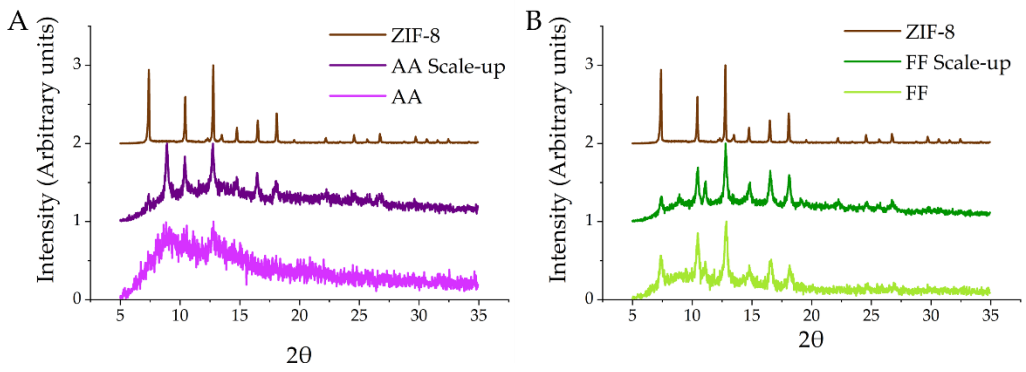

Figure 46. a) XRPD of ZIF-8 obtained in water (brown), by diffusion protocol at 37 ºC (Fmoc-FF 20 mM and HmIm:Zn ratio of 2:1) scale-up (dark green), by diffusion protocol at 37 ºC (Fmoc-FF 20 mM and HmIm:Zn ratio of 2:1) scale-up (light green); b) XRPD of ZIF-8 obtained in water (brown), by diffusion protocol at 37 ºC (Fmoc-AA 10 mM and HmIm:Zn ratio of 2:1) scale-up (dark violet), by diffusion protocol at 37 ºC (Fmoc-AA 10 mM and HmIm:Zn ratio of 2:1) scale-up (light violet).

Finally, the swelling capacity of these biocomposites was evaluated. Therefore, hydrogels comprising ZIF-8 developed in Fmoc-FF at 20 mM with an HmIm/Zn ratio of 5:1 at 37 °C for 48 hours were produced. The dried samples were observed by optical microscopy at x2 zoom, exhibiting a smooth surface devoid of amorphous MOF aggregates. Rehydration was conducted gradually by adding 5 μL of water over a 5-minute period. ZIF-8 samples demonstrate a swelling percentage of 1.6%, exhibiting the capacity to absorb up to 15 μL of water. However, as the volume of water increased, the sample degraded, releasing material into the surrounding medium (Figure 98).

3.3. *In situ* growth of ZIF-8: Simultaneous protocol

This protocol pursues the simultaneous formation of peptide fibers and ZIF-8 crystals by mixing all the necessary components Figure 42.a. Thus, following a protocol similar to the previous one, a solution of Fmoc-FF at concentrations of 10 mM and 20 mM was prepared and mixed with HmIm and $Zn(OAc)_2$ at 50 mM. Again, three different ratios of HmIm/Zn (2:1, 5:1 and 10:1) were tested. After mixing of the three components, instantaneous formation of translucent gels was observed at all HmIm concentrations tested (Figure 47.a). As with the diffusion protocol, the mechanical properties of the composite hydrogels underwent a substantial alteration following the formation of MOFs, as shown in Figure 47.b.

XRPD analysis indicated the formation of ZIF-8 as a distinctive crystalline polymorph with high purity at HmIm/Zn ratios of 10:1 and 5:1. At the 20 mM concentration of Fmoc-FF, the resulting material was notably purer (Figure 47**¡Error! No se encuentra el origen de la referencia.**.c). However, the 2:1 ratio exhibited the presence of residual impurities. Images obtained by SEM of the samples with HmIm/Zn ratios of 2:1 and 5:1 demonstrated that the ZIF-8 particles exhibited a comparable morphology and size to those observed in the diffusion protocol (Figure 44.c).

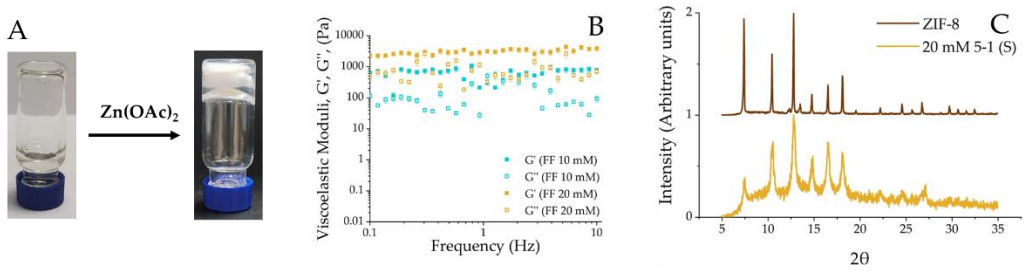

Figure 47. a) Picture of a composite hydrogel after Zn^{2+} addition; b) rheology of composite hydrogels (Fmoc-FF 10 and 20 mM; HmIm/Zn ratio of 5:1) after 1 week of incubation; c) XRPD pattern of ZIF-8 obtained in water (in brown) and that obtained in the Fmoc-FF Zn^{2+} hydrogel (in orange) at a HmIm/Zn ratio of 5:1 after 1 week of incubation.

EDX and CLSM analysis of the composites reveal comparable outcomes to those obtain with the diffusion protocol (Figure 48).

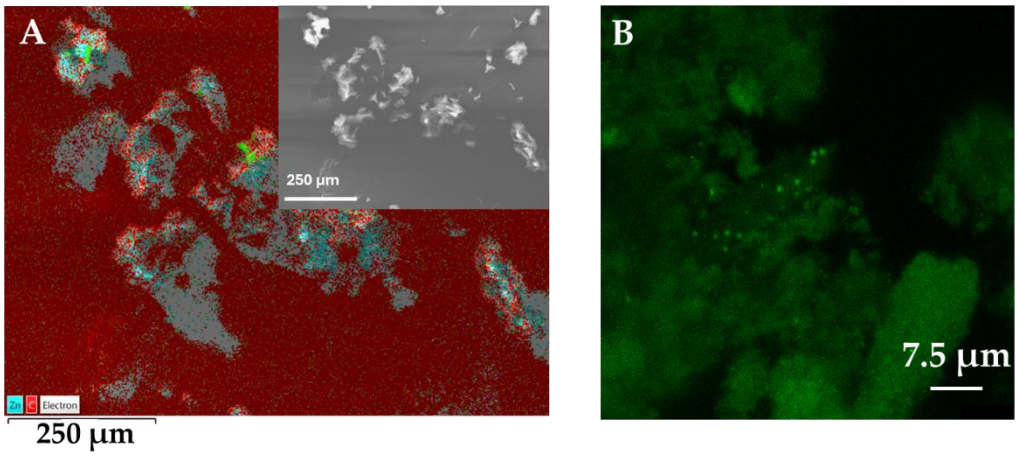

Figure 48. a) EDX analysis of the ZIF-8 composite (Fmoc-FF 10 mM; HmIm/Zn ratio of 5:1) after 1 week of incubation; b) CLSM of the ZIF-8 composite hydrogel (Fmoc-FF 20 mM, HmIm/Zn ratio of 5:1) after 1 week of incubation

The dimensions of the ZIF-8 particles formed in the presence of Fmoc-FF at concentrations of 10 and 20 mM with an HmIm/Zn ratio of 5:1 was determined, and size distribution histograms were generated (see the Experimental Section in Chapter 8). Figure 49.c shows the average particle size obtained by both protocols. While the average sizes were nearly identical across both protocols and peptide concentrations, the diffusion protocol yielded slightly larger particles, which was to be expected given the diffusion gradient present in that protocol, similar to what is observed in the crystallization of proteins in hydrogels.[114]

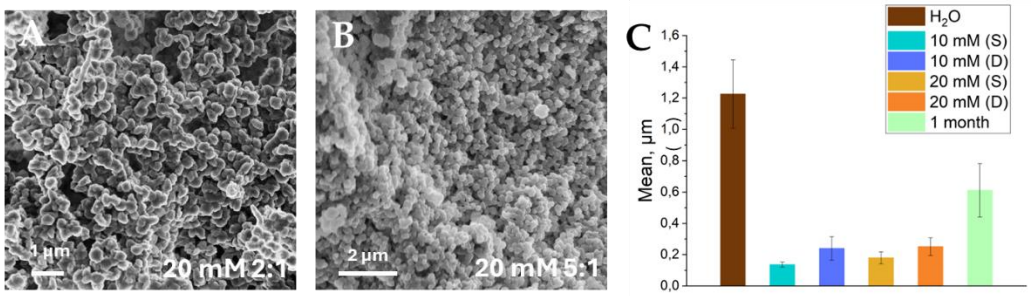

Figure 49. a) and b) ZIF-8 obtained in the Fmoc-FF Zn^{2+} hydrogel after 1 week of incubation at HmIm/Zn ratios of 2:1 and 5:1, respectively; c) mean size of ZIF-8 particles obtained in water and in both protocols (S means simultaneous; D means diffusion).

In addition to the composite characterization, a further test was performed by reducing the amount of HmIm and reaching HmIm/Zn ratios of 1:1 and 0.5:1 but failing to form ZIF-8. Moreover, decreasing the amount of Zn^{2+} cation to 20 mM and 10 mM was tested. SEM images in Figure 50 for the Zn^{2+} concentration at 20 mM with a HmIm/Zn ratio of 5:1 show the presence of small aggregates formed

[114] a) Conejero-Muriel, M.; Gavira, J. A.; Pineda-Molina, E.; *et al. Chem. Commun.* **2015**, *51* (18), 3862–3865. b) Conejero-Muriel, M.; Contreras-Montoya, R.; Díaz-Mochón, J. J.; Álvarez De Cienfuegos, L.; Gavira, J. A. *CrystEngComm* **2015**, *17* (42), 8072–8078.

by thin stacked layers that can be attributed to an intermediated phase in the synthesis of ZIF-8, already reported in literature.[115]

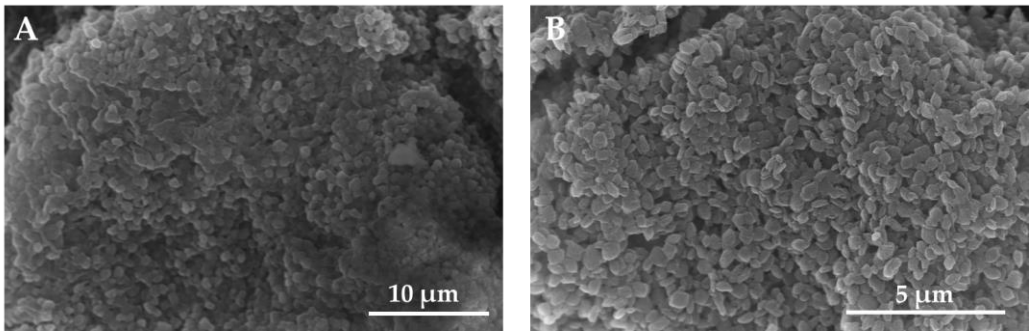

Figure 50. a) SEM image of ZIF-8 obtained by diffusion protocol (Fmoc-FF 20 mM and 10 mM of Zn^{2+}); b) SEM image of ZIF-8 obtained by diffusion protocol (Fmoc-FF 20 mM and 20 mM of Zn^{2+}).

It is noteworthy that ZIF-8 is one of the most extensively researched MOFs for reversible drug encapsulation. The porosity of MOF-based composites is a critical factor in their potential applications as drug delivery systems. Accordingly, the porosity of ZIF-8 composite hydrogels was assessed in the group of Doctor Carmona through the evaluation of composites formed by diffusion protocol with a HmIm/Zn ratio of 5:1, employing Fmoc-FF at 10 and 20 mM.

The N_2 adsorption analysis indicates that both dry composites (xerogels) are microporous, thereby demonstrating the permanent porosity of the ZIF-8 particles formed in the gel after thermal activation (Figure 99). The nitrogen adsorption at 77 K in the various materials was inversely correlated with their peptide content with a BET (Brunauer, Emmett and Teller) surface area of 1625, 1090, and 775 m^2/g for ZIF-8 microparticles and ZIF-8 composites with Fmoc-FF

[115] Jian, M.; Liu, B.; Liu, R.; Qu, J.; Wang, H.; Zhang, X. *RSC Adv.* **2015**, *5* (60), 48433–48441.

at 10 and 20 mM, respectively. This fact is due to the non-microporous nature of the Fmoc-FF hydrogel.

3.4. *In situ* growth of MOF-808: Simultaneous protocol

Once demonstrated the capacity of these peptides to act as a template for the growth of ZIF-8, we assessed the potential of Fmoc-FF to form other types of MOFs. Consequently, MOF-808 was selected as a model system, given the recent report of its synthesis at room temperature and in water, starting from preformed Zr_6 oxoclusters.[116]

MOF-808 could be grown *in situ* in Fmoc-FF (10 mM) hydrogels following the simultaneous protocol, with the minor modification that fiber formation was now triggered by lowering the pH due to the addition of formic acid in the presence of the oxoclusters of Zr_6 (Figure 42.c). Addition of formic acid leads to the quick formation of a hydrogel composed of long fibers, as it can be seen in Figure 51.b.

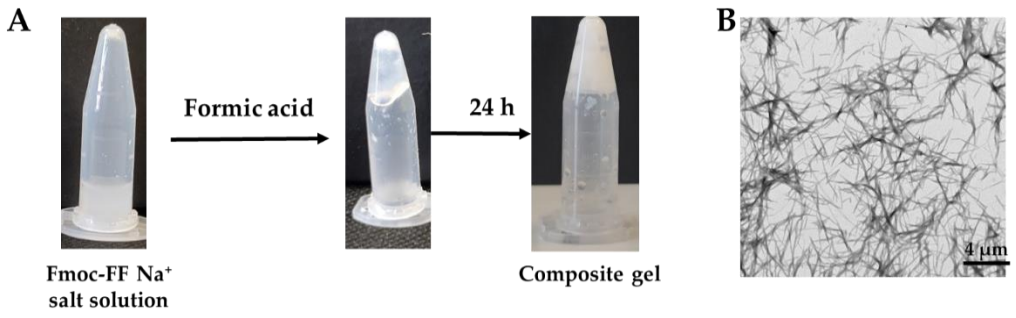

Figure 51. a) Picture of the gel after addition of formic acid and composite-MOF-808 formation after 24 h; b) TEM picture of Fmoc-FF formed by the addition of formic acid.

[116] Dai, S.; Simms, C.; Dovgaliuk, I.; Patriarche, G.; Tissot, A.; Parac-Vogt, T. N.; Serre, C. *Chem. Mater.* **2021**, *33* (17), 7057–7066.

The mechanical properties of the hydrogel were studied using rheology measurements. The results, collected in Figure 52 demonstrated a gel-like behaviour, although of a weaker nature (lower G′ and G″ values) compared to the equivalent gel prepared by addition of a $Zn(OAc)_2$ solution (Figure 41). However, gelation in this case was much faster than for its counterparts (compare Figure 41.b and Figure 100.a in Chapter 8). This faster gelation rate was due to the instantaneous drop in pH induced by the addition of formic acid.

The formation of a white precipitate after 24 h indicated the formation of the MOF (Figure 51.a). The rheology of the composite hydrogels showed a strong improvement in the robustness of the samples with respect to those without the MOF (Figure 52). This result is opposite to that observed for the samples prepared by addition of $Zn(OAc)_2$, but is not surprising. For the samples prepared by Zn addition, the formation of the MOF involves competition for Zn with the Fmoc-FF fibers. However, in the case of formic acid addition, the Fmoc-FF fibers are formed by a change in pH. Consequently, MOF growth does not cause MOF degradation. Instead, the MOF adheres to the Fmoc-FF fibers, making them more robust, which justifies the reinforcement manifested by the higher G′ values in the presence of MOF.

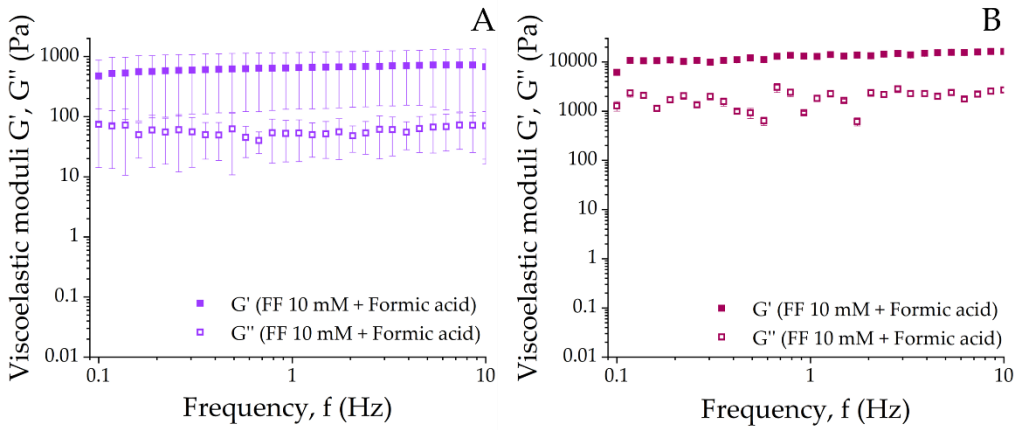

Figure 52. a) Mechanical spectra under shear of the hydrogel (Fmoc-FF 10 mM). b) Mechanical spectra of the composite hydrogel (Fmoc-FF 10 mM) after 1 week of incubation.

The XRPD and SEM analyses were conducted on the lyophilized samples after one week of incubation, following the same procedure as previously described. SEM images revealed a large number of homogeneous tetragonal bipyramidal MOF-808 particles, similar to those obtained through water-based synthesis, shown in Figure 53.a, b and c.

The EDX analysis showed zirconium (Zr) distributed throughout the composite material (Figure 53.d). Additionally, the CLSM analysis presented images similar to those obtained for the ZIF-8 composites, where the MOF particles appear well integrated within the peptide network (Figure 53.e).

The XRPD analysis of the samples obtained in the gel and in water was nearly identical, yielding the diffraction pattern characteristic of MOF-808 (Figure 53.c). In contrast to the results obtained for the synthesis of ZIF-8, the gel did not appear to influence the size of the MOFs (Figure 53.f). It is important to note that, in this case, the peptide fibers do not compete for any of the MOF components, and the gel simply serves as a physical medium in which the Zr_6 seeds are evenly

distributed. Thanks to the high porosity of these gels, the growth of the MOF within them is unrestricted, resulting in sizes similar to those obtained in water.

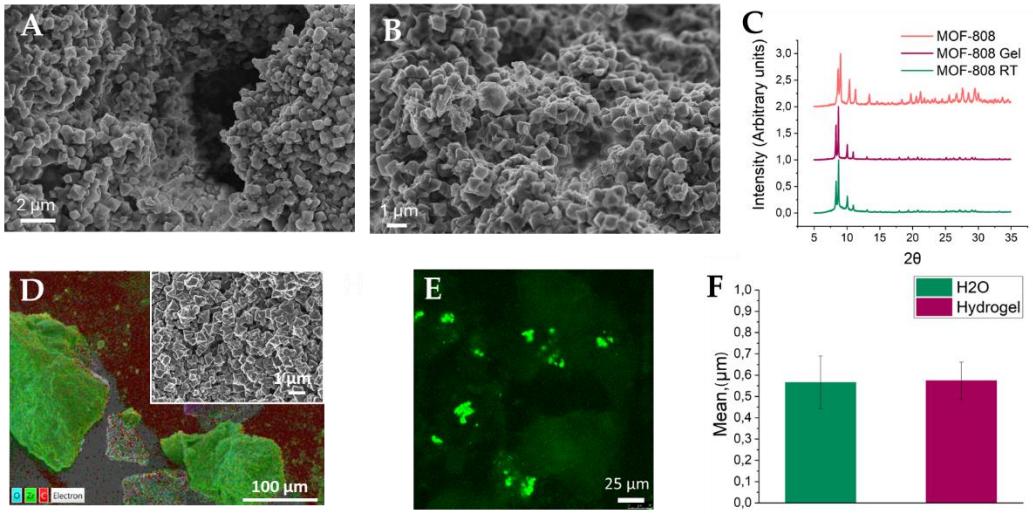

Figure 53. a) SEM picture of MOF-808 obtained in water; b) SEM picture of MOF-808 obtained in the Fmoc-FF hydrogel after 1 week of incubation; c) XRPD pattern of MOF-808 obtained by solvothermal synthesis (in orange), that obtained in the Fmoc-FF hydrogel (in burgundy), and that obtained in water (in green); d) EDX analysis of the MOF-808 composite (Fmoc-FF 10 mM) after 1 week of incubation; e) CLSM of the MOF-808 composite hydrogel (Fmoc-FF 10 mM) after 1 week of incubation; f) mean size of MOF-808 particles obtained in water and in the Fmoc-FF hydrogel.

The dried samples in this case exhibited irregular surfaces formed by a multitude of spherical aggregates. These samples were more compact than those of ZIF-8 and, after the addition of water, lacked the ability to absorb it, indicating a higher degree of hydrophobicity (Figure 54).

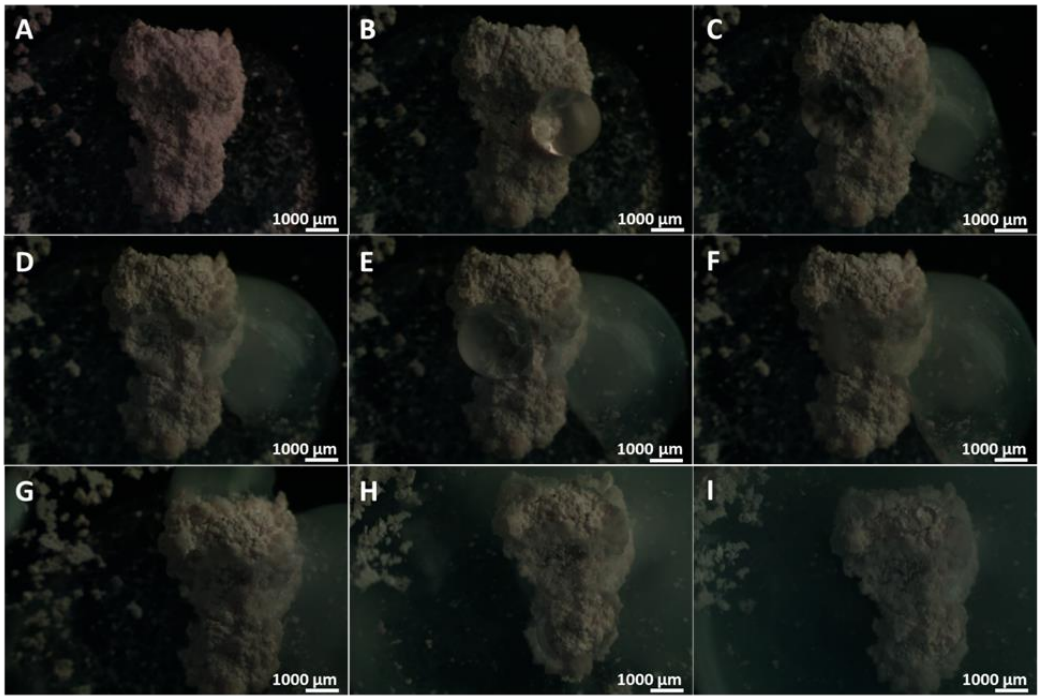

Figure 54. Optical pictures of MOF-808 composite material: a) after slow-drying (37 ºC 48 h); b) after adding 5 µL of water; c) after adding another 5 µL of water (10 µL total); d) after adding 15 µL of water (25 µL total); e) after adding 10 µL of water (35 µL total); f) after adding 20 µL of water (55 µL total); g) after adding 35 µL of water (90 µL total); h) after adding 360 µL of water (450 µL total); i) after 15 h in contact with 450 µL of water.

The combination of multiple components to create composite materials has proven to be an effective strategy for developing materials with enhanced properties. Such composites not only retain the individual characteristics of their components but also offer new properties or synergistic effects.

The potential to develop a biocompatible peptide hydrogel functionalized with MOF-808, which exhibits notable adsorption and degradation capabilities, presents an opportunity to create a composite material with potentially valuable properties for novel detoxification or purification applications.

Accordingly, composite hydrogels have been tested as adsorbents for the removal of phosphate ions from water—a typical phosphorus contaminant with severe negative impacts on aquatic ecosystems, such as eutrophication. Additionally, the capability of the composite hydrogel to degrade an organophosphorus compound, specifically methyl paraoxon, has also been evaluated.

First, the porosity of the MOF-808 particles grown within the gel was determined through gas adsorption. The N_2 adsorption isotherm at 77 K for the thermally activated dry biocomposite (xerogel) demonstrated that its porosity was retained, with a calculated BET surface area of 1580 m^2/g. This value is slightly lower than that observed for pure MOF-808 (2050 m^2/g), likely due to the non-microporous nature of the gel within the biocomposite ($S_{BET} = 6.5\ m^2\ g^{-1}$) (Figure 55.a). Despite this, these results suggest that the cavities of MOF-808 grown within the gel may be accessible to guest molecules such as phosphate ions, and therefore, P-pollutants could be trapped within the pores.

To assess the phosphate ion adsorption capacity, a phosphate solution (0.41 mM) was added to the *in situ* grown MOF-808-gel biocomposite that was incubated for 1 week, with Fmoc-FF hydrogel used as a control. Both mixtures were maintained at room temperature, and the evolution of phosphate concentration was monitored spectrophotometrically using the molybdenum blue method. Fmoc-FF hydrogel exhibited negligible phosphate adsorption capacity after 24 hours of incubation due to its lack of phosphate adsorption sites. In contrast, the MOF-gel biocomposite effectively captures phosphate ions from the water, achieving cumulative removals of 33.0 ± 1.7% and 55.3 ± 1.6% after 1 and 24 hours, respectively (Figure 103. Experimental section). These results confirmed

that phosphate ions can diffuse through the MOF-gel biocomposite and reach adsorption sites within the MOF-808 cavities, where they become trapped.

The phosphate adsorption performance of MOF-808 grown in water and in gel was compared, using the biocomposite in the form of xerogel to avoid diffusion constraints. A phosphate concentration typically found in wastewater (0.08 mM) was mixed with water-prepared MOF-808 crystals (109.1 mg L^{-1}, 0.080 μmol MOF-808) and with the dry MOF-808 biocomposite (109.1 mg L^{-1} containing 0.024 μmol MOF-808). The resulting suspensions were stirred at 25°C, and the phosphate concentration in the solution was monitored spectrophotometrically using the molybdenum blue method. Figure 55 shows that both materials exhibited efficient phosphate ion removal from the water after 24 hours, with cumulative phosphate removal rates of 88 ± 2% and 99.0 ± 0.1% for MOF-808 crystals and the biocomposite, respectively.

The MOF-808 biocomposite demonstrated faster phosphate adsorption kinetics compared to MOF-808 grown in water, reaching the maximum adsorption rate after 60 minutes of stirring. The growth of MOF-808 particles along the peptide fibers in the biocomposite may enhance their exposure to the solution and improve the diffusion of phosphate ions into their cavities. Notably, the phosphate concentration after treatment with the biocomposite (0.80 ± 0.08 μM) was below the EPA and EU criterion for phosphate content in water (1 μM), indicating the effective performance of the new material for the decontamination of phosphate-polluted water.

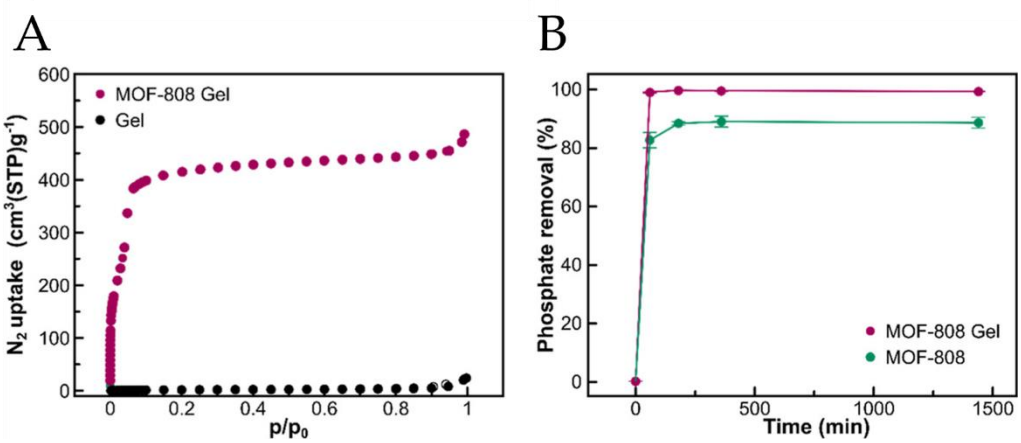

Figure 55. N2 isotermas y captación de iones fosfato of MOF-808.

While several Zr-MOFs have demonstrated rapid and efficient degradation of organophosphorus compounds in buffered basic media containing organic amines such as N-ethylmorpholine, their catalytic activity significantly decreases in unbuffered media, such as pure water. Unfortunately, the use of nucleophilic bases like N-ethylmorpholine is restricted in certain applications, such as wastewater purification and medical treatment for organophosphorus poisoning. This necessitates the development of alternative strategies for catalyzing the degradation of organophosphorus compounds in unbuffered media.

To this end, the catalytic ability of MOF-808 and the biocomposites of Fmoc-FF and MOF-808-hydrogel was evaluated for the hydrolysis of a model organophosphorus compound, methyl paraoxon (MP, LD50 oral in rats = 3 mg kg^{-1}), into less toxic products, namely 4-nitrophenol (LD50 oral in rats = 667 mg kg^{-1}) and dimethyl phosphate (LD50 oral in rats = 3283 mg kg^{-1}), in unbuffered aqueous solutions (Figure 56.a). To test this, MOF-808 (0.22 mg, 0.16 μmol MOF-808), dry Fmoc-FF xerogel (0.22 mg), and MOF-808 xerogel biocomposite (0.22

mg, 0.05 μmol MOF-808) were exposed to an aqueous solution of methyl paraoxon (0.16 mM, 1 mL), and the mixtures were stirred at room temperature. The progress of the catalytic reaction was monitored by UV-Vis spectroscopy, quantifying the amount of 4-nitrophenol formed.

An insignificant formation of 4-nitrophenol was observed when using Fmoc-FF xerogel as a catalyst (Figure 56.c). In contrast, both MOF-808 crystals and the MOF-808 xerogel biocomposite effectively hydrolysed MP into 4-nitrophenol (Figure 56.b). In these cases, the Lewis acidic sites in the MOF-808 particles activate the phosphate center in MP, while the nucleophilic OH sites of the MOF cluster hydrolyzed the toxic compound. Despite this, while MOF-808 crystals exhibit moderate MP degradation with a conversion rate of 0.7 mol of MP per mol of MOF after 24 hours, the MOF-808 biocomposite with Fmoc-FF achieves a faster and more efficient degradation performance, with conversion rates of 1.4 and 2.2 mol of MP per mol of MOF after 60 minutes and 24 hours, respectively. As previously observed in phosphate adsorption experiments, the synergistic effect seen in the catalysis driven by the biocomposite is attributed to the homogeneous distribution of MOF-808 particles along the peptide fibrils, enhancing the interaction of catalytic sites on the MOF particles' surface with toxic molecules in the solution.

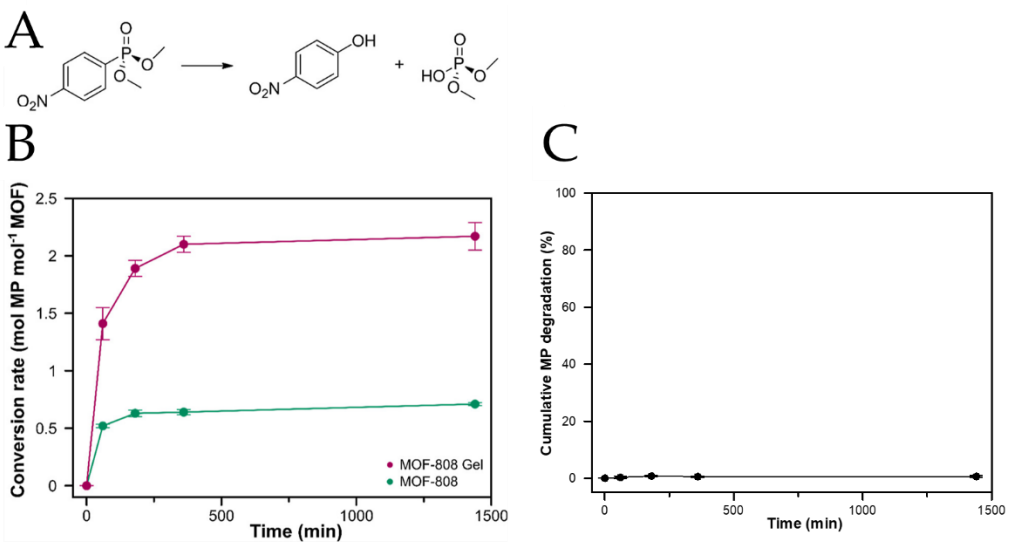

Figure 56. MP degradation

4. Conclusions

A synthesis of the presented results allows for the drawing of a series of conclusions, as detailed below:

1. New biocomposite MOFs have been synthesized using peptide supramolecular hydrogels and two protocols have been successfully developed for the synthesis of these materials.
2. With respect to the ZIF-8 obtained through this methodology, it has been observed that both protocols improve the formation of MOF particles, largely due to the high accessibility of Zn^{2+} cations, since they are distributed along the peptide fibers interacting electrostatically with the peptide molecules. This allows for the use of a considerably lower HmIm/$Zn(OAc)_2$ ratio than described for water synthesis protocols. Furthermore, the ZIF-8 particles obtained in gel are significantly smaller in size than those obtained in water and decorate the peptide fibers along their entire length, resulting in a well-integrated and homogeneous composite material.
3. Additionally, another biocomposite based on MOF-808 has also been successfully obtained through the formation of the hydrogel using formic acid and $Zr_6O_4(OH)_4(OAc)_{12}$ seeds as nucleation agents. This highlights the versatility of supramolecular peptide hydrogels as a template for the growth of crystalline particles, in this case, MOFs.
4. The distribution of MOF-808 in the Fmoc-FF hydrogel matrix in the final composite material has been shown to favour, on the one hand, the diffusion of phosphate ions towards the porous cavities, allowing a faster adsorption than in pure crystals and, on the other hand, the interaction of the catalytic sites of MOF with the substrate molecules, which has tripled the catalytic

activity of MOF-808 in the degradation of methyl paraoxon with respect to MOF-808 synthesized in water.

Chapter 5

Supramolecular Short-peptides Hydrogels with Antibacterial Activity

1. Background

Almost a century after Alexander Fleming's discovery of penicillin in 1928, which enabled the treatment of bacterial infections and a significant reduction in mortality rates associated with these infections, there is once again a global problem with these infections. Antibiotic pressure favours the selection of resistant strains. This has led to the proliferation of multi-resistant pathogens. Thus, infections, which are increasingly difficult to treat, have become a public health problem.[117]

Wounds that occur in daily life as a result of surgery, burns, scalds and other injuries compromise the skin's protective function. Pathogenic bacteria can infect environmentally exposed wounds and significantly delay healing. This process involves four phases: hemostasis, inflammation, proliferation and remodeling, but can be interrupted by infection with bacteria such as *Staphylococcus aureus*, *Escherichia coli* and *Pseudomonas aeruginosa*.[118]

[117] a) Wang, Q.; Feng, X.; Xu, H.; Guo, G.; Li, Y.; Zhang, Q. *J. Mater. Chem. C* **2023**, *11* (38), 12848–12876. b) Sun, H.; Fu, X.; Yang, C.; Yuan, C.; Yan, X. *Curr. Opin. Colloid Interface Sci.* **2024**, *73*, 101828. c) Murray, C. J.; Ikuta, K. S.; Sharara, F.; Swetschinski, L.; Robles Aguilar, G.; Gray, A.; *et al. Lancet* **2022**, *399* (10325), 629–655. d) Zhang, M.; Gu, G.; Xu, Y.; Luan, X.; Liu, J.; He, P.; Wei, G. *Macromol. Rapid Commun.* **2024**, 2400173. e) Song, J.; Yuan, C.; Jiao, T.; Xing, R.; Yang, M.; Adams, D. J.; Yan, X. *Small* **2020**, *16* (8). f) Luo, Z. W.; Huang, A.; Deng, Y.; Huang, J.; Bu, Z. Q.; Xie, H. Lou. *Chem. - A Eur. J.* **2023**, *29* (32), e202300498.

[118] a) Das Gupta, B.; Halder, A.; Vijayakanth, T.; Ghosh, N.; Konar, R.; Mukherjee, O.; Gazit, E.; Mondal, S. *J. Mater. Chem. B* **2024**, *12* (34), 8444–8453. b) Liu, K.; Zhang, H.; Wang, Z.; Zhou, J.; He, Y.; Li, J.; Wang, X.; Su, J.; Wang, P.; Shen, Z.; Fareed, M. S.; Wan, D.; Ma, T.; Li, M.; Li, Y.; Zhang, J.; Wang, K. *ACS Appl. Nano Mater.* **2024**, *7* (14), 16585–16598.

These bacterial infections cause prolonged inflammation, tissue damage and, in severe cases, the formation of biofilms that chronify the wound and can lead to ulcers or gangrene. The emergence of multidrug-resistant bacteria has exacerbated the situation, making these infections more difficult to treat. In addition, bacterial adhesion to medical implants is a common cause of infections associated with devices such as orthopedic and dental implants, catheters and intraocular lenses.[119]

Therefore, the development of new materials is therefore necessary due to the limited efficacy of actual treatments that is behind the increased mortality of current nosocomial bacterial and fungal infections.[120]

Supramolecular hydrogels have emerged as a versatile class of soft materials with diverse biological applications, including drug delivery, tissue engineering, and biosensors. These materials have gained prominence due to their ease of fabrication, response to stimuli, and rheological properties. The joint self-assembly of different peptides or in conjunction with other biomolecules allows for the creation of nanostructures with structural and functional diversity, with

---

[119] a) Das Gupta, B.; Halder, A.; Vijayakanth, T.; Ghosh, N.; Konar, R.; Mukherjee, O.; Gazit, E.; Mondal, S. *J. Mater. Chem. B* **2024**, *12* (34), 8444–8453. b) Liu, K.; Zhang, H.; Wang, Z.; Zhou, J.; He, Y.; Li, J.; Wang, X.; Su, J.; Wang, P.; Shen, Z.; Fareed, M. S.; Wan, D.; Ma, T.; Li, M.; Li, Y.; Zhang, J.; Wang, K. *ACS Appl. Nano Mater.* **2024**, *7* (14), 16585–16598.

[120] a) Sun, H.; Fu, X.; Yang, C.; Yuan, C.; Yan, X. *Curr. Opin. Colloid Interface Sci.* **2024**, *73*, 101828. b) Zhang, M.; Gu, G.; Xu, Y.; Luan, X.; Liu, J.; He, P.; Wei, G. *Macromol. Rapid Commun.* **2024**, 2400173. c) Song, J.; Yuan, C.; Jiao, T.; Xing, R.; Yang, M.; Adams, D. J.; Yan, X. *Small* **2020**, *16* (8). d) Singh, R.; Sharma, S.; Kautu, A.; Joshi, K. B. *Chem. Commun.* **2024**, *60* (60), 7687–7696. e) Janzen, L.; Miller, R. G.; Metzler-Nolte, N. *Dalt. Trans.* **2024**. f) Lohse, M. B.; Gulati, M.; Johnson, A. D.; Nobile, C. J. *Nat. Rev. Microbiol. 2017 161* **2017**, *16* (1), 19–31. g) Liu, K.; Zhang, H.; Wang, Z.; Zhou, J.; He, Y.; Li, J.; *et al*. *ACS Appl. Nano Mater.* **2024**, *7* (14), 16585–16598. h) Singh, R.; Sharma, S.; Kautu, A.; Joshi, K. B. *Chem. Commun.* **2024**, *60* (60), 7687–7696.

promising applications in cell biology, bionanotechnology, and tissue engineering. This is achieved by combining peptides with different sequences and properties.[121]

Regarding wound infections, hydrogel dressings have been considered a promising alternative to traditional dressings due to their multiple advantages, such as maintaining a moist environment that accelerates healing, reducing the risk of infection, and their ease of use. In addition, hydrogel coatings can have bactericidal and antifouling effects in response to the microenvironment of bacterial infection. Furthermore, hydrogels with high water content mimic soft tissues and integrate effectively with biological components. Antimicrobial peptide hydrogels are notable for being biocompatible, biodegradable and effective in preventing bacterial resistance, due to the nonspecific mechanisms they establish when interacting with bacteria.[122]

[121] a) Wang, Q.; Feng, X.; Xu, H.; Guo, G.; Li, Y.; Zhang, Q. *J. Mater. Chem. C* **2023**, *11* (38), 12848–12876. b) Das Gupta, B.; Halder, A.; Vijayakanth, T.; Ghosh, N.; Konar, R.; Mukherjee, O.; Gazit, E.; Mondal, S. *J. Mater. Chem. B* **2024**, *12* (34), 8444–8453. c) Liu, K.; Zhang, H.; Wang, Z.; Zhou, J.; He, Y.; Li, J.; Wang, X.; Su, J.; Wang, P.; Shen, Z.; Fareed, M. S.; Wan, D.; Ma, T.; Li, M.; Li, Y.; Zhang, J.; Wang, K. *ACS Appl. Nano Mater.* **2024**, *7* (14), 16585–16598. d) Singh, R.; Sharma, S.; Kautu, A.; Joshi, K. B. *Chem. Commun.* **2024**, *60* (60), 7687–7696. e) Yu, X.; Cai, J.; Xu, M.; Li, Q.; Yang, Y.; Wan, Z.; Yang, X. *Nanoscale* **2024**. f) Hekmat, A.; Kostova, I.; Saboury, A. A. *Colloids Surfaces B Biointerfaces* **2024**, *244*, 114185. g) Wu, C.; Liao, W.; Zhang, Y.; Yan, Y. *Biomater. Sci.* **2024**.

[122] a) Liu, K.; Zhang, H.; Wang, Z.; Zhou, J.; He, Y.; Li, J.; Wang, X.; Su, J.; Wang, P.; Shen, Z.; Fareed, M. S.; Wan, D.; Ma, T.; Li, M.; Li, Y.; Zhang, J.; Wang, K. *ACS Appl. Nano Mater.* **2024**, *7* (14), 16585–16598. b) Ran, P.; Qiu, B.; Zheng, H.; Xie, S.; Zhang, G.; Cao, W.; Li, X. *Acta Biomater.* **2024**. c) Das Gupta, B.; Halder, A.; Vijayakanth, T.; Ghosh, N.; Konar, R.; Mukherjee, O.; Gazit, E.; Mondal, S. *J. Mater. Chem. B* **2024**, *25* (13), 23.

Another emerging material in the treatment of infections is nanoparticles (NPs) due to their unique properties. They are defined as particles with a diameter typically in the range from 1 to 100 nm and can be formed from a variety of materials. Plasmonic nanoparticles, mainly made from metals like gold and silver, exhibit unique optical properties that make them highly effective in biomedical applications such as sensing, diagnosis, and therapy.[123]

Metal nanoparticles, especially silver nanoparticles (AgNPs), have been demonstrated to exhibit strong antibacterial activity and, at the same time, low microbial resistance compared to antibiotics and small molecule biocides. Nevertheless, the use of individual AgNPs as substitutes for antibiotic drugs is not without limitations. The accumulation of AgNPs in tissues has been observed, and high doses or prolonged use of silver cations can result in local or systemic side effects, including allergic reactions, skin staining, and cell toxicity.[124]

To address the limitations of both formulations and achieve a more comprehensive solution, the concept of hybrid materials has emerged. These materials combine the advantages of hydrogels as a biocompatible matrix with the broad-spectrum antimicrobial capabilities of nanoparticles.[125] Furthermore,

---

[123] a) Song, J.; Yuan, C.; Jiao, T.; Xing, R.; Yang, M.; Adams, D. J.; Yan, X. *Small* **2020**, *16* (8). b) Choi, W.; Kohane, D. S. *ACS Nano* **2024**, *18* (34), 22780–22792. c) Silvestre, O. F.; Rao, A.; Liz-Marzán, L. M. *Eur. J. Mater.* **2023**, *3* (1), 2202676. d) de la Encarnación, C.; Jimenez de Aberasturi, D.; Liz-Marzán, L. M. *Adv. Drug Deliv. Rev.* **2022**, *189*, 114484. e) Tadgell, B.; Liz-Marzán, L. M. *Chem. – A Eur. J.* **2023**, *29* (62), e202301691.

[124] a) Song, J.; Yuan, C.; Jiao, T.; Xing, R.; Yang, M.; Adams, D. J.; Yan, X. *Small* **2020**, *16* (8). b) Choi, W.; Kohane, D. S. *ACS Nano* **2024**, *18* (34), 22780–22792.

[125] a) Song, J.; Yuan, C.; Jiao, T.; Xing, R.; Yang, M.; Adams, D. J.; Yan, X. *Small* **2020**, *16* (8). b) Singh, R.; Sharma, S.; Kautu, A.; Joshi, K. B. *Chem. Commun.* **2024**, *60* (60), 7687–7696. c) Janzen, L.; Miller, R. G.; Metzler-Nolte, N. *Dalt. Trans.* **2024**. d) Choi, W.; Kohane, D. S. *ACS Nano* **2024**, *18* (34), 22780–22792.

the integration of various components into the hydrogel matrix contributes to optimizing the mechanical properties, resulting in a texture that facilitates ease of application, as will be discussed further.

Considering this, herein it has been prepared different short-peptide supramolecular composite hydrogels with the final goal to obtain highly biocompatible materials having a strong antimicrobial activity. For this purpose, Fmoc-FF, Fmoc-RGD and collagen has been combined with AgNPs and gold nanoparticles (AuNPs). It is interesting to note, that the antibacterial properties of AuNPs have been significantly less studied compared to AgNPs, as well as mild methods to obtain them.[126]

In this case, these hydrogels were capable to produce both types of metallic nanoparticles by a simple sunlight photoirradiation methodology avoiding the use of external reducing agents that could affect the biocompatibility of the system. Composite hydrogels acted as both protecting and reducing nanoparticle agents. The incorporation of Fmoc-RGD and collagen made the hydrogel more biocompatible.

[126] a) Lemire, J. A.; Harrison, J. J.; Turner, R. J. *Nat. Rev. Microbiol. 2013 116* **2013**, *11* (6), 371–384. b) Yang, K.; Han, Q.; Chen, B.; Zheng, Y.; Zhang, K.; Li, Q.; Wang, J. *Int. J. Nanomedicine* **2018**, *13*, 2217–2263. c) Batool, Z.; Muhammad, G.; Iqbal, M. M.; Aslam, M. S.; Raza, M. A.; Sajjad, N.; *et al*. *Sci. Reports 2022 121* **2022**, *12* (1), 1–10.

2. Objectives

The rise of multidrug-resistant pathogens and the overuse of pharmaceuticals highlight the need for new broad-spectrum antimicrobial materials. While silver-based formulations have been extensively investigated, their cellular toxicity remains a concern, encouraging the search for more biocompatible alternatives.

Supramolecular hydrogels offer a promising solution as a template for nanoparticles growth and as a delivery vehicle. In contrast, gold nanoparticles have been less studied in this context, presenting an opportunity for further exploration of their antimicrobial properties and toxicity profiles.

With these considerations in mind, the objectives of this chapter are as follows:

1. Assess the capacity of peptide supramolecular hydrogels to facilitate the formation of metal nanoparticles, acting not only as protective agents but also as reducing agents.
2. Establish a highly biocompatible hydrogel formulation and study its physicochemical properties.
3. Characterization of hydrogels composed with metallic nanoparticles and the evaluation of their toxicity profiles and antimicrobial properties.

3. Results and discussion

3.1. *In situ* formation of silver and gold nanoparticles in Fmoc-FF hydrogels

The success of this work is significantly dependent on the *in situ* formation capacity of Ag and Au nanoparticles (AgNPs and AuNPs) within the peptide supramolecular hydrogel. For the ease of evaluation, this study has been conducted with single component hydrogels, specifically the dipeptide Fmoc-diphenylalanine (Fmoc-FF).

As discussed before, the self-assembly can be promoted by various stimuli, including pH or solvent change, enzymatic action, or addition of salts. In this case, the gelation was carried out by the addition of highly concentrated solution (100 mM) of silver or gold precursor ($AgNO_3$ and $HAuCl_4$, respectively) to a basic solution of Fmoc-FF (10 mM), avoiding the influence of external factors and minimizing the dilution of peptide. This leads to the formation of a coordination complex where the corresponding cation is interacting with the peptide molecules through the carboxylic groups.[127] After 24 hours, the reduction of the cations (Ag^+ and Au^{3+}) to metal nanoparticles (MNPs) took place by the action of sunlight. Peptide acts as the protecting and reducing agent at the same time. A schematic representation of the process is shown in Figure 57.

[127] Mañas-Torres, M. C.; Gila-Vilchez, C.; González-Vera, J. A.; Conejero-Lara, F.; Blanco, V.; Cuerva, J. M.; Lopez-Lopez, M. T.; Orte, A.; Álvarez De Cienfuegos, L. *Mater. Chem. Front.* **2021**, *5* (14), 5452–5462.

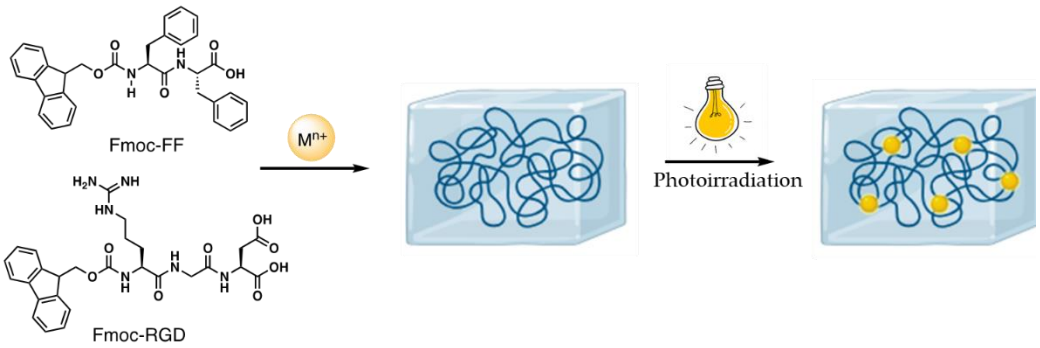

Figure 57. Schematic representation of the metal nanoparticles preparation.

The efficacy of the procedure can be readily determined by observing a change in the colour of the hydrogels. For hydrogels containing Ag^{+}, the colour shifted from translucent and colourless to a yellow-to-brown tone (Figure 58.a). In contrast, hydrogels with Au^{3+} exhibited a change from a bright yellow to a red tone (Figure 58.b).

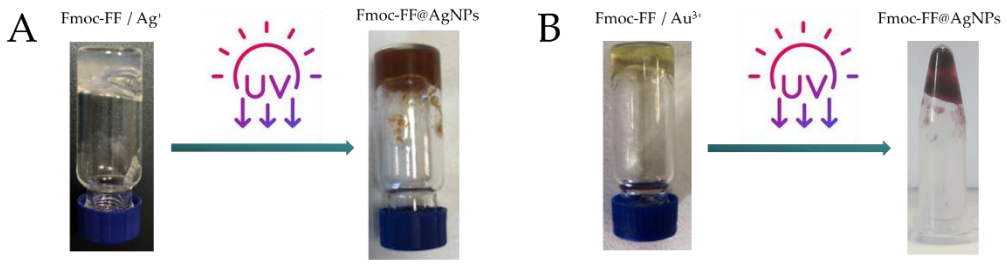

Figure 58. Vial colour change. a) Formation of AgNPs and b) formation of AuNPs.

For further confirmation, both colourless and coloured dried hydrogels (xerogels) were observed by transmission electron microscopy (TEM). It is important to note that the control hydrogel (colourless) was obtained employing GdL as promotor of the gelation. While the results obtained for the colourless xerogel shown only the typical fibers of these hydrogels, for the coloured xerogels the fibers appeared decorated with spherical particles for both Ag and Au xerogels.

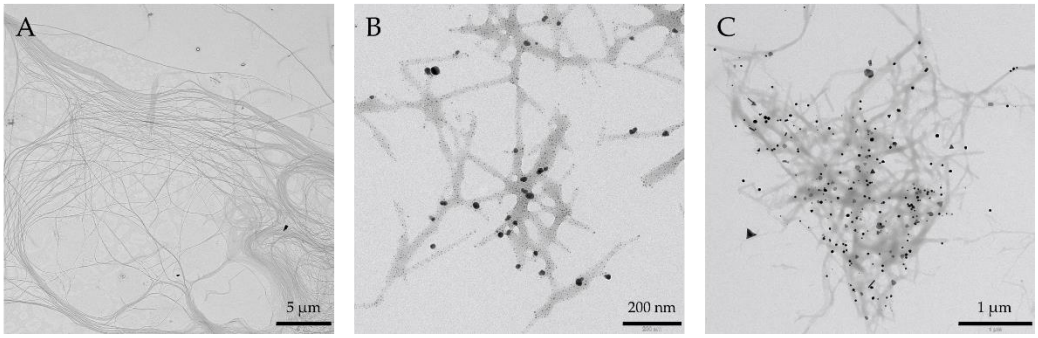

Figure 59. TEM images of a) Fmoc-FF with GdL, b) Fmoc-FF with AgNPs and c) Fmoc-FF with AuNPs.

3.2. Characterization of supramolecular composite hydrogels

The application of these materials requires a high degree of biocompatibility. Therefore, it was proposed to design a composite hydrogel, combining Fmoc-FF (20 mM), Fmoc-RGD (20 mM) and collagen (3 mg/mL) in a ratio of 3.5:1.5:5 (V/V) (Figure 60), with a view to improving this on the final material.

The incorporation of collagen in the composite serves to enhance its biocompatibility, with the maximum proportion of collagen allowed to form good quality hydrogels. On the other hand, Fmoc-RGD is a widely used component in tissue engineering[128] due to its ability to enhance cell adhesion. In addition, it acts as a promotor for gelation in this study by reducing the pH of the overall mixture. Finally, Fmoc-FF possesses an invaluable ability to form hydrogels with exceptional mechanical properties.[129]

[128] Kumar, V. B.; Tiwari, O. S.; Finkelstein-Zuta, G.; Rencus-Lazar, S.; Gazit, E. *Pharmaceutics* **2023**, *15* (2), 345.
[129] Wang, Y.; Geng, Q.; Zhang, Y.; Adler-Abramovich, L.; Fan, X.; Mei, D.; Gazit, E.; Tao, K. *J. Colloid Interface Sci.* **2023**, *636*, 113–133.

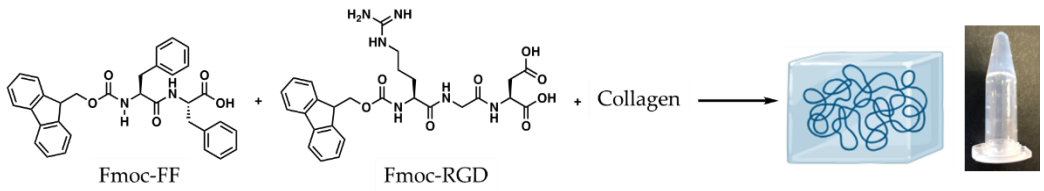

Figure 60. Components of hydrogels

The results of TEM (Figure 61.a) obtained for the composite xerogels shown fibers with microns in length indicating that the presence of collagen in the final composite does not affect the formation of hydrogel. In contrast, ESEM (Figure 61.b) images displayed depict spherical aggregates that are not visible under transmission electron microscopy (TEM). The origin of these aggregates is uncertain but may be attributed to the presence of collagen in the composite.

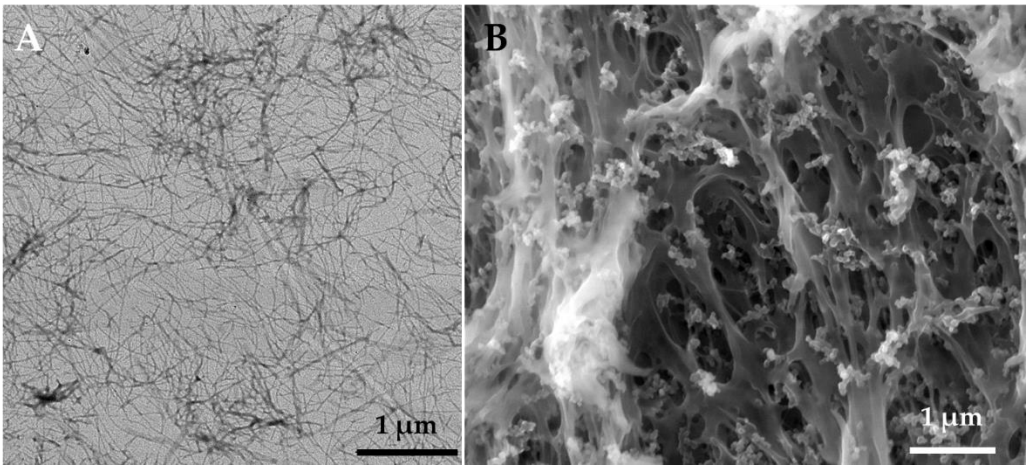

Figure 61. a) TEM and b) ESEM for composite xerogels.

Regarding the spectroscopy studies, CD and FT-IR were conducted. The CD spectrum obtained for a dilute solution of the composite (Figure 62.a) is complex and difficult to analyse due to the contribution of the three components. However, some conclusions can be drawn if it is compared with a typical spectrum of Fmoc-FF (Figure 62.b) and with the CD spectra for Fmoc-RGD and

collagen Type I described in literature.[130] Fmoc-peptide supramolecular aggregates show, typically, two characteristic Cotton bands. One is observed at 220 nm and is attributed to the n-π^* transition of the amino acids, while the other band appears at 275 nm and is ascribed to the π-π^* transition of the Fmoc group (Figure 62.b). Additionally, the negative signal at approximately 222 nm suggests a β-sheet secondary structure usual in these peptides.

Attending to the Figure 62.a, the signals exhibit lower intensity, which is likely attributable to the fact that they were obtained from a dilution of a preformed hydrogel rather than a properly solution.

The aforementioned signals are also present but require further clarification. The Fmoc-group band is easily observable, suggesting the possibility that these groups may be preferentially targeted. The signal associated with the amino acid transition can be observed as a shoulder at 214 nm in the high-intensity 205 nm peak. This last peak may be related to the collagen, but this is difficult to assert since the peaks are overlapping.

Considering all of these factors, it is evident that the CD spectrum is not easily interpretable and may indicate the involvement of both types of components in the final material, namely the Fmoc peptides (Fmoc-FF and Fmoc-RGD) and collagen.

[130] a) Cheng, G.; Castelletto, V.; Jones, R. R.; Connon, C. J.; Hamley, I. W. *Soft Matter* **2011**, *7* (4), 1326–1333. b) Drzewiecki, K. E.; Grisham, D. R.; Parmar, A. S.; Nanda, V.; Shreiber, D. I. *Biophys. J.* **2016**, *111* (11), 2377–2386.

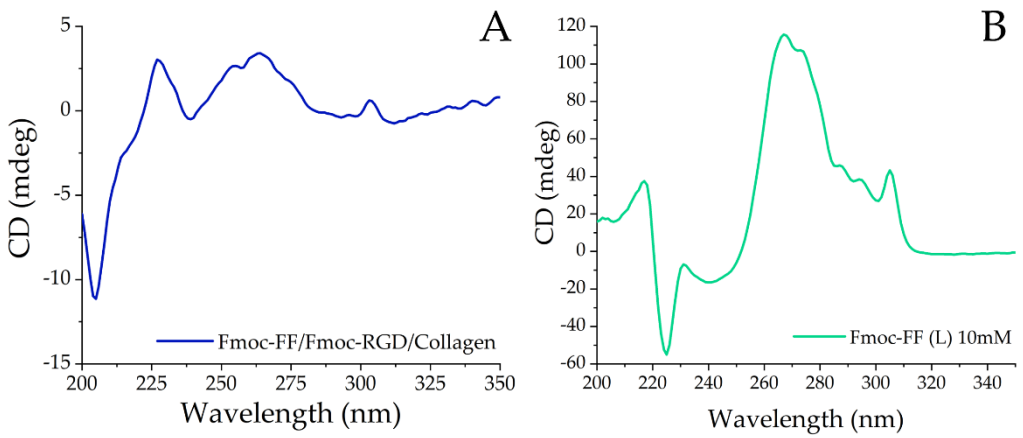

Figure 62. CD spectra for a) composite (Fmoc-FF + Fmoc-RGD + collagen) hydrogel and b) Fmoc-FF (10 mM) basic solution.

On the other hand, FT-IR spectrum was obtained from the xerogel, and it is shown in Figure 63.a. The presence of the bands of amide I at 1652 cm^{-1} could be attributed to α-helix secondary structure, since the β-sheet structures usually presents bands around 1630 cm^{-1}. Amide II bands at 1534 cm^{-1} are related with N–H bending vibrations but also with aromatic amino acids side chains and COO– stretching and are sensitive to protein secondary structure, while the band at 1692 cm^{-1} could correspond to the stacking of the carbamate group.[131] Therefore, it is difficult to settled down a preferred secondary structure from this data.

Finally, the mechanical properties of the composite were determined through rheological analysis. The results of frequency sweep (Figure 63.b) demonstrate the gel-like behaviour of the material, as evidenced by the values of the storage (G′) and loss (G″) moduli, which remain practically constant as the oscillation frequency varies. Additionally, G′ maintains values that are significantly higher

[131] Gila-Vilchez, C.; Mañas-Torres, M. C.; García-García, Ó. D.; Escribano-Huesca, A.; Rodríguez-Arco, L.; Carriel, V.; *et al. ACS Appl. Polym. Mater.* **2023**, *5* (3), 2154–2165.

than G". Furthermore, the results of the final amplitude sweep (Figure 106.a in Experimental section) indicate that the hydrogel undergoes breakage when a shear stress in excess of around 8 Pa is exceeded.

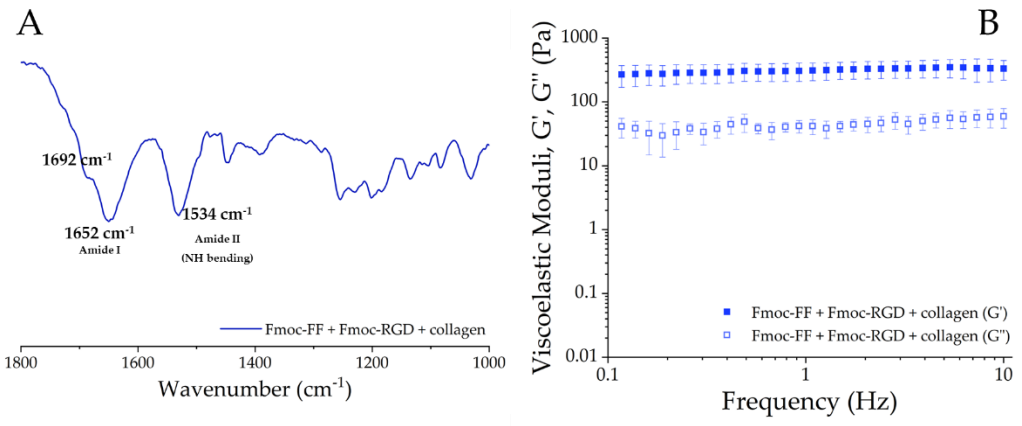

Figure 63. a) FT-IR spectrum of composite. b) Mechanical properties of composite hydrogel.

3.3. Characterization of composite hydrogels doped with MNPs

The experiment described in section 1 provided evidence that the Fmoc-FF is capable of forming MNPs. It is expected that the composite will exhibit a similar capacity, with the additional contribution of the polar groups of the Fmoc-RGD. Therefore, the formation of MNPs was investigated by testing different final concentrations of both precursors in the final material (see the experimental section of Chapter 8 for details). After the hemolysis analysis discussed below in this work, the nanoparticle concentrations that showed the best toxicity profiles were selected. The concentrations of the AgNPs and AuNPs hydrogels were 0.1 mM and 1 mM, respectively, and the characterization presented here corresponds to these values.

First, the formation of MNPs was confirmed by a visual examination of the change in colour of the hydrogels shown in Figure 64. The control hydrogels exhibited a colour change from translucent and colourless to an intense yellow, indicative of AgNPs formation. While the change from translucent and slightly yellow to red confirmed the formation of AuNPs.

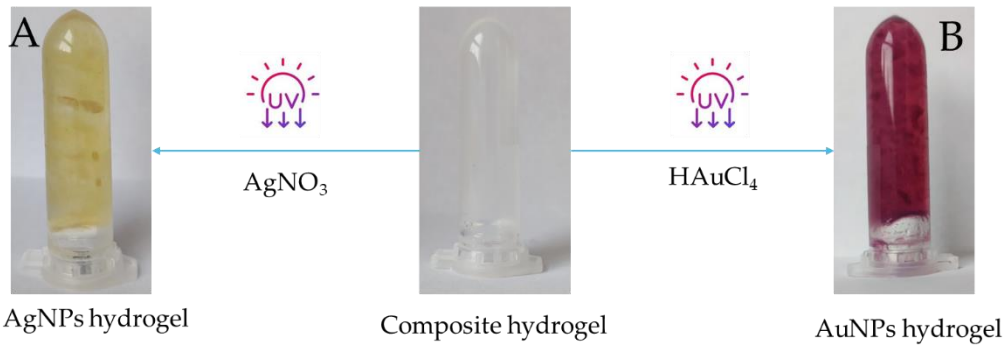

Figure 64. Visual confirmation of the formation of a) AgNPs and b) AuNPs.

The characterization of these hydrogels was carried out by the combination of different techniques. TEM studies by AgNPs xerogel and AuNPs xerogel showed in both cases the formation of low polydisperse spherical nanoparticles into the hydrogel fibers. In the case of AgNPs, the statistical data (taken from the measurement of 30 particles) reveals de formation of spherical NPs with a size of 19 ± 4 nm. For AuNPs, the statistical analysis showed the formation of NPs with spherical morphology and diameters of 6 ± 2 nm.

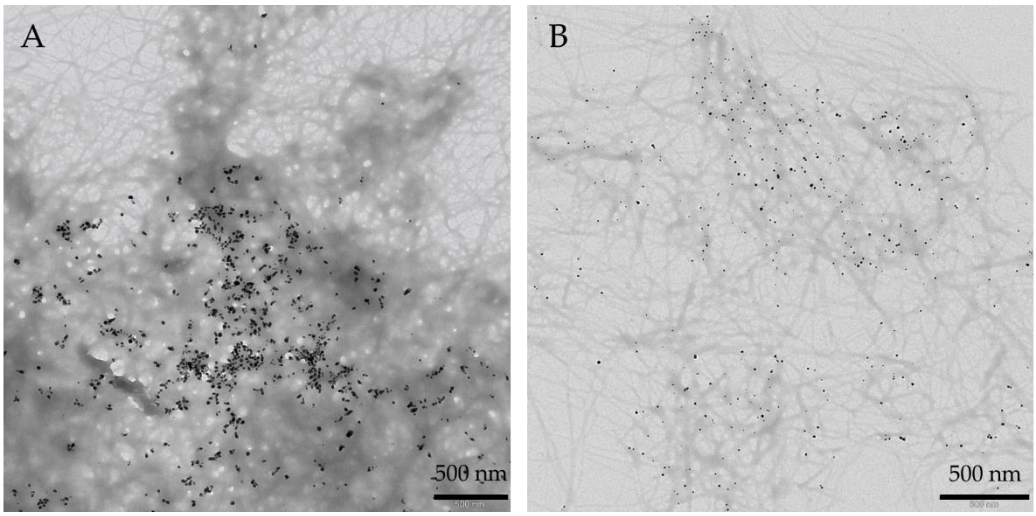

Figure 65. TEM images of a) AgNPs xerogel and b) AuNPs xerogel.

ESEM was carried out to study not only the three-dimensional structure of the hydrogels with MNPs (Figure 66), but also to obtain the elemental analysis of the samples, confirming the presence of silver and gold in the hydrogels (Figure 107 and Figure 108, experimental section). Figure 66.a,b shows silver and gold nanoparticles on the hydrogel, respectively.

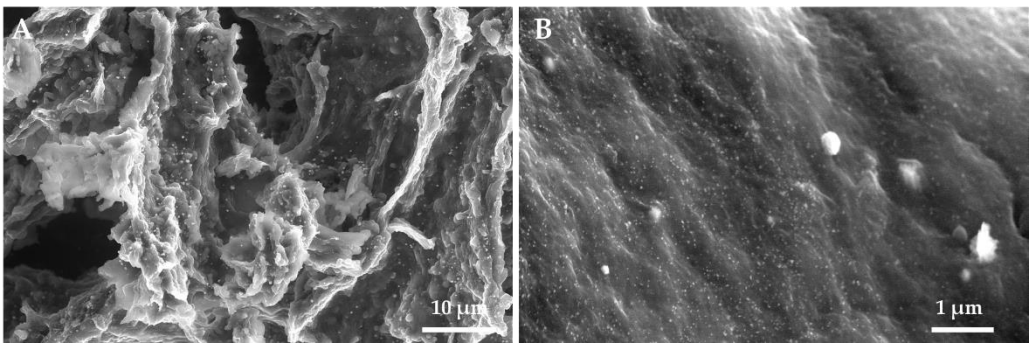

Figure 66. ESEM images of a) AgNPs hydrogel and b) AuNPs hydrogel.

The optical properties of the MNPs hydrogels were studied by UV-Vis spectroscopy. These nanoparticles are characterized by localized surface plasmon resonances (LSPR), which occur when conduction electrons oscillate in resonance with incident electromagnetic radiation, typically in the visible or near-infrared range. This phenomenon leads to light confinement at the nanoscale and enhances the local electromagnetic field, significantly influencing nearby molecules' spectroscopy. Gold nanoparticles (AuNPs) are especially valuable in biosensing due to their biocompatibility, colloidal stability, and sensitivity to changes in the local dielectric environment caused by biomolecule interactions. These interactions result in shifts in the nanoparticles' optical properties, enabling precise detection and analysis of biomolecular processes.[132] Then, the spectra for hydrogels MNPs showed the typical LSPR band at 545 nm associated to the formation of spherical AuNPs (Figure 67.b) and at 441 nm that correspond to the formation of spherical AgNPs (Figure 67.a). These broad bands can be related with the presence of Ag and AuNPs close to each other, affecting to the optical properties.

Moreover, FT-IR studies for the MNPs hydrogel reveals enormous similarities to the results obtained for composite hydrogels confirming that the formation of the MNPs within the fibers does not affect to the folding of the supramolecular hydrogel (Figure 67).

[132] a) Song, J.; Yuan, C.; Jiao, T.; Xing, R.; Yang, M.; Adams, D. J.; Yan, X. *Small* **2020**, *16* (8). b) Choi, W.; Kohane, D. S. *ACS Nano* **2024**, *18* (34), 22780–22792. c) Silvestre, O. F.; Rao, A.; Liz-Marzán, L. M. *Eur. J. Mater.* **2023**, *3* (1), 2202676. d) de la Encarnación, C.; Jimenez de Aberasturi, D.; Liz-Marzán, L. M. *Adv. Drug Deliv. Rev.* **2022**, *189*, 114484. e) Tadgell, B.; Liz-Marzán, L. M. *Chem. – A Eur. J.* **2023**, *29* (62), e202301691.

Finally, the rheological measurements of mechanical properties of the MNPs hydrogels were carried out. The results of frequency sweep demonstrate the gel-like behaviour for both AgNPs (Figure 67.a) and AuNPs (Figure 67.b) hydrogels, as evidenced by the values of the storage (G') and loss (G") moduli, which remain practically constant as the oscillation frequency varies. Moreover, it is observed that the modulus values are highly similar when compared to one another and to the control hydrogel, indicating that the formation of the nanoparticles does not significantly impact the mechanical properties of the gels.

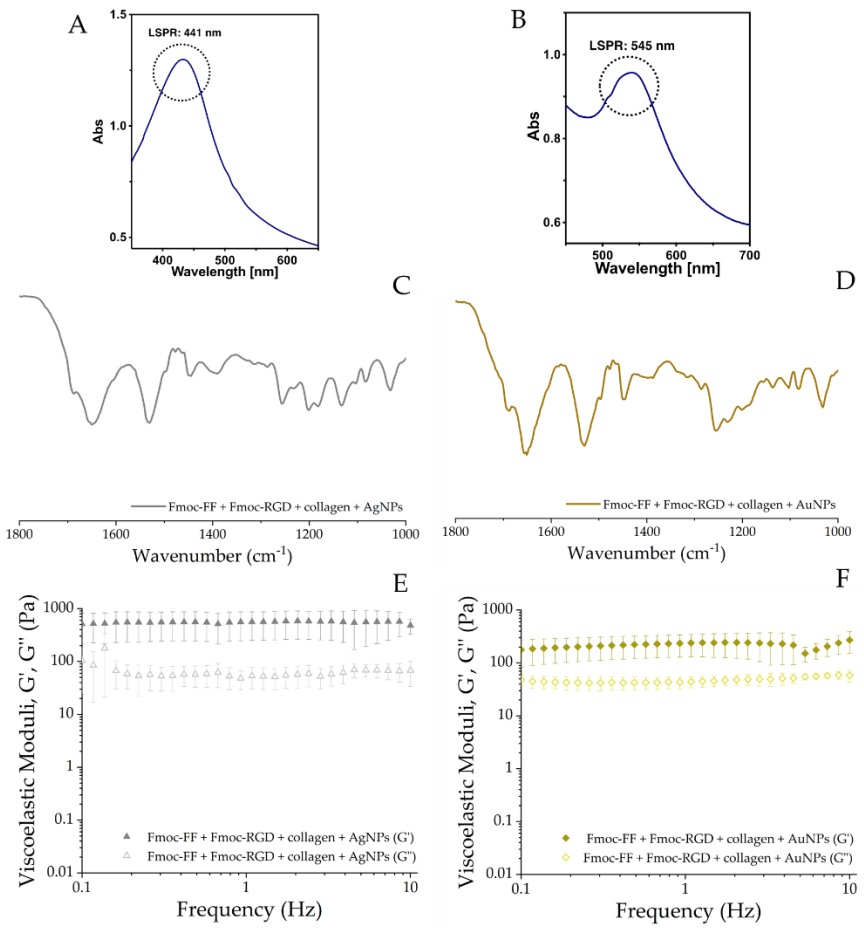

Figure 67. LSPR band of a) AgNPs hydrogel and b) AuNP hydrogel. FT-IR spectra of a) AgNPs hydrogel and b) AuNP hydrogel. Mechanical spectra of e) AgNPs hydrogel and f) AuNP hydrogel.

The observations that neither the mechanical properties nor the secondary structure of the gel are affected by the presence of the nanoparticles were to be expected, given the low concentration at which the precursors are added. Therefore, the cations interact with the polar groups of the components of the hydrogel without altering the three-dimensional structure or fiber formation. Thus, a novel composite hydrogel has been developed with a low concentration of MNPs to reduce toxicity. This low concentration of MNPs, that do not allow the formation of a gel with Fmoc-FF, can be used in here thanks to the use of Fmoc-RGD that acts as gelation inducer, lowering the pH of the mixture.

3.4. Evaluation of the biocompatibility and antimicrobial activity

The toxicity of both MNPs and the control hydrogels was evaluated *in vitro* through the quantification of hemolysis that they produce. The percentage of hemolysis (Figure 68.a) was evaluated for the complete range of concentrations of silver and gold tested (see the experimental section in Chapter 8). The findings of this investigation demonstrated that AuNPs (pink bars) exhibited a better toxicity profile compared to AgNPs (blue bars). Consequently, to ensure the minimal toxicity of the hydrogels containing AgNPs, the lowest concentration was selected (0.01 eq, corresponding to a 0.1 mM concentration). Conversely, that containing 0.1 eq (1 mM) of Au^{3+} precursor was chosen for subsequent experiments *in vitro* and *in vivo*.

In vitro tests were conducted in the group of Profesor Haldar to evaluate the efficacy of the MNPs hydrogels against Gram-positive and Gram-negative bacteria, as well as their capacity to eradicate fungal infections and disrupt biofilm formation.

The preliminary results of antibacterial studies carried out against *methicillin-resistant Staphylococcus aureus* (MRSA) as Gram-positive bacteria and *Escherichia coli* as Gram-negative bacteria demonstrated that the hydrogels containing AgNPs exhibited a rapid bacterial killing, with a reduction in bacterial count below the limit of detection within three hours, while hydrogels containing AuNPs were capable of killing bacteria within six hours (Figure 109, Experimental section). Furthermore, to evaluate the antibacterial capacity against a broader spectrum of pathogens, the ESKAPE pathogens were assessed. This group comprises six types of bacteria both Gram-positive and Gram-negative, which are resistant to many of the available antibiotics, is responsible for the majority of nosocomial diseases.[133] The six bacterial species that are most responsible for mortality due to antibiotic resistance are, in order of importance: *Escherichia coli*, *Staphylococcus aureus*, *Klebsiella pneumoniae*, *Streptococcus pneumoniae*, *Acinetobacter baumannii*, and *Pseudomonas aeruginosa*.[134]

[133] Mulani, M. S.; Kamble, E. E.; Kumkar, S. N.; Tawre, M. S.; Pardesi, K. R. *Front. Microbiol.* **2019**, *10* (APR), 403107.
[134] Murray, C. J.; Ikuta, K. S.; Sharara, F.; Swetschinski, L.; Robles Aguilar, G.; Gray, A.; *et al*. *Lancet* **2022**, *399* (10325), 629–655.

Therefore, it is crucial to develop materials capable of combating them. Consequently, the antibacterial assays of control and MNPs hydrogels have been expanded to include, in addition to *E. coli* and MRSA, *Klebsiella pneumoniae* (KP), *Acinetobacter baumanii* (AB) and *Pseudomonas aeruginosa* (PA) (Figure 68.b). The findings reveal that MNPs hydrogels are capable of eliminating the bacterial population within six hours.

Moreover, the fungicidal capacity of the MNPs hydrogels was also evaluated and the results are shown in Figure 68.c. The assays performed against *Candida albicans* demonstrated that the MNPs hydrogels exhibit not only antibacterial activity, but also fungicidal capacity with a complete eradication of the colonies within 6 hours.

Finally, the capacity to disrupt the formation of polymicrobial biofilm was studied in comparison to commercially available formulations as Amphotericin B (5 μg/mL), Vancomycin (32 μg/mL) and Silverex, a commercially available gel that contains 0.2 % (w/w) of $AgNO_3$ and it is indicated for the prevention of the infection in burns and wounds. Bacterial infections of medical implants represent a significant public health concern, given the potential for systemic infection, the high cost of treatment, and the emergence of drug resistance.[135]

[135] Ran, P.; Qiu, B.; Zheng, H.; Xie, S.; Zhang, G.; Cao, W.; Li, X. *Acta Biomater.* **2024**.

Figure 68.d shows that Amphotericin B exhibited the best results against bacterial infection, however presented the worst results against the fungal colonies. Vancomycin and Silverex showed poor results in general for both, bacterial and fungal infections. Regarding the hydrogels, they caused >90% reduction in the MRSA as well as *C. albicans* count in polymicrobial biofilms, showing the higher efficacy of all compounds tested against *Candida albicans*, especially the hybrid hydrogel with AuNPs. Thus, hydrogels with MNPs have a better overall capacity than commercial controls.

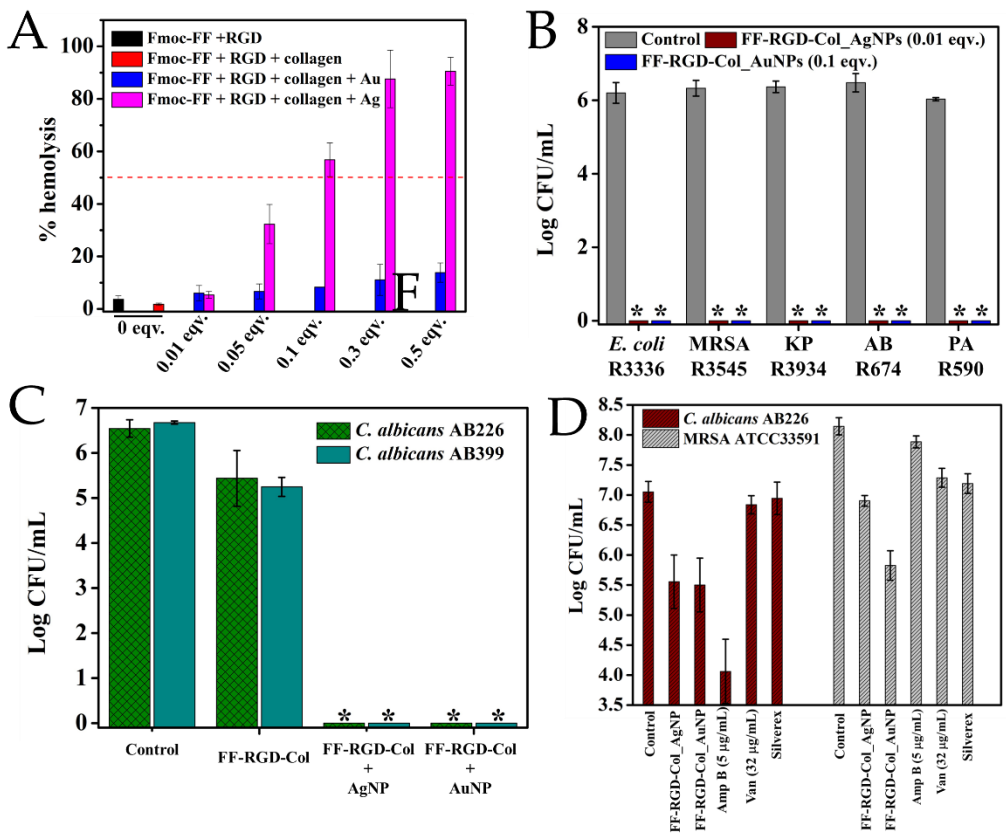

Figure 68. a) Percentage of hemolysis. b) Efficacy against ESKAPE bacteria of the control (grey bars), AgNPs (red bars) and AuNPs (blue bars) hydrogels within 6 hours. c) Antifungal activity. d) Disruption of polymicrobial biofilm capacity.

In vivo experiments were conducted in the company TheraIndx Lifesciences Pvt. Ltd. to evaluate the efficacy of the treatment in facilitating wound healing and combating MRSA infection. The results demonstrate that both MNPs hydrogels and commercial hydrogel exhibited wound healing rates exceeding 65% after 14 days. Furthermore, the treated wounds exhibited a significantly faster progression than the untreated wounds from day 7 onwards (Figure 69.a).

Furthermore, a notable reduction in bacterial load was observed in the wounds by day 7, with the hydrogel containing AgNPs demonstrating the most efficacious outcomes of the two novel materials under investigation (Figure 69.b).

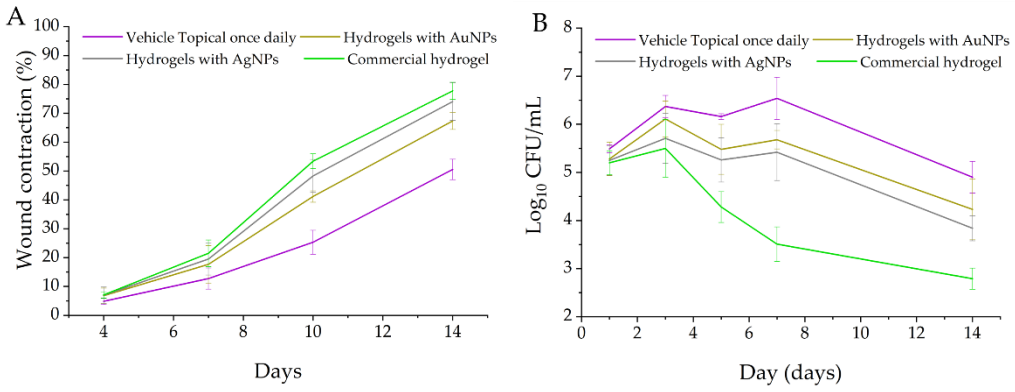

Figure 69. Progression of a) wound contraction and b) MRSA load.

The healing process is particularly noticeable when observing the progression of the wounds over time in the mice (Figure 70), showing once again that for *in vivo* experiments the composite hydrogel containing AgNPs is slightly better than the one that contains AuNPs.

Furthermore, histological analysis demonstrated a notable elevation in fibroblast proliferation, collagen formation, and epithelialization within the treatment groups comprising AuNPs hydrogels, AgNPs hydrogels, and a commercially available hydrogel (Group 2, Group 3, and Group 4, respectively) by day 14. This finding corroborates the efficacy results observed (Figure 110 in Chapter 8).

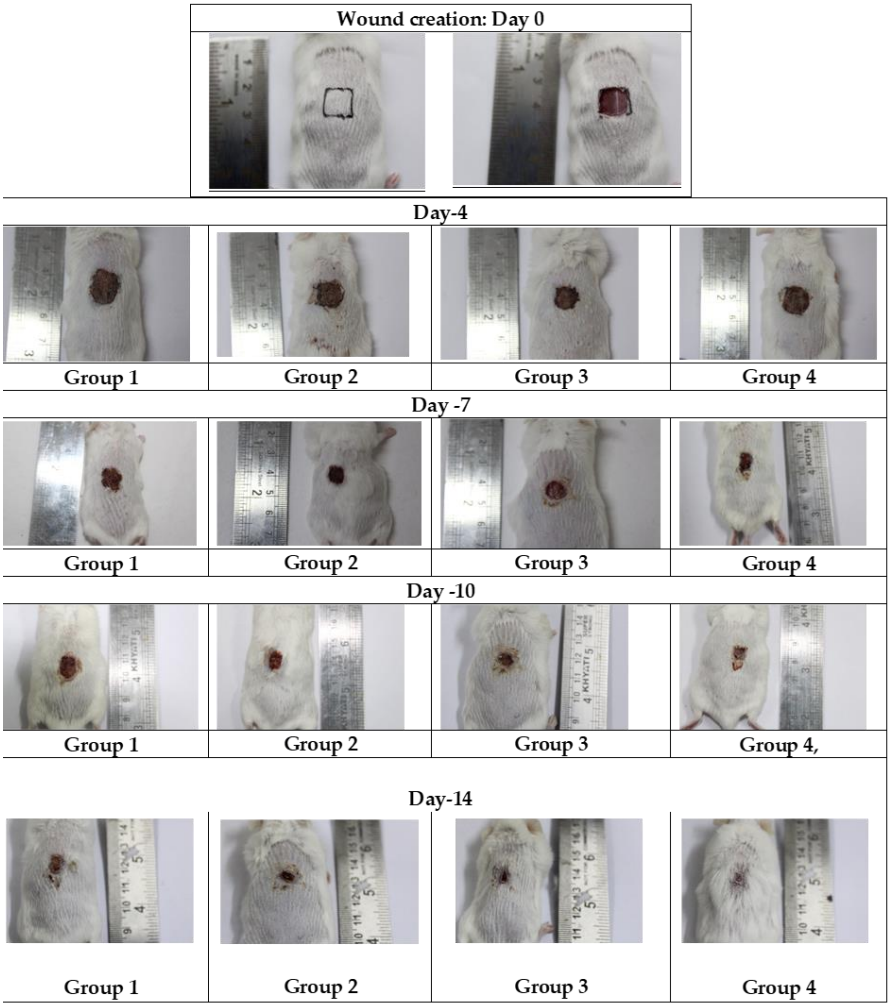

Figure 70. Progression of wound contraction with group 1: Excision Wound with MRSA (ATCC 43300) infection + Vehicle, group 2: Excision Wound with MRSA (ATCC 43300) infection + Hydrogels with gold nanoparticle, group 3: Excision Wound with MRSA (ATCC 43300) infection + Hydrogels with silver nanoparticle and group 4: Excision Wound with MRSA (ATCC 43300) infection + Commercially available hydrogel.

4. Conclusions

The findings presented in this chapter allow us to draw the following conclusions:

1. The peptide supramolecular hydrogels have the capacity to form nanoparticles *in situ*, acting both as a protecting agent and as a reducing agent.
2. A new composite hydrogel has been developed with a design aimed at reducing the quantity of metal nanoparticles used while maintaining gelation capability, which is induced by one of the intrinsic components of the mixture (Fmoc-RGD).
3. Control hydrogel composed of Fmoc-FF, Fmoc-RGD, and collagen is biocompatible and represents an excellent candidate for the encapsulation of noble metal nanoparticles. This approach has the potential to reduce the toxicity of these nanoparticles and facilitate their use in biological systems.
4. Hydrogels of silver and gold nanoparticles have demonstrated remarkable antimicrobial efficacy in vitro, exhibiting potent activity against bacterial and fungal pathogens, as well as against biofilm formation.
5. Furthermore, in vivo studies have revealed that these hydrogels facilitate wound healing and reduce the incidence of MRSA infections, exhibiting comparable outcomes to a commercial formulation

Chapter 6

Short-Peptide Supramolecular Hydrogels as Templates for Composite Protein Crystal Formation

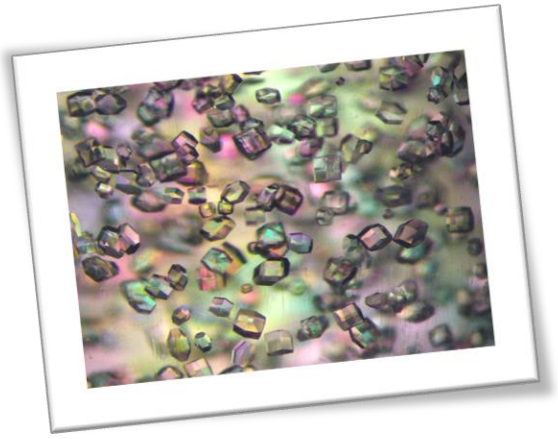

1. Background

Protein crystallization was initially employed as a method for purification. However, with the introduction of X-ray crystallography applied to biological molecules, protein crystals have become crucial for elucidating their three-dimensional structures. Consequently, the attainment of high-quality protein crystals has emerged as a fundamental objective in this field.[136]

The crystallization in conventional macromolecular hydrogels, including agarose, silica, and polyacrylamide, has been a well-established technique. This strategy has been employed as a means of obtaining high-quality crystals that are more stable and less sensitive to changes in the medium. This can be attributed to two factors: a) the hydrogel network acts as a filter for impurities, while eliminating sedimentation and convection currents in the medium, and b) the crystals incorporate the gel fibers into their structure during growth.[137] Considering the favourable outcomes observed with conventional hydrogels and the increasing interest in supramolecular ones, the possibility of crystallization in this particular class of hydrogels is worthy of consideration. This approach was first adopted by the research group in 2015.[138]

---

[136] McPherson, A.; Gavira, J. A. *Acta Crystallogr. F-Struct. Biol. Commun.* **2014**, *70* (1), 2–20.
[137] a) Conejero-Muriel, M.; Contreras-Montoya, R.; Díaz-Mochón, J. J.; Álvarez De Cienfuegos, L.; Gavira, J. A. *CrystEngComm* **2015**, *17* (42), 8072–8078. b) Gavira, J. A.; Van Driessche, A. E. S.; Garcia-Ruiz, J. M. *Cryst. Growth Des.* **2013**, *13* (6), 2522–2529. c) Artusio, F.; Castellví, A.; Sacristán, A.; Pisano, R.; Gavira, J. A. *Cryst. Growth Des.* **2020**, *20* (8), 5564–5571. d) García-Ruiz, J. M.; Gavira, J. A.; Otálora, F.; Guasch, A.; Coll, M. *Mater. Res. Bull.* **1998**, *33* (11), 1593–1598.
[138] Conejero-Muriel, M.; Gavira, J. A.; Pineda-Molina, E.; Belsom, A.; Bradley, M.; Moral, M.; *et al. Chem. Commun.* **2015**, *51* (18), 3862–3865.

The development of this pioneering strategy has enabled the investigation of the impact of chirality on the final crystals,[139] as well as the enhancement of their stability against radiation damage through the incorporation of hydrogels containing scavengers groups.[140] Furthermore, a novel insulin formulation has been developed based on the crystallization of this therapeutic molecule in supramolecular hydrogels of Fmoc-AA. These crystals exhibit enhanced thermal stability and a slower release profile.[141]

The physicochemical characteristics of peptide supramolecular hydrogels render them optimal materials for a multitude of applications, as described in Chapter 1.[142] The chemical and mechanical properties of these materials can be modified to a considerable extent by selecting an appropriate amino acid sequence or gelation method. Moreover, these properties facilitate their combination with other types of compounds and their utilization as a growth template for both

[139] Conejero-Muriel, M.; Gavira, J. A.; Pineda-Molina, E.; Belsom, A.; Bradley, M.; Moral, M.; *et al. Chem. Commun.* **2015**, *51* (18), 3862–3865.

[140] Contreras-Montoya, R.; Castellví, A.; Escolano-Casado, G.; Juanhuix, J.; Conejero-Muriel, M.; Lopez-Lopez, M. T.; *et* al. *Cryst. Growth Des.* **2019**, *19* (8), 4229–4233.

[141] a) Conejero-Muriel, M.; Contreras-Montoya, R.; Díaz-Mochón, J. J.; Álvarez De Cienfuegos, L.; Gavira, J. A. *CrystEngComm* **2015**, *17* (42), 8072–8078. b) Escolano-Casado, G.; Contreras-Montoya, R.; Conejero-Muriel, M.; Castellví, A.; Juanhuix, J.; Lopez-Lopez, M. T.; *et al. Crystals* **2019**, *9* (5), 244. e) Contreras-Montoya, R.; Arredondo-Amador, M.; Escolano-Casado, G.; Mañas-Torres, M. C.; González, M.; Conejero-Muriel, M.; *et al. ACS Appl. Mater. Interfaces* **2021**, *13* (10), 11672–11682.

[142] a) Gerbelli, B. B.; Vassiliades, S. V; Rojas, J. E. U.; Pelin, J. N. B. D.; Mancini, R. S. N.; Pereira, W. S. G.; *et al*. *Macromol. Chem. Phys.* **2019**, *220* (14), 1900085. b) Huo, Y.; Hu, J.; Yin, Y.; Liu, P.; Cai, K.; Ji, W. *ChemBioChem* **2023**, *24* (2), e202200582. c) Singh, N.; Kumar, M.; Miravet, J. F.; Ulijn, R. V.; Escuder, B. *Chem. - A Eur. J.* **2017**, *23* (5), 981–993. d) Tao, K.; Levin, A.; Adler-Abramovich, L.; Gazit, E. *Chem. Soc. Rev.* **2016**, *45* (14), 3935–3953. e) Sato, K.; Hendricks, M. P.; Palmer, L. C.; Stupp, S. I. *Chem. Soc. Rev.* **2018**, *47* (20), 7539–7551.

organic and inorganic crystals.[143] Consequently, the combination of hybrid hydrogels with protein crystals provides a promising avenue for the development of novel multicomponent materials with unique properties and potential applications.

The crystallization process occurs in two phases: *nucleation and growth*. Nucleation represents the most complex phase, as it involves a transition from a disordered to an ordered state. This process occurs via partially ordered intermediates, which eventually give rise to small, ordered assemblies known as *critical nuclei*.[144]

The process of protein crystal growth is more thoroughly understood than nucleation, with well-characterized mechanisms including dislocation growth and two-dimensional nucleation, alongside less prevalent mechanisms such as normal growth and three-dimensional nucleation. It should be note that both nucleation and crystal growth are critically dependent on the degree of

[143] a) Contreras-Montoya, R.; Arredondo-Amador, M.; Escolano-Casado, G.; Mañas-Torres, M. C.; González, M.; Conejero-Muriel, M.; *et al. ACS Appl. Mater. Interfaces* **2021**, *13* (10), 11672–11682. b) Mañas-Torres, M. C.; Ramírez-Rodríguez, G. B.; Garcia-Peiro, J. I.; Parra-Torrejón, B.; Cuerva, J. M.; Lopez-Lopez, M. T.; *et al*. *Inorg. Chem. Front.* **2022**. c) Illescas-Lopez, S.; Martin-Romera, J. D.; Mañas-Torres, M. C.; Lopez-Lopez, M. T.; Cuerva, J. M.; Gavira, J. A.; *et al*. *ACS Appl. Mater. Interfaces* **2023**, *15* (27), 32597–32609. d) Choi, W.; Kohane, D. S. *ACS Nano* **2024**, *18* (34), 22780–22792.

[144] a) McPherson, A.; Gavira, J. A. *Acta Crystallogr. F-Struct. Biol. Commun.* **2014**, *70* (1), 2–20. b) Lu, J.; Wang, X. J.; Ching, C. B. *Prog. Cryst. Growth Charact. Mater.* **2002**, *45* (3), 201–217. c) McPherson, A. Protein Crystallization. In *Methods in Molecular Biology*; Humana Press Inc., 2017; Vol. 1607, pp 17–50. d) Durbin, S. D.; Feher, G. *Annu. Rev. Phys. Chem.* **1996**, *47* (1), 171–204.

supersaturation in the mother liquor, which governs and drives these processes, determining their initiation, extent, and kinetic behaviour.[145]

The phase diagram for crystallization (Figure 71.a) collects the various states in which a protein solution can be situated. This diagram comprises two principal stages: *undersaturation* and ***supersaturation***, delineated by a line that represents the solubility at specific concentrations of precipitants, such as salts or polymers. This line signifies the equilibrium between the solid phase and the free molecular phase. Within the supersaturation region, two distinct areas are identified: the ***metastable zone***, where nucleation does not occur spontaneously but where supersaturation is sufficient for crystal growth, and the ***nucleation zone***, where both nucleation and crystal growth are feasible. A high supersaturation region, termed the *precipitation region*, is where the formation of precipitates is most probable.[146]

The crystallization of a protein requires the establishment of a supersaturated state, in which the protein concentration exceeds its solubility limit. Under these conditions, crystal formation occurs as equilibrium is gradually restored. However, the solid phase does not form spontaneously, as an energy barrier must be overcome to produce a stable crystal nucleus. Once this nucleus is present in the supersaturated solution, crystal growth will proceed until equilibrium is reestablished. As long as non-equilibrium forces persist and a

---

[145] a) McPherson, A. Protein Crystallization. In *Methods in Molecular Biology*; Humana Press Inc., 2017; Vol. 1607, pp 17–50. b) McPherson, A.; Gavira, J. A. *Acta Crystallogr. F-Struct. Biol. Commun.* **2014**, *70* (1), 2–20. c) Durbin, S. D.; Feher, G. *Annu. Rev. Phys. Chem.* **1996**, *47* (1), 171–204.

[146] a) McPherson, A.; Gavira, J. A. *Acta Crystallogr. F-Struct. Biol. Commun.* **2014**, *70* (1), 2–20. b) Koruza, K.; Lafumat, B.; Nyblom, M.; Knecht, W.; Fisher, Z. *Cryst. 2018, Vol. 8, Page 434* **2018**, *8* (11), 434.

certain degree of supersaturation drives the process, crystal growth or precipitate formation will continue.[147]

However, the free nucleation process often results in crystals of variable and uncontrolled size. While size may be less critical for X-ray crystallography compared to quality, achieving a narrow size distribution is a significant challenge for other applications, such as therapeutics. Consequently, seeding has emerged as a promising solution to this issue. This method involves using finely crushed crystals as "seeds" to replace natural nucleation and control the final crystal size.[148]

There are different techniques to obtain protein crystals, the most typical being ***vapor diffusion, batch*** and ***counter-diffusion*** (Figure 71.b, c, d, e). Although the composition of the final crystals is the same in all of them, the choice of each one is related to the final objective of the crystallization process. It is therefore important to note that the optimal method for selecting initial crystallization conditions may not necessarily be the optimal method for optimization. It is

[147] a) McPherson, A. Protein Crystallization. In *Methods in Molecular Biology*; Humana Press Inc., 2017; Vol. 1607, pp 17–50. b) McPherson, A.; Gavira, J. A. *Acta Crystallogr. F-Struct. Biol. Commun.* **2014**, *70* (1), 2–20. c) Durbin, S. D.; Feher, G. *Annu. Rev. Phys. Chem.* **1996**, *47* (1), 171–204.

[148] a) Contreras-Montoya, R.; Arredondo-Amador, M.; Escolano-Casado, G.; Mañas-Torres, M. C.; González, M.; Conejero-Muriel, M.; Bhatia, V.; Díaz-Mochón, J. J.; Martínez-Augustin, O.; de Medina, F. S.; Lopez-Lopez, M. T.; Conejero-Lara, F.; Gavira, J. A.; de Cienfuegos, L. Á. *ACS Appl. Mater. Interfaces* **2021**, *13* (10), 11672–11682. b) Gavira, J. A. *Arch. Biochem. Biophys.* **2016**, *602*, 3–11. c) McPherson, A.; Gavira, J. A. *Acta Crystallogr. F-Struct. Biol. Commun.* **2014**, *70* (1), 2–20.
d) Koruza, K.; Lafumat, B.; Nyblom, M.; Knecht, W.; Fisher, Z. *Cryst. 2018, Vol. 8, Page 434* **2018**, *8* (11), 434. e) Yan, E. K.; Zhao, F. Z.; Zhang, C. Y.; Yang, X. Z.; Shi, M.; He, J.; Liu, Y. L.; Liu, Y.; Hou, H.; Yin, D. C. *Cryst. Growth Des.* **2018**, *18* (2), 1090–1100.

possible to initiate the process with one technique, only to discover that an alternative produces larger and higher-quality crystals.[149]

Vapor diffusion is the most common method for screening crystal-producing conditions (Figure 71.b, c). It has two main configurations: sitting drop and hanging drop. In both, a droplet of protein and precipitant is equilibrated by evaporation with a reservoir of higher concentration, which increases the concentration in the droplet and can lead to supersaturation.[150]

Batch crystallization, schematically represented in Figure 71.b and d involve the mixing of the protein with the precipitant in a single reservoir. One disadvantage of this technique is that it only permits the use of a single supersaturation value per experiment. However, it allows for precise control of the conditions, which improves the quality of the crystals.[149]

The free interface diffusion method, which reduces convective transport, is mainly used in microfluidic devices for crystallization. The counter-diffusion technique is a variant of this method (Figure 71.b, e). This methodology, developed by the group of J.M. García-Ruíz, induces a high supersaturation at the beginning of the experiment, allowing to explore a wide region of the phase diagram in a single direction. This approach optimizes the crystallization

[149] a) Gavira, J. A. *Arch. Biochem. Biophys.* **2016**, *602*, 3–11. b) McPherson, A.; Gavira, J. A. *Acta Crystallogr. F-Struct. Biol. Commun.* **2014**, *70* (1), 2–20.
[150] a) Gavira, J. A. *Arch. Biochem. Biophys.* **2016**, *602*, 3–11. b) Otálora, F.; Gavira, J. A.; Ng, J. D.; García-Ruiz, J. M. *Prog. Biophys. Mol. Biol.* **2009**, *101* (1–3), 26–37.

conditions and produces high quality crystals thanks to the slow supply of molecules and the filtering of impurities.[151]

The counter-diffusion method offers the advantage of enabling crystallization when one or more components of the crystallization mixture cannot be mixed initially or cannot be distributed homogeneously in the medium. In this context, the group previously applied this protocol to obtain lysozyme crystals with electrical conductivity by growing them in Fmoc-FF hydrogels doped with SWCNT.[152]

[151] a) Gavira, J. A. *Arch. Biochem. Biophys.* **2016**, *602*, 3–11. b) McPherson, A.; Gavira, J. A. *Acta Crystallogr. F-Struct. Biol. Commun.* **2014**, *70* (1), 2–20. c) Otálora, F.; Gavira, J. A.; Ng, J. D.; García-Ruiz, J. M. *Prog. Biophys. Mol. Biol.* **2009**, *101* (1–3), 26–37. d) Ng, J. D.; Gavira, J. A.; García-Ruíz, J. M. *J. Struct. Biol.* **2003**, *142* (1), 218–231.

[152] Contreras-Montoya, R.; Escolano, G.; Roy, S.; Lopez-Lopez, M. T.; Delgado-López, J. M.; Cuerva, J. M.; Díaz-Mochón, J. J.; Ashkenasy, N.; Gavira, J. A.; Álvarez de Cienfuegos, L. *Adv. Funct. Mater.* **2019**, *29* (5), 1807351.

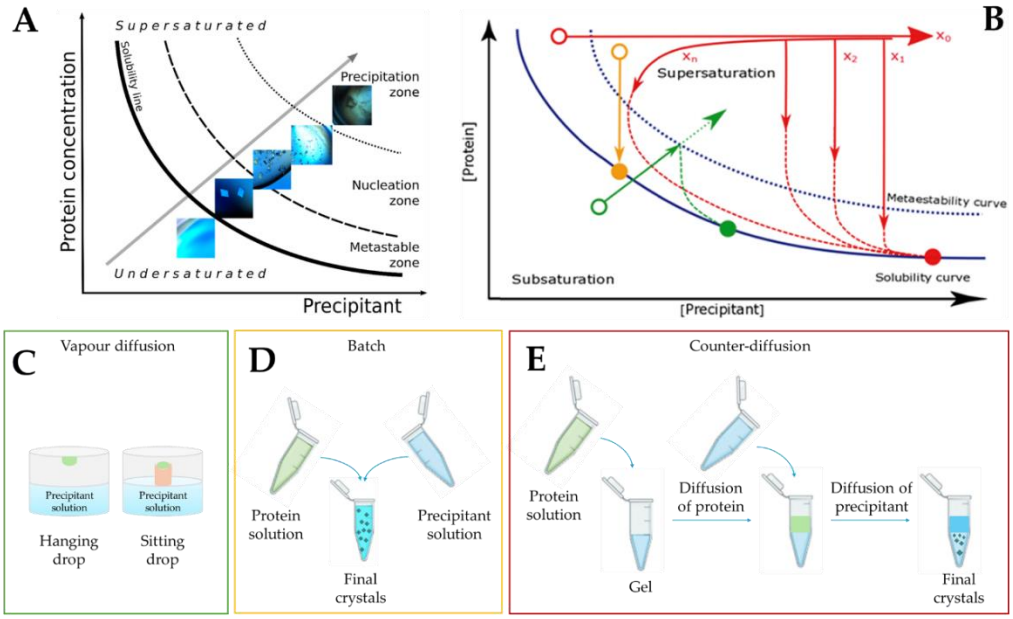

Figure 71. a) Crystallization phase diagram,[153] b) evolution of saturation in each methodology through crystallization phase diagram[154] and c), d), e) schematic representation of crystallization protocols.[155]

Finally, while crystals grown in hydrogels show a slower release profile, this do not maintain long-term crystal integrity and lack adaptability to different dissolution rates. Therefore, cross-linking protein crystals to enhance their mechanical and chemical stability has been recognized as a valuable strategy. Additionally, by regulating the degree of cross-linking, the release profile of

[153] Koruza, K.; Lafumat, B.; Nyblom, M.; Knecht, W.; Fisher, Z. *Crystals* **2018**, *8* (11), 434.
[154] Gavira, J. A. *Arch. Biochem. Biophys.* **2016**, *602*, 3–11.
[155] Contreras-Montoya, R.; Arredondo-Amador, M.; Escolano-Casado, G.; Mañas-Torres, M. C.; González, M.; Conejero-Muriel, M.; *et al*. *ACS Appl. Mater. Interfaces* **2021**, *13* (10), 11672–11682.

cross-linked protein crystals (CLPCs) can be precisely adjusted and therefore their application expanded.[156]

[156]a) Contreras-Montoya, R.; Escolano, G.; Roy, S.; Lopez-Lopez, M. T.; Delgado-López, J. M.; Cuerva, J. M.; Díaz-Mochón, J. J.; *et al*. *Adv. Funct. Mater.* **2019**, *29* (5), 1807351. b) Margolin, A. L.; Navia, M. A. *Angew. Chemie - Int. Ed.* **2001**, *40* (12), 2204–2222. c) Fernández-Penas, R.; Verdugo-Escamilla, C.; Martínez-Rodríguez, S.; Gavira, J. A. *Cryst. Growth Des.* **2021**, *21* (3), 1698–1707.

2. Objectives

Protein crystals hold promise as a tool due to their biocompatibility and catalytic properties. However, their integration with hybrid supramolecular hydrogels represents a novel advancement in the field of biomaterials. Therefore, the objectives of this research are:

1. Utilize lysozyme (LZM) crystals grown within Fmoc-peptide hydrogels doped with SWCNTs to investigate the CISS effect in complex three-dimensional ordered systems. Given that proteins in their crystalline state also demonstrate a supramolecular arrangement, their application in this context is highly relevant. This setup enables CNTs to interact with two distinct supramolecular chiral environments (peptide fibers and protein) simultaneously.
2. Grow LZM crystals within Fmoc-methionine-phenylalanine (Fmoc-MF) hydrogels doped with plasmonic nanoparticles (gold and silver) to develop an active release vehicle for antibacterial applications. Additionally, investigate the potential to achieve various release profiles by modulating the degree of cross-linking.
3. Functionalize cross-linked lysozyme crystals (CLLCs) of controlled size with Pd(II) and Pd(0) to create a size exclusion barrier for proteins while allowing an efficient, recyclable, and tolerable processing of small molecule substrates allowing the application of this catalytic system *ex vivo* to facilitate stem cell differentiation into salivary glands through drug uncaging.

3. Results and discussion

3.1. Protein Crystals and Supramolecular Hydrogels as Dual Sources for Investigating the CISS Effect

The exceptional results obtained from the application of supramolecular hydrogels in the study of the CISS effect, as discussed in Chapter 3, paved the way for the use of conductive protein crystals, previously developed by the group, for the same purpose.[157]

Lysozyme crystals (LZM) are grown within an Fmoc-dipeptide hydrogel that contains single-walled carbon nanotubes (SWCNT) (Figure 72.a). As previously described, during the growth phase, the crystals incorporate hydrogel fibers and, consequently, SWCNT, thereby acquiring the ability to conduct electrons. Consequently, SWCNTs have two layers attached on their walls, the inner layer is the peptide, and the outer layer is LZM, schematically described in Figure 72.e. These two layers cause that the CNTs being influenced by two chiral environments, on one hand, Fmoc-FF (L/D) and, on the other hand, LZM (L).

To investigate this consideration and the CISS signal, SWCNT@CLLC samples with varying SWCNT concentrations (0.1, 0.25, 0.5, and 0.7 mg/mL) were tested. Additionally, the role of peptide chirality was contrasted by substituting Fmoc-FF with achiral Fmoc-GG. For control samples, crystals grown in water without gel or SWCNT, as well as crystals grown in undoped Fmoc-FF, were also tested.

[157] Contreras-Montoya, R.; Escolano, G.; Roy, S.; Lopez-Lopez, M. T.; Delgado-López, J. M.; Cuerva, J. M.; Díaz-Mochón, J. J.; *et al*. *Adv. Funct. Mater.* **2019**, *29* (5), 1807351.

Figure 72.b and c show the appearance of SWCNT@CLLC observed by optical microscopy. Typical crystals grown in gel-free media or colourless hydrogels are completely transparent and colourless, while those grown in SWCNT-containing hydrogels are opaque black. Figure 72.d and f show the electron microscopic characterisation of SWCNT@CLLC (TEM and SEM, respectively). SWCNTs can be seen inside the crystals in both figures, as white filaments in d and as black dots in e, both well-distributed throughout the study area.

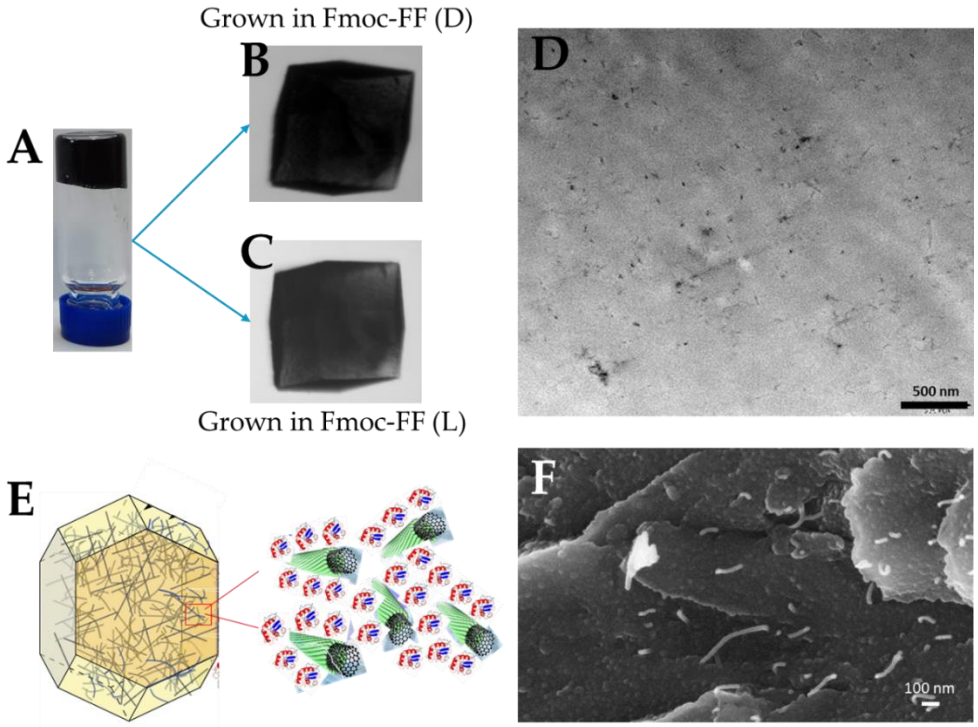

Figure 72. a) Fmoc-FF hydrogels with SWCNT, b) SWCNT@CLLC grown in Fmoc-FF (D) and c) SWCNT@CLLC grown in Fmoc-FF (L). d) TEM image of the interior of SWCNT@CLLC, black spots are bundles of CNTs. e) Schematic representation of the composite chiral hybrid materials in which CNTs are surrounded by two chiral compounds arranged supramolecularly. f) SEM image of the interior of SWCNT@CLLC, white filaments are bundles of CNTs.

Figure 73.a shows an optical microscope image of a slice of SWCNT@CLLC of around 900 nm thickness placed on SiO_2 substrate. To prepare the device for the electrical measurements, these slices were transferred between two electrodes and then, thermally annealed to improve the electrical contact (Figure 73.b). SEM image of the device shows that the SWCNTs (white strands) are embedded within the composite protein crystal and interconnected (Figure 73.c).

The Raman spectra (Figure 73.d) recorded before and after annealing exhibit minimal variation, suggesting that thermal annealing did not impact the crystal structure of the SWCNTs or their interaction with the chiral media. The spectra display the characteristic signals of SWCNTs. Firstly, at wavelengths of 240-280 cm^{-1}, the RBM bands are observed, and secondly, at wavelengths of 1500-1600 cm^{-1}, the tangential mode (TM) or G^+ and G^- peaks are located.

Considering the Raman spectra presented in Chapter 3 and in the published works for the Fmoc-FF samples with graphene allotropes[158] and the fact that these properties have also been previously investigated for SWCNT@CLLCs[159], a comparison of the results can be undertaken.

---

[158] a) Firouzeh, S.; Illescas-Lopez, S.; Hossain, M. A.; Cuerva, J. M.; Álvarez de Cienfuegos, L.; Pramanik, S. *ACS Nano* **2023**, *17* (20), 20424–20433. b) Rahman, M. W.; Mañas-Torres, M. C.; Firouzeh, S.; Cuerva, J. M.; Álvarez de Cienfuegos, L.; Pramanik, S. *ACS Nano* **2021**, *15* (12), 20056–20066. c) Rahman, M. W.; Mañas-Torres, M. C.; Firouzeh, S.; Illescas-Lopez, S.; Cuerva, J. M.; Lopez-Lopez, M. T.; de Cienfuegos, L. Á.; Pramanik, S. *ACS Nano* **2022**, *16* (10), 16941–16953. d) Firouzeh, S.; Illescas-Lopez, S.; Hossain, M. A.; Cuerva, J. M.; Álvarez de Cienfuegos, L.; Pramanik, S. *J. Chem. Phys.* **2023**, *159* (3). e) Hossain, M. A.; Illescas-Lopez, S.; Nair, R.; Cuerva, J. M.; Álvarez de Cienfuegos, L.; Pramanik, S. *Nanoscale Horizons* **2023**, *8* (3), 320–330.

[159] Contreras-Montoya, R.; Escolano, G.; Roy, S.; Lopez-Lopez, M. T.; Delgado-López, J. M.; Cuerva, J. M.; Díaz-Mochón, J. J.; *et al*. *Adv. Funct. Mater.* **2019**, *29* (5), 1807351.

The introduction of Fmoc-FF results in an increase in the G^+ band relative to unfunctionalised CNTs, with a particularly pronounced effect observed in the case of SWCNT@CLLCs. A similar trend is observed for the G^-/G^+ intensity ratio, which demonstrates a systematic decrease from bare CNTs to Fmoc-FF+CNTs and SWCNT@CLLC. Figure 73.d illustrates a G^-/G^+ ratio of approximately 32%, whereas the ratio for Fmoc-FF with CNTs is 39%. The molecular bonds in the CNT walls have been observed to suppress this vibration and reduce the G^- peak, as previously noted. These features collectively indicate a synergistic interaction between the two chiral molecules and the SWCNTs. This synergy may be attributed to an enhanced interaction between the Fmoc-FF and the SWCNT, potentially due to the outer crystal layer exerting compression on the Fmoc-FF molecules.

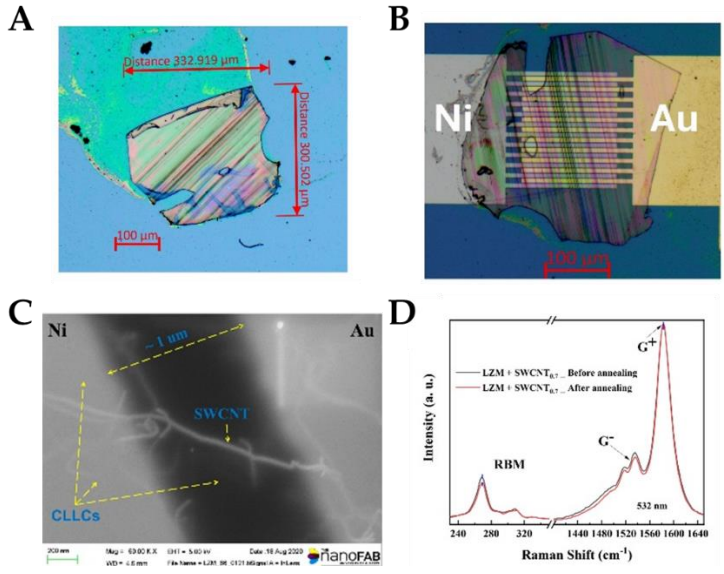

Figure 73. a), b) Optical microscope images of a typical slice of SWCNT@CLLC placed on SiO_2 substrate and interdigitated Ni/Au electrodes respectively. c) FESEM image of a SWCNT@CLLC (SWCNT concentration: 0.7 mg/ml, tubes coated with Fmoc-FF-L) slice, placed on top of pre-patterned Ni-Au electrodes. d) Room temperature Raman characterization of SWCNT@CLLC (SWCNT concentration: 0.7 mg/ml, Fmoc-FF-L coated). Signature Raman peaks are indicated, with no significant change because of annealing.

To further investigate the question of the difference caused by the presence of LZM, in collaboration with the group of Professor Pramanik, temperature-dependent current-voltage curves were measured using Au-Au and Ni-Au electrodes under zero magnetic field. It is important to note that the control crystal samples, which lacked SWCNTs and those with lower SWCNT concentrations, exhibited currents that were below the detection limit. Accordingly, the subsequent analysis will be based on data obtained from samples with SWCNT concentrations of 0.5 and 0.7 mg/ml. It can be postulated that the chiral matrix is not directly involved in electron conduction, at least not on this length scale. Furthermore, the absence of significant conductance from samples with lower nanotube concentrations indicates that the nanotube networks are not interconnected by extending between the electrodes in these samples. Figure 74 illustrates the data for the 0.7 and 0.5 mg/ml SWCNT samples, which display a semiconducting temperature dependence. The *I-V* data for samples with 0.7 mg/mL SWCNT using Au-Au and Ni-Au contacts, and for samples with 0.5 mg/mL, are shown in Figure 74.a, c and e. Non-linear transport is observed within the measured polarization range. The insets reveal that the device resistance, *R*, decreases by several orders of magnitude as the sample temperature increases. As noted in Chapter 3, this strong temperature dependence suggests phonon-assisted hopping, a key feature of SWCNT networks, regardless of chiral functionalization.

The carrier transmission between localised states in the nanotube network can be modelled using the VRH model, as described in Chapter 3. Figure 74.b, d and f display fits with the VRH model for d = 2, demonstrating a linear relationship across a wide temperature range (60-300 K). At lower temperatures (9-60 K), the fit remains linear but with a reduced slope, consistent with previous discussions on single-walled carbon nanotubes (SWCNTs).

Therefore, although the Raman spectra exhibited some discrepancies between samples with and without LZM, these discrepancies did not impact the electrical properties of the SWCNTs. This corroborates the scheme in Figure 1(f), which illustrates that electrical transport through SWCNTs is governed by the molecular layer (Fmoc-FF) attached to the CNT walls.

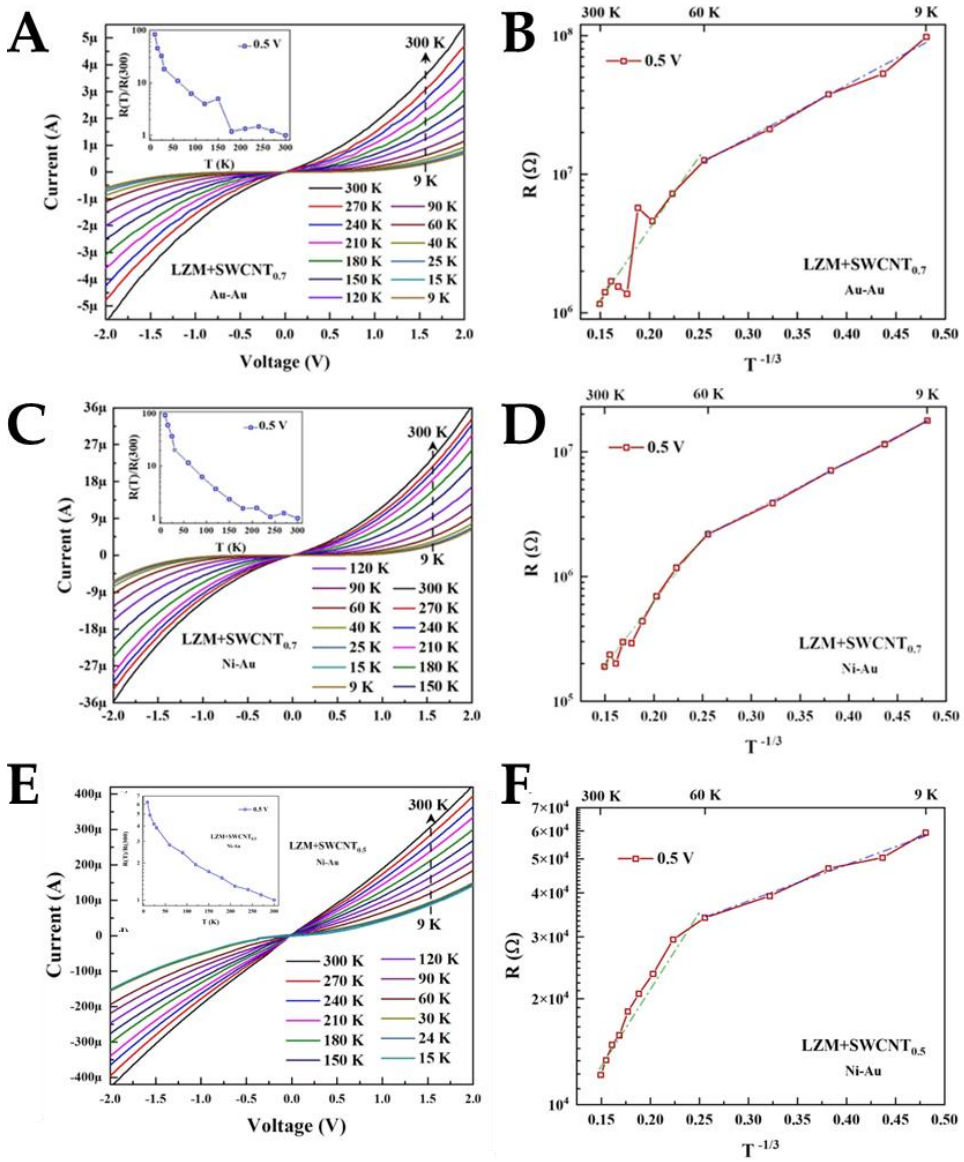

Figure 74. Current-voltage (*I-V*) characteristics at $B = 0$ and fitting with the VRH model with $d = 2$ for SWCNT@CLLC (SWCNT concentration: 0.7 mg/ml, tubes coated with Fmoc-FF-L) samples. a), b) Au-Au electrodes and c), d) Ni-Au electrodes. The *insets* in a) and c) show normalized resistance, measured at 0.5 V, as a function of temperature. e) Current-voltage (*I-V*) characteristics at $B = 0$ and fitting with the VRH model with $d = 2$ for SWCNT@CLLC (SWCNT concentration: 0.5 mg/ml, tubes coated with Fmoc-FF-L) samples Ni-Au electrodes. The *insets* in e) show normalized resistance, measured at 0.5 V, as a function of temperature. f) Fitting with the VRH model for $d = 2$.

Subsequently, the impact of the LZM crystalline outer layer on CISS characteristics was assessed through the performance of MR studies. In this case, the selected measurement configuration was longitudinal, with the magnetic field aligned parallel to the current pathway. This was due to the observation that the CISS signal was more pronounced in this configuration than in the transverse configuration.

Figure 75.a, b and c display the MR data for the SWCNT@CLLC samples (0.7 mg/ml) in the range ±12 kG, measured at 0.5 V bias, employing non-magnetic Au-Au contacts. A negative background MR of approximately 4% is observed, exhibiting symmetry with respect to the direction of the magnetic field, across the entire temperature range (Figure 75.d). It is noteworthy that the background MR temperature exhibits a non-monotonic evolution, which is only observable when chiral functionalisation of the nanotubes is employed. As illustrated in Figure 75.d, a 'double peak' is evident in the background MR response, with the initial peak occurring within the 10-20 K range and the subsequent peak occurring within the 20-40 K range. The background MR becomes undetectable at temperatures exceeding 40 K within the measured field range. This behaviour has been reproducible for several samples.

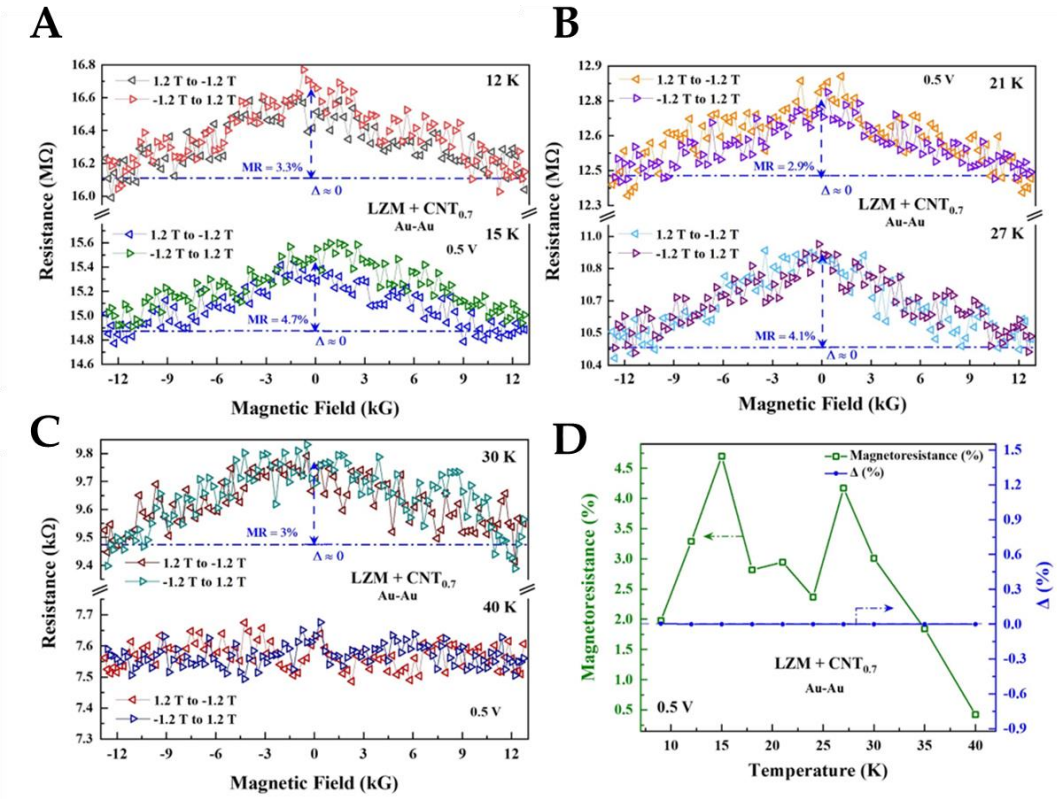

Figure 75. (a)-(c) *Symmetric* MR of SWCNT@CLLC crystals (SWCNT concentration 0.7 mg/ml, tubes coated with Fmoc-FF-L) with Au-Au contacts at representative temperatures (applied bias is 0.5 V in all cases). Note the non-monotonicity of the MR values as the temperature increases. (d) Temperature-dependence of background MR. MR asymmetry $\Delta = 0$ at all temperatures.

As the Au contacts are non-magnetic, they are unable to detect the presence of any spin polarization induced by the chirality of the charge carriers in the nanotubes. Consequently, the overall RM is symmetric. In order to detect the presence of any CISS-induced spin polarisation resulting from the chiral medium surrounding the nanotubes, one of the Au contacts has been replaced with a ferromagnetic Ni contact, which serves as a spin detector.

The Figure 76.a-e show the MR data for the SWCNT@CLLC (0.7 mg/ml) samples with Ni-Au contacts. The background MR and its non-monotonic temperature

dependence observed above remain evident, as depicted in Figure 5(f). The distinctive feature is that the MR responses are asymmetric, resulting in a non-zero Δ (~1.5%). This asymmetry could be attributed to the presence of CISS-induced spin polarisation in the nanotubes, which experience different transmission probabilities when the Ni magnetisation is reversed. It is noteworthy that the temperature dependence of Δ exhibits a zero-crossing, indicating a reversal of the spin polarisation, before it disappears completely at approximately 60 K. The temperature evolution of Δ is summarised in Figure 76.f. It is noteworthy that the zero-crossing of Δ and the second MR peak occur in the same temperature range.

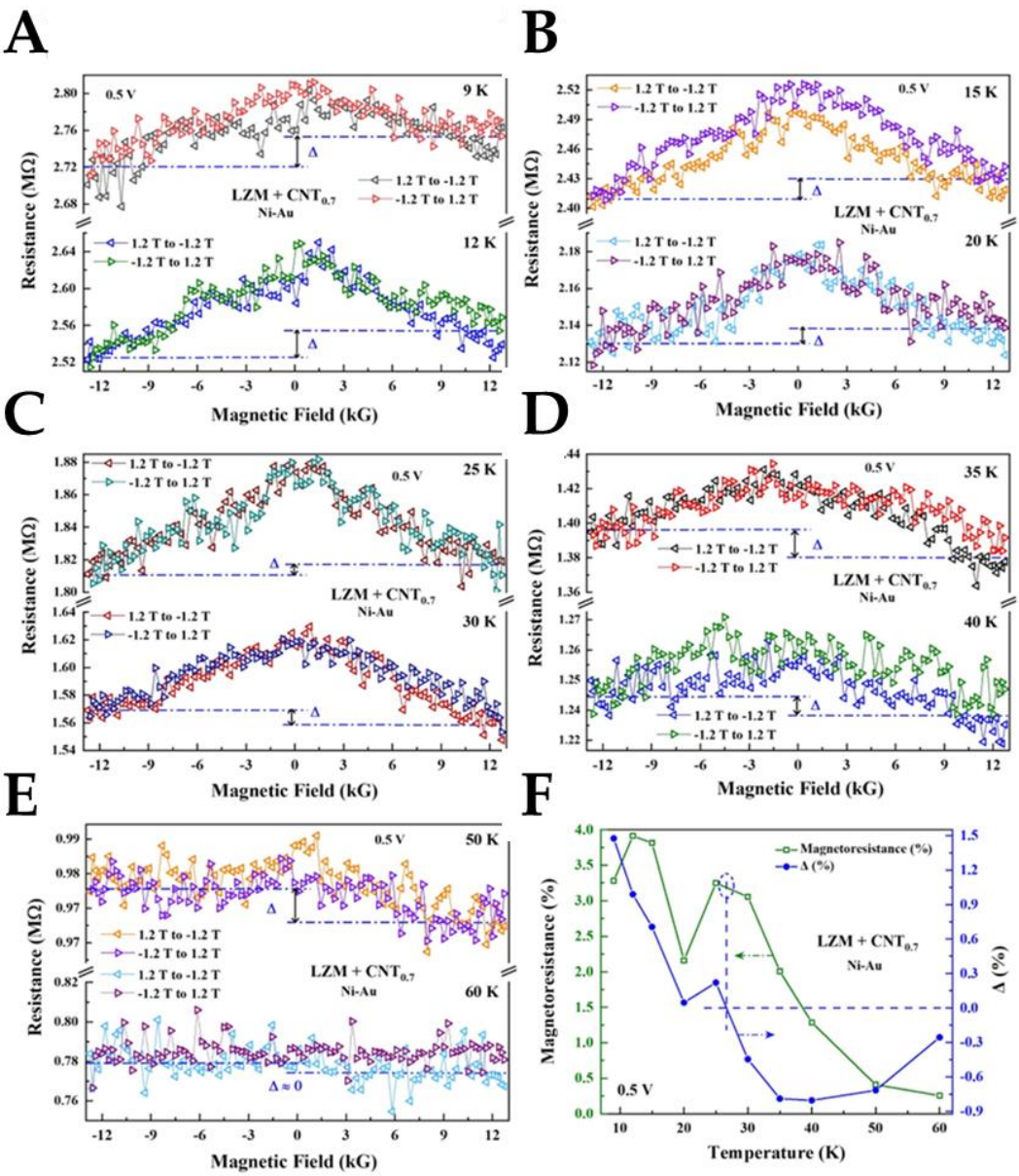

Figure 76. (a)-(e) Asymmetric MR of SWCNT@CLLC crystals (SWCNT concentration 0.7 mg/ml, tubes coated with Fmoc-FF-L) with Ni-Au contacts at representative temperatures (applied bias is 0.5 V in all cases). Note that the MR asymmetry Δ flips as temperature is increased. (f) Temperature-dependence of background MR and Δ.

Similar features have also been observed in the SWCNT@CLLC samples (SWCNT concentration: 0.5 mg/ml) (Figure 77).

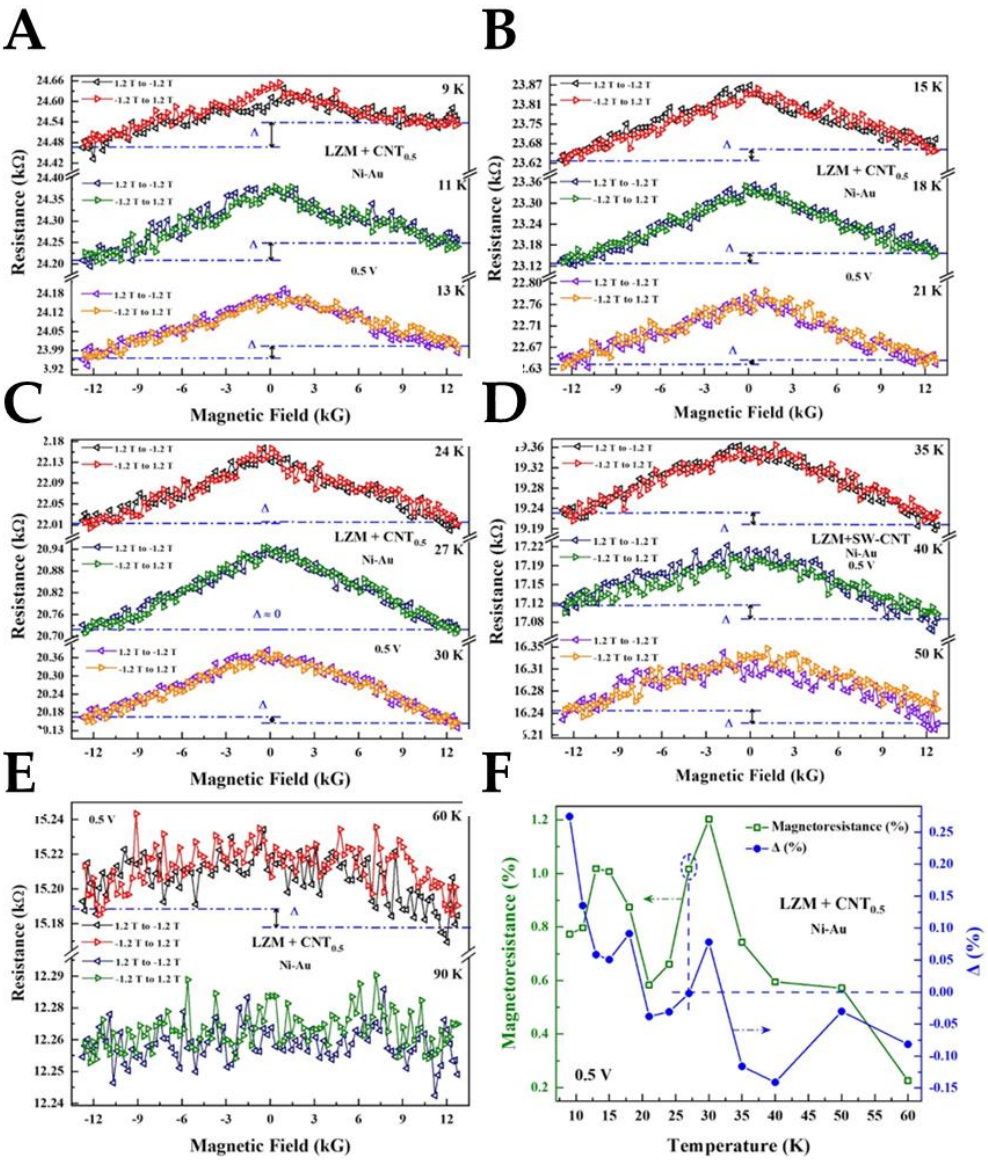

Figure 77. (a)-(e) *Asymmetric* MR of SWCNT@CLLC (SWCNT concentration: 0.5 mg/ml, tubes coated with Fmoc-FF-L) with Ni-Au contacts at different temperatures. Applied bias is 0.5 V in all cases. Note that the MR asymmetry Δ flips as temperature is increased. (f) Temperature-dependence of background MR and Δ.

It is important to note that the zero-crossing of the CISS Δ signal must be due to LZM, as this effect was not observed in Fmoc-FF (L/D) hydrogels with SWCNT measured in longitudinal configuration (see Figure 78). As previously discussed, since the mechanism is the same in both cases, this difference cannot be attributed to any fundamental difference on it. As a result of this inversion, the CISS Δ signal remains non-zero up to ~60 K in SWCNT@CLLC samples, while in Fmoc-FF (L/D) with SWCNT samples, it reaches zero around 25-30 K (Figure 78.b).

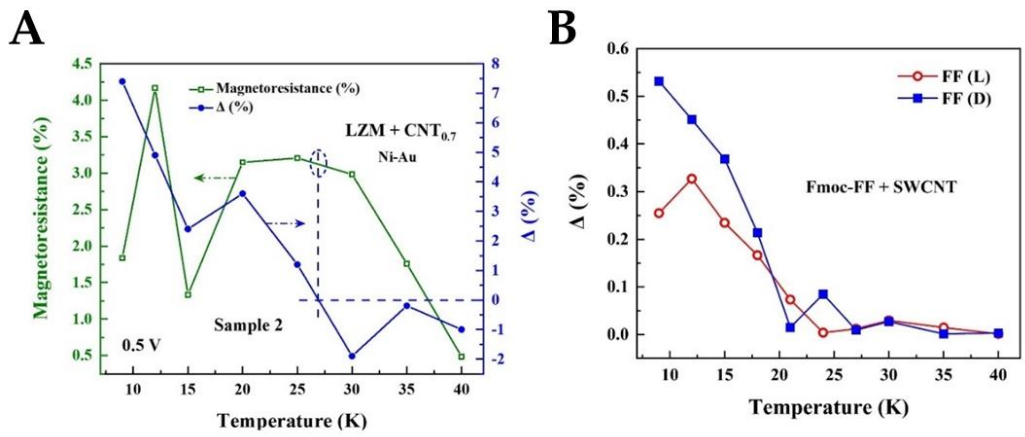

Figure 78. (a) Temperature-dependence of background MR and Δ for a second SWCNT@CLLC (SWCNT concentration: 0.7 mg/ml, tubes coated with Fmoc-FF-L) sample; (b) Temperature dependence of the CISS signal Δ for Fmoc-FF + SWCNT samples (i.e. without LZM) in the longitudinal configuration. The decay is monotonic, unlike the SWCNT@CLLC samples reported in Figures 5(f), 6(a). As demonstrated in our previous work, chirality dependence of the CISS signal Δ appears in the transverse configuration for Fmoc-FF + SWCNT hybrid systems.

As shown in Figure 74, charge transport through embedded SWCNT networks is due to phonon-assisted hopping. Furthermore, previous studies on chirally functionalized SWCNTs have indicated that the negative background MR results from quantum interference between forward and backward hopping paths.

The zero-crossing of Δ in the 20–30 K range is a key finding of this study (Figure 76.f, Figure 77.f, Figure 78.a). This zero-crossing indicates spin flipping within the nanotubes. Additionally, the second MR peak and the zero-crossing/spin flipping are observed in the same temperature range.

These features can be qualitatively explained by a characteristic of CISS where spin polarization (s) is "locked" with the momentum direction (p).[160] In one-dimensional systems like nanotubes, carrier backpropagation (or momentum reversal) is restricted by the requirement for simultaneous spin flipping. This is because most scattering processes, including phonons, conserve spin, suppressing such events in CISS systems.

Here, the CISS-induced spin signal (Δ) is maximum at the lowest temperature (~10 K). At this temperature, reduced carrier backpropagation leads to lower background MR. As the temperature increases from 10 to 20 K, the spin signal Δ decreases, facilitating backpropagation and increasing background MR. However, higher temperatures also reduce this effect due to phonon scattering. Thus, background MR is influenced by the interplay between these two factors.

This explains both the first MR peak around ~15 K and the second peak in the 20–40 K range, where spin polarization crosses zero. Beyond this range, the monotonic decrease in MR is due to the combined effects of reversed spin polarization and rising temperature. Therefore, the multiple MR peaks can be attributed to the interplay between quantum interference and CISS-induced spin polarization that suppresses carrier backpropagation.

---

[160] a) Evers, F.; Aharony, A.; Bar-Gill, N.; Entin-Wohlman, O.; Hedegård, P.; Hod, O.; *et al*. *Adv. Mater.* **2022**, *34* (13), 2106629. b) Aiello, C. D.; Abendroth, J. M.; Abbas, M.; Afanasev, A.; Agarwal, S.; Banerjee, A. S.; *et al*. *ACS Nano* **2022**, *16*, 4989–5035.

As mentioned previously, the reversal of the CISS signal and its persistence at higher temperatures could be attributed to the presence of the LZM. To clarify the role of LZM, the CISS response of SWCNT@CLLCs, where the SWCNTs are coated with achiral Fmoc-GG was studied and the results are shown in Figure 79.

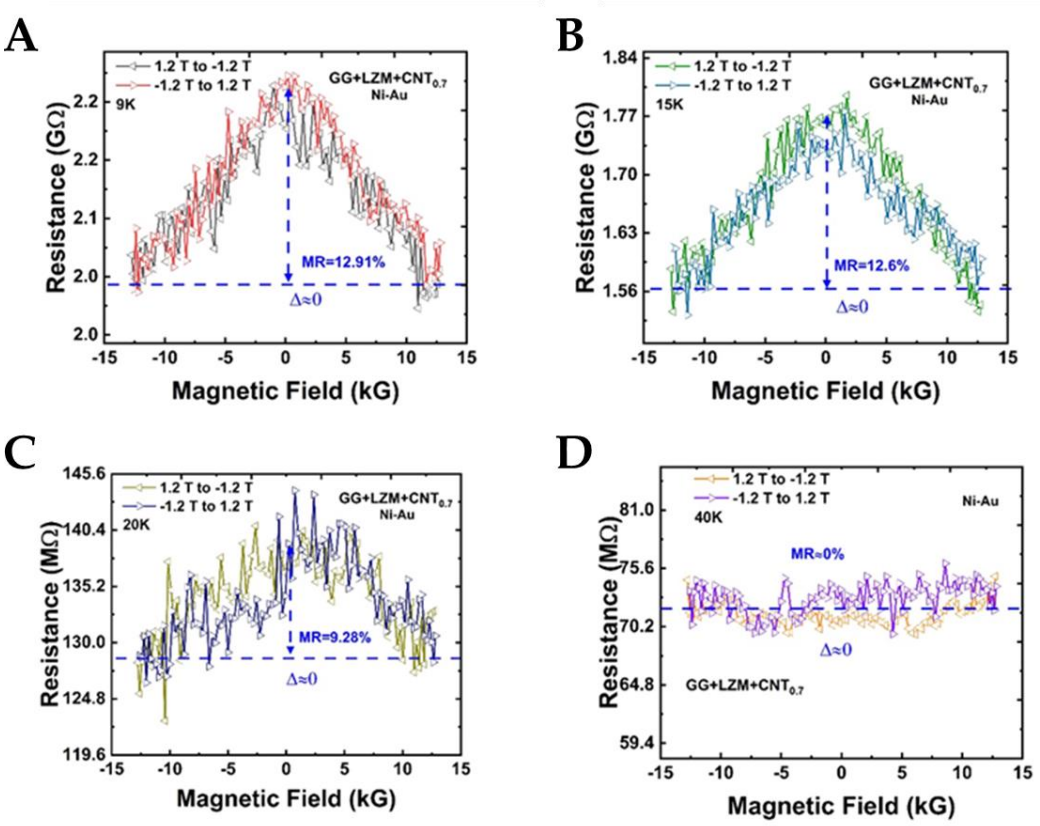

Figure 79. Symmetric MR of SWCNT@CLLC crystals (SWCNT concentration 0.7 mg/ml, tubes coated with achiral Fmoc-GG) with Ni-Au contacts at representative temperatures. The background MR decreases monotonically with temperature.

In this case, no CISS signal Δ was observed despite the presence of LZM. This indicates that chirality transfer to the SWCNTs occurs only through the peptides. LZM merely compresses the peptides onto the nanotubes, enhancing their interaction. Thus, only chiral molecules exhibit a more persistent CISS signal.

This means that LZM exerts a synergistic influence on the CISS signal, even though it does not interact directly with the CNTs. Here, the background MR decreases monotonically with temperature. This is expected given the previous explanation, as no CISS effect is present due to the achiral nature of Fmoc-GG.

All the discussion thus far has been based on the results obtained for samples with Fmoc-FF (L). To study both enantiomers, samples with Fmoc-FF (D) were also prepared. Although it was expected that the enantiomers would show opposite signs, as discussed in Chapter 3, the data reveal similar results for both enantiomers. This is because, in the chosen configuration for this study, both Fmoc-FF (L) and Fmoc-FF (D) exhibit the same sign. These data are summarized in Figure 80.

The comparison of the Δ values for SWCNT@CLLC and Fmoc-FF + SWCNT, showed that the CISS signal was approximately an order of magnitude stronger with the presence of LZM. This observation underscores the synergistic effect of the two chiral sources, even though the outer LZM layer does not directly interact with the CNTs.

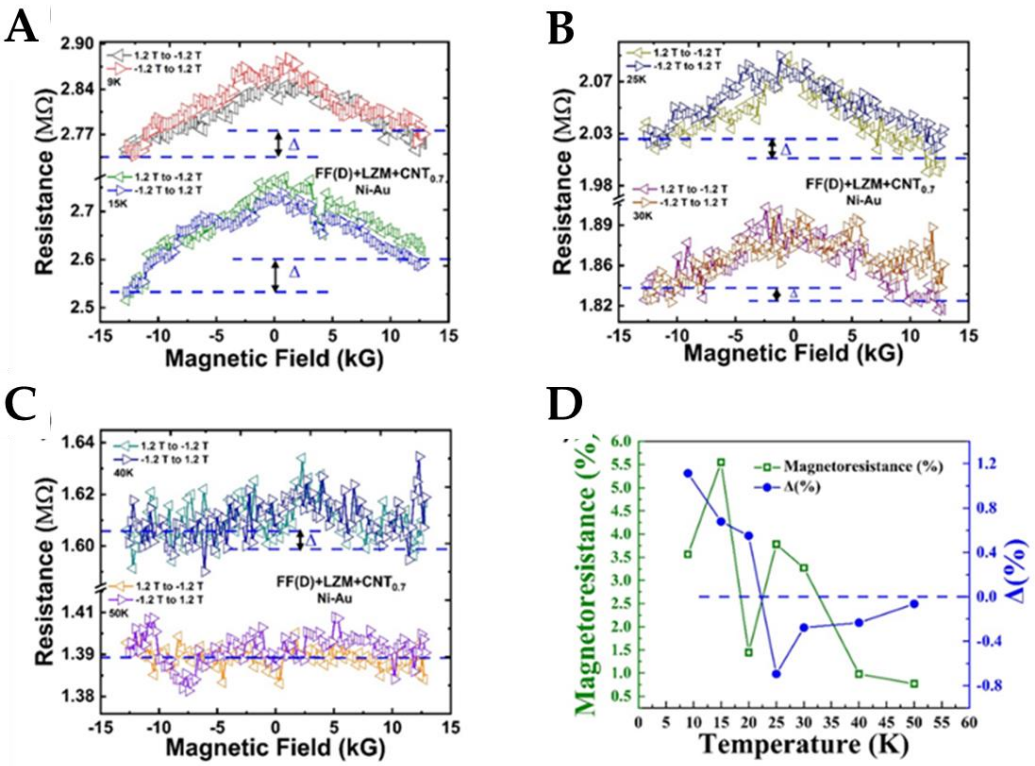

Figure 80. (a)-(c) Asymmetric MR of SWCNT@CLLC crystals (SWCNT concentration 0.7 mg/ml, tubes coated with Fmoc-FF-D) with Ni-Au contacts at representative temperatures. Note that the MR asymmetry Δ flips as temperature is increased. (d) Temperature-dependence of background MR and Δ.

The temperature-dependent reversal of the CISS signal Δ is noteworthy. As highlighted at the beginning of this discussion, there are two chiral environments: one from LZM (L) and another from Fmoc-FF (L/D). The stacking of Fmoc-FF forms fibers with "supramolecular chirality," which is sensitive to environmental changes. This supramolecular chirality, along with the intrinsic chirality of protein and peptide building blocks, influences the CISS effect. Changes in these supramolecular structures due to temperature variations may account for the observed reversal in Δ.

3.2. Hybrid protein crystals grown in supramolecular hydrogels: development of a broad-spectrum antibacterial drug delivery vehicle

It has been demonstrated that the release profile of therapeutic protein crystals can be slowed down due to the incorporation of hydrogels fibers. Furthermore, peptide supramolecular hydrogels exhibit the capacity to act as template for the growth of plasmonic nanoparticles (gold and silver), leading to hybrid materials with antimicrobial activity. However, neither the dissolution rate of insulin crystals nor delivery profile of plasmonic nanoparticles are susceptible to tune and adapt for different ratios employing the same material.

A strategy for integrating these features into a hybrid material has therefore been developed. It has been established that protein crystals incorporate hydrogel fibers during the growth stage. Consequently, lysozyme (LZM) crystals were grown in hybrid nanoparticles hydrogels in order to obtain a broad-spectrum antibacterial material. Here, lysozyme serves a dual function, acting as an active compound against Gram-positive bacteria and as a biocompatible drug delivery vehicle. Furthermore, the final material exhibited the potential for regulating the release profile through the control of the cross-linking reaction extension.

3.1.1. Controlling cross-linking degree through the reaction time

First, to test the hypothesis of the control over the release profile of lysozyme crystals grown in hydrogels, a simplistic approach was tested. LZM crystals were grown in agarose hydrogels with a well stablished batch protocol.

Briefly, a solution of lysozyme in sodium acetate (AcONa) was mixed with agarose in sol state and a solution of sodium chloride (NaCl) to obtain crystals in final conditions of 45 mg/mL of protein and 3% (m/V) of precipitant (see experimental details in Chapter 8). These crystals were subsequently cross-linked with glutaraldehyde in different extension through the control of the reaction time and cross-linker concentration. Since glutaraldehyde exerts its role reacting with free amino groups in the amino acid sequence, the reaction could be stopped by the addition of a solution containing amines. In this case, a buffered solution of Tris at pH 7.0 with 3% (m/V) of NaCl were used for this purpose, in relation to keep a friendly environment for the crystals less cross-linked.

First, it should be necessary to establish an optimal concentration of glutaraldehyde which would allow to obtain crystals with different degrees of crosslinking within a certain time of action, which in this case was set as 1 hour. Thus, different final concentrations of glutaraldehyde were tested (0.1, 0.5, 1.0, 2.5 and 5.0 % (m/V)) and evaluated by SDS-Page electrophoresis (Figure 81.a).

The results showed that higher concentrations of 2.5 and 5 % (m/V) fully cross-linked the crystals as it can be seen from the absence of any band in the gel for 5 % concentration and for2.5 % a very clear, barely visible band is observed. On the other hand, 0.1 % (m/V) of glutaraldehyde was very low since the observable bands were the same that from native crystals and the protein in solution. Similar results were observed for 0.5 % (m/V) concentration, very weak band. The best results were observed when using 1%. Thus, the 1 % (m/V) concentration of glutaraldehyde was selected for the purpose of controlling the cross-linking degree through the reaction time.

The success of this methodology is shown in Figure 81.b. This technique allowed a directly comparison between CLLC at different times under the same conditions. Figure 81.b shows that an increase in the cross-linking time gave rise to more stable crystals with slower release profile, illustrating by the bands with higher molecular weights as the increase of time. It is noteworthy that control crystals (CC), grown withing agarose without any cross-linking, and lysozyme solution (LZM) exhibit, as expected, the same bands, with the main corresponding to the weight of lysozyme monomer, 14.3 KDa.

To obtain the release profiles, the dissolution rate curves of LZM crystals against MiliQ water and saline solution both at 37 °C were evaluated by measuring the protein concentration on the supernatant by UV-Vis spectroscopy (see experimental section in Chapter 8). The results in Figure 81 showed that the control crystals had the fastest dissolution rate, reaching the maximum concentration in 24 hours. It should be noted that the crystals were grown at a final concentration of 45 mg/mL; however, the maximum concentration that could be observed was 22.5 mg/mL. This was due to the fact that the experiments were conducted by adding 100 μL of saline or MiliQ water on top of the hydrogels containing crystals, thereby diluting the overall concentration by a factor of two. In contrast, the samples with different degrees of cross-linking showed a much slower dissolution profile, highly correlated with the extent of it. As expected, the release profile was inversely related to the degree of crosslinking, indicating that a faster dissolution rate was associated with a shorter cross-linking time. It is noteworthy that none of the cross-linked crystals at any extension reached the maximum dissolution concentration within the 24 hours.

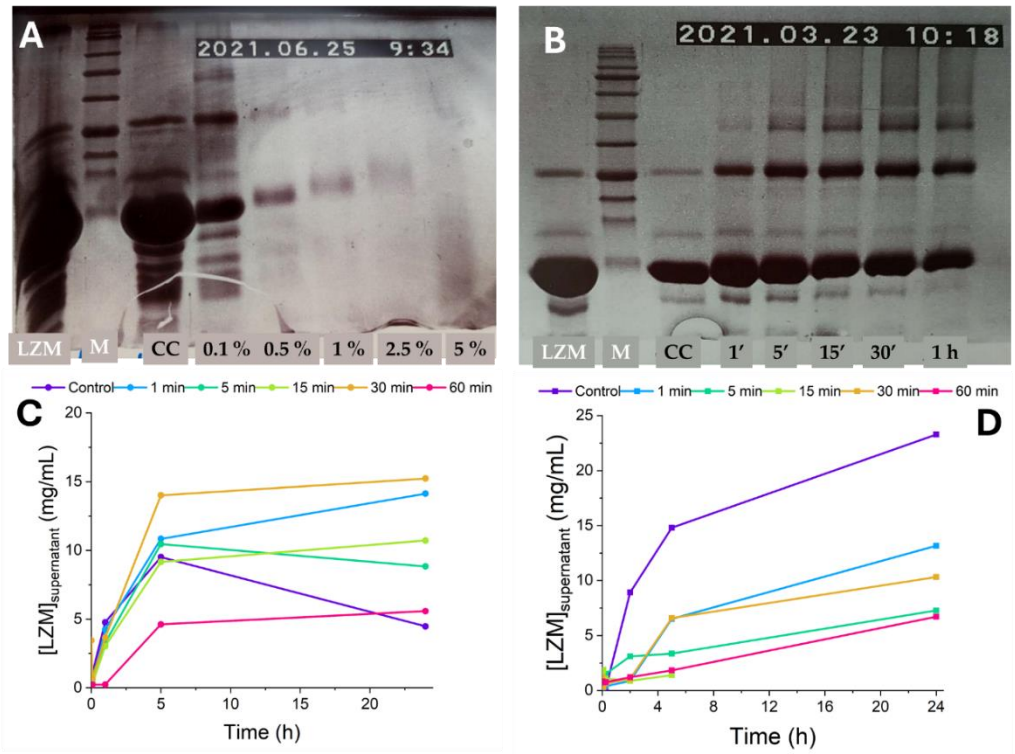

Figure 81. SDS-PAGE analysis of cross-linking degree at a) different final concentration of glutaraldehyde and b) different reaction time. Release profile of LZM crystals in c) saline at 37 °C and d in MiliQ water at 37 °C for 24 h.

The results above mentioned shows that this approach could be used to obtain materials with a highly sustained release profile over time.

3.1.2. Development of targeted design of Fmoc-MF hybrid hydrogels

Preliminary results showed the possibility to form silver nanoparticles within agarose hydrogels. Nevertheless, the lack of specific interaction sites in chemical structure of agarose led to the disappearance of nanoparticles when attempting to grow lysozyme crystals on them.

The nanoparticles destabilized in acidic environments, and the presence of NaCl favoured the formation of AgCl over the preservation of the nanoparticles.[161] Therefore the crystallization conditions required to form lysozyme crystals destabilized silver nanoparticles impeding the formation of the composite lysozyme crystals.

The findings presented in Chapter 5 have demonstrated that peptide supramolecular hydrogels can act as an effective template for plasmonic nanoparticles. Furthermore, the high chemical adaptability of peptides allows for the design of a peptide sequence incorporating metal-binding groups, which can enhance the stability of nanoparticles when coated with these molecules. It was thus resolved to synthesize a Fmoc-dipeptide comprising L-methionine and L-phenylalanine Figure 82.a (for synthesis details see Experimental Section in Chapter 8). Methionine possesses a thioether group (-SCH_3) containing sulphur (S), which exhibits a marked affinity for metal ions. The phenylalanine was selected with a view to enhancing the supramolecular interactions through the π-π stacking established between aromatic rings in different molecules. Thus, the formation of hydrogels with optimal mechanical strength is facilitated.

Furthermore, to keep the implementation of the green chemistry and biocompatible conditions, the protocol to growth the NPs was the same employed for Fmoc-FF in Chapter 5. Briefly, a basic solution of the peptide (10 mM) was mixed with a highly concentrated solution of metal precursor ($AgNO_3$ or $HAuCl_4$) to promote the self-assembly by binding metal cations to the deprotonated carboxylic acid, cross-linking different molecules, as group

[161] Xiong, S.; Cao, X.; Fang, H.; Guo, H.; Xing, B. *Sci. Total Environ.* **2021**, *775*, 145867.

previously described for other Fmoc-dipeptides and cations.[162] Subsequently, the formation of NPs was carried out by the exposition of hydrogels to sun light leading to the reduction of metal cations. In the literature it has been described that the mechanism of NPs formation is through a metal translocation from the carboxylic group to the sulphur.[163] This led to the formation of NPs anchored to the thioeter group and well-distributed in the fibers, as will be discussed below. The hydrogels changed the colour after de NPs growth, showing a dark brown colour in the case of AgNPs and dark purple in the case of AuNPs. The hydrogel without MNPs was colourless.

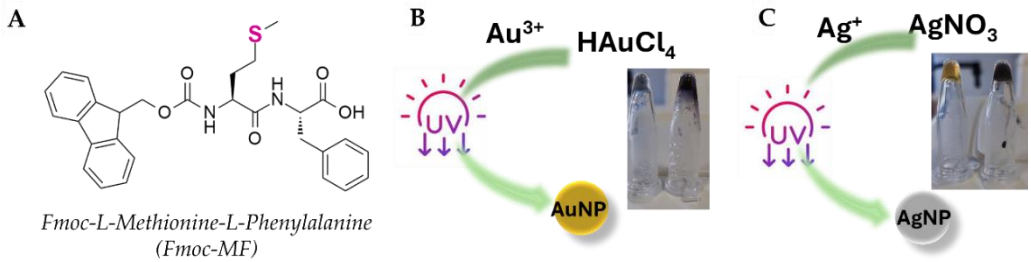

Figure 82. a) Chemical structure of Fmoc-MF. Schematic representation of the reduction process and image of hydrogels with b) AuNPs and c) AgNPs.

The formation and distribution of MNPs within the hydrogels were evaluated by TEM and ESEM. It has been tested different concentrations of precursor (0.1, 0.5 and 0.7 eq). However, while AgNPs exhibited spherical NPs in the full range, AuNPs samples with gold nanoparticles exhibited high polydispersity in size and shape when the concentration was above 0.1 eq (Figure 83). In addition, TEM images show the well distribution of MNPs and that they are completely

[162] Mañas-Torres, M. C.; Gila-Vilchez, C.; González-Vera, J. A.; Conejero-Lara, F.; Blanco, V.; Cuerva, J. M.; Lopez-Lopez, M. T.; Orte, A.; Álvarez De Cienfuegos, L. *Mater. Chem. Front.* **2021**, *5* (14), 5452–5462.

[163] Núñez-Martínez, M.; Quiñoá, E.; Freire, F. *Nanoscale* **2022**, *14* (36), 13066–13072.

associated to the fibers, with some fibers fully coating and aligning the nanoparticles. The statistical treatment of the measurements carried out in 100 MNPs showed that AgNPs have a mean size of 8.5 ± 2.4 nm and AuNPs have a mean size of 7.4 ± 2.1 nm. ESEM images (Figure XX in experimental section) showed the presence of Au and Ag in the hydrogel samples.

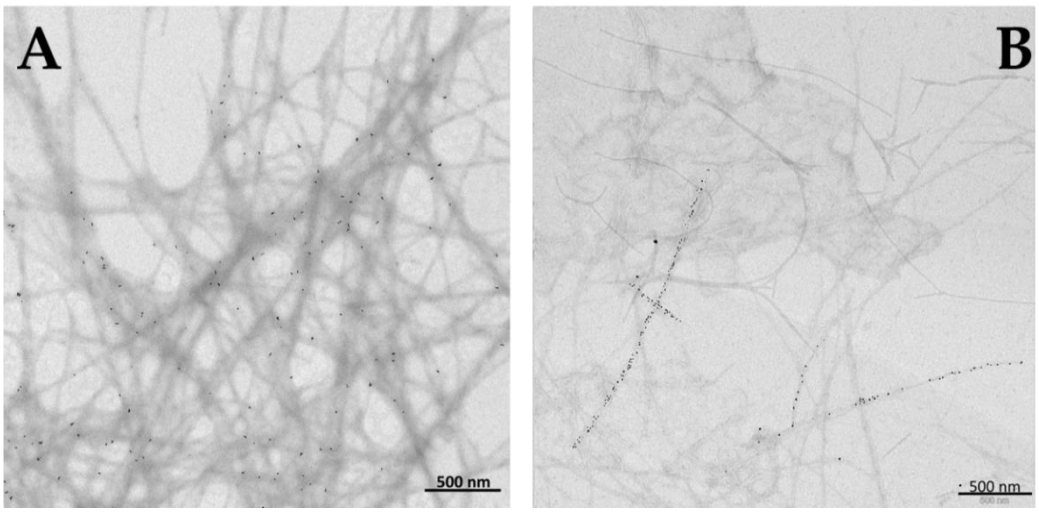

Figure 83. TEM image of Fmoc-MF hydrogels at a concentration of 5 mg/mL of peptide and a) 0.1 eq of Au^{3+} and b) 0.5 eq of Ag^{+}.

3.1.3. Obtention of protein crystals in hybrid hydrogels

Once the hybrid hydrogels were obtained and characterized, the challenge was the capability of Fmoc-MF to protect the MNPs during the crystallization step of lysozyme. The selected hybrid hydrogels for this purpose were 0.1 eq in both cases, according to the toxicity results obtained in Chapter 5. Moreover, the greater possibility that the lower the NPs concentration, the more intense the dissolution of the NPs makes these gels an interesting case of study for evaluate the effectiveness of the protection.

The growth of crystals was conducted using the counter diffusion method. In summary, once the hybrid hydrogel was formed, a solution of LZM (at a concentration double that of the desired solution and of the same volume as the gel) was permitted to diffuse through the hydrogel until the two phases reached equilibrium in terms of concentration. The process may be monitored through the use of UV-Vis spectroscopy, whereby the concentration of LZM in the supernatant may be determined. Thereafter, the protein solution was replaced with a solution of NaCl, which was allowed to diffuse for a period of approximately one week in order to facilitate crystal growth. Crystals were visible after a period of 24 to 48 hours. This method is schematically summarized in Figure 71.e.

It is noteworthy that the hydrogels maintained their colouration following the crystallization process, with the crystals displaying a subtle pigmentation. While this was encouraging, the confirmation of the presence of MNPs within the crystals was to be conducted through TEM. Consequently, the composite crystals were fully cross-linked and extracted from the hydrogel. They were then incorporated into resin and embedded in resin, subsequently cut with a microtome to facilitate examination under a transmission electron microscope.

Figure 84 show the results of TEM studies for both crystals grown in hydrogels with AgNPs and AuNPs. Both images illustrate the presence of spherical nanoparticles inside the body of the crystals. AgNPs in crystals exhibited a size of 35.3 ± 9.9 nm and AuNPs in crystal has a mean size of 21.7 ± 7.7. These values were obtained through a statistical analysis of measurements taken for 30 MNPs of each type.

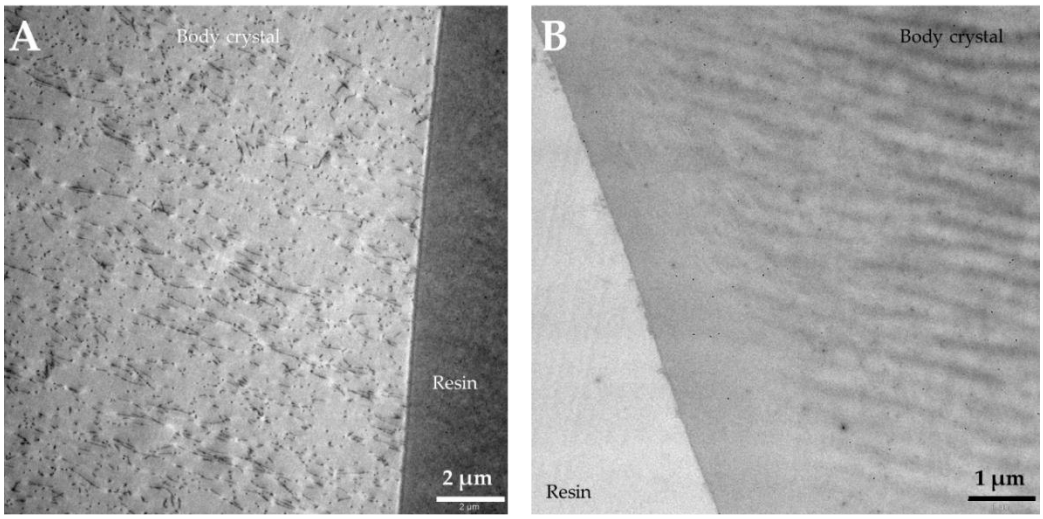

Figure 84. TEM images of LZM grown in Fmoc-MF hydrogels with a) AgNPs (0.1 eq) and b) AuNPs (0.1 eq).

3.3. Protein crystals as platforms for bioorthogonal chemistry

The last proof of the versatility of protein crystals as a material for different applications was the obtention of palladium-doped crystals to develop a biocompatible device with a high potential in bioorthogonal chemistry.

The crystals employed in this investigation were obtained through agarose gelated batch seeding, thereby ensuring a controlled size distribution. This is a highly beneficial property for their use in biomedicine, as it enables the desired size to be produced in accordance with the intended application. In summary, 1 µL of crushed crystals is added to a solution of agarose (0.2% (m/V)), lysozyme (40 mg/mL) and NaCl (2.7% (m/V)). Then the solution was cold and keep at 20 °C until the growth of desired crystals. The crushed crystals acted as seeds for the subsequent growth of crystalline structures. The last step was cross-linked and lyophilized the crystals to extract them from the hydrogel.

The pore size of the lysozyme crystals is less than 10 nm in diameter , which permits the passage of small molecules but not macromolecules (Figure 85.a).[164] It is noteworthy that these crystals are ultimately biodegraded by the organism, a process that addresses a significant challenge associated with non-degradable strategies, such as polystyrene-based catalytic devices.[165]

Palladium ion capture was subjected to a systematic optimisation process utilising a range of reagents and conditions, with the objective of obtaining materials that are functionally reproducible. The optimal functionalisation conditions were found to be the treatment of the CLLCs (with an average diameter of 250 μm) in an aqueous Na_2PdCl_4 solution (0.1 M) for a period of four days. Subsequently, two-day washing cycles were performed with distilled water to remove excess unbound Pd(II) from inside the crystals. The crystals obtained, named Pd(II)@CLLCs, exhibited an intense red colour (Figure 85.b middle). This methodology was readily scalable, allowing the production of functional materials with reproducible catalytic properties and enabling the functionalisation of batches of between 10 and 200 crystals simultaneously. *In situ* reduction of Pd(II) into Pd(0) was carried out by treatment with sodium ascorbate (NaAsc, 100 mg/mL) for 3 d at 37 ºC to generate black-coloured crystals (Figure 85.b, right), which were subsequently named Pd(0)@CLLC.

[164] Margolin, A. L.; Navia, M. A. *Angew. Chemie - Int. Ed.* **2001**, *40* (12), 2204–2222.
[165] a) Pérez-López, A. M.; Rubio-Ruiz, B.; Valero, T.; Contreras-Montoya, R.; Álvarez De Cienfuegos, L.; Sebastián, V.; Santamaría, J.; Unciti-Broceta, A. *J. Med. Chem.* **2020**, *63* (17), 9650–9659. c) Ding, Y.; Shi, L.; Wei, H. *J. Mater. Chem. B* **2014**, *2* (47), 8268–8291.

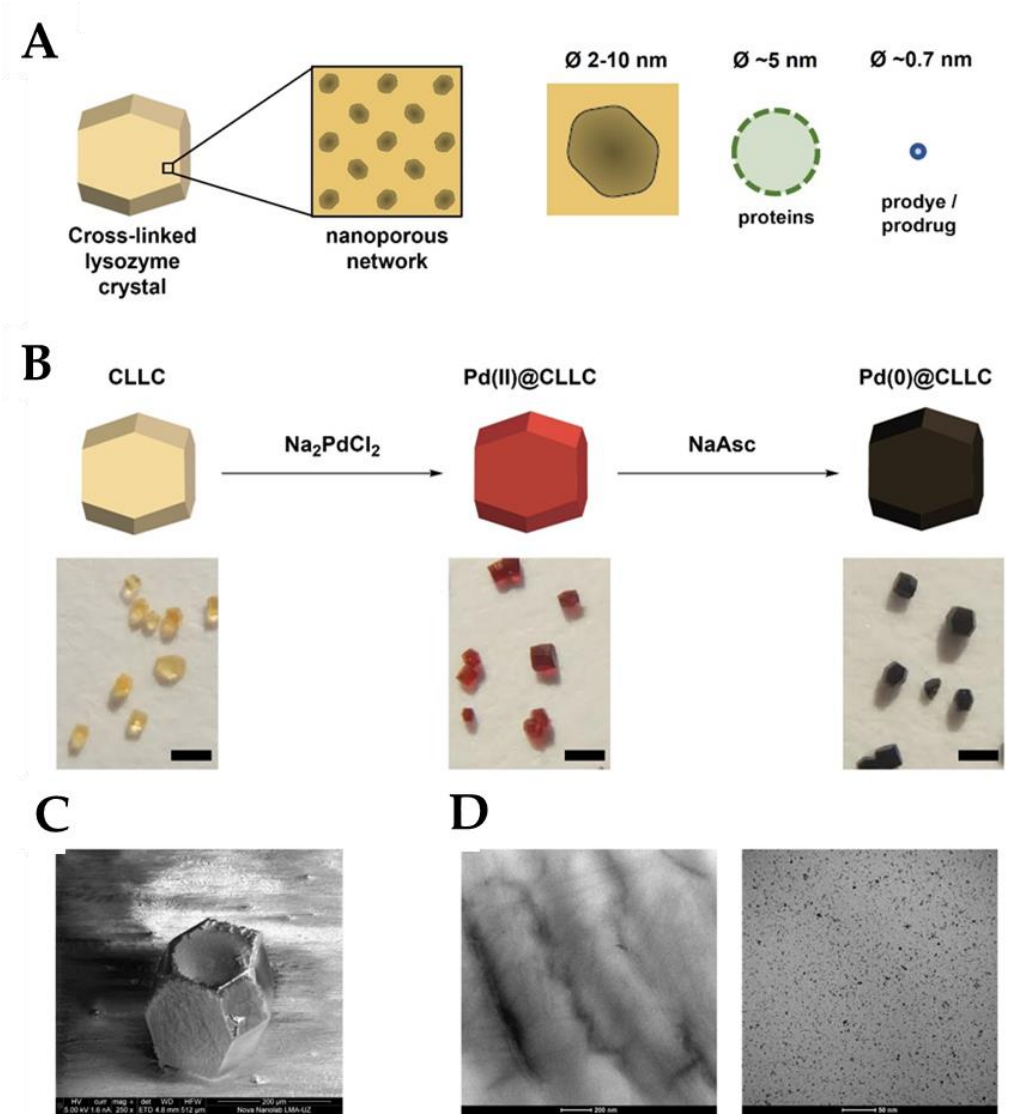

Figure 85. Synthesis and characterization of Pd(II)@CLLCs and Pd(0)@CLLCs. a, Schematic representation of a CLLC and its nanoporous network. Comparison between the diameter of a CLLC's pore with the effective transversal section of serum proteins and small molecules. b, Synthesis of Pd(II)@CLLCs and Pd(0)NPs@CLLCs and pictures of untreated and treated crystals (~250 μm in average diameter). Scale bar = 500 μm. c, SEM picture of a Pd(0)@CLLC. d, TEM pictures of an inner section of a CLLC (left) and a Pd(0)@CLLC (right). Ultra-small Pd nanoparticles can be clearly distinguished in the right picture.

To study the size, morphology and distribution of the metal nanoparticles within the crystals, the Pd(0)@CLLC were fully characterised by transmission electron

microscopy (TEM), scanning electron microscopy (SEM) coupled to an ion beam milling system and energy dispersive X-ray (EDX) analysis, and X-ray photoelectron spectroscopy (XPS) (Figure 85.c, d). Transmission electron microscopy (TEM) images confirmed the presence of ultra-small PdNPs with low polydispersity inside the crystals. This indicates that the nanoscale dimensions of the CLLC channels can effectively control the size of the nanoparticles during nucleation and growth. TEM and energy-dispersive X-ray (EDX) analysis demonstrated that the metal is uniformly distributed throughout the crystal. Inductively coupled plasma mass spectrometry (ICP-MS) analysis of the crystals revealed a Pd content of 22.5% (w/w), indicating that each crystal contains approximately 3.8 μg Pd. It is crucial to note that only a portion of this Pd content is accessible to the substrates through the channels.

Radiotherapy for head and neck cancer (HCN) has improved survival and life expectancy, but it also damages healthy tissues such as the salivary glands, causing xerostomia (chronic dry mouth). This affects quality of life because the damage to the acinar cells that produce saliva is irreversible. Although temporary palliative treatments are available, there is no permanent cure.[166]

[166] a) Destito, P.; Vidal, C.; López, F.; Mascareñas, J. L. *Chem. – A Eur. J.* **2021**, *27* (15), 4789–4816. b) Scinto, S. L.; Bilodeau, D. A.; Hincapie, R.; Lee, W.; Nguyen, S. S.; Xu, M.; *et al*. *Nat. Rev. Methods Prim. 2021 11* **2021**, *1* (1), 1–23. c) Wang, J.; Wang, X.; Fan, X.; Chen, P. R. *ACS Cent. Sci.* **2021**, *7* (6), 929–943. d) Zhang, H.; Qin, X.; Wang, J.; Ma, L.; Chen, T. *Sci. China Chem. 2023 672* **2023**, *67* (2), 428–449.

It has been demonstrated that SOX2+ progenitor cells can replace damaged acinar cells in mice, but this process is contingent upon cholinergic neuronal signals, which are altered following radiotherapy. Cholinergic agonists, such as pilocarpine and carbachol, have been shown to enhance SOX2-mediated regeneration; however, their systemic use has been associated with adverse side effects.[167]

A targeted therapy that activates cholinergic signals directly in damaged tissue may offer a viable alternative. The objective was to demonstrate the potential for SOX2-mediated epithelial regeneration by an inactive cholinergic agonist, activated *in situ* by catalytic conversion using a novel salivary gland culture assay with palladium-doped CLLC catalysts.[168]

[167] a) Emmerson, E.; May, A. J.; Berthoin, L.; Cruz-Pacheco, N.; Nathan, S.; Mattingly, A. J.; Chang, J. L.; Ryan, W. R.; Tward, A. D.; Knox, S. M. *EMBO Mol. Med.* **2018**, *10* (3). b) Knox, S. M.; Lombaert, I. M. A.; Haddox, C. L.; Abrams, S. R.; Cotrim, A.; Wilson, A. J.; Hoffman, M. P. *Nat. Commun.* **2013**, *4*.

[168] a) Emmerson, E.; May, A. J.; Berthoin, L.; Cruz-Pacheco, N.; Nathan, S.; Mattingly, A. J.; Chang, J. L.; Ryan, W. R.; Tward, A. D.; Knox, S. M. *EMBO Mol. Med.* **2018**, *10* (3). b) Rocchi, C.; Emmerson, E. *Trends Mol. Med.* **2020**, *26* (7), 649–669. c) Kapourani, A.; Kontogiannopoulos, K. N.; Barmpalexis, P. *Pharm. 2022, Vol. 15, Page 762* **2022**, *15* (6), 762.

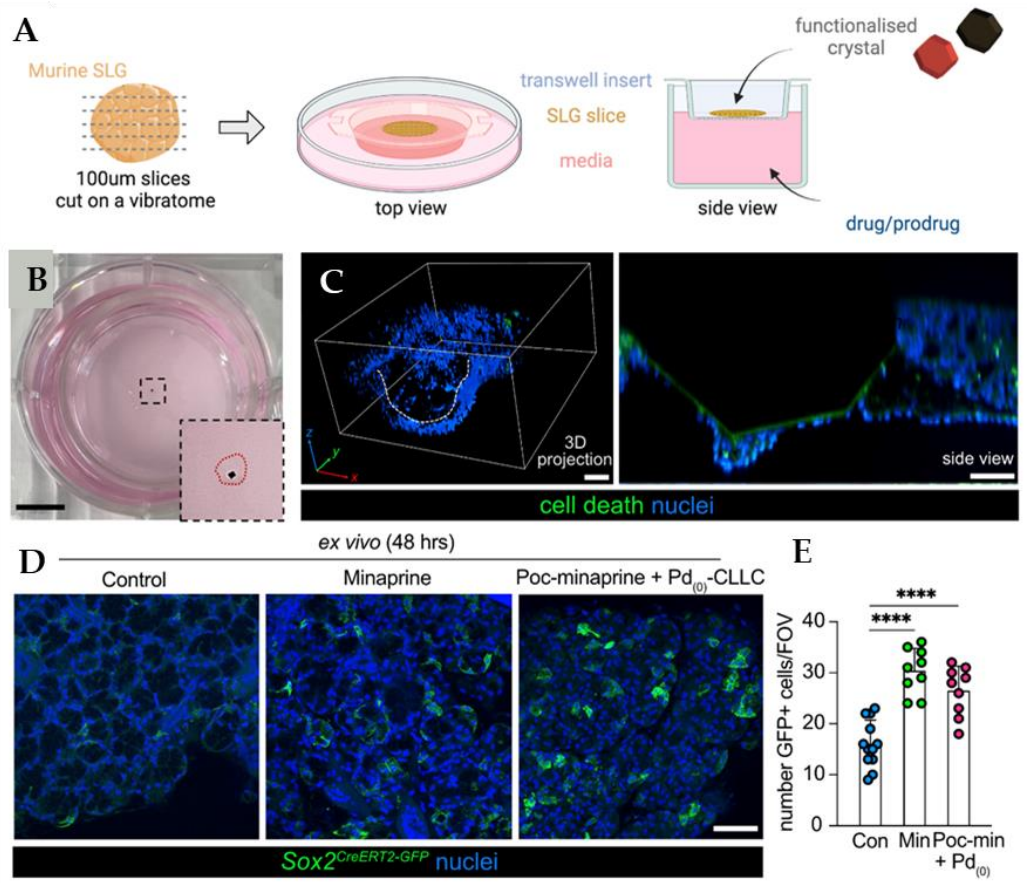

Figure 86. a) Schematic of the salivary gland organotypic slice culture assay. b). Image of a single well of the organotypic slice culture assay. The black dashed line indicates the area which is presented as a magnified view in the inset image in the bottom right. The red dashed line outlines the organotypic slice, with the black crystal situated in the middle of the tissue. Scale bar = 1cm. c) 3D projection (left) and side view (right) of an organotypic slice after 48 h in culture stained for cell death (NucView; Casp3/7) and nuclei. Scale bar = 50⊚m. d) Representative images of SMG slices from Sox2CreERT2; R26mTmG mice treated with saline, minaprine or prodrug + Pd(0)@CLLC and analysed after 48 h. Scale bar = 50⊚m. . Enumeration of GFP+ cells from Sox2CreERT2; R26mTmG SMG slices treated with saline, minaprine or prodrug + Pd(0)@CLLC and analyzed after 48 h. **** $p<0.0001$.

The efficiency of palladium-doped crystals was evaluated with a prodrug, synthesized and tested in the group of Professor Unciti Broceta. The stability of the prodrug in physiological media and the in vitro conversion to minaprine was investigated using Pd(0)@CLLC with liquid chromatography. The molecule demonstrated complete stability at 37°C for up to four days. The decapsulation experiment was conducted at 37 °C in an aqueous solution (200 μL) of prodrug (100 μM) in the presence of Pd(0)@CLLCs for 24 h, and the results were analysed by HPLC-MS-ELSD. The reaction yielded an estimated 9.5 μM of active drug, with an estimated unencapsulated drug per crystal of approximately 0.4 μM. The Pd(II)@CLLCs did not yield comparable levels of uncapsulation, even with an increasing number of crystals employed (up to 86 per experiment). This phenomenon may be attributed to the chelating characteristics of the Pd(II) atoms, which have the potential to coordinate and trap minaprin within the crystal. This phenomenon has been previously observed with other small molecules that possess two or more positively charged amino groups.

Salivary glands are composed of a wide range of cell types and structures, making in vitro cell models insufficient to represent the complexity of this tissue. Therefore, a novel ex vivo model was used, consisting of thin slices of sublingual glands (SLG) from modified mice, to investigate the *in situ* release of minaprine using catalysts embedded in the salivary gland (Figure 3A). Freshly extracted SLG were sliced with a vibratome and cultured at an air-liquid interface. Given the ability of catalytic crystals to produce significant levels of minaprine in a relatively large volume, it was considered that local minaprine generation from a single crystal in the gland's center could mimic cholinergic signals from a nerve ending. Thus, a single Pd(II)@CLLC or Pd(0)@CLLC crystal was implanted per gland (Figure 86.a, e). Minaprine or the prodrug was administered in the

medium under the tissue. After 48 hours, slices were stained to identify surface markers and assess cell viability, and images were taken. 3D imaging clearly showed the area lacking nuclei where the crystal was located (Figure 86.f). Subsequently, the proliferation of SOX2+ acinar cells was measured by analysing the number of GFP-expressing cells using confocal microscopy.

As anticipated, a 2-day treatment with either the prodrug alone or Pd-functionalized crystals alone (catalyst) showed no increase in GFP+ cell . However, when the prodrug was applied to SLG slices containing an embedded Pd(0)@CLLC, there was a significant rise in GFP+ cells compared to the untreated control, resulting in a comparable number of differentiated cells to the positive control, minaprine. In line with the HPLC findings, Pd(II)@CLLC did not enhance the proportion of GFP+ cells. Notably, no heightened cell death was detected in the presence of the prodrug, catalytic crystals, or both together, when compared to control slices after 48 hours in culture. This study confirmed the effectiveness and biocompatibility of this Pd-mediated prodrug approach and validated the proof-of-concept for this local stem cell differentiation method.

4. Conclusions

1. Synergistic influence of multiple supramolecular chiral media can induce non-trivial features in the CISS effect that are not observed in the homochiral case. A detailed comparison between both cases has revealed three non-trivial changes:
   1.1. Enhancement of the CISS signal (Δ) due to a synergistic role played by multiple chiral sources.
   1.2. Sign reversal of the CISS signal as a function of temperature
   1.3. Persistence of the CISS signal at higher temperatures.
2. Controlling the degree of cross-linking has been shown to be an effective method for obtaining crystals with tuneable release profiles.
3. The strong and specific interaction between thioether groups on Fmoc-MF and plasmonic nanoparticles has been shown to enhance the incorporation of AgNPs and AuNPs into LZM crystals. Consequently, LZM serves as an effective drug delivery vehicle due to its antibacterial properties and ability to host metal nanoparticles.
4. It has been developed a robust catalytic system by the functionalization of CLLCs with Pd catalysts following a mild green two-step procedure. The catalyst scaffold was selected because of its porosity to restrict molecule entry by function of their dimensions. Various small molecule substrates were efficiently transformed by the catalytic devices, both under physiological conditions and in the presence of complex media.
5. A Pd-activatable prodrug of a muscarinic agonist has been tested, which, due to its high toxicity, cannot be used directly. The prodrug remains inactive in its caged form; however, it can be activated by a single Pd(0)@CLLC to release

the active drug, thereby inducing stem cell differentiation into saliva-producing acinar cells in an ex vivo model.

Chapter 7

General conclusions

General conclusions

The results exposed along this doctoral thesis highlight the versatility of ***peptide supramolecular hydrogels*** both regarding open the door to new applications fields and expanding this application in fields where they are well-established. Therefore, some general conclusions can be settled from bringing together all the results achieved, answering each general objective which was proposed.

Thus, the general conclusions that it can be extracted are as follows:

1. Control and hybrid hydrogels has been successfully synthesized.
2. Physicochemical properties of these hydrogels have been established and have expanded their areas of application.
   2.1. Hybrid hydrogels containing carbon allotropes have been successfully applied in the study of the CISS effect.
   2.2. Hybrid hydrogels doped with plasmonic nanoparticles of gold and silver (AuNPs and AgNPs, respectively) have been tested and have been demonstrated to possess not only a high antibacterial capacity, but also activity against fungal infections and biofilms. Furthermore, they have exhibited high biocompatibility and have been evaluated in both *in vitro* and *in vivo* systems.
3. Finally, the application of hybrid hydrogels as templates for the growth of inorganic crystals (MOFs) and protein crystals has led to:
   3.1. The development of two new families of bio-MOFs (Fmoc-FF@ZIF-8 and Fmoc-FF@MOF-808). Furthermore, the potential of this family as a bioremediation agent has been extensively evaluated, demonstrating nearly 100 % efficiency in removing phosphates from aqueous

environments. In addition, its efficacy in degrading the highly toxic pesticide methyl paraoxon has significantly improved, exhibiting a threefold increase than for the MOF-808 grown in water.

3.2. The obtention of composite protein crystals has enabled the design of multi-component solid systems that can be deployed in a variety of fields of application:

3.2.1. Lysozyme crystals grown in hydrogels with singled-walled carbon nanotubes have been employed to study the CISS effect.

3.2.2. A targeted design hydrogel has been employed as a template and protective agent for silver and gold plasmonic nanoparticles, thereby facilitating the growth of lysozyme crystals doped with these nanoparticles. Furthermore, a controlled dissolution strategy was assessed for its potential to facilitate the utilisation of these materials as broad-spectrum antibacterial agents with sustained release.

3.2.3. At last, lysozyme crystals of a predetermined size have been developed as biocompatible support for palladium catalysts for bioorthogonal chemistry.

Chapter 8

Experimental Section

1. Reagents

General

N-Fluorenyl methoxycarbonyl-L-diphenylalanine (Fmoc-FF(L)) and N-Fluorenyl methoxycarbonyl-D-diphenylalanine (Fmoc-FF(D)) were purchased from LifeTein, USA, and were used without further purification. N-Fluorenyl methoxycarbonyl-diglycine (Fmoc-GG) was purchased from Fluorochem, UK, and was used without further purification. Sodium hydroxide was purchased from Merck, Germany. D-(+)-Glucono-1,5-lactone (99%) was purchased from Alfa Aesar, Germany.

CISS effect studies

Sodium carbonate (≥99.9%) (Na_2CO_3, for analysis) was purchased from Alfa Aesar, Germany. Carbon nanotubes (single-walled (6,5) chirality; CAS 308068-56-6) were provided by Sigma-Aldrich, USA. Carbon nanotube, double walled, CAS: 308068-56-6 were provided by Sigma-Aldrich, USA. Carbon nanotube, multi walled, Product ref.: Nanocyl-3100 were provided by Nanocyl S.A., Belgium. As purchased SLG samples (Alfa Chemistry, CAS No.: 7782−42−5), prepared by thermal exfoliation reduction and hydrogen reduction of graphite oxide (GO), consist of one to five atomic layers of graphene with a typical flake size of ~0.5−5μm. The oxygen content is estimated to be ~7−7.5%. The MLG samples were procured from TCI Europe (product code: G0442, CAS No.: 1034343−98−0) and are 6−8 nm thick nanoplatelets with a width of~15 μm. No exfoliation step has been employed for the MLG samples; hence, it is expected that the chiral functionalization (described below) occurs only on the surface,

whereas the inner layers remain impervious to it. This allows an investigation of the effect of sample thickness on the observed behaviour.

Development of new MOFs biocomposites

Zinc acetate ($Zn(AcO)_2 \cdot 2H_2O$), 2-methylimidazole (HmIm), zirconium (IV) tetrachloride ($ZrCl_4$), trimesic acid, and methyl paraoxon were purchased from Sigma- Aldrich. Formic acid (98%) was purchased from Acros Organics.

Antibacterial activity

N-Fluorenyl methoxycarbonyl-arginine-glycine-aspartic acid (Fmoc-RGD) was purchased from SynPeptide Shanghai, China, and Hydrolyzed collagen was purchased from Guinama, Spain. All gellators were used without further purification. Gold(III) chloride trihydrate ($HAuCl4 \cdot 3H2O$) was purchased from Sigma-Aldrich and silver nitrate ($AgNO3$) was purchased from Scharlau.

Protein crystals

2. General procedures

Peptide basic solutions

Fmoc-FF(L/D) and Fmoc-GG peptides were weighed separately into a vial, and deionized water was added to obtain a final concentration of 10 mM. The suspension was sonicated (in a HSt Powersonic 603 ultrasonic bath) for 1 h. Then, a NaOH solution (0.5 M) was added dropwise until a clear solution (pH 10.5) was obtained. The pH was measured using a HACH sension+ PH 3 pH meter. The pH meter was calibrated using pH 4, 7, and 10 buffer solutions.

Circular Dichroism (CD)

The CD spectra were recorded using a Jasco J-815 spectropolarimeter with a 150 W xenon lamp. The hydrogels were gelified into a 0.1 mm quartz cell (Hellma 0.1 mm quartz Suprasil) using the protocol described above. Spectra were obtained from 210 to 350 nm with a 1 nm step and 0.5 s integration time per step at 20 °C.

Transmission Electron Microscopy (TEM)

Dried gels (xerogels) were studied using a LIBRA 120 PLUS Carl Zeiss. Hydrogels were vortexed and diluted twice with water. A drop of the fiber suspension obtained was placed on a 300-mesh copper grid. The sample was dried at room temperature for 24 h.

High-Resolution Scanning Electron Microscopy (HR-SEM)

Samples were deposited on SEM supports and then were coated with a fine carbon layer and examined by SEM using Carl Zeiss SMT, AURIGA (FIB-FESEM), equipment to acquire EDX data.

Environmental Scanning Electron Microscopy (ESEM)

Refrigerated samples of peptide hydrogels were examined by ESEM using an FEI Quanta 400 equipped with a Peltier effect cooling stage.

3. Chapter 3. CISS effect

3.1. General procedures

Hydrogel Control Preparation

Gelation was induced by adding 2 mol equiv of glucono-δ-lactone (GdL) or a 25 mM final concentration of sodium carbonate (Na2CO3), depending on the case, and mixing was carried out by vortexing.

Composite solutions preparation

1. Carbon nanotubes (CNTs)

To prepare solution of peptides with carbon nanotubes, 0.7 mg of each CNT were weighed separately into a vial tube. The carbon nanotubes were suspended in 1 mL of an aqueous basic solution of: Fmoc-L-FF or Fmoc-D-FF (prepared above). The suspension was sonicated for 2.5 h in a cold ultrasonic bath and then centrifuged for 5 min at 10.000 rpm (Sigma 1-14 centrifuge). Finally, the supernatant was collected carefully.

2. Graphene layers (LG)

To prepare the graphene flake peptide solution (SLG or MLG), 0.7 mg of each graphene flake was separately weighed in a vial tube. The graphene flakes were suspended in 1 mL of a basic aqueous solution of Fmoc-FF (L/D) or Fmoc-GG (prepared above). The suspension was sonicated for 2.5 h in a cold ultrasonic bath and then centrifuged for 5 min at 10 000 rpm (Sigma 1−14 centrifuge). Finally, the supernatant was carefully collected.

Composite Hydrogel Preparation.

1. Carbon nanotubes (CNTs)

To prepare hydrogels with carbon nanotubes, 0.7 mg of chiral SWCNTs was weighed into a vial tube. The carbon nanotubes were suspended in 1 mL of a 10 mM aqueous basic solution of Fmoc-FF(L/D) or Fmoc-GG (prepared above). The suspension was sonicated for 2 h in a cold ultrasonic bath and then centrifuged for 5 min at 10000 rpm (Sigma 1-14 centrifuge). Finally, the supernatant was collected carefully. Gelation was then carried out following the same method described above for the hydrogel control.

2. Graphene layers (LG)

Final hydrogels were obtained using GdL (glucono-δ-lactone) as a gelling agent for the Fmoc-FF + SLG/MLG composite solutions by adding 2 mol equivalents of GdL and mixing by vortexing.12 Fmoc-GG + SLG/MLG hydrogels were obtained using Na2CO3 as a gelling agent by adding a final concentration of 25 mM sodium carbonate and mixed by vortexing.

Raman Microscopy

Raman spectra of commercial carbon nanotubes were collected on a Raman microscope NRS-5100 (JASCO, Japan) equipped with a Peltier cooled charge-coupled device (CCD) (1064 x 256 pixels) detector. The excitation line, provided by a diode laser emitting at 532 nm, was focused on the surface of the sample through a 100x objective lens. The spectral resolution was 2.1 cm-1 and each spectrum resulted from the average of 3 acquisitions, with 50 s of accumulation each. The samples were deposited on glass slides directly from the bottle and crushed to form a thin film.

CD spectra

The CD spectra were recorded using a Jasco J-815 spectropolarimeter with a xenon lamp of 150 W. The samples were measured into a 0.1 mm quartz cell (Hellma 0.1 mm quartz Suprasils) and the spectra were obtained from 200 to 350 nm with a 1 nm step and 1 s integration time per step at 20 ºC. Measurements were performed with a 1:1 dilution ratio of peptide basic solutions or composite solutions in MiliQ water to keep sample absorbance below 2.

Transmission electron microscopy (TEM)

For TEM, the samples were sonicated for 10 min and then drop cast onto a TEM Cu grid, coated with lacey carbon film. After 24 h drying in a normal atmosphere, the grid was mounted on the JEM-ARM200cfS/ TEM, to obtain the TEM images.

Number of measurements of CISS devices

Multiple samples (~10) of each tube type of carbon allotropes have been tested, and each sample has been scanned multiple times.

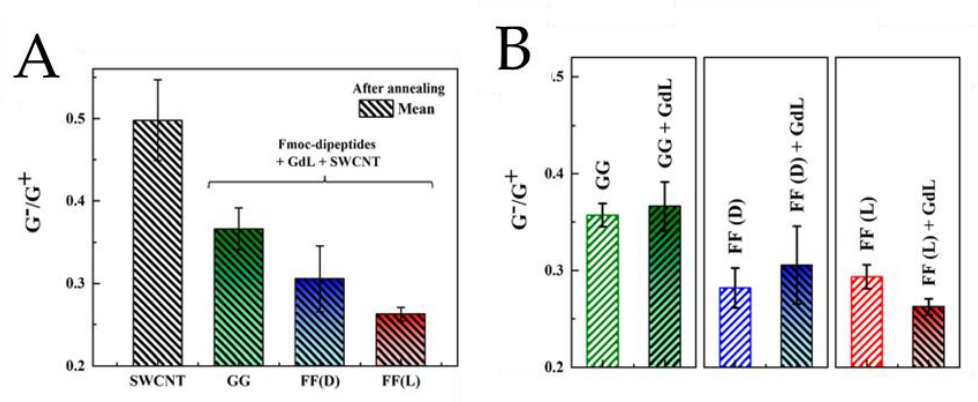

Figure 87. a) Ratio G^-/G^+ for raw SWCNT in comparison with supramolecularly functionalized SWCNT and b) comparative ratio G^-/G^+ between gelation promoted by Na_2CO_3 and GdL.

3.2. Influence of GdL

Rheology

Mechanical properties were characterized under oscillatory shear stress at a temperature of 25.0 ± 0.1 °C, using a Haake MARS III controlled-stress rheometer (Thermo Fisher Scientific, Waltham, MA, USA), provided with a plate−plate sensor 35 mm of diameter. For the rheological characterization of the hydrogels under shear, we first subjected the samples to frequency sweep tests of fixed stress (P0 = 1 Pa for GdL gels and P0 = 0.5 Pa for Na_2CO_3 gels) within the linear viscoelastic region (LVR) and increasing frequency in the range 0.1−10 Hz. We carried out at least three repetitions for different aliquots.

Supporting information

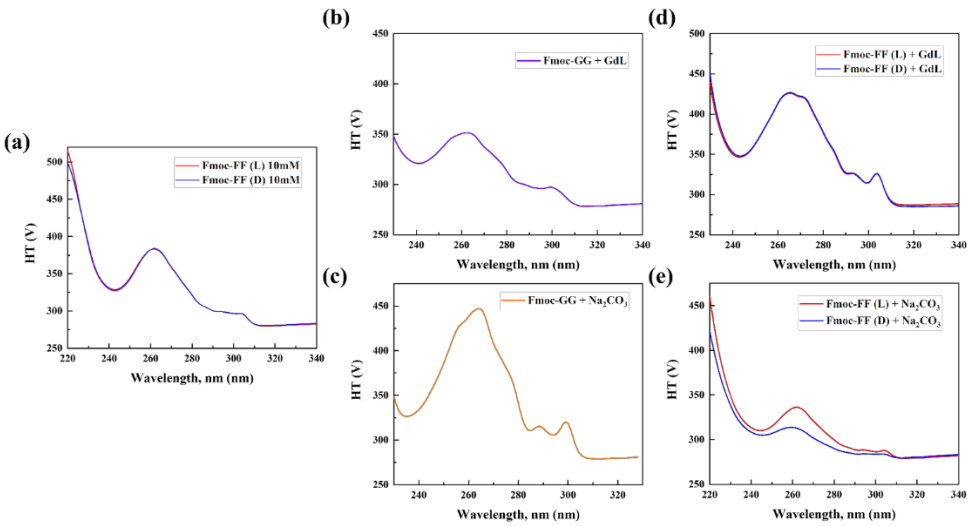

Figure 88. HT spectra.

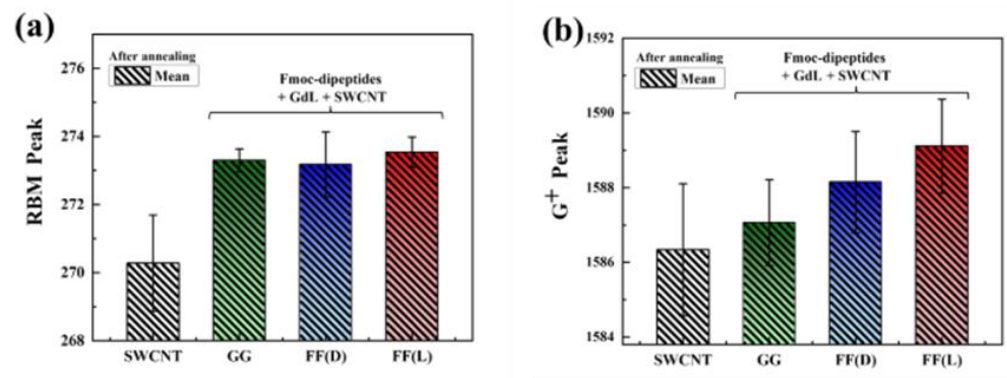

Figure 89. (a) Shift of RBM peak as a result of functionalization. (b) Shift of the G+ peak location due to functionalization. The shift is more in the case of Fmoc-FF.

3.3. Transverse magnetoconductance in two-terminal chiral spin-selective devices

Supporting information

Estimation of conductance values in linear region

According to the literature, they can be calculated as follows: [169]

$$I^{D/L}(\pm m, V) = \sum_{i=1,2,3,\ldots} G_i^{D/L}(\pm m)V^i$$

Equation 3. Linear region conductance.

Where D/L represents sample chirality and, for the linear range (small voltage), it can be simplified to:

$$I^{D/L}(\pm m, V) = G_1^{D/L}(\pm m)V^i$$

Equation 4. Simplified linear region conductance

Current difference between both enantiomers

This current difference between the two enantiomers can be calculated as:

$$\Delta I^{D/L} = \sum_{i=2,3,4,\ldots} \Delta G_i^{D/L} V^i$$

Equation 5. ΔI

Where $\Delta G_i = G_i(+m) - G_i(-m)$ and $\Delta G_1 = G_1(+m) - G_1(-m) = 0$, since $G_1(+m) = G_1(-m)$.

[169] Huisman, K. H.; Thijssen, J. M. *J. Phys. Chem. C* **2021**, *125* (42), 23364–23369.

HT values correspond to CD spectra

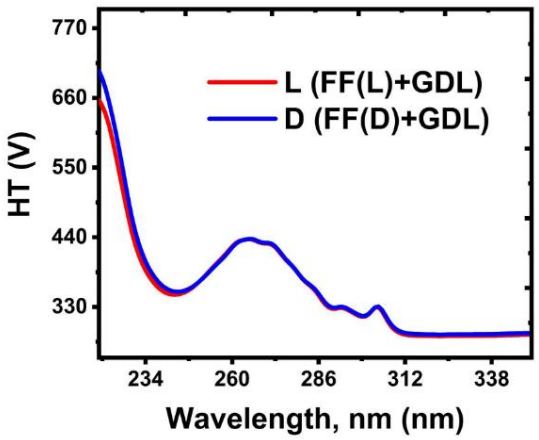

Figure 90. HT spectra of Fmoc-FF (L/D) hydrogels formed in presence of GdL

3.4. Role of spin-orbit coupling on the CISS effect signal

Supporting information

Mathematica expression for the calculation of asymmetric and symmetric components of the MR response

$$R^{Sym/Assym} = \frac{R(B) \pm R(-B)}{2}$$

Equation 6. Asymmetric and symmetric components of MR response.

And their magnitudes are calculated as:

$$\delta^{Sym} = R^{Sym}(0) - R^{Sym}(\pm 10\ kG)$$

Equation 7. Magnitude of the symmetric components of MR response.

$$\delta^{Asym} = R^{Asym}(+10\ kG) - R^{Asym}(-10\ kG)$$

Equation 8. Magnitude of the asymmetric components of MR response.

Experimental estimation of the diameter of SWCNTs and DWCNTs

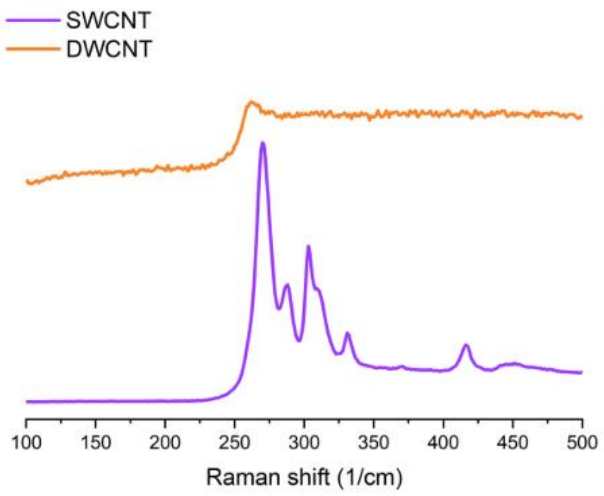

Figure 91. Raman RBM mode of raw SWCNTs and raw DWCNTs, taken at 532 nm laser. Raw MWCNTs did not show any detectable RBM signal.

Using RBM frequency ωRBM, we used the following formula to estimate the diameter dt of the raw CNTs:1 ωRBM = A/dt + B where A and B have values of ~234 nm.cm^{-1}, and ~10 cm^{-1} for SWCNTs. For DWCNTs, the parameter B is zero. Using ωRBM ~ 260–330 cm^{-1} for SWCNTs from Figure 91, we obtain SWCNT diameter dt ~ 0.73 – 0.92 nm, resulting in an average SWCNT diameter of ~ 0.82 nm, which also matches closely with vendor specification. Using ωRBM ~ 260 cm^{-1} for DWCNTs from Figure S1, we obtain DWCNT diameter dt ~ 0.9 nm. However, presence of larger diameter DW tubes is possible, which are not detected in the RBM scan above.

Mathematical expression for the calculation of CISS signal

$$\delta^{CISS} = \frac{R(-10\ kG) - R(+10\ kG)}{\min\left(R(\pm 10\ kG)\right)} x100$$

Equation 9. CISS signal.

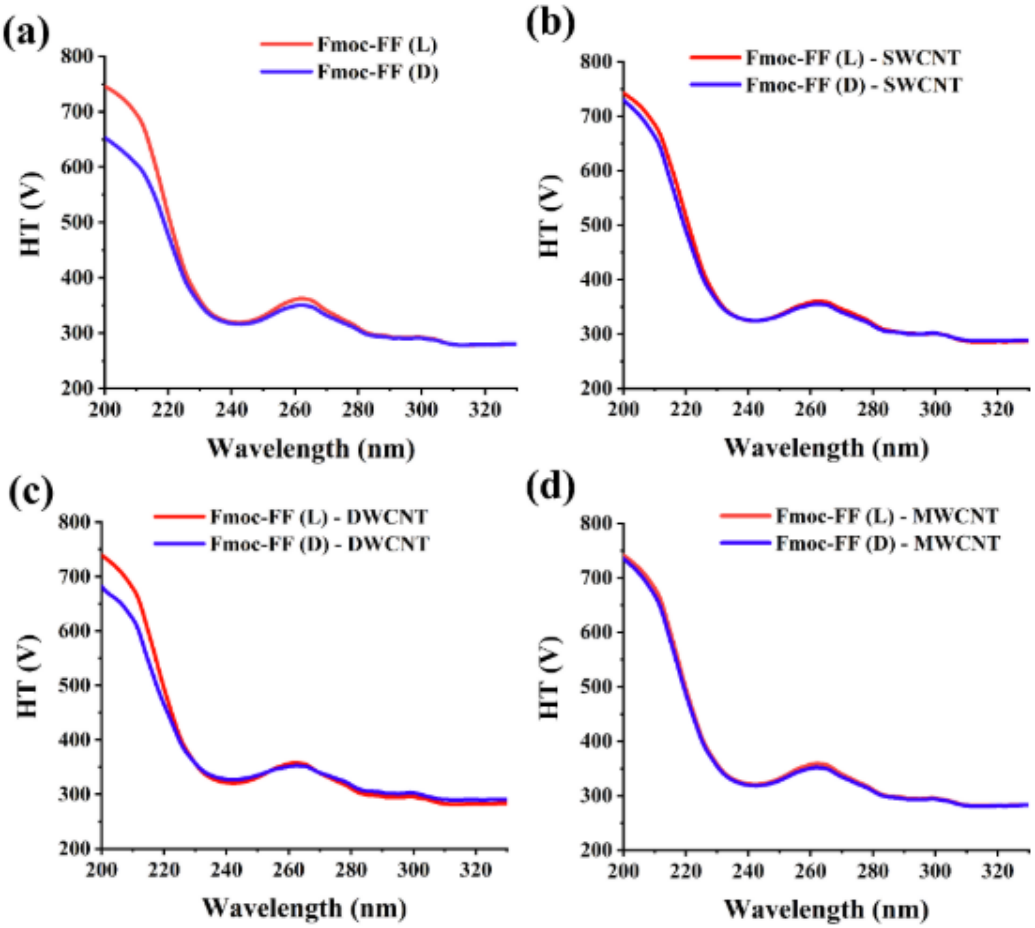

Figure 92. HT spectra.

3.5. CISS effect in functionalized graphene layers

Supporting information

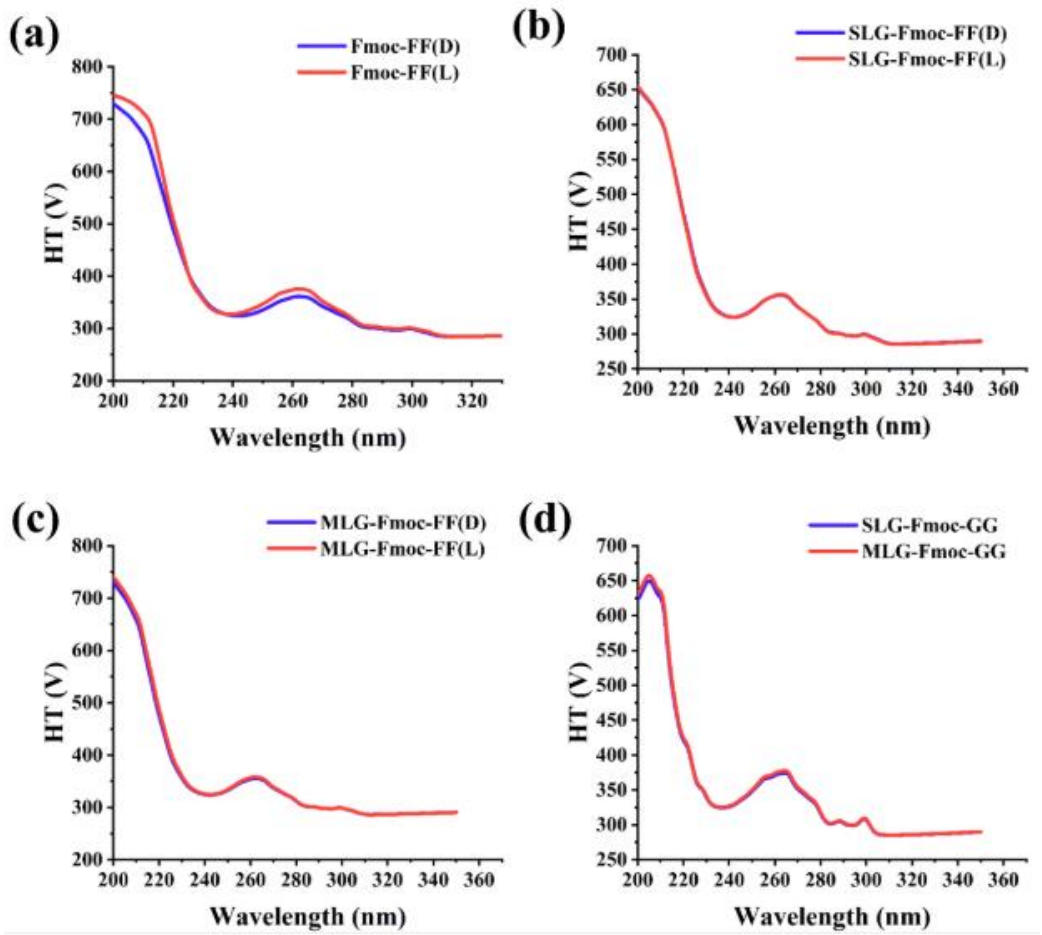

Figure 93. HT spectra.

4. Chapter 4. Bio-MOFs

In Situ ZIF-8 Growth by Diffusion of HmIm.

Gelation of the peptide's basic solution was induced by adding an aqueous solution of $Zn(OAc)_2$ (300 mM) to obtain a Zn^{2+} final concentration of 50 mM. Gelation was completed instantaneously, determined by test tube inversion. After 30 min, an aqueous solution of HmIm was added on top of the Zn hydrogel, allowing it to diffuse for 24 h. Different ratios of HmIm/Zn were evaluated, and 2:1 and 5:1 ratios were selected, in which the amount of HmIm was 100 mM for 2:1 and 250 mM for 5:1. After adding $Zn(OAc)_2$, the pH of the solution was 7.1 and 6.9 after the formation of ZIF-8. These pH values were equal to those obtained in the formation of ZIF-8 in water. The system was kept at 37 °C for 1 week to reach equilibrium, as described in water, although after 24 h, a white precipitate appeared.

In situ ZIF-8 growth by simultaneous promotion of peptide self-assembly.

The peptide solution (20 or 30 mM initial peptide concentration) was mixed with an aqueous solution of HmIm (1,8 M) at pH = 10.7 to obtain a mixture with a final peptide concentration of 10 or 20 mM and 100 mM (2:1 ratio) or 250 mM (5:1) mM of HmIm, respectively. Then, an aqueous solution of $Zn(OAc)_2$ (300 mM) was added to trigger gel formation (a Zn^{2+} final concentration of 50 mM). Different ratios of HmIm/Zn were evaluated, and 2:1 and 5:1 ratios were selected. The pH after adding the $Zn(AcO)_2$ solution was 7.1, equal to the pH obtained in the formation of ZIF-8 in water. The system was kept at 37 °C for 1 week to reach equilibrium, although a white precipitate appeared after 24 h.

Formation of Zr6 Oxoclusters.

The synthesis of $Zr_6O_4(OH)_4(OAc)_{12}$ clusters was carried out following a described protocol.[170] In brief, 1 g of zirconium tetrachloride ($ZrCl_4$), 1.67 mL of acetic acid, and 2.67 mL of 2-propanol were heated in a Schlenk flask at 120 °C for 1 h. The white precipitate was washed with 2-propanol and recovered by filtration (see Figure 104 for XRPD of the Zr_6 oxocluster).

In Situ MOF-808 Growth by Simultaneous Promotion of Peptide Self-Assembly.

For a final volume of 500 μL, 37.5 mg of $Zr_6O_4(OH)_4(OAc)_{12}$ clusters was added. Formic acid (10 mM final concentration) was added to the clusters and mixed by vortexing. To this solution, water was added and mixed until a completely clear solution was obtained. Finally, trimesic acid (0.03 mM) was added to this solution and mixed. To obtain the gel, a basic solution of Fmoc- FF (for 10 mM final concentration) was added and mixed quickly, giving rise to a hydrogel after 15 min. The system was kept at 37 °C for 1 week until equilibrium was reached, although a white precipitate appeared after 24 h.

In order to quantify the amount of MOF-808 in the MOF-gel biocomposite, 20 mg of the lyophilized MOF-808-gel composite was digested in 600 μL of NaOD 1 M for 24 h at 25 °C. Afterward, 3 μL of N,N-dimethylacetamide (DMA, final concentration 0.029 M) was added as an internal standard and the concentration of trimesate ions in the solution was determined by ^{1}H NMR spectroscopy in a 400 MHz Bruker Nanobay AVANCE III HD spectrometer (CIC, University of

[170] Dai, S.; Simms, C.; Dovgaliuk, I.; Patriarche, G.; Tissot, A.; Parac-Vogt, T. N.; Serre, C. *Chem. Mater.* **2021**, *33* (17), 7057–7066.

Granada) (Figure 105). The results indicate that the MOF-808-gel biocomposite contains 0.22 mmol per gram of material (dry basis).

Phosphate Adsorption Experiments.

In the case of the phosphate adsorption experiments performed with the materials in the gel state, 100 μL of the MOF-808-gel biocomposite (10 mM of Fmoc-FF) and 100 μL of Fmoc-FF (10 mM of Fmoc-FF) were formed for 1 week, following the protocol described above. 900 μL of an aqueous solution of K2HPO4 (0.41 mM) was added on the top of the gel, and the mixtures were kept under orbital shaking at 25 °C for 1, 3, 6, and 24 h. At each time, 100 μL of the supernatant was collected by centrifugation (9168g/15 min) and diluted with 900 μL of water. The phosphate concentration in the solutions was determined spectrophotometrically by means of the molybdenum blue method,58 using the absorbance maximum at λ = 880 nm. The UV−vis spectra were collected on a Shimadzu UV spectropho- tometer. All the experiments were performed in triplicate.

For the phosphate adsorption experiments performed with the dried samples, aqueous solutions of K_2HPO_4 (0.08 mM, 1 mL) were mixed with 0.11 mg of the dry gel (10 mM Fmoc-FF), 0.11 mg of dry MOF-808-gel biocomposite (10 mM Fmoc-FF, corresponding to 0.024 μmol MOF-808), or 0.11 mg of MOF-808 (0.080 μmol). The suspensions were shaken at 25 °C for 1, 3, 6, and 24 h. At each time, 800 μL of the supernatant was collected by centrifugation (9168 g/15 min). The concentration of phosphate ions was determined spectrophotometrically by means of the molybdenum blue method as explained above. All the experiments were performed in triplicate.

Methyl paraoxon Degradation Studies.

Aqueous solutions of methyl paraoxon (0.16 mM) were mixed with 0.22 mg of the dry gel (10 mM Fmoc-FF), 0.22 mg of the MOF-808-gel biocomposite (containing 0.05 μmol MOF-808), and 0.22 mg of MOF-808 (0.16 μmol). The suspensions were shaken at 25 °C for 1, 3, 6, and 24 h. Each time, the supernatant was collected by centrifugation (9168g/15 min) and analyzed by means of a high-performance liquid chromatography instrument equipped with a DAD detector, Thermo Fisher Scientific SpectraSystem UV-8000, column: silica-based Hypersil GOLD C18 (100 × 4.6 mm I.D., 5 μm particle size, mobile phases: water (A) and acetonitrile (B), gradient: 5–95% B over 15 min, flow rate: 0.8 mL min^{-1}, volume of injection: 100 μL). The methyl paraoxon concentration in the supernatants was determined spectrophotometrically (λmax = 271 nm). All the experiments were performed in triplicate.

MOF Particle Size Analysis.

Particle size distribution was measured from SEM images using ImageJ 1.47 software. Data were processed with Excel to calculate mean values and standard deviation. Results were expressed as the average size of 100 crystals per sample. In each analyzed image, all crystals with at least one defined face were measured taking the diagonal length of the biggest exposed face.

Rheological Characterization of Hydrogels

Mechanical properties were characterized under oscillatory shear stress using a Bohlin CS10 controlled-stress rheometer (UK) provided with a plate−plate geometry 40 mm in diameter. We subjected the samples to frequency sweep tests of fixed shear stress ($\tau 0$ = 1 Pa) within the linear viscoelastic region (LVR) and increasing frequency in the range of 0.1−10 Hz. From these measurements, we obtained the storage (G′) and loss (G″) moduli of the samples as a function of frequency within the LVR (mechanical spectra). Three different samples were measured to ensure the statistical significance of the results. The mean values and standard deviations of each magnitude were provided in this work. Gelation kinetics were investigated by oscillatory shear under fixed stress ($\tau 0$ = 1 Pa) and frequency (1 Hz), starting from pregel mixtures immediately after their preparation, by using a Bohlin CS10 controlled-stress rheometer (UK) provided with concentric cylinders geometry 14.1 mm in diameter. In these experiments, G′ and G″ were monitored for 1 h. Three different samples were measured to ensure the statistical significance of the results. The mean values and standard deviations of each magnitude are provided in this work.

Rheological Characterization of Composites

Mechanical properties were characterized under oscillatory shear stress using a Bohlin CS10 controlled-stress rheometer (UK) provided with a plate−plate geometry 40 mm in diameter. We subjected the samples to frequency sweep tests of fixed shear stress ($\tau 0$ = 0.1 Pa) within the LVR and increasing frequency in the range of 0.1−10 Hz. From these measurements, we obtained the storage (G′) and loss (G″) moduli of the samples as a function of frequency within the LVR (mechanical spectra). Three different samples were measured to ensure the

statistical significance of the results. The mean values and standard errors of each magnitude are provided in this work.

Scanning Electron Microscopy (SEM)

Samples were deposited on SEM supports and then were coated with a fine carbon layer and examined by SEM using HITACHI, S-510 equipment.

X-ray Powder Diffraction

XRPD data were collected on a Bruker D2 PHASER Bruker diffractometer: Cu Kα radiation (λ = 1.5418 Å), measurement range 2θ = 5–35°, time per step = 1.0, and step size = 0.02°. Prior to each measurement, the samples were manually ground in an agate mortar and then deposited in the hollow of a zero-background silicon sample holder.

Nitrogen Adsorption Experiments

The nitrogen adsorption isotherms were measured at 77 K on Micromeritics Tristar 3000 and 3-flex volumetric instruments. In the case of the MOF-808-based materials, the samples were heated for 8 h at 333 K and outgassed to 10−1 Pa before the adsorption measurements.

In the case of the ZIF-8-based materials, namely, ZIF-8 nanoparticles, Fmoc-FF gel, and ZIF-8 composite of Fmoc-FF 10 mM and ZIF-8 composite of Fmoc-FF 20 mM, the materials were soaked in MeOH (15 mL) for 3 days, replacing the solvent with fresh MeOH every 24 h. Afterward, the materials were heated for 12 h under dynamic vacuum (10−1 Pa) before the adsorption measurements.

Optical Microscopy

Optical images were recorded using the Image-Focus-Alpha software of the Nikon AZ100 microscope with a zoom of 1 × 1 × 0.6 for MOF-808 and a zoom of 1 × 2 × 0.6 for ZIF-8. The time lapse between each drop of water (5 μL) was 2 min for both MOFs. The final photo was taken after 15 h for MOF- 808 and after 1 h for ZIF-8 due to its decay.

Confocal Laser Scanning Microscopy

Supramolecular peptide hydrogels and MOF biocomposites were studied using an Inverted Microscope Leica DMI6000 at a fixed excitation wavelength of 405 nm and an emission read range of 510−545 nm. Samples were observed in their hydrated state.

Swelling Ratio Calculations

The sample of dried ZIF-8 was weighted in a high-precision balance before starting the swelling experiment and after the addition of 15 μL of water. The calculation of the swelling ratio (SR) was made using the following formula:

$$\%\, SR = \frac{dry\ compound\ weight}{rehydrated\ compound\ weight} x\ 100$$

Equation 10. Swelling ratio.

Supporting Information

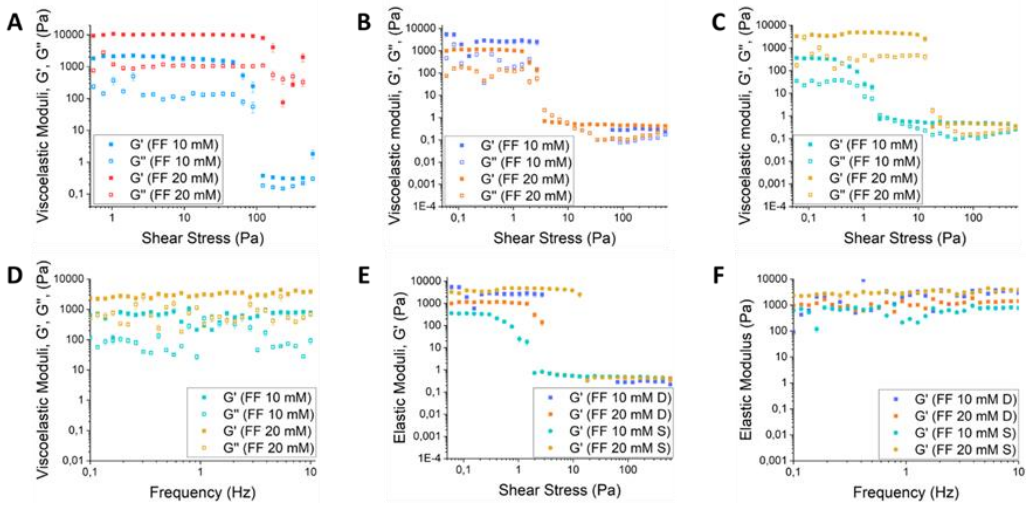

Figure 94. a) Evolution of viscoelastic moduli as a function of shear stress at a constant frequency of 1 Hz of Fmoc-FF hydrogels (10 mM (blue) and 20 mM (red)) formed by the addition of $Zn(AcO)_2$; b) Evolution of viscoelastic moduli as a function of shear stress at a constant frequency of 1 Hz of ZIF-8 composites formed by diffusion protocol (Fmoc-FF 10 mM and HmIm:Zn ratio of 5:1 (violet) and Fmoc-FF 20 mM and HmIm:Zn ratio of 5:1 (orange); c) Evolution of viscoelastic moduli as a function of shear stress at a constant frequency of 1 Hz of ZIF-8 composites formed by simultaneous protocol (Fmoc-FF 10 mM and HmIm:Zn ratio of 5:1 (cyan) and Fmoc-FF 20 mM and HmIm:Zn ratio of 5:1 (mustard); d) Evolution of viscoelastic moduli as a function of frequency at a constant stress of 0.1 Pa of ZIF-8 composites formed by simultaneous protocol (Fmoc-FF 10 mM and HmIm:Zn ratio of 5:1 (cyan) and Fmoc-FF 20 mM and HmIm:Zn ratio of 5:1 (mustard); e) Comparison of the values of the elastic modulus as a function of shear stress of ZIF-8 composites under a constant frequency of 1 Hz; f) Comparison of the values of the elastic modulus as a function of frequency of ZIF-8 composites under a constant shear stress of 0.1 Pa.

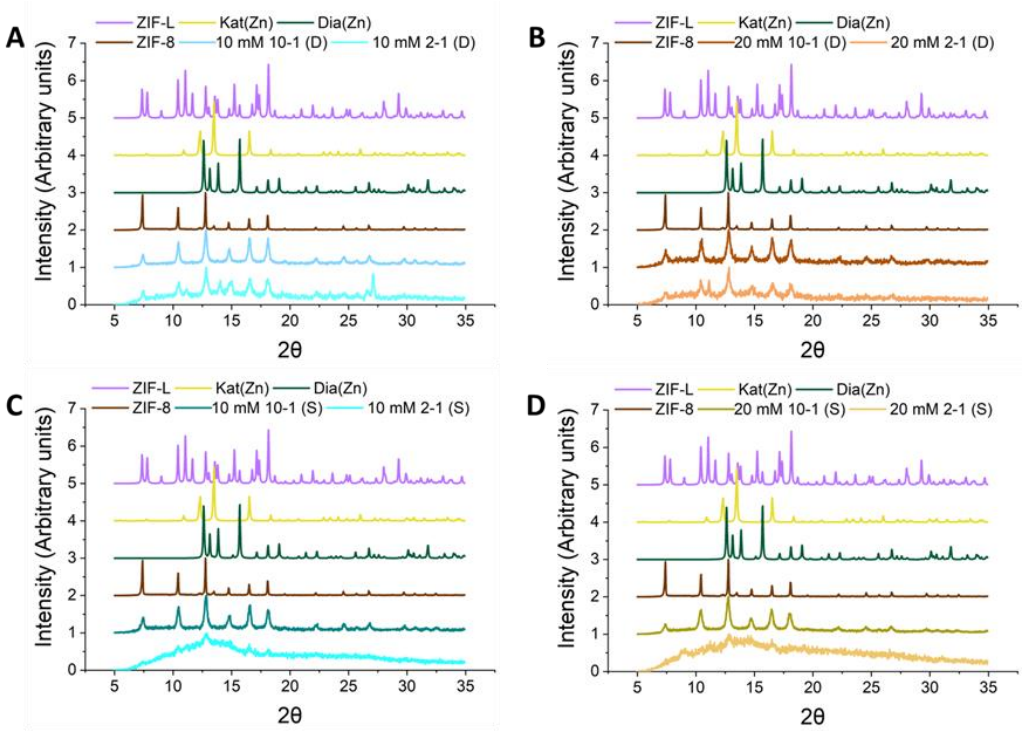

Figure 95. XRPD of ZIF-8 composites obtained in Fmoc-FF hydrogel at different concentrations and protocols compared with the different forms of Zn-MOF obtained in water: in violet ZIF-L, in yellow Kat(Zn), in dark green Dia(Zn), in brown ZIF-8 obtained in water. a) ZIF-8 formed by diffusion protocol (Fmoc-FF 10 mM and HmIm:Zn ratio of 10:1 (light blue) and Fmoc-FF 10 mM and HmIm:Zn ratio of 2:1 (cyan)); a) ZIF-8 formed by diffusion protocol (Fmoc-FF 20 mM and HmIm:Zn ratio of 10:1 (dark orange) and Fmoc-FF 20 mM and HmIm:Zn ratio of 2:1 (light orange)); c) ZIF-8 formed by simultaneous protocol (Fmoc-FF 10 mM and HmIm:Zn ratio of 10:1 (turquoise) and Fmoc-FF 10 mM and HmIm:Zn ratio of 2:1 (cyan)); d) ZIF-8 formed by simultaneous protocol (Fmoc-FF 20 mM and HmIm:Zn ratio of 10:1 (gold) and Fmoc-FF 20 mM and HmIm:Zn ratio of 2:1 (pumpkin)).

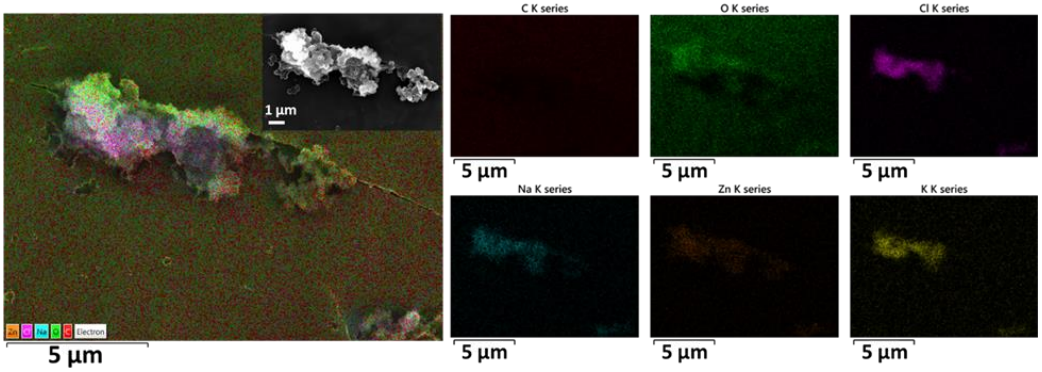

Figure 96. Energy Dispersive Spectroscopy (EDX) analysis of ZIF-8 composites (Fmoc-FF 10 mM, HmIm:Zn ratio of 5:1).

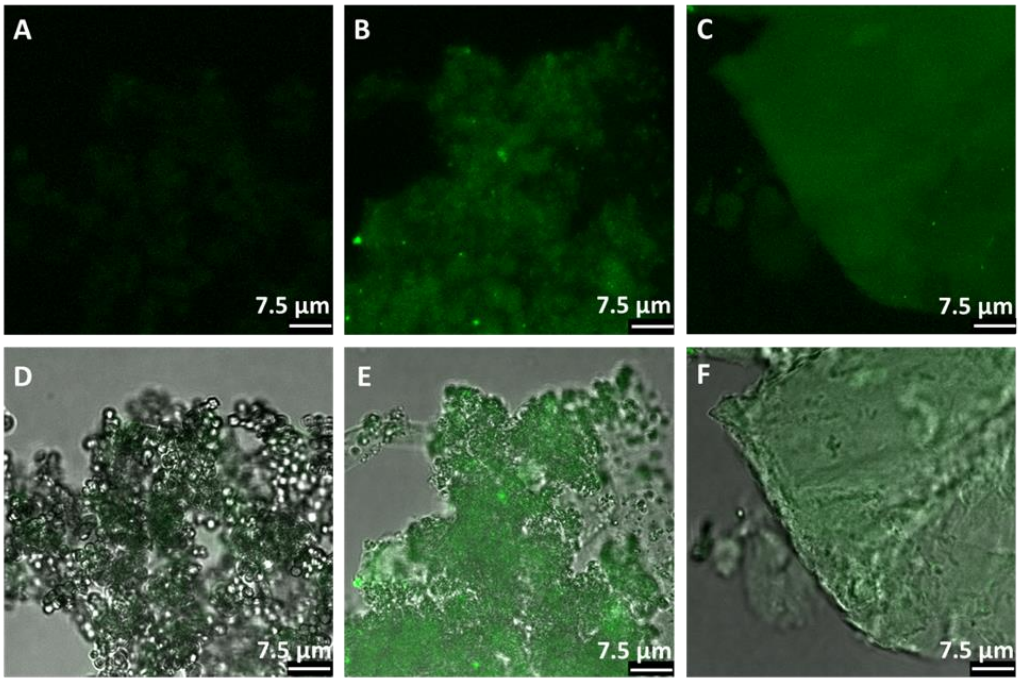

Figure 97. CLSM of a) and d) ZIF-8 grown in water; b) and e) ZIF-8 grown in Fmoc-FF hydrogel formed by diffusion protocol (Fmoc-FF 20 mM and HmIm:Zn ratio of 5:1); c) and f) Fmoc-FF 20 mM hydrogel. a-c) are fluorescence images and d-f) are the overlay with their corresponding visible images.

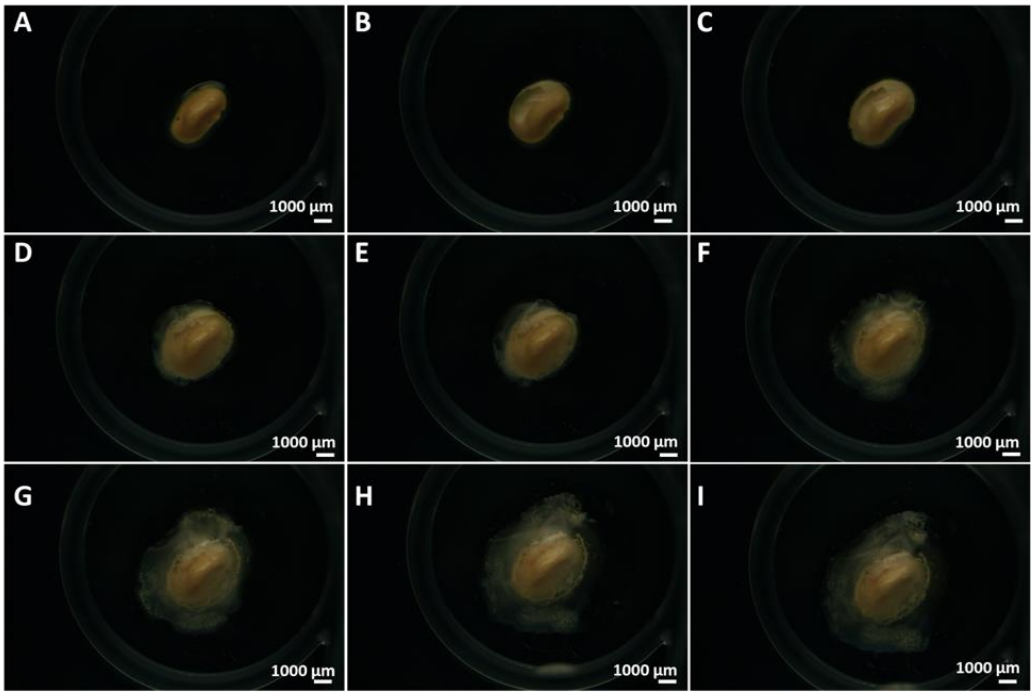

Figure 98. Optical pictures of ZIF-8 composite material: A) after slow-drying (37 ºC 48 h); B) after adding 5 µL of water; C) after 30 s in contact with 5 µL of water; D) after 60 s in contact with 5 µL of water E) after 90 s in contact with 5 µL of water; F) after adding another 5 µL of water (10 µL total); G) after adding another 5 µL of water (15 µL total); H) after adding 15 µL of water (30 µL total); I) after 1 h in contact with 30 µL of water.

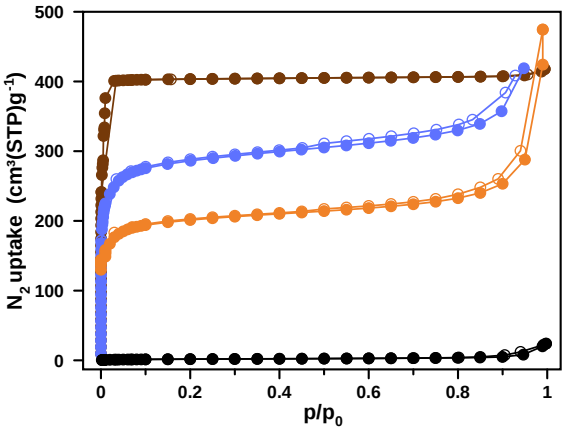

Figure 99. N_2 adsorption isotherms at 77 K of ZIF-8 nanoparticles (brown circles), Fmoc-FF xerogel (black circles) and ZIF-8 composites of Fmoc-FF 10 mM (blue circles) and of Fmoc-FF 20 mM (orange circles).

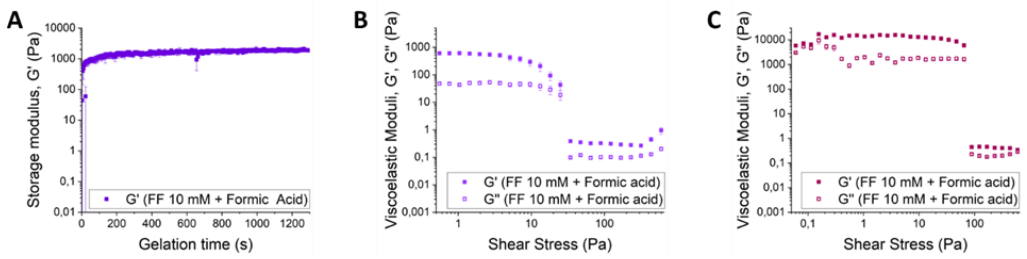

Figure 100. a) Evolution of storage modulus (G′) during gelation for Fmoc-FF hydrogels (10 mM) formed with formic acid; b) Evolution of viscoelastic moduli as a function of shear stress of Fmoc-FF hydrogels with formic acid under a constant frequency of 1 Hz; c) Evolution of viscoelastic moduli as a function of shear stress of MOF-808 composite (Fmoc-FF 10 Mm) under a constant frequency of 1 Hz.

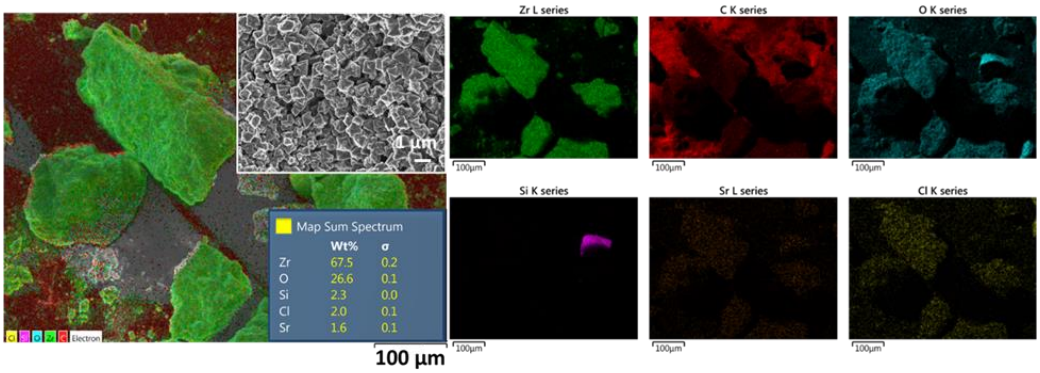

Figure 101. EDX analysis of MOF-808 composites (Fmoc-FF 10 Mm).

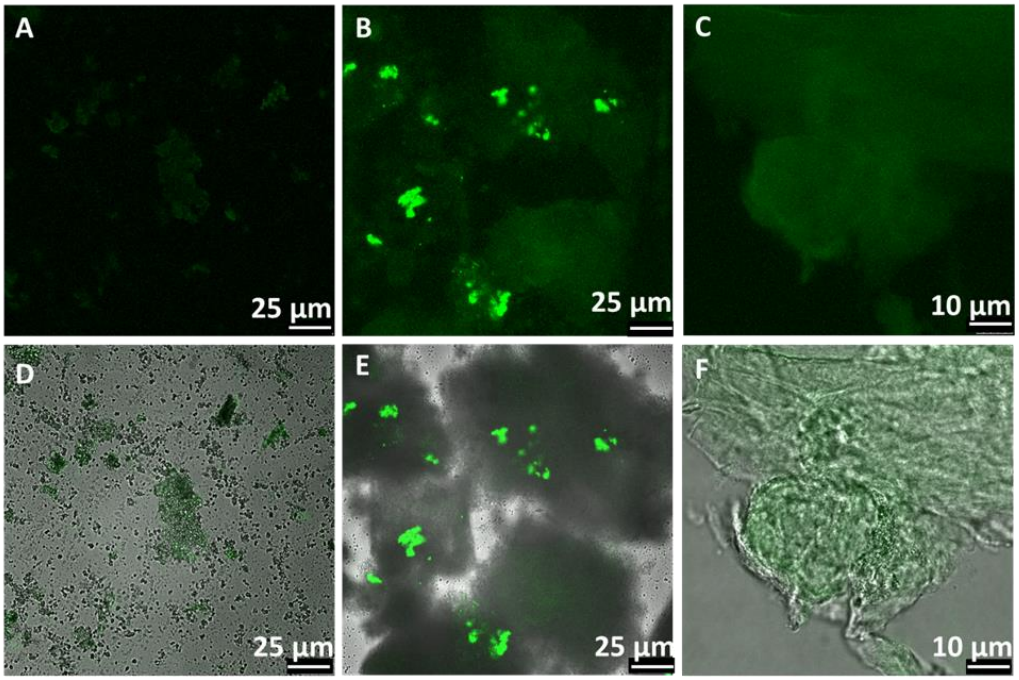

Figure 102. CLSM of a) and d) MOF-808 grown in water; b) and e) MOF-808 grown in Fmoc-FF hydrogel (10 Mm); c) and f) Fmoc-FF 10 mM hydrogel formed with formic acid. a-c) are fluorescence images and d-f) are the overlay with their corresponding visible images.

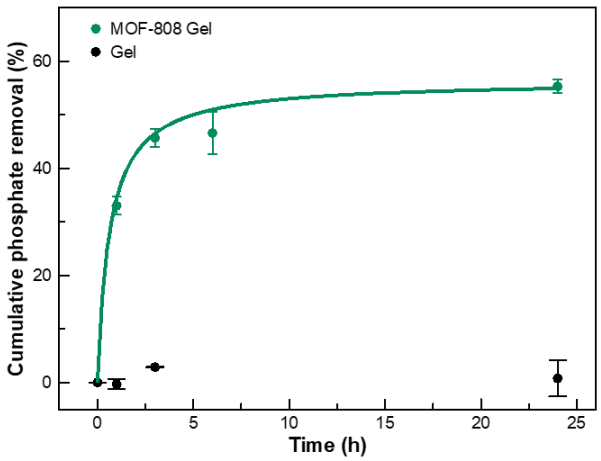

Figure 103. Cumulative phosphate adsorption of MOF-808 peptide hydrogel (green circles) and peptide hydrogel (black circles) at room temperature.

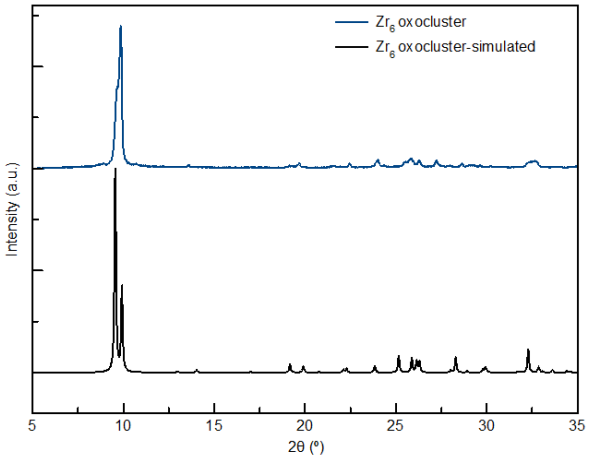

Figure 104. XRPD of Zr_6 oxocluster as synthesized (curve line) and simulated (black line).

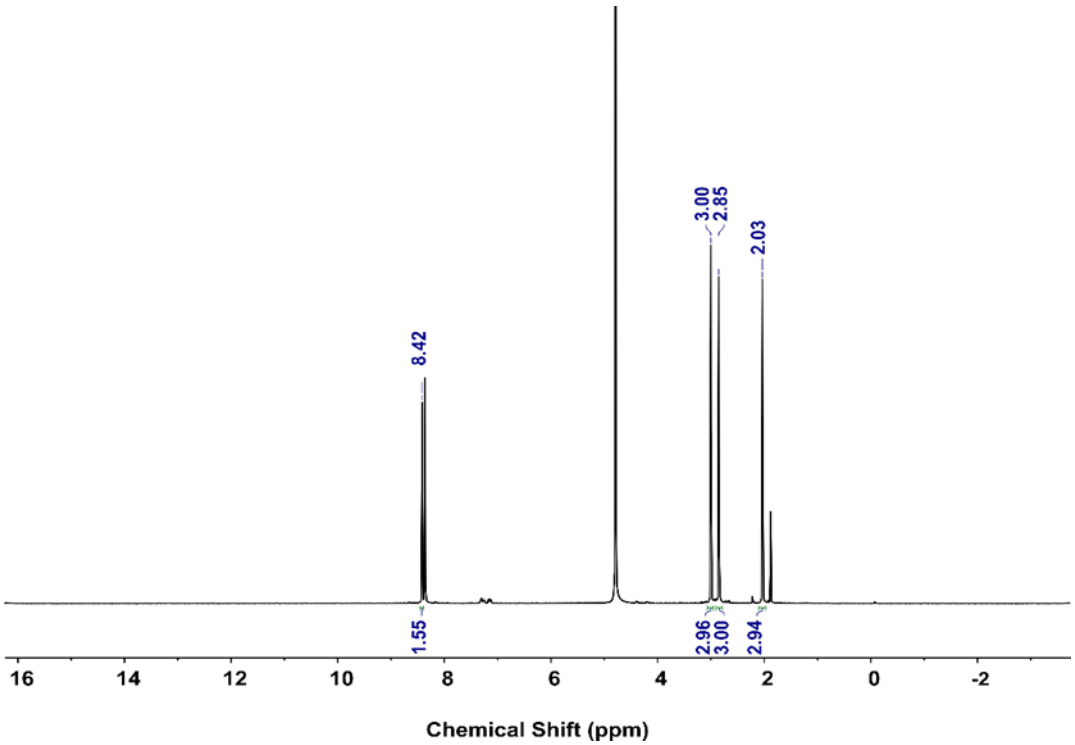

Figure 105. ^{1}H-NMR spectrum of the solution after the digestion of MOF-808-gel (20 mg) with NaOD 1 M during 24 hours at 25 ºC. Internal Reference: Dimethylacetamide (DMA, 0.028 M). The signal at δ = 8.42 is assigned to trimesate ions (3H).

5. Chapter 5. Antibacterial Activity

Formation of composite supramolecular hydrogels

To obtain the composite hydrogels formed with Fmoc-FF, collagen and Fmoc-RGD, they were mixture following this sequence with a ratio of 3.5:5:1.5 and for a final concentration of 6,95 mg/mL of the organic materials.

Formation of Hybrid Hydrogels

To obtain the hybrid hydrogels with Fmoc-FF, metallic salt of gold and silver were added to the basic solution of the peptide, inducing gelation (for the concentration of 1.18-2.76 mg/mL for Au3+ and 0.51-1.19 mg/mL for Ag+, for the less concentrated sample, hydrogels are not obtained). The final concentration of Fmoc-FF in all samples was 10 mM and and for salts, a screening was carried out with the following concentrations:

Cations			
Metal	**Equivalents**	**[Metallic salt] (mg/mL)**	**[Metallic salt] (ppm)**
Au^{3+} (100 mM)	0.01, 0.05, 0.1, 0.3, 0.5, 0.7	0.04, 0.20, 0.39, 1.18, 1.97, 2.76	40, 200, 390, 1180, 1970, 2760
Ag^{+} (100 mM)	0.01, 0.05, 0.1, 0.3, 0.5, 0.7	0.02, 0.08, 0.17, 0.51, 0.85, 1.19	20, 80, 170, 510, 850, 1190

To obtain the hybrid hydrogels with the composite formed with Fmoc-FF, Fmoc-RGD and collagen, the sequence of mixture was Fmoc-FF, collagen, metallic salt of gold and silver and, finally, Fmoc-RGD, inducing gelation for all concentrations due to the drop in the pH values because of the addition of Fmoc-RGD.

Rheological characterization of hydrogels

Mechanical properties were characterized under oscillatory shear stress using a Bohlin CS10 controlled-stress rheometer (UK) provided with a plate-plate geometry of 40 mm of diameter. We subjected the samples to frequency sweep tests of fixed shear stress (⊚0 = 1 (Pa)) within the Linear Viscoelastic Region (LVR) and increasing frequency in the range 0.1–10 Hz. From these measurements, we obtained the storage (G′) and loss (G′′) moduli of the samples as a function of frequency within the LVR (mechanical spectra). Three different samples were measured to ensure statistical significance of the results. The mean values and standard deviations of each magnitude were provided in this work. Gelation kinetics were investigated by oscillatory shear under fixed stress (⊚0 = 1 Pa) and frequency (1 Hz), starting from pre-gel mixtures immediately after their preparation, by using a Bohlin CS10 controlled-stress rheometer (UK) provided with concentric cylinders geometry of 14.1 mm of diameter. In these experiments, G′ and G′′ were monitored for 1 h. Three different samples were measured to ensure statistical significance of the results. The mean values and standard deviations of each magnitude were provided in this work.

Uv-Vis spectrophotometry

Fourier transform infra-red (FT-IR) spectroscopy

Spectra were recorded using a Perkin-Elemer Two FT-IR ATR spectrometer. The hydrogels were dryed at room temperature to obtain the xerogels and then they were compressed onto the diamond crystal. All spectra were scanned over the range between 4000 and 450 cm^{-1}.

Supporting information

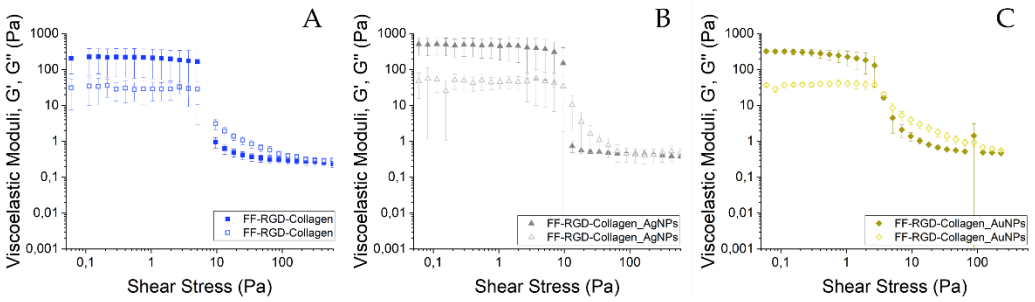

Figure 106. Final amplitude sweeps spectra for a) composite (Fmoc-FF + Fmoc-RDG + collagen) hydrogels, b) composite + AgNPs hydrogels and c) composite + AuNPs hydrogels.

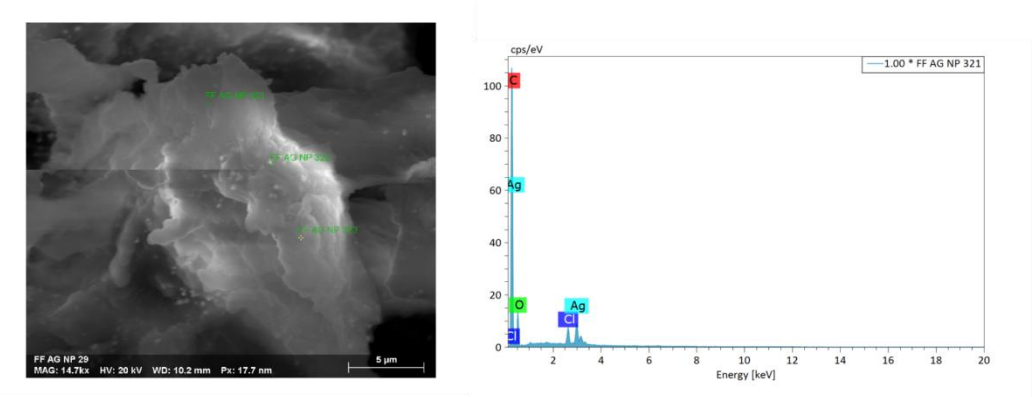

Figure 107. Elemental analysis in Fmoc-FF + Fmoc-RGD + collagen hydrogels with AgNPs (0.01 eq.)

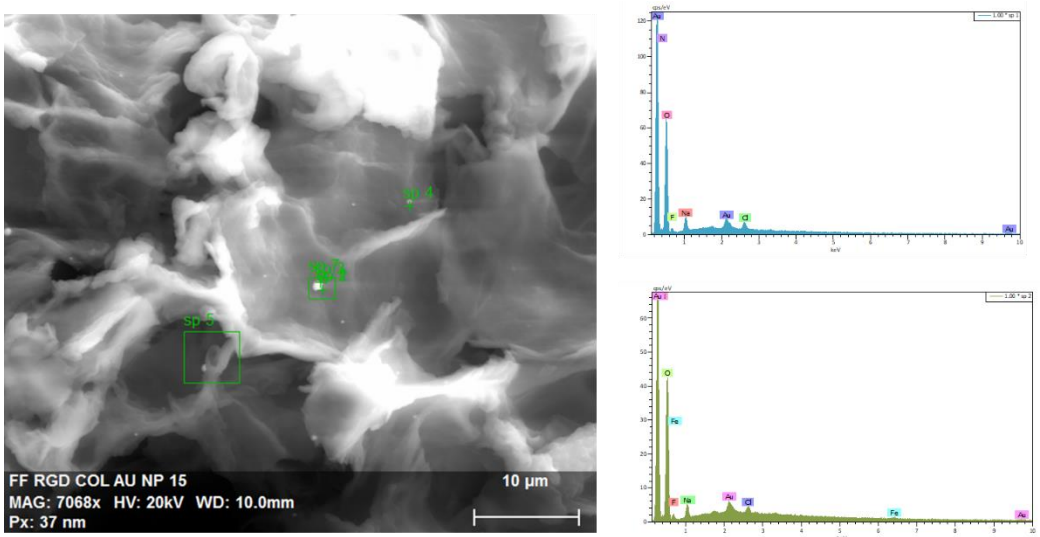

Figure 108. Elemental analysis in Fmoc-FF + Fmoc-RGD + collagen hydrogels with AuNPs (0.01 eq.)

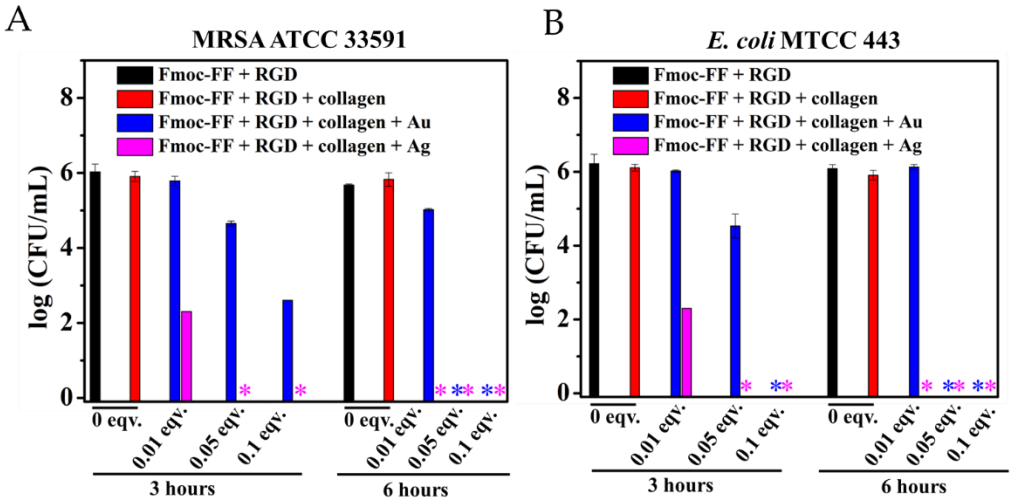

Figure 109. Antibacterial tests against a) *Staphylococcus aureus methicillin-resistant (MRSA)* and b) *Escherichia coli.*

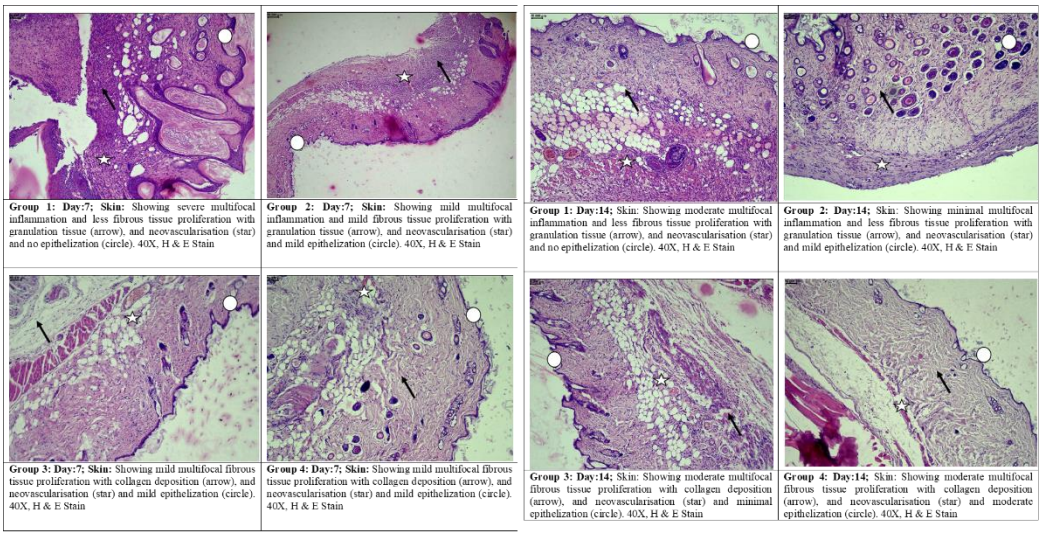

Figure 110. Histopathology analysis.

6. Chapter 6. Composite protein crystals

6.1. Protein Crystals and Supramolecular Hydrogels as Dual Sources for Investigating the CISS Effect

Hydrogel Control Preparation

N-Fluorenylmethoxycarbonyl-L-diphenylalanine (Fmoc-L-FF) was purchased from Bachem Co., Switzerland and was used without further purification. N-Fluorenylmethoxycarbonyl-D-diphenylalanine (Fmoc-D-FF) was purchased from LifeTein, USA and was used without further purification. N-Fluorenylmethoxycarbonyl-diglycine (Fmoc-GG) was purchased from Fluorochem, UK and was used without further purification. Fmoc-FF (L or D chiral) and Fmoc-GG peptides were weighed separately into vial and deionised water were added to obtain a final

concentration of 0.5% (w/v). This suspension was then sonicated (in a HSt Powersonic 603-ultrasonic bath) for 1 hour. NaOH solution 0.5 M was then added dropwise and an aqueous basic solution was obtained (pH ≈ 10.5). Gelation was induced by adding 2 molar equivalents of glucono-δ-lactone (GdL) and mixed by vortexing. Full gelification was achieved after 12 h at room temperature.

Composite Hydrogel Preparation

A suspension of SWCNTs was prepared weighting 0.7 mg of SWCNTs (single wall carbon nanotubes, Sigma-Aldrich, 308068-56-6, ~95% semiconducting with ~41% having (6,5) chirality) into a vial tube. The carbon nanotubes were suspended in 1 mL of an aqueous basic solution of Fmoc-FF (L or D chiral) or Fmoc-GG 0.5% w/v (prepared as above). The suspension was then sonicated for 2 h in a cold ultrasonic bath and then centrifuged for 5 min at 10.000 rpm (Sigma 1-14 centrifuge). Finally, the supernatant was collected carefully. Gelation was then carried out following the same method described above for the hydrogel control. Protocol for the production of Fmoc-FF hydrogels having 0.5 mg of SWCNTs or less can be found in our previous work.

Crystallization Protocol

A commercial lysozyme (HEWL chicken) was used as a lyophilized powder from Sigma and dissolved in 50 mM of sodium acetate pH 4.5. The concentration of the lysozyme was determined spectrophotometrically at 280 nm using ε = 2.65 mL mg^{-1} cm^{-1}. Crystallization experiments were carried out using the counterdiffusion technique in the two-chambers

method in Eppendorf tubes following the protocol described elsewhere. Composite hydrogels were dialyzed against 100 μL of Milli-Q water for one week, changing the water every day. Next, 100 μL of the buffered protein solution, at 120 mg mL^{-1}, was added on top of the hydrogels and they were allowed to diffuse at 20 °C for one week. After that time, the solution was replaced by 100 μL of precipitant solution (5-7% w/v sodium chloride in 50 mM sodium acetate, pH 4.5) and allowed to diffuse at 20 °C. Eppendorf were kept in incubators at 20 °C and periodically observed with the aid of an optical microscope. The first crystals appeared earlier than 24 hours reaching their maximum size in a week. The largest dimension of the grown crystals was 60 μm.

Cross-Linking Protocol

CLLC were obtained by diffusing the crosslinker throughout the crystallization chamber. The precipitant solution was replaced by an isotonic solution containing 5% v/v glutaraldehyde as a crosslinking agent and allowed to diffuse at 20 °C for 24 h. After that time, the hydrogel containing the crystals was extracted into a Petri dish filled with Milli-Q water. The crystals were removed from the gel with the aid of a brush and micro-tools, collected and stored in Milli-Q water in an Eppendorf tube at 20 °C.

Devices fabrication for transport experiments

The SWCNT@CLLC crystals were embedded in epoxy resin EMbed-812 (Electron Microscopy Sciences, USA) and placed in a 60 °C oven for 48–72 hours for polymerization. Serial ultrathin sections (~100–900 nm range) were sliced sequentially by a Reichert Ultracut S microtome (Leica Microsystems, Germany). Next, the sections were transferred on Au-Au and Ni-Au electrodes (electrode thickness ~100 nm, electrode gap ~2 μm) photolithographically patterned on SiO_2 (500 nm)/Si wafer. Finally, the devices were vacuum annealed (200 ºC for 30 min) to improve electrical contacts between the electrodes and the transferred sections.

Raman Spectroscopy

For Raman characterization, the sections were placed on glass substrates. Data were collected using Thermo Scientific DXR2 Raman Microscope, 100X confocal, 532 nm laser, and 5 mW power.

Transmission electron microscopy

The crystals were studied with a Carl Zeiss POUND 120 PLUS. The cross-linked lysozyme crystals (CLLC) with nanotubes (SWCNT@CLLC) were dehydrated with ethanol and embedded in Embed 812 resin. Ultrathin sections (50-70 nm) were prepared using a Reichert Ultracut S microtome (Leica Microsystems GmbH, Wetzlar, Germany), after which the sections were deposited on copper grids.

Scanning electron microscopy (SEM)

SEM Images of SWCNT@CLLCs cut with a scalpel were put on an adhesive surface, coat with a fine carbon layer and examined by SEM using a field emission scanning electron microscope (FESEM) GEMINI, LEO 1500 Carl Zeiss.

Optical Microscopy

Optical images were recorded using the Image-Focus-Alpha software of the Nikon AZ100 microscope with a zoom of 4x2x0.6.

6.2. Hybrid protein crystals grown in supramolecular hydrogels: development of a broad-spectrum antibacterial drug delivery vehicle

Crystallization Protocol

A commercial lysozyme (HEWL chicken) was used as a lyophilized powder from Sigma and dissolved in 50 mM of sodium acetate pH 4.5. The concentration of the lysozyme was determined spectrophotometrically at 280 nm using ε = 2.65 mL mg^{-1} cm^{-1}. Crystallization experiments were carried out using the counter diffusion technique in the two-chambers method in Eppendorf tubes following the protocol described elsewhere. First, 100 μL of the buffered protein solution, at 90 mg mL^{-1}, was added on top of the hydrogels and they were allowed to diffuse at 20 °C for one week. After that time, the solution was replaced by 100 μL of precipitant solution (2.7% w/v sodium chloride in 50 mM sodium acetate, pH 4.5) and allowed to diffuse at 20 °C. Eppendorf were kept in incubators at 20 °C and

periodically observed with the aid of an optical microscope. The first crystals appeared earlier than 24 hours reaching their maximum size in a week.

Cross-Linking Protocol

CLLC were obtained by diffusing the crosslinker throughout the crystallization chamber. The precipitant solution was replaced by an isotonic solution containing different ratios (0.1, 0.5, 1.0, 2.5, 5.0 % (V/V)) of glutaraldehyde as a crosslinking agent and allowed to diffuse at 20 °C for different times (1, 5, 15, 30, 60 min). After that time, an isotonic solution of Tris pH 7.0 was added to stop the glutaraldehyde reaction.

Dissolution rate

Formation of Hybrid Hydrogels

To obtain the hybrid hydrogels with Fmoc-FF, metallic salt of gold and silver were added to the basic solution of the peptide, inducing gelation (for the concentration of 1.18-2.76 mg/mL for Au3+ and 0.51-1.19 mg/mL for Ag+, for the less concentrated sample, hydrogels are not obtained). The final concentration of Fmoc-FF in all samples was 10 mM and and for salts, a screening was carried out with the following concentrations.

Transmission electron microscopy

The crystals were studied with a Carl Zeiss POUND 120 PLUS. The cross-linked lysozyme crystals (CLLC) with nanotubes (SWCNT@CLLC) were dehydrated with ethanol and embedded in Embed 812 resin. Ultrathin sections (50-70 nm) were prepared using a Reichert Ultracut S microtome (Leica Microsystems GmbH, Wetzlar, Germany), after which the sections were deposited on copper grids.

<u>Supporting information</u>

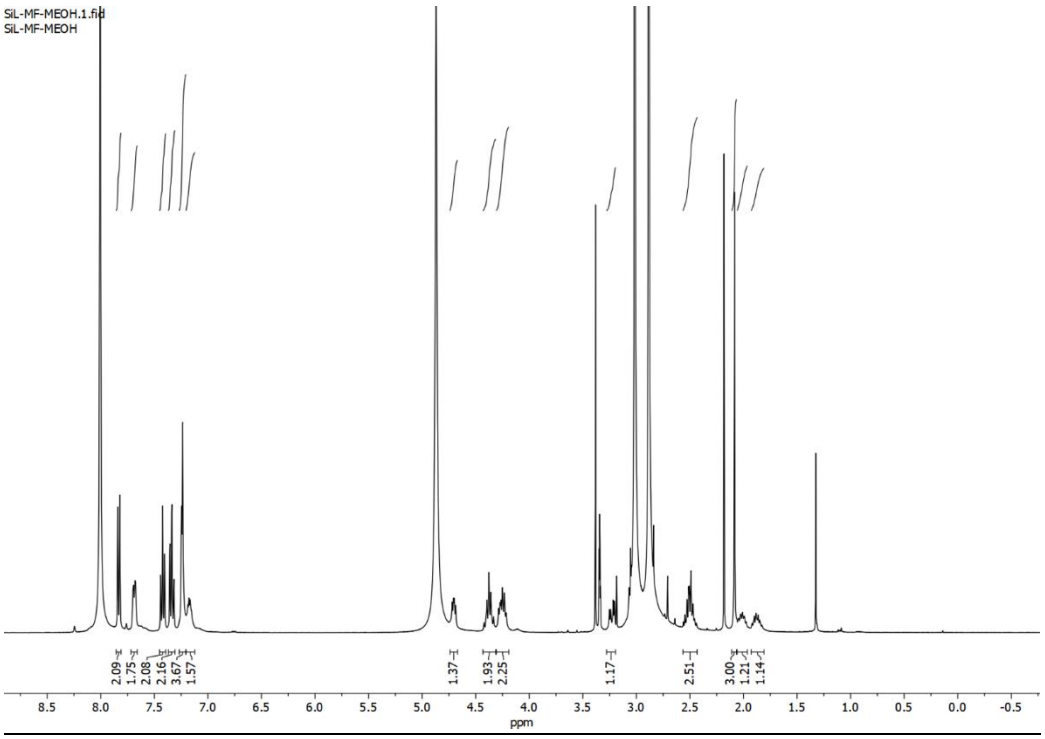

Figure 111. ^{1}H NMR of Fmoc-MF.

6.3. Protein crystals as platforms for bioorthogonal chemistry

Obtention of seeds

First, a stock solution of lysozyme at 150 mg/mL theoretical concentration is prepared and crystallized following the general procedure of batch without gel media. Lysozyme is mixed with sodium chloride and sodium acetate 50 mM, pH 4.5 to reach a final concentration of 40 mg/mL for protein and 2.7 % (w/V) for NaCl. The mix is incubate at 20°C until crystals form.

Using a cat whisker, separate the crystals from the walls of the Eppendorf tube and centrifuge at 10,000 RPM for 1 minute. Using a glass rod or microballs, grind the crystals until no crystalline particles can be distinguished under the magnifying glass or for the specified time.

Seeding in gelled batch of agarose 0.2 % (w/V)

First, agarose solution is prepared by adding 50 mg of Agarose D5 to a 15 mL Falcon tube and 5 mL of water to achieve a final concentration of 1% (w/v). Then, the tube is placed in a baker, cover it with water, and heat it in the microwave until the water boils. Manually stir until the agarose is fully dissolved, reheat to boiling, and stir again. The agarose solution is kept at 70 °C.

To prepare the stock solution, the required volume of lysozyme, buffer, and salt is taken, placed in separately Eppendorf tubes, and maintain them at 40 °C. Then the calculated volume of buffer is added to an Eppendorf

tube and kept at 40 °C. Then, the lysozyme addition carries out to the buffer, homogenized, and kept at 40 °C. After this, the salt is added to the stock solution and homogenized, maintaining at 40 °C. The necessary volume of agarose is added to the solution and homogenized. Finally, the seed suspension is added, homogenized, and kept at 20 °C for 24 hours. Last step is lyophilized the obtained crystals to recover them from the gel.

Functionalization with Pd (II)

Reduction of Pd (II) to Pd (0)

Appendices

1. List of publications

This section comprises the articles published as a result of the research conducted during the pre-doctoral stage.

"Interactions Between Peptide Assemblies and Proteins for Medicine." Mañas-Torres, M. C.; Illescas-Lopez, S.; Gavira, J.A.; Álvarez de Cienfuegos, L.; Marchesan, S. *Isr. J. Chem.* **2022**, e202200018.

"Chirality-Induced Spin Selectivity in Heterochiral Short-Peptide-Carbon-Nanotube Hybrid Networks: Role of Supramolecular Chirality." Rahman, M. W.; Mañas-Torres, M. C.; Firouzeh, S.; Illescas-Lopez, S.; Cuerva, J. M.; Lopez-Lopez, M. T.; de Cienfuegos, L. Á.; Pramanik, S. *ACS Nano* **2022**, 16 (10), 16941–16953.

"Short-Peptide Supramolecular Hydrogels for In Situ Growth of Metal–Organic Framework-Peptide Biocomposites" Illescas-Lopez, S.; Martin-Romera, J. D.; Mañas-Torres, M. C.; Lopez-Lopez, M. T.; Cuerva, J. M.; Gavira, J. A.; Carmona, F. J.; Álvarez de Cienfuegos, L. *ACS Appl. Mater. Interfaces* **2023**, 15 (27), 32597–32609.

"Transverse Magnetoconductance in Two-Terminal Chiral Spin-Selective Devices" Hossain, M. A.; Illescas-Lopez, S.; Nair, R.; Cuerva, J. M.; Álvarez de Cienfuegos, L.; Pramanik, S. *Nanoscale Horizons* **2023**, 8 (3), 320–330.

"Chirality-Induced Spin Selectivity in Functionalized Carbon Nanotube Networks: The Role of Spin-Orbit Coupling" Firouzeh, S.; Illescas-Lopez, S.; Hossain, M. A.; Cuerva, J. M.; Álvarez de Cienfuegos, L.; Pramanik, S. *J. Chem. Phys.* **2023**, 159 (3).

"Chirality-Induced Spin Selectivity in Supramolecular Chirally Functionalized Graphene" Firouzeh, S.; Illescas-Lopez, S.; Hossain, M. A.; Cuerva, J. M.; Álvarez de Cienfuegos, L.; Pramanik, S. *ACS Nano* **2023**, *17* (20), 20424–20433.

"Efficient Transfer of Chirality in Complex Hybrid Materials and Impact on Chirality-induced Spin Selectivity" Hossain, M. A.; Illescas-Lopez, S.; Rahman, M. W.; Mañas Torres, M. C.; Contreras-Montoya, R.; Firouzeh, S.; Gavira, J.A.; Álvarez de Cienfuegos, L.; Pramanik, S. (*Manuscript submitted)*

2. List of figures